Hydrothermally Etched Titanium for the Mitigation of Implant Associated Infection

By

Andrew Hayles
BSc. Biomedical Science

Thesis
Submitted to Flinders University
for the degree of

Doctor of Philosophy (PhD)
College of Medicine and Public Health
28/08/2023

TABLE OF CONTENTS

ABSTRACT

The growing demand for titanium-based implants and the subsequent rise in implant-associated infections necessitates novel developments in anti-infective technologies. Recent research has drawn inspiration from nature to solve this problem. The nanoscale topography observed on cicada and dragonfly wings serves as a blueprint for synthetic analogues which seek to kill bacteria on contact through mechanical forces. This type of interaction has been dubbed the mechano-bactericidal effect. Various techniques have been utilized to mimic and improve-upon these natural bactericidal surfaces. Alkaline hydrothermal etching is a simple and cost-effective technique to fabricate nanoscale protrusions on titanium and its alloys.

In recent years, hydrothermally etched titanium, along with similar nanostructured surfaces, has been the focus of much research. Currently, the existing literature is centred around the capacity for these mechano-bactericidal surfaces to eliminate pathogens relevant to orthopaedic implant-associated bacterial infections in an aerobic environment. However, there is much to learn regarding the interactions between hydrothermally etched titanium and fungal species, anaerobic dental pathogens and multi-species infections. Furthermore, it may be possible that the mechano-bactericidal effect could be harnessed to augment existing antibiotic treatments.

The research questions proposed herein are aimed at further elucidating these areas, such that a broader basis of knowledge can be built to facilitate the translation of these technologies into commercial outputs. Each section of the present thesis is based on publications that were submitted and accepted during candidature.

DECLARATION

I certify that this thesis:

1. does not incorporate without acknowledgment any material previously submitted for a degree or diploma in any university

2. and the research within will not be submitted for any other future degree or diploma without the permission of Flinders University; and

3. to the best of my knowledge and belief, does not contain any material previously published or written by another person except where due reference is made in the text.

Signed

Date............14/04/2023...............

ACKNOWLEDGEMENTS

First and foremost, I would like to thank Prof. Krasimir Vasilev, my principal supervisor. Krasi gave me the opportunity to lay the foundations for my career in research by hiring me to work on two impactful industry-based projects. I am appreciative of his supervision and support, which has allowed me to develop both academically and professionally. Being a part of his broad, diverse research group continues to be a highly worthwhile and productive experience.

I would also like to thank Mr. (soon to be Dr.) Richard Bright. Richard recommended me for a research position in the Vasilev group, which was the catalyst to initiate my research career. Richard has taught me many lab techniques and has guided me in many aspects of academia. He is both a colleague and a friend, and he is always good for a beer after the papers have been written. I would also like to acknowledge Dr. Dennis Palms, Dr. Jonathan Wood, Dr. Jafar Hasan and Dr. Daniel Fernandes, with whom I shared an office during the Corin and Anisop industry projects. Workdays were always enjoyable with these blokes, and many coffees were consumed between us. Another thanks is extended to Dr. Vi Khanh Truong, who always has good advice for emerging academics. An appreciative acknowledgement also goes to Assoc. Prof. Peter Zilm, who allowed me to gain my first real-world research experience in his laboratory, and who continues to offer valuable support. An honourable mention goes to Dr. Stephen Kidd who referred me to Peter Zilm at the end of my undergraduate studies.

I would also like to thank my loving wife, Pia Zhang（张飘飘）, who continues to support me in every corner of my life, and always brings out the best in me. Further, I would love to acknowledge my little boy Oliver Zhang Hayles (张安一). Despite being a cheeky toddler, he has the curiosity and wonder of a scientist.

I would like to express my gratitude to my mother, Carmel Vincent for raising me and encouraging me to pursue a career in science. Another thanks is extended to my grandpa Terry Durward, who always shows a keen interest in the work that I do.

LIST OF FIGURES

INTRODUCTION

CHAPTER 1

CHAPTER 2

CHAPTER 3

CHAPTER 4

LIST OF TABLES

INTRODUCTION

CHAPTER 1

CHAPTER 2

CHAPTER 3

CHAPTER 4

INTRODUCTION:

HYDROTHERMALLY ETCHED TITANIUM: A REVIEW ON A PROMISING MECHANO-BACTERICIDAL SURFACE FOR IMPLANT APPLICATIONS

Andrew Hayles[a], Jafar Hasan[a], Richard Bright[a], Dennis Palms[a], Toby Brown[b], Dan Barker[b], Krasimir Vasilev[a]*

[a]Academic Unit of STEM, University of South Australia, Mawson Lakes, Adelaide, 5095, South Australia, Australia.

[b]Corin Australia, Baulkham Hills, New South Wales, 2153, Australia

*Corresponding author email address: krasimir.vasilev@unisa.edu.au

Keywords: biomimetic, bioinspired, mechano-bactericidal, nanostructured, hydrothermal, titanium, implant

Published in Materials Today Chemistry, vol. 22 on 21st October 2021
https://doi.org/10.1016/j.mtchem.2021.100622

Abstract

The growing demand for titanium-based implants and the subsequent rise in implant-associated infections necessitates novel developments in anti-infective technologies. Recent research has drawn inspiration from nature to solve this problem. The nanoscale topography observed on cicada and dragonfly wings serves as a blueprint for synthetic analogues which seek to kill bacteria on contact through mechanical forces. This type of interaction has been dubbed the mechano-bactericidal effect. Various techniques have been utilized to mimic and improve-upon these natural bactericidal surfaces. Alkaline hydrothermal etching is a simple and cost-effective technique to fabricate nanoscale protrusions on titanium and its alloys. This review aims to consolidate the current knowledge surrounding how fabrication parameters lead to varying surface topographies on titanium substrates, and subsequently how surface topography and bacterial characteristics affect bactericidal activity. The bactericidal mechanism of hydrothermally etched titanium is inferred from comparisons with similar mechano-bactericidal biomaterials. The hostility of hydrothermally etched titanium towards bacteria is discussed in contrast to the observed host cell compatibility. Lastly, suggestions are made for the standardization of terminology in this emerging field.

1. Introduction

Titanium-based implants are one of the most widely used biomaterials for joint replacements, trauma fixation devices and dental implants. Titanium stands out among other biomaterials due to its strength, corrosion resistance, biocompatibility and osseointegration properties [1]. While titanium is a highly suitable biomaterial, it is not devoid of potential complications. Implanted medical devices are often compromised by bacterial and/or fungal pathogens, leading to acute and recurrent infections [2, 3]. Microbial invaders colonize implant surfaces and progressively form biofilms. Biofilms are commonly defined as aggregates of microbial cells adhered to each other or a surface, which are embedded in a matrix of extracellular polymeric substance (EPS) [4]. EPS is largely composed of polysaccharides, lipids, proteins, and extracellular DNA. Bacterial subcommunities can coordinate within a biofilm by secreting quorum sensing molecules into the surrounding EPS. One example of this is N-acyl homoserine lactone, which is secreted by Gram-negative bacteria and is believed to be associated with biofilm formation [5, 6]. The formation of EPS is a key virulence factor of bacteria which provides both structural and functional benefits [7]. Implant surfaces are an ideal substrate for bacteria to form biofilm. In part, this is because they are solid and do not shed material, as opposed to the surrounding host tissue, which has a high turnover of cells, making it difficult to establish long-term bacterial communities [8]. Reflecting on this, it is not surprising that fewer bacterial cells are required to infect rabbits when an implant is present [9]. Biofilm formation can be typically divided into 3 distinct events: attachment, maturation and dispersal **(Figure 1)** [10]. Attachment to a medical device surface is governed by an initial van der Waals attraction, followed by mechanical adhesion facilitated by adsorbed proteins. Maturation involves further proliferation and secretion of EPS. Late-stage biofilms then disperse aggregates of cells as well as individual planktonic bacteria which can act as vehicles for infecting additional sites. Once an implant-associated biofilm has matured to form EPS, it is able to evade the host immune response as well as assist bacteria to develop resistance to antimicrobial drugs [2, 4, 7]. This pathogenic persistence makes treatment difficult, often requiring further operative procedures and long-term antibiotic usage, which carries a danger of systemic toxicity and promotion of antimicrobial resistance [11, 12]. Due to the difficulty of treating an established implant infection, the most obvious solution is to develop measures that prevent this event occurring [13].

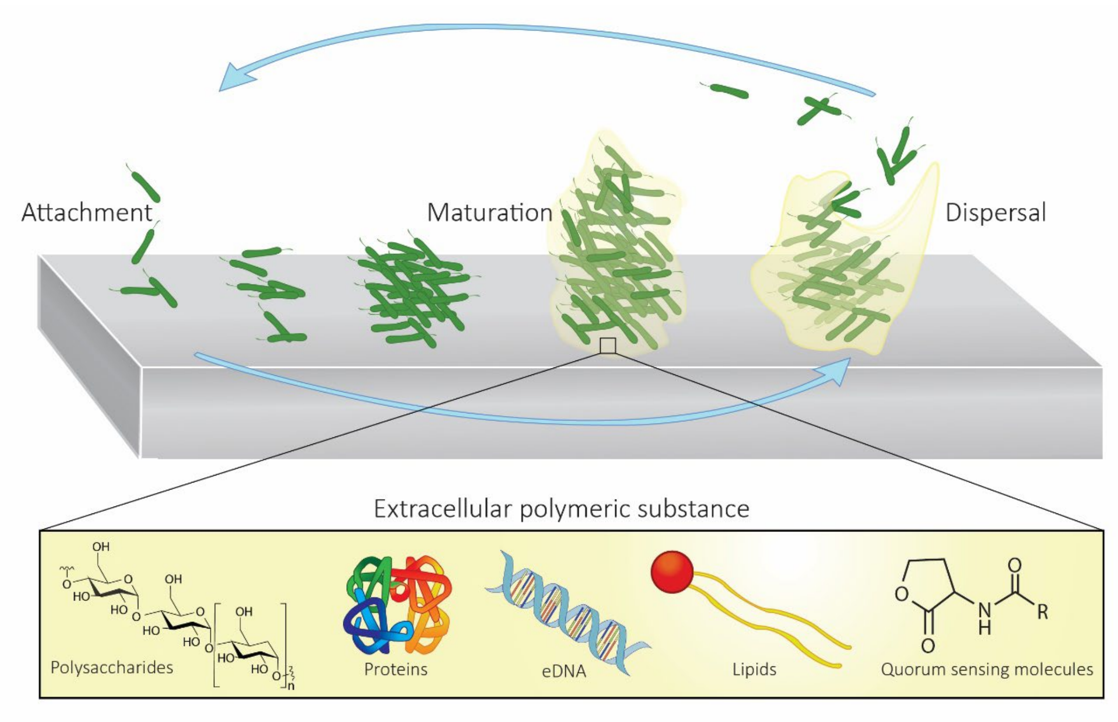

Figure 1. The establishment and lifecycle of a biofilm on a solid surface

Currently, preventative measures involve sterilization procedures of operating tools, the surgical site and the surgical theatre, laminar air flow, use of novel antimicrobial implants, as well as prophylactic antibiotic regimes [14-18]. However, while these procedures certainly help mitigate the risk of infection, they have not succeeded in eliminating the problem. There has been much research into the development of surfaces which can resist colonization of pathogens [19, 20]. By repelling or inactivating pathogens on contact, it may be possible for such surfaces to prevent the establishment of implant-associated infection. Various anti-infective surfaces have been generated, generally falling into two broad categories: surface coatings, where a physical or chemical layer is coated over the material surface and surface modification, where the chemical or physical makeup of the substrate is altered [13]. Surface coatings come in an extensive range of forms, from antifouling polymers which repel bacteria [21-23] to antimicrobial coatings which actively kill bacteria [24, 25]. These surfaces are beyond the scope of this review, but the interested reader is directed to more thorough reviews [24, 26, 27]. Surface modification can involve covalent grafting of antimicrobial compounds or bioactive molecules to the surface of the substrate, or modification of the topography of the substrate itself [28, 29]. The latter process has gained recent attention for its capacity to generate nanoscale structures which physically impede and inactivate bacterial cells. This has been termed the 'mechano-bactericidal' effect [30].

The mechano-bactericidal effect was first reported by Ivanova and colleagues, when they investigated the bactericidal nature of the wings of *Psaltoda claripennis* (a species of cicada) [31]. On the nanoscale, the cicada wing is covered by an ordered array of pillars, spaced 170 nm apart, with a height of 200 nm and a tip diameter of 60 nm. To rule out a surface chemistry-based mode of action, the wing surface was coated with a thin layer of gold, which did not influence the bactericidal efficacy. Since this pioneering report, mechano-bactericidal nanostructures have been observed to occur on multiple different species. Notable examples include the cicada wing [32, 33] dragonfly wing **(Figure 2)** [34, 35], and gecko feet [36].

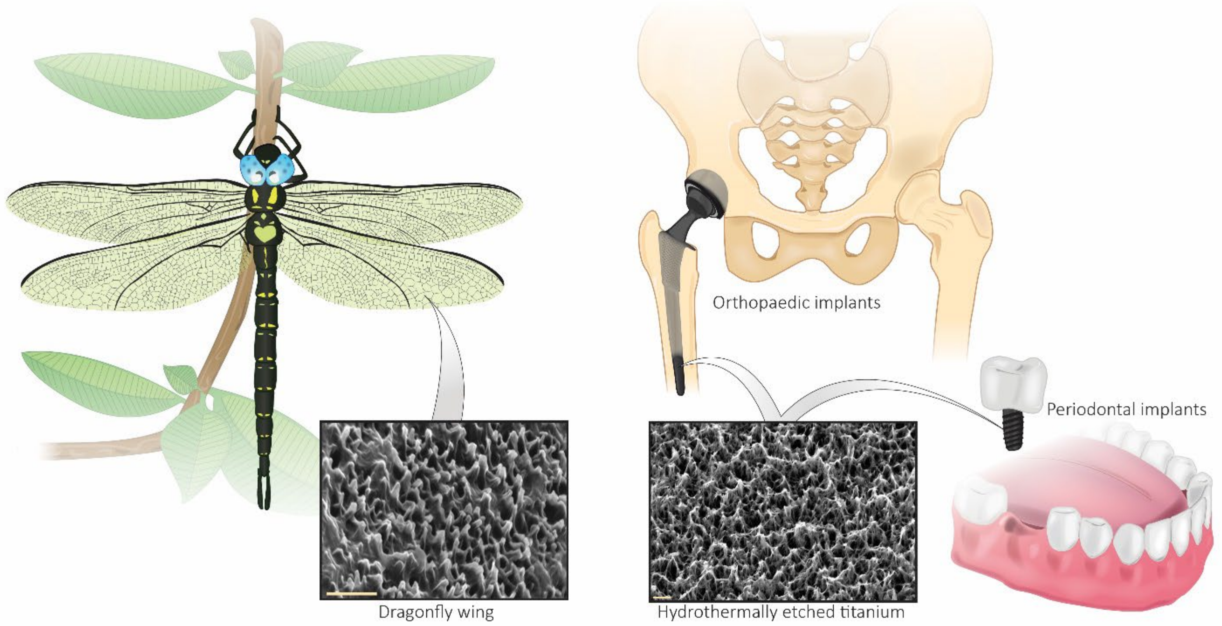

Figure 2. The nanoscale topography of hydrothermally etched titanium is inspired by the natural topography of the Dragonfly wing. Scale bars represent 1 μm.

The potential for mechano-bactericidal surfaces was soon realized and spurred an interest in developing synthetic analogues which could be fabricated on implantable devices [37]. Many such surfaces were fabricated with varying degrees of bactericidal efficacy. For example, black silicon (bSi) is a modified silicon surface which bears a nanopatterned array of protrusions similar to the dragonfly wing [38]. The bactericidal activity of this synthetic surface was comparable to its natural inspiration, providing the first evidence of the possibility to fabricate biomimetic mechano-bactericidal surfaces. Since then, several fabrication techniques have been developed to generate similar nanostructured surfaces on titanium, which will be discussed in the following section.

2. Fabrication Methods for Nanoscale Protrusions on Titanium

2.1. Alkaline Hydrothermal (AH)

Briefly, AH is a process by which a material (in this case titanium) is immersed in an alkaline solution and subjected to high temperatures (typically 150 – 250 °C) in a sealed vessel **(Figure 3)** [39-44]. This can be followed by annealing or calcination to achieve the desired morphology and crystallite phase of titanium oxide [40, 45, 46]. The AH process etches the material surface via the dissolution of titanium and growth of titanium oxides [41]. The end-product bears a titanate-based surface with nanoscale features which can manifest in a variety of forms depending on the preceding conditions [41, 43, 47-51]. The AH process is simple, has a high-throughput, low cost, is environmentally friendly and does not require specialized equipment [52].

2.2. Thermal Oxidation (TO)

TO is comparable to AH due to its simplicity and low cost. In contrast to AH, TO is a dry etching technique that relies on heating the substrate between 400 and 900 °C in a carbon-containing cylindrical furnace. The carbon within the TO system is incorporated into the resultant nanostructures, which generates a superhydrophobic surface that may reduce mammalian cell attachment [52]. Due to this, post-treatment annealing is a necessity if the material is to be used as a medically implanted device. This adds an extra step into the production cycle which may not be required with the AH method, which generates a hydrophilic surface. Ti nanospikes generated by TO are highly like those generated by AH, and they have shown impressive bactericidal activity [53, 54].

2.3. Reactive Ion Etching (RIE)

RIE is a more complicated method of fabricating nanoscale protrusions. In RIE, a substrate is placed between two electrodes and bombarded with plasma ions in one direction. RIE can be performed with or without a mask depending on the desired outcome. A mask is an object used to shield the substrate with a specific pattern, to rationally direct the formation of the generated protrusions. Without a mask, nanofeatures generated by RIE are less ordered than mask-assisted structures [55]. For a more ordered pattern, a mask may firstly be generated by lithography-based techniques [56, 57]. Titanium treated with the maskless RIE process has been referred to as ‘black titanium’ due to the way it absorbs light, like bSi [55, 58]. Black titanium nanostructures are randomly distributed and vertically oriented having a high aspect ratio. Surfaces produced by this method have shown impressive bactericidal performance [55]. A drawback of RIE may be the use of specialized equipment which requires significant up-front investment. Additionally, due to the unidirectional nature of the etching process, only the top plane of the substrate is etched. This would not be an issue when nanopatterning flat surfaces such as a medical scalpel, but it may be impractical to generate black titanium on medical implants with complex 3D geometries.

2.4. Glancing Angle Deposition (GLAD)

GLAD is an alternative technique which involves angled vapor deposition upon a substrate which sits atop a dynamic rotating stage. GLAD can be tuned to generate reproducible, defined nanoscale structures such as pillars, spirals or zigzags. Antibacterial and anti-biofilm effects have been observed on GLAD-based surfaces [59, 60], but their bactericidal efficacy has not been as impressive as the other described techniques. In one study [59], a GLAD-based surface eliminated approximately 60% of Gram-negative *Escherichia coli*, but did not affect Gram-positive

Staphylococcus aureus. Further, much like RIE, GLAD requires highly specialized equipment and precision operation, which makes it less appealing for clinical scale implementation.

2.5. Electron Beam Lithography (EBL)

EBL is another fabrication technique which can generate nanoscale protrusions with highly defined proportions and spacing, but it cannot directly etch metal substrates. To produce nanoscale protrusions on a titanium substrate, a polymer mask must first be applied to the surface, which is then exposed to an electron beam. The desired pattern is then transferred from the polymer to the titanium substrate using either an etching or lift-off technique [61, 62], EBL-based nanostructures can be highly similar to those seen on cicada wings, but at the time of writing there is no quantitative data to support their antibacterial efficacy. This like likely because EBL-based titanium nanostructures are still an emerging technology.

2.6. Through-Mask Anodization (TMA)

TMA involves the use of an electrochemical cell with titanium as the anode, causing the build-up of a titanium oxide layer [63, 64]. The forming oxide layer is directed through a porous aluminium mask to generate pillars with a diameter equal to the mask pores. Though this technique does produce nanoscale protrusions, the potential bactericidal application of this has not yet been demonstrated.

2.7. Scaling Up to Large-Scale Manufacturing

Clearly, there are a variety of options for fabricating nanoscale protrusions on titanium in the laboratory. Scaling these methods up for the manufacture of implanted devices presents another layer of challenges. Apart from being effective *in vitro* and *in vivo*, the ideal biomaterial should not be prohibitive in cost, through-put, environmental impact, equipment requirements or operator technical specialization. A review by Ishak and colleagues [52] focused on titanium mechano-bactericidal surfaces, and included a detailed description of 4 techniques which may have the potential to be scaled-up to industrial production. Namely, these are AH, TO, RIE and GLAD. While all these techniques have their merits, AH stands out as the most attractive for large-scale manufacturing. Compared to RIE and GLAD, the AH method is much more simple, scalable, cost effective, high-throughput and does not require specialized equipment. Further to this, as the AH etching process is carried out in a liquid immersion, it can provide total surface coverage to complex geometries such as those seen on screws. This is not possible with fabrication techniques such as RIE, which rely on a bombardment of ions from a specific direction. TO is a promising alternative due to its simplicity and low cost, however, current literature suggests TO-based surfaces are not as effective at killing bacteria as AH-based surfaces (Table 1). Alkaline hydrothermal treatment has been used for decades prior to its adoption as a technique to fabricate anti-infective biomaterials [65]. This deep history in research and development has generated a wealth of literature characterizing the fabrication process and its varying outputs. For these reasons, surface modification by the AH process is well positioned to be the fabrication method of choice for future biomaterials in the orthopedic and periodontal fields which can protect patients from infections.

Table 1. The antibacterial efficacy and host compatibility of titanium nanoscale protrusions fabricated by various methods. The antibacterial efficacy is reported as a maximum bacterial reduction found in the current literature. The antibacterial assay used in the cited studies is included. NA = not available, as no quantitative data were found

Fabrication method	Bactericidal activity	Host compatibility	References
Alkaline hydrothermal	Gram-positive: Up to ~90% (fluorescence) Gram-negative: Up to ~99% (fluorescence)	• Increased contact area of human adipose stem cells without increased senescence • Promotion of osteogenesis	[44, 51]
Thermal oxidation	Gram-positive: Up to ~80% (colony enumeration) Gram-negative: Up to ~75% (colony enumeration)	• Increased cell adhesion and proliferation of human osteosarcoma cells	[53, 66]
Reactive ion etching	Gram-positive: Up to 92% (fluorescence) Gram-negative: Up to 98% (fluorescence)	• Promotion of osteogenic commitment of human mesenchymal stem cells	[55]
Glancing angle deposition	Gram-positive: No significant reduction Gram-negative: Up to ~60% (fluorescence)	• Increased coverage and reduced cell death of preosteoblasts in bacterial co-culture models	[59, 60]
Electron beam lithography	NA	• Undisturbed morphology and equal metabolic activity compared to control titanium surface	[61]
Through-mask anodization	NA	• Increased cell spreading of human mesenchymal stem cells, potentially indicative of early-stage osteogenesis	[63]

2.8. Mechano-bactericidal Structures on Non-Titanium Metals

Although titanium is one of the most frequently used materials for implant applications, it should be acknowledged that other metals are still commonly used. Surface modification techniques have been utilized to generate mechano-bactericidal structures on other metals for potential implant applications. For example, anodization [67] and ultrafast laser pulse [68] methods have been used to fabricate nanoscale protrusion and nanopores on stainless steel, which have shown promising bactericidal activity. Similarly, gold nanospikes have been electrodeposited on a silicon/titanium substrate, resulting in between 40-90% bactericidal activity against Gram-negative bacteria [69]. While these developments are interesting, they are beyond the scope of this report.

3. Hydrothermally Etched Titanium as an Anti-Infective Biomaterial

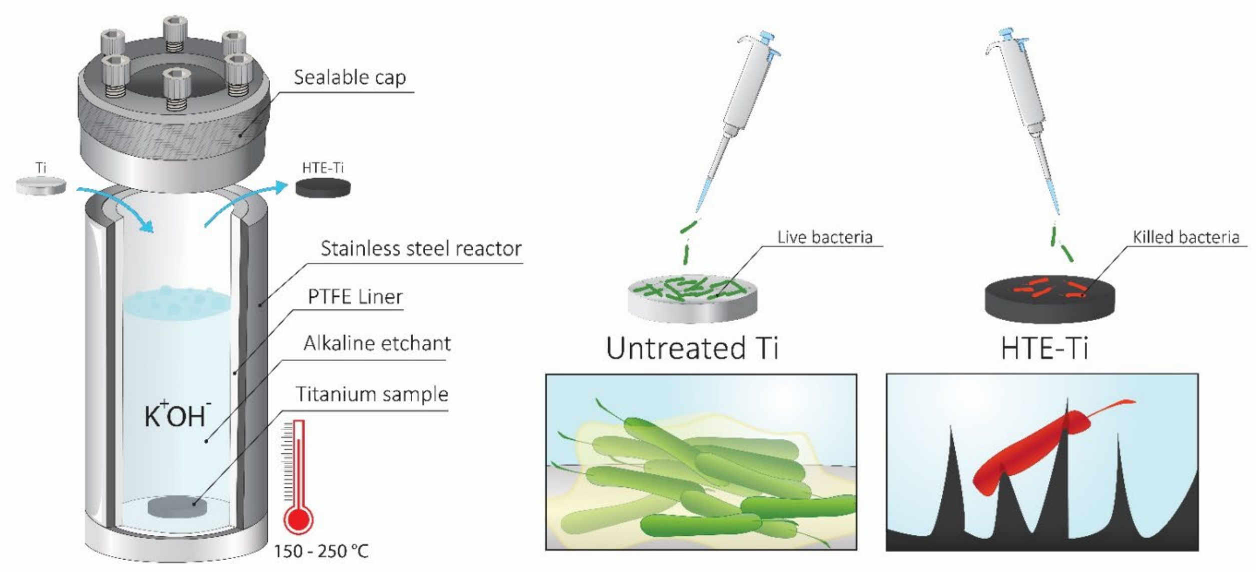

Figure 3. The alkaline hydrothermal etching process modifies titanium with bactericidal nanoscale properties.

3.1. Surface Topography is Determined by Fabrication Parameters

The AH process generates many variations of surface topographies, most involve discrete protrusions, sharp two-dimensional sheets, or a combination of both. Different applications may take advantage of these topographical variations. Consequently, it is of great interest to determine how fabrication parameters can be modified to produce the desired outcome. The primary variables are etchants/alkali, concentrations of etchants, reaction temperature, and etching time [48, 50, 51]. The chosen alkali etchant influences the resulting structure of the surface. NaOH and KOH are commonly used to generate nanoscale structures, KOH being considered to have greater reactivity with TiO_2 [70]. The hydrothermal etching process is thought to constitute the simultaneous reactions of titanium dissolution and oxide growth [41]. At low alkaline concentrations, the oxide growth reaction is favoured, resulting in small, discrete structures formed with random orientation [41]. As the alkaline concentration is increased, dissolution begins to contribute more strongly. This leads to etching away the interstitial space between protrusions, which begin to coalesce resulting in a web-like, porous network [41]. Alkaline concentration is positively correlated with nanostructure height [49, 71]. The morphological outcome of varying the alkaline concentration is also dependent on the temperature of the hydrothermal environment. At 150°C, Anitha and colleagues observed 2D platelet-like features which increased in porosity with alkaline concentration. When the reaction temperature was increased to 250°C, the morphology was characterized by individual, discrete pillars [41]. The morphological characteristics of HTE-Ti are also dependent on etching duration. Wandiyanto and colleagues investigated the effects of etching times between 0.5 and 60 hours. Similar to alkaline concentration, etching time was shown to be positively correlated with structure height [51]. At very short etching times, the surface takes on a dense array of short nanocrystallite structures, which serve as nucleation sites for larger structures formed under longer etching times. For the first 6 hours of etching, nanopillars became progressively sharper and less dense and the frequency of pillar intersection decreased. Beyond 24 hours of etching, the individual pillars curled downward creating a dull topography [51].

Jaggessar [43] developed a model to predict nanostructure height as a function of variable fabrication parameters. Using this model, it is possible to predict nanostructure height by inputting the values of NaOH concentration, etching time and reaction temperature. The model was shown to be highly accurate in its prediction, but it is limited by the experimental conditions used to generate the statistical data – only accommodating NaOH concentrations between 0.1 and 2.0 M, etching times between 1 and 10 h, and reaction temperatures between 120 and 240°C. Such a model is a step toward designing nanostructures with a defined set of properties for specific applications (such as infection prevention and osseointegration). Further refined models should allow for the input of expanded ranges of fabrication parameters and predict other morphological properties such as diameter and density.

3.2. Mechanism of Bactericidal Action of Hydrothermally Etched Titanium

The exact mechanism by which mechano-bactericidal surfaces inactivate bacteria has been a hot topic of interest since the effect was first observed to occur on insect wings [31]. Numerous research groups have proposed different, and sometimes contradictory mechanisms to explain the bactericidal effect imposed by such surfaces [54, 72-75]. To complicate the issue, mechano-bactericidal surfaces can take on many different surface morphologies, and the bactericidal mechanisms described on one surface may not exclusively apply to other surfaces. It is likely that the bactericidal mechanism of HTE-Ti is not attributable to one lone factor but is multifaceted. It must be noted that modelling a surface interaction with bacteria has only been carried out on patterned geometries of surfaces with specific nanopillar height, spacing, pillar-angle, and diameter interacting against the commonly tested rod-shaped bacterium. Furthermore, HTE-Ti protrusions are randomly oriented, owing to the fabrication method. Modelling a randomly oriented nanopillared surface would require complex mathematical and simulation tools. Currently, there are no published models centred on the killing mechanism of a randomly oriented nanostructure such as HTE-Ti. Therefore, to further elucidate the killing mechanism of HTE-Ti it is useful to draw comparisons with similar mechano-bactericidal surfaces.

3.2.1. The Primary Mechanical Influence

It is well documented that the mechano-bactericidal effect is characterized by interactions between the nanostructured surface and the adherent bacterial cell. The precise sequence of events which follows cell attachment has been debated in the literature, but it is frequently agreed that the bactericidal action is due to lethal envelope stretching [76, 77]. Nevertheless, it is important to discern the precise mechanics of the interaction, and in particular, the critical point of weakness on the cell adhered to the nanostructure. To that end, Pogodin et al [74] developed a biophysical model which posited that the adherent bacterial cell is drawn down along the length of the nanostructure, causing lethal stretching of the region of cell envelope suspended between protrusions **(Figure 4A)**. The suspended region was thereafter thought to be the weakest point from which envelope rupture originates. Although the biophysical model soon became established dogma, it was limited in its reliability because it modelled a cell with only a thin elastic monolayer and neglected the structural nuances of a real bacterial envelope. An improved model was more recently developed by Velic and colleagues [72]. In this model, a Gram-negative bacterium was reduced to its load-bearing components – the outer membrane and the peptidoglycan layer, which are covalently linked together by abundant lipoprotein. The authors used a finite element modelling simulation to assess the interaction between the cell and the nanostructure. Their analysis compared the maximal strain experienced separately in the outer and inner leaflets of the membrane bilayer, as well as the peptidoglycan layer. Interestingly, the outer leaflet of the membrane experienced strain in the regions suspended in between nanostructures, acting similarly to the biophysical model developed by Pogodin et al [74]. However, the strain experienced by the inner leaflet and the peptidoglycan layer was always centred on the region directly in contact with the pillar apex (Figure 4B), and this was more severe than the strain on the outer leaflet suspended between pillars. In many cases, the membrane stress at the pillar apex is enough for the pillar to penetrate the cell envelope, leading to loss of cell contents [31, 72, 78, 79]. Another recent finite element model developed by Cui et al [80] was similar to Velic et al, but included turgor pressure in the equation. This model predicted that the critical point of action was at the 'three phase contact line' between the cell, nanopillar and liquid interface. Although the supposed critical point of weakness is slightly different between the Velic and Cui models, these models combined strongly refute the suspended membrane hypothesis of the biophysical model. Further, the application of both models support the use of slimmer nanostructures, which maximises envelope strain at or around the nanostructure tip.

3.2.2. Downstream Effects of Mechanical Perturbance

Apart from the membrane-damaging effects of nanoscale protrusions, the bactericidal activity of HTE-Ti may be also attributed to other related factors. Jenkins and colleagues conducted a proteomic analysis of *Staphylococcus aureus* and *Escherichia coli* incubated on nanostructured Ti. They observed an increase in antioxidant proteins and proteins associated with DNA repair, both of which would be expected from an oxidative stress response [54, 81, 82]. Further, the group quantified reactive oxygen species (ROS) in the form of H_2O_2 in the culture media and found a greater concentration associated with HTE-Ti. Together, these results form a convincing case that oxidative stress played a role in the bactericidal effect of HTE-Ti. The exact mechanism through which oxidative stress is generated remains unclear. The Jenkins group noted that when bacteria were not present, there was negligible H_2O_2 detected, suggesting that H_2O_2 was not primarily generated by photocatalysis [83]. It is plausible that the mechanically induced membrane stress causes downstream physiological effects which promote the generation of oxidant compounds

(Figure 5C) [52]. However, to the authors knowledge, there is no available evidence to support or refute this notion. Nevertheless, indirect support for this interpretation can be found in other nanostructured materials, which have been investigated for their ability to induce oxidative stress in bacteria. Liu and colleagues observed that *E. coli* treated with graphene-based nanomaterials showed an increased oxidation of glutathione [84], indicative of oxidative stress [85, 86]. The group attempted to detect the presence of superoxide to determine whether ROS were the cause of the observed oxidative stress. They did not find evidence of superoxide, but their measurement looked only at the graphene-based nanomaterials in suspension without bacteria [84]. This therefore does not rule out the possibility that intracellular ROS generation occurred as a downstream effect of membrane stress.

Interestingly, the bactericidal effects of oxidative stress may not be confined to the cells in contact with the nanostructured surface. Bacteria exposed to oxidative stress can generate genetically encoded signals causing programmed cell death (PCD) in other members of the bacterial community, which occurs through a type II toxin-antitoxin system [87, 88]. In this way, bacterial cells under stress kill neighbouring cells to preserve genetic integrity of the population and reduce the nutritional requirements of the community as a whole [89]. Stress-induced PCD may be the reason why cell death seems to occur even in the upper layers of bacterial biomass, which aren't in contact with the nanostructured surface [90], but this potential effect needs further interrogation.

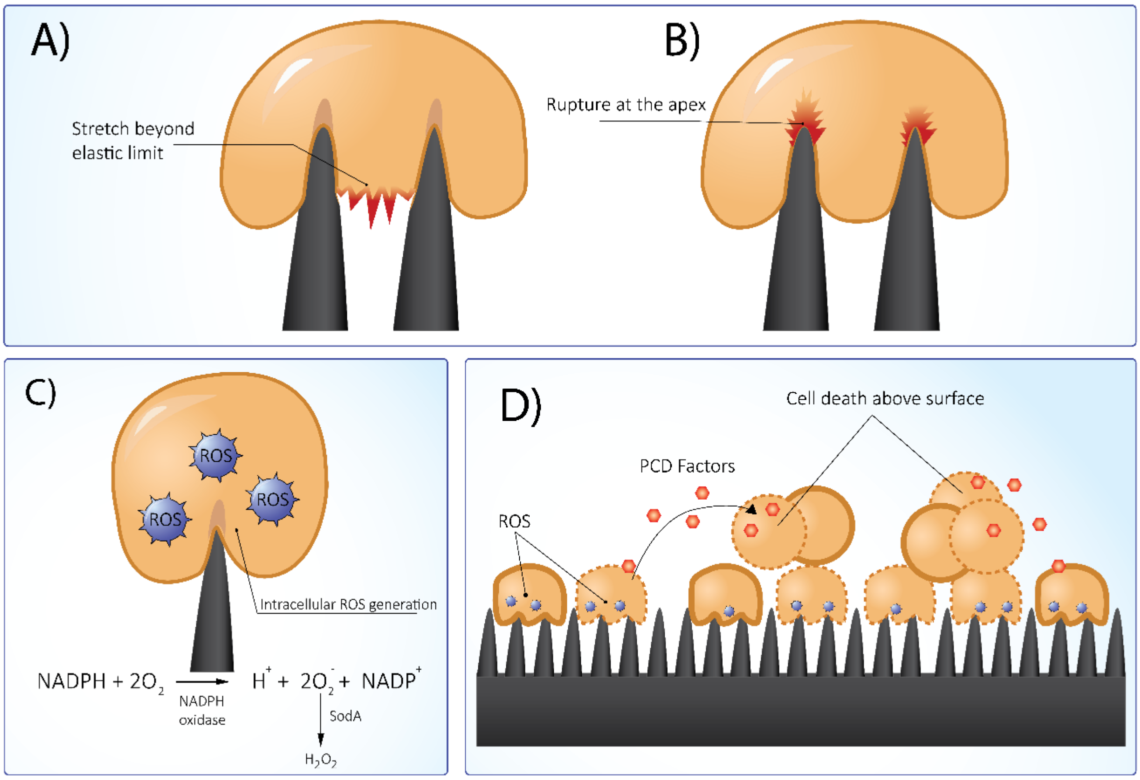

Figure 4. Proposed bactericidal mechanisms of protruding nanostructured surfaces. A) Suspended membrane is stretched beyond its elastic limit between two nanostructures. B) Membrane deformation and penetration occurs at or around the nanopillar apex. C) Intracellular ROS generation as a downstream effect of membrane perturbation. D) PCD factors are

secreted as a response to oxidative stress, inducing the programmed cell death of cells in areas protected from the hostile effects of the nanostructure

Based on the current literature on this novel and rapidly evolving field, these primary and secondary bactericidal effects seem to be the most plausible mechanisms. We are at a cross-roads of very interesting technologies and modelling being developed that will further enhance our understanding. Very high resolution spatial-temporal imaging will be instrumental in identifying the exact bacterial membrane behaviour on nanostructured surfaces. Super-resolution microscopies such as Photo-Activated Localization Microscopy (PALM) [91] and high-speed phase atomic force microscopy (AFM) [92] imaging may provide more insights into these biophysical interactions, allowing for further developments of the proposed bactericidal mechanism.

3.3. Bactericidal Activity is Influenced by Surface Topography

By definition, mechano-bactericidal surfaces inactivate bacteria through physical, rather than chemical means [31]. Mechanically induced cell death is therefore governed by the interactions at the interface between bacterial cells and the modified surface [93]. Nanostructured surfaces come in a variety of forms differing in structure height, diameter, sharpness, density, arrangement, hydrophobicity, electrical conductivity, and flexibility. Assessment of the bactericidal contribution of individual factors is made difficult because most morphological comparisons vary by more than one parameter. Beyond biomaterial surface topography, different species of bacteria possess a range of characteristics which influence the susceptibility of their membranes to mechanical disruption. It is therefore important to generate an understanding of all the different nanotopographical and biological factors which determine the bactericidal efficacy of such surfaces.

3.3.1. Structure Height, Diameter and Spacing

Height:

It is intuitive to presume that above a certain threshold, structure height does not play a key role in the degree of bactericidal potency of a nanopillar surface. From the perspective of a cell, two nanopillar surfaces differing only in height are superficially equal. This is because the pillar tips obstruct the cell from interacting with the lower portions of the pillar shafts. Indeed, multiple models predicted that height would not have a substantial effect on the bactericidal activity of a nanopillar surface [94, 95]. This notion is thought to hold true so long as the nanopillars are taller than the depth that the cell would 'sink' between pillars **(Figure 5)** [94]. The sinking depth may vary between surface morphologies and bacterial species. As an example, on the *P. claripennis* nanostructure, the sinking depth of *P. aeruginosa* was 200 nm [31]. Incidentally, the thermodynamic model developed by Li [76] suggested that the degree of membrane stretching would be unchanged when pillar height is increased beyond 200 nm. Despite this, in an experiment varying the height of silicon nanopillars between 220 and 420 nm, it was found that the taller nanopillars were more bactericidal, with an approximate 30-40% increase in bactericidal activity based on live/dead fluorescence analysis [93].

Similarly, in a study comparing vertically aligned carbon nanotubes with heights of 1 and 30 μm, the shorter structures were approximately 50-60% more bactericidal against Gram-positive cells [96]. However, it is difficult to compare these two surfaces due to their different material properties. With the currently available literature, it cannot be determined whether pillar height really does play a significant role. If it does, the optimal range may vary between bacterial species.

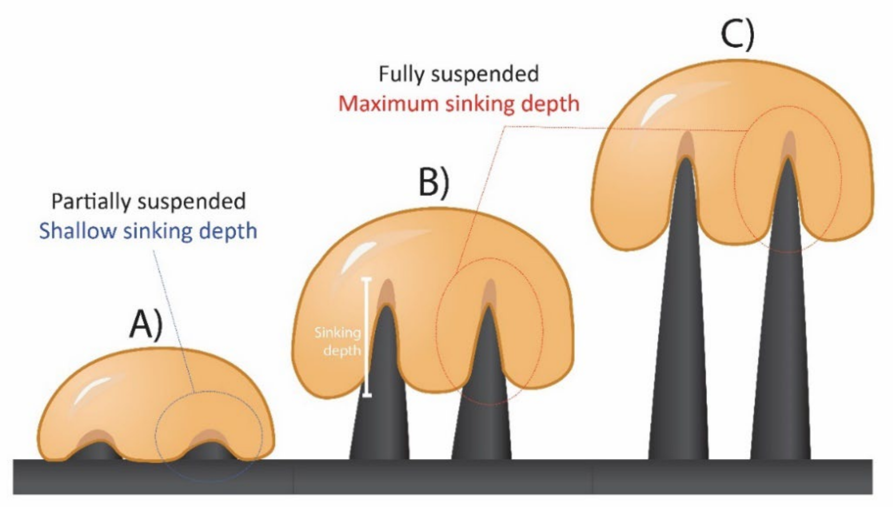

Figure 5. The purported relationship between pillar height and sinking depth. A) Very short nanopillars do not provide enough interstitial space for the cell to sink into. B) Taller nanopillars completely suspend the cell above the substrate, allowing for the maximum sinking depth to be reached. C) Further increasing the pillar height suspends the cell higher from the substrate bulk but does not increase the sinking depth. The extra height of the tallest nanopillars is not “felt” by the cell.

Diameter:

According to a systematic review by Modaresifar and colleagues [97], the bactericidal nanostructures reported in the literature range in diameter from 10 to 300 nm, but most of these are slimmer than 100 nm. Linklater and colleagues suggest that the nanopillar width should be in the same order of magnitude as the thickness of the peptidoglycan layer [75]. This is approximately the case for many nanopillar structures. For instance, the *P. claripennis* nanopillars have a tip diameter of 60 nm, while the *P. aeruginosa* peptidoglycan layer is 2.4 nm thick, which is slightly more than 1 magnitude difference [31, 98]. A mathematical model by Watson and colleagues [79] suggests that pillar width should not have a substantial effect on antibacterial efficacy unless the bacterial cell wall is sufficiently thick, in which case a wider diameter is more effective**.** However, the available experimental evidence shows that antibacterial effects do indeed vary according to pillar diameter. A study of different cicada species analyzed nanopillars between 156 and 206 nm, and found the greatest bactericidal activity on the slimmer structures [32]. A similar observation was made by Kim et al [99]. The bactericidal efficacy of slim, sharp nanopillars is supported by multiple models [72, 80, 100].

Spacing:

Pillar spacing must have an optimal range within an upper and lower limit of efficacy. If the spacing is larger than the cell’s dimensions, bacteria could settle between pillars and avoid the lethal effect of the pillar tips [101]. However, if there is very little interstitial space between pillars, the pillar tips would more closely resemble a flat surface. Even with sufficient interstitial space for the cell to sink downward, a high density has been thought to lead to a ‘bed of nails’ effect, where the damaging effect of the individual pillars is reduced [75]. To this end, a mathematical model was developed by Xue, which predicted that greater pillar spacing would enhance the bactericidal effect [102]. However, as pointed out by Velic et al [72], this model only considers cell weight as the driving force drawing the cell into the nanopillars**.** This neglects the adhesion forces driven by van der Waals interaction and cell surface proteins [103]. Contrary to the ‘bed of nails’ hypothesis, a higher density of pillars serves to provide more points of cell contact and subsequently a stronger adhesive force, which drives the cell downward to its demise [72, 100]. Further, the load-bearing peptidoglycan layer is not uniform [104] and is porous [105], so it is conceivable that the structural integrity is variable across the cell surface. Increasing the pillar density may increase the contact rate between pillars and any potential weak points across the peptidoglycan layer. In a study measuring *E. coli* viability when pillar spacing was varied between 100 and 380 nm, the 100 nm surface demonstrated the greatest killing effect [106]. Similar observations of the effect of pillar density has been reported [32].

When considering the height, diameter and spacing of protruding nanostructures, it should be noted that they may not each have independent effects on the nanostructure’s bactericidal efficiency but rather work together to provide a physical killing mechanism. The currently available literature primarily focuses on the individual contributions of these factors. More data and modelling/simulations are needed to fully reveal whether structural parameters work independently or in an ensemble.

3.3.2. Other Material Factors

It is tempting to predict that hydrophobic nanostructures may be more bactericidal than hydrophilic ones. For example, hydrophobic graphene nanosheets were shown to lethally extract lipids from the phospholipid bilayer [107]. However, hydrophilic nanopillar surfaces do not appear to perform any less effectively than hydrophobic ones [31, 71, 96, 108]. In one study, bactericidal activity of single-walled carbon nanotubes (SWNTs) was shown to be proportionate to electrical conductivity, however, the relevance of this finding to HTE-Ti remains to be seen [86]. The elasticity of nanopillars is another factor which has been reported to enhance bactericidal properties [93, 96], but the validity of this hypothesis has been debated [72]. Further, the purported link between elasticity and bactericidal capacity was discussed in relation to carbon nanotubes and silicon nanopillars but may be irrelevant to HTE-Ti. The mathematical model proposed by Watson [79] suggests that a hexagonal distribution of nanopillars is preferable to a rectangular one, i.e. each nanopillar has 3 closest neighbors rather than 4. However, due to the random arrangement of features that are typically obtained on HTE-Ti, this parameter may be disregarded. Similarly, the orientation of features should be approximately perpendicular, but not necessarily 90˚. Bactericidal effects have been noted on nanostructures with angles as low as 37˚ [75]. However, if the tips are curled downward, bactericidal activity is substantially reduced [51]. Lastly, titanium implants can be composed of a variety of different titanium grades, from commercially pure titanium to its various alloys (e.g. Ti-6Al-4V, Ti-6Al-7Nb, Ti-5Al-2.5Fe) [109, 110]. On that note, it may be predicted that titanium alloys would leach toxic metals such as vanadium and aluminium to contribute to bacterial cell death. However, this does not seem to be the case. Kapat and colleagues assessed the viability of bacteria on HTE-Ti and untreated Ti-6Al-4V [111]. On the untreated Ti-6Al-4V surface, both *E. coli* and *S. aureus* maintained a cell viability close to 100%, indicating that leached metals had little to no effect on bacterial cell viability. Further, as hydrothermal etching creates a thicker oxide layer on the titanium surface, it is highly unlikely that leached metals contributed to the bactericidal effect of the HTE-Ti surface.

3.3.3. Biological Factors

Beyond the properties of the nanostructure itself, the susceptibility of bacteria to HTE-Ti is almost certainly influenced by the biological properties of the species. As envelope stress is likely a key factor in the bactericidal activity of HTE-Ti, Gram-positive species are better equipped to resist these effects. Gram-positive species, such as the clinically relevant *S. aureus*, possess a thick peptidoglycan layer which confers a greater level of rigidity to the cell compared to Gram-negatives [112]. It is no surprise then that nanostructured surfaces tend to be more effective against Gram-negative species, whose peptidoglycan layer is much thinner and more prone to warping [74, 102]. Although the Gram-positive or negative status of a pathogen is often at the centre of the discussion regarding susceptibility to mechanically induced cell death, the reality is likely more complicated. Bacterial cells come in a variety of shapes and forms, including spherical, rod-shaped, and spiral-shaped, among others. The morphology of a bacterium will influence its interaction with the nanostructured surface. For example, one study looked at the different nanostructure interactions of oral pathogens of different shapes and sizes [113]. It was found that the 10 µm long *Fusobacterium nucleatum* was penetrated and ruptured by interacting with many nanostructured tips. However, due to its slim diameter, it would occasionally orient itself between the structures. In this orientation, *F. nucleatum* was observed to overstretch and rupture itself with many fimbriae attachments to the sides of the structures. Smaller cells, such as the ovococcoid *Porphyromonas gingivalis* were observed to primarily settle between structures. In this case, the cells escape the hostile effect of the structure apex but may still have their cell division physically impeded by the narrow interstitial spaces between structures.

Cell turgor also appears to be an important factor, and this makes sense because a turgid cell should be more resistant to envelope warping. In one experiment, cell turgor was reduced using a non-lethal exposure to microwave radiation, which creates reversible pores in the cell envelope allowing the leakage of cytosol. Following microwave exposure, Gram-positive cells became less resistant to the bactericidal effect of a nanopillar surface [74]. Motility may also play a role in susceptibility to mechano-bactericidal surfaces [34]. In one study, Diu and colleagues [42] measured cell viability of 3 motile and 3 non-motile species on an HTE-Ti surface. Both motile and non-motile groups included Gram-positive and Gram-negative bacteria to control for the effect of cell rigidity. The authors found that the motile group were appreciably more susceptible to the bactericidal effect of the HTE-Ti surface compared to the non-motile group [42]. This is likely because a motile cell will attempt to travel laterally over the surface, imposing membrane stress on all points in contact with nanopillar tips. Although it is speculative, the mode of cell division may also play a role in bacterial sensitivity to nanopillars. Rod shaped bacteria tend to elongate during cell division [114], which could plausibly cause membrane stress comparable to a motile cell moving laterally across the nanostructure. Staphylococcus species divide along 3 planes, creating clusters of cells that extend across 3 dimensions. This mode of division may allow *S. aureus* to divide away from the hostile topography of HTE-Ti. Contrasting this, Streptococcus species divide along a single plane, creating long chains of cocci [115]. This would likely result in Streptococci chains forming laterally across the surface topography, increasing its vulnerability to mechano-bactericidal inactivation.

3.4. The Selective Bactericidal Nature of Hydrothermally Etched Titanium

Considering the hostile nature of HTE-Ti toward bacteria, it is logical to question its compatibility with mammalian cells. Indeed, if HTE-Ti is to be successfully implemented in medically implanted devices, the surface needs to be permissive to the host tissue. While there is limited evidence of nanostructured surfaces killing or impeding mammalian cells [116, 117], the prevailing consensus is that mammalian cells are either resistant to, or enhanced by such nanostructured surfaces [48, 118-120]. HTE-Ti has been shown to increase the attachment and proliferation of osteoblast-like MG-63 cells, as well as cause the upregulation of osteogenic markers.[120] This bodes very well for implant applications which require bone integration. The selectively bactericidal nature of mechano-bactericidal surfaces may be centered on the inherent morphological and structural differences between prokaryotes and eukaryotes [78]. Eukaryotic cells are larger than prokaryotic cells by at least an order of magnitude, and membrane perturbation caused by nanoscale protrusions may be proportionately less significant for eukaryotic cells. Further, eukaryotic cells tend to be more flexible than prokaryotes, in part because they lack the rigid peptidoglycan layer. This allows eukaryotic cells to wrap around and conform to a nanostructured landscape [121]. It is speculated that the resistance of eukaryotic cells to mechano-bactericidal surfaces is afforded by their greater extensibility – granted by the presence of cholesterol in the eukaryotic lipid bilayer [72]. However, this highlights an apparent paradox: Gram-negative bacteria are commonly thought to be more sensitive to envelope rupture due to their less rigid nature compared to Gram-positives. Thus, it may be that the greatest sensitivity to mechano-bactericidal structures is found in a proverbial “goldilocks” zone between flexibility and rigidity; that is, if a cell is highly flexible it will conform unhindered to the topography of the surface – but if the cell is highly rigid it will better resist the deforming pressures of the nanostructure. If a cell can neither conform to the structure nor resist deformation and penetration, then it will succumb to the hostile surface.

3.5. Standardization of Terminology

Surface modification to generate nanoscale protrusions is still a relatively young field of science and technology, and perhaps because of this there is much ambiguity in the associated terminology. A general literature search using the terms “hydrothermal etching TiO2” yields an abundance of publications using a variety of terms to describe similar topographies. Some commonly used terms are *nanopillar, nanowire, nanorod, nanospike, nanosheet* and *nanoplatelet*. In many cases, a search for one specific term will yield reports of surfaces that are strikingly different. The term *nanopillar* has been used to describe the morphology of both the cicada wing [31] and HTE-Ti [54]. These two surfaces bear little resemblance, making the common use of term problematic. In some cases, groups have described a single nanostructure as having both *nanopillars* and *nanowires* in the same publication [49]. Future research and building a knowledge base in the field would benefit from a standardization of terminology. The difficulty in clearly terming and categorizing nanostructured surfaces is centered on the fact that there is almost a spectrum of different morphologies to consider.

While mechano-bactericidal HTE-Ti surfaces can take on a range of different morphologies, they can broadly be divided into two general forms. They can either be composed of networks of 2-dimensional features, or they can have individual, pointed protrusions. For HTE-Ti surfaces comprised of 2-dimensional features, the term *nanosheet* is consistently used in publications focused on bactericidal activity [44, 51]. The term *nanoplatelet* has also been used [41, 122], but these publications are not centered on mechano-bactericidal activity, so the inconsistency is unsurprising. Going forward, the authors recommend that these 2-dimensional networked surfaces be labelled with *nanosheet*, as the ‘platelet’ description may be confused with blood platelets. Likewise, HTE-Ti surfaces consisting of individual protrusions have been labelled with *nanowire* [49, 50, 119], *nanopillar* [49, 54], *nanospike* [123] and *nanorod* [41, 50]. The ‘pillar’ description confers imagery of highly ordered, vertically aligned columns and should be reserved for surfaces resembling the wing of *Psaltoda claripennis*. ‘Rod’ is suggestive of a straight structure, which is too restrictive for HTE-Ti because the protrusions often have curvature. ‘Wire’ is suggestive of a very slim structure, and may be reserved for surfaces with very high aspect ratio, such as the thermally oxidized TiO2 which has protrusions of only 20 nm diameter [53]. ‘Spike’ may be the most appropriate term as it is not restrictive of diameter, orientation, or arrangement. Therefore, the authors propose that HTE-Ti surfaces with 2-dimensional features be labelled as *nanosheet,* and those with individual protrusions be labelled as *nanospikes*.

4. Outlook and Conclusions

The growing demand for implantable medical devices and the growing problem of antibiotic resistant bacteria necessitates novel anti-infective technologies which prevent microbial colonization. In this space, various surface coatings and modifications have been explored to varying degrees of success. Biomimetic mechano-bactericidal surfaces are well positioned to fill the need for a biocompatible, osteogenic, anti-infective biomaterial. While there are multiple fabrication pathways to generate mechano-bactericidal surfaces on titanium implants, the alkaline hydrothermal method is the most appealing due to its simplicity, cost-effectiveness, and potential for upscaling. Abundant in vitro studies suggest that HTE-Ti meets the two key criteria for clinical implementation: its bactericidal capability and its support of osteogenesis. There is yet a significant amount of research required to fully elucidate the precise bactericidal mechanisms of action of HTE-Ti. It is still unclear how and to what extent oxidative stress plays a role in the bactericidal action of the surface. Further systematic fabrication studies may be undertaken to aid the refinement of topography prediction models, such that highly defined and predictable nanostructures can be designed. As a prerequisite to the goal of clinical implementation, there must be robust in vivo studies which validate the capability of HTE-Ti to resist implant-associated infection. The latter presents an important gap of knowledge which needs to be urgently filled to fully benefit from the potential of this promising material in protecting patients from infections.

Acknowledgements

This study was co-funded by the Department of Industry, Science, Energy and Resources (Innovative Manufacturing CRC Ltd) Global Orthopaedic Technology Pty Ltd (IMCRC/GOT/13032018). The authors acknowledge the funding and in-kind support from Corin Australia and the University of South Australia. The authors would also like to acknowledge the instruments and scientific and technical assistance of Microscopy Australia at the University of South Australia, Mawson Lakes Campus, a facility that is funded by the University, and State and Federal Governments. The authors would also like to acknowledge Dr. Daniel Fernandes for providing the SEM image of the Dragonfly wing in Figure 2. KV thanks to ARC for grant DP180101254 and NHMRC for Fellowship GNT1194466

5. References

1. Geetha, M., et al., *Ti based biomaterials, the ultimate choice for orthopaedic implants - A review.* Progress in Materials Science, 2009. **54**(3): p. 397-425.
2. Campoccia, D., L. Montanaro, and C.R. Arciola, *The significance of infection related to orthopedic devices and issues of antibiotic resistance.* Biomaterials, 2006. **27**(11): p. 2331-2339.
3. Mombelli, A. and F. Décaillet, *The characteristics of biofilms in peri-implant disease.* J Clin Periodontol, 2011. **38 Suppl 11**: p. 203-13.
4. Flemming, H.-C., et al., *Biofilms: an emergent form of bacterial life.* Nature Reviews Microbiology, 2016. **14**(9): p. 563-575.
5. Verbeke, F., et al., *Peptides as Quorum Sensing Molecules: Measurement Techniques and Obtained Levels In vitro and In vivo.* Frontiers in Neuroscience, 2017. **11**(183).
6. Muras, A., et al., *Acyl homoserine lactone-mediated quorum sensing in the oral cavity: a paradigm revisited.* Scientific Reports, 2020. **10**(1): p. 9800.
7. Koo, H., et al., *Targeting microbial biofilms: current and prospective therapeutic strategies.* Nature Reviews Microbiology, 2017. **15**(12): p. 740-755.
8. Song, F., H. Koo, and D. Ren, *Effects of Material Properties on Bacterial Adhesion and Biofilm Formation.* J Dent Res, 2015. **94**(8): p. 1027-34.
9. Arciola, C.R., D. Campoccia, and L. Montanaro, *Implant infections: adhesion, biofilm formation and immune evasion.* Nat Rev Microbiol, 2018. **16**(7): p. 397-409.
10. Rabin, N., et al., *Biofilm formation mechanisms and targets for developing antibiofilm agents.* Future Medicinal Chemistry, 2015. **7**(4): p. 493-512.
11. Widmer, A.F., *New developments in diagnosis and treatment of infection in orthopedic implants.* Clin Infect Dis, 2001. **33 Suppl 2**: p. S94-106.
12. Hansen, E.N., B. Zmistowski, and J. Parvizi, *Periprosthetic joint infection: what is on the horizon?* Int J Artif Organs, 2012. **35**(10): p. 935-50.
13. Chouirfa, H., et al., *Review of titanium surface modification techniques and coatings for antibacterial applications.* Acta Biomaterialia, 2019. **83**: p. 37-54.
14. Shahi, A. and J. Parvizi, *Prevention of Periprosthetic Joint Infection.* Arch Bone Jt Surg, 2015. **3**(2): p. 72-81.
15. Parvizi, J., N. Shohat, and T. Gehrke, *Prevention of periprosthetic joint infection: new guidelines.* Bone Joint J, 2017. **99-B**(4 Supple B): p. 3-10.
16. Esposito, S. and S. Leone, *Prosthetic joint infections: microbiology, diagnosis, management and prevention.* Int J Antimicrob Agents, 2008. **32**(4): p. 287-93.
17. Evans, R.P., *Current concepts for clean air and total joint arthroplasty: laminar airflow and ultraviolet radiation: a systematic review.* Clinical orthopaedics and related research, 2011. **469**(4): p. 945-953.
18. Abdel Karim, M., et al., *Hip and Knee Section, Diagnosis, Algorithm: Proceedings of International Consensus on Orthopedic Infections.* The Journal of Arthroplasty, 2019. **34**(2, Supplement): p. S339-S350.
19. Vasilev, K., *Nanoengineered Antibacterial Coatings and Materials: A Perspective.* Coatings, 2019. **9**(10).
20. Vasilev, K., J. Cook, and H.J. Griesser, *Antibacterial surfaces for biomedical devices.* Expert Rev Med Devices, 2009. **6**(5): p. 553-67.
21. Maan, A.M.C., et al., *Recent Developments and Practical Feasibility of Polymer-Based Antifouling Coatings.* Advanced Functional Materials, 2020. **30**(32): p. 2000936.
22. Mizrahi, B., et al., *Long-Lasting Antifouling Coating from Multi-Armed Polymer.* Langmuir, 2013. **29**(32): p. 10087-10094.
23. Vasilev, K., S.S. Griesser, and H.J. Griesser, *Antibacterial Surfaces and Coatings Produced by Plasma Techniques.* Plasma Processes and Polymers, 2011. **8**(11): p. 1010-1023.
24. Romanò, C.L., et al., *Antibacterial coating of implants in orthopaedics and trauma: a classification proposal in an evolving panorama.* J Orthop Surg Res, 2015. **10**: p. 157.
25. Romanò, C.L., et al., *Antibacterial coating of implants: are we missing something?* Bone & joint research, 2019. **8**(5): p. 199-206.
26. Lowe, S., N.M. O'Brien-Simpson, and L.A. Connal, *Antibiofouling polymer interfaces: poly(ethylene glycol) and other promising candidates.* Polymer Chemistry, 2015. **6**(2): p. 198-212.

27. Cavallaro, A., S. Taheri, and K. Vasilev, *Responsive and "smart" antibacterial surfaces: common approaches and new developments (Review).* Biointerphases, 2014. **9**(2): p. 029005.
28. Cavallaro, A.A., M.N. Macgregor-Ramiasa, and K. Vasilev, *Antibiofouling Properties of Plasma-Deposited Oxazoline-Based Thin Films.* ACS Applied Materials & Interfaces, 2016. **8**(10): p. 6354-6362.
29. Griesser, S.S., et al., *Antimicrobial Peptides Grafted onto a Plasma Polymer Interlayer Platform: Performance upon Extended Bacterial Challenge.* Coatings, 2021. **11**(1).
30. Linklater, D.P., S. Juodkazis, and E.P. Ivanova, *Nanofabrication of mechano-bactericidal surfaces.* Nanoscale, 2017. **9**(43): p. 16564-16585.
31. Ivanova, E.P., et al., *Natural bactericidal surfaces: mechanical rupture of Pseudomonas aeruginosa cells by cicada wings.* Small, 2012. **8**(16): p. 2489-94.
32. Kelleher, S.M., et al., *Cicada Wing Surface Topography: An Investigation into the Bactericidal Properties of Nanostructural Features.* ACS Appl Mater Interfaces, 2016. **8**(24): p. 14966-74.
33. Nowlin, K., et al., *Adhesion-dependent rupturing of Saccharomyces cerevisiae on biological antimicrobial nanostructured surfaces.* Journal of The Royal Society Interface, 2015. **12**(102): p. 20140999.
34. Bandara, C.D., et al., *Bactericidal Effects of Natural Nanotopography of Dragonfly Wing on Escherichia coli.* ACS Appl Mater Interfaces, 2017. **9**(8): p. 6746-6760.
35. Mainwaring, D.E., et al., *The nature of inherent bactericidal activity: insights from the nanotopology of three species of dragonfly.* Nanoscale, 2016. **8**(12): p. 6527-6534.
36. Li, X., et al., *The nanotipped hairs of gecko skin and biotemplated replicas impair and/or kill pathogenic bacteria with high efficiency.* Nanoscale, 2016. **8**(45): p. 18860-18869.
37. Elbourne, A., R.J. Crawford, and E.P. Ivanova, *Nano-structured antimicrobial surfaces: From nature to synthetic analogues.* J Colloid Interface Sci, 2017. **508**: p. 603-616.
38. Ivanova, E.P., et al., *Bactericidal activity of black silicon.* Nat Commun, 2013. **4**: p. 2838.
39. Hamada, K., et al., *Hydrothermal modification of titanium surface in calcium solutions.* Biomaterials, 2002. **23**(10): p. 2265-2272.
40. Bavykin, D.V., J.M. Friedrich, and F.C. Walsh, *Protonated Titanates and TiO2 Nanostructured Materials: Synthesis, Properties, and Applications.* Advanced Materials, 2006. **18**(21): p. 2807-2824.
41. Anitha, V.C., et al., *Morphology-dependent low macroscopic field emission properties of titania/titanate nanorods synthesized by alkali-controlled hydrothermal treatment of a metallic Ti surface.* Nanotechnology, 2015. **26**(35): p. 355705.
42. Diu, T., et al., *Cicada-inspired cell-instructive nanopatterned arrays.* Scientific Reports, 2014. **4**(1): p. 7122.
43. Jaggessar, A. and P.K.D.V. Yarlagadda, *Modelling the growth of hydrothermally synthesised bactericidal nanostructures, as a function of processing conditions.* Materials Science and Engineering C, 2020. **108**.
44. Clainche, T.L., et al., *Mechano-Bactericidal Titanium Surfaces for Bone Tissue Engineering.* ACS Applied Materials & Interfaces, 2020. **12**(43): p. 48272-48283.
45. Ovenstone, J. and K. Yanagisawa, *Effect of Hydrothermal Treatment of Amorphous Titania on the Phase Change from Anatase to Rutile during Calcination.* Chemistry of Materials, 1999. **11**(10): p. 2770-2774.
46. López Zavala, M.Á., S.A. Lozano Morales, and M. Ávila-Santos, *Synthesis of stable TiO(2) nanotubes: effect of hydrothermal treatment, acid washing and annealing temperature.* Heliyon, 2017. **3**(11): p. e00456-e00456.
47. Lu, H., et al., *A systematic study on evolution mechanism of titanate nanostructures in the hydrothermal process.* Chemical Physics Letters, 2011. **508**(4): p. 258-264.
48. Tsimbouri, P.M., et al., *Osteogenic and bactericidal surfaces from hydrothermal titania nanowires on titanium substrates.* Sci Rep, 2016. **6**: p. 36857.
49. Jaggessar, A., et al., *Mechanical, bactericidal and osteogenic behaviours of hydrothermally synthesised TiO2 nanowire arrays.* Journal of the Mechanical Behavior of Biomedical Materials, 2018. **80**: p. 311-319.
50. Jaggessar, A., et al. *Investigation of mechanical properties and morphology of hydrothermally manufactured titanium dioxide nanostructured surfaces*. in *Procedia Manufacturing*. 2019.

51. Wandiyanto, J.V., et al., *Tunable morphological changes of asymmetric titanium nanosheets with bactericidal properties.* J Colloid Interface Sci, 2020. **560**: p. 572-580.
52. Ishak, M.I., et al., *Protruding Nanostructured Surfaces for Antimicrobial and Osteogenic Titanium Implants.* Coatings, 2020. **10**(8).
53. Sjöström, T., A.H. Nobbs, and B. Su, *Bactericidal nanospike surfaces via thermal oxidation of Ti alloy substrates.* Materials Letters, 2016. **167**: p. 22-26.
54. Jenkins, J., et al., *Antibacterial effects of nanopillar surfaces are mediated by cell impedance, penetration and induction of oxidative stress.* Nat Commun, 2020. **11**(1): p. 1626.
55. Hasan, J., S. Jain, and K. Chatterjee, *Nanoscale Topography on Black Titanium Imparts Multi-biofunctional Properties for Orthopedic Applications.* Sci Rep, 2017. **7**: p. 41118.
56. Domanski, M., et al., *Submicron-patterning of bulk titanium by nanoimprint lithography and reactive ion etching.* Nanotechnology, 2012. **23**(6): p. 065306.
57. Hotovy, I., et al., *Patterning of titanium oxide nanostructures by electron-beam lithography combined with plasma etching.* Journal of Micromechanics and Microengineering, 2015. **25**(7): p. 074006.
58. Ganjian, M., et al., *Reactive ion etching for fabrication of biofunctional titanium nanostructures.* Sci Rep, 2019. **9**(1): p. 18815.
59. Sengstock, C., et al., *Structure-related antibacterial activity of a titanium nanostructured surface fabricated by glancing angle sputter deposition.* Nanotechnology, 2014. **25**(19): p. 195101.
60. Alvarez, R., et al., *Antibacterial Nanostructured Ti Coatings by Magnetron Sputtering: From Laboratory Scales to Industrial Reactors.* Nanomaterials (Basel, Switzerland), 2019. **9**(9): p. 1217.
61. Shahali, H., et al., *Multi-biofunctional properties of three species of cicada wings and biomimetic fabrication of nanopatterned titanium pillars.* Journal of Materials Chemistry B, 2019. **7**(8): p. 1300-1310.
62. Shahali, H., et al., *A systematic approach towards biomimicry of nanopatterned cicada wings on titanium using electron beam lithography.* Nanotechnology, 2020. **32**(6): p. 065301.
63. Sjöström, T., et al., *Fabrication of pillar-like titania nanostructures on titanium and their interactions with human skeletal stem cells.* Acta Biomater, 2009. **5**(5): p. 1433-41.
64. Sjöström, T., N. Fox, and B. Su, *Through-mask anodization of titania dot- and pillar-like nanostructures on bulk Ti substrates using a nanoporous anodic alumina mask.* Nanotechnology, 2009. **20**(13): p. 135305.
65. Kuznetsov, V.A., *Crystallization of the Oxides of Titanium Subgroup Metals*, in *Crystallization Processes under Hydrothermal Conditions*, A.N. Lobachev, Editor. 1973, Springer US: Boston, MA. p. 43-55.
66. Dinan, B., et al., *Thermally grown TiO2 nanowires to improve cell growth and proliferation on titanium based materials.* Ceramics International, 2013. **39**(5): p. 5949-5954.
67. Jang, Y., et al., *Inhibition of Bacterial Adhesion on Nanotextured Stainless Steel 316L by Electrochemical Etching.* ACS biomaterials science & engineering, 2018. **4**(1): p. 90-97.
68. Nastulyavichus, A.A., et al., *Nanostructured steel for antibacterial applications.* Laser Physics Letters, 2019. **17**(1): p. 016003.
69. Elbourne, A., et al., *Multi-directional electrodeposited gold nanospikes for antibacterial surface applications.* Nanoscale Advances, 2019. **1**(1): p. 203-212.
70. Sikhwivhilu, L.M., S. Sinha Ray, and N.J. Coville, *Influence of bases on hydrothermal synthesis of titanate nanostructures.* Applied Physics A, 2009. **94**(4): p. 963-973.
71. Jaggessar, A., et al., *Bacteria Death and Osteoblast Metabolic Activity Correlated to Hydrothermally Synthesised TiO(2) Surface Properties.* Molecules, 2019. **24**(7).
72. Velic, A., et al., *Mechanics of Bacterial Interaction and Death on Nanopatterned Surfaces.* Biophys J, 2021. **120**(2): p. 217-231.
73. Hasan, J., et al., *Selective bactericidal activity of nanopatterned superhydrophobic cicada Psaltoda claripennis wing surfaces.* Appl Microbiol Biotechnol, 2013. **97**(20): p. 9257-62.
74. Pogodin, S., et al., *Biophysical model of bacterial cell interactions with nanopatterned cicada wing surfaces.* Biophys J, 2013. **104**(4): p. 835-40.
75. Linklater, D.P., et al., *Mechano-bactericidal actions of nanostructured surfaces.* Nat Rev Microbiol, 2021. **19**(1): p. 8-22.

76. Li, X., *Bactericidal mechanism of nanopatterned surfaces.* Physical Chemistry Chemical Physics, 2016. **18**(2): p. 1311-1316.
77. Xue, F., et al., *Theoretical study on the bactericidal nature of nanopatterned surfaces.* J Theor Biol, 2015. **385**: p. 1-7.
78. Lin, N., et al., *Nanodarts, nanoblades, and nanospikes: Mechano-bactericidal nanostructures and where to find them.* Advances in Colloid and Interface Science, 2018. **252**: p. 55-68.
79. Watson, G.S., et al., *A Simple Model for Binding and Rupture of Bacterial Cells on Nanopillar Surfaces.* Advanced Materials Interfaces, 2019. **6**(10): p. 1801646.
80. Cui, Q., et al., *Validation of the mechano-bactericidal mechanism of nanostructured surfaces with finite element simulation.* Colloids and Surfaces B: Biointerfaces, 2021. **206**: p. 111929.
81. Chang, W., et al., *Global Transcriptome Analysis of Staphylococcus aureus Response to Hydrogen Peroxide.* Journal of Bacteriology, 2006. **188**(4): p. 1648.
82. Cosgrove, K., et al., *Catalase (KatA) and alkyl hydroperoxide reductase (AhpC) have compensatory roles in peroxide stress resistance and are required for survival, persistence, and nasal colonization in Staphylococcus aureus.* J Bacteriol, 2007. **189**(3): p. 1025-35.
83. Nosaka, Y. and A.Y. Nosaka, *Generation and Detection of Reactive Oxygen Species in Photocatalysis.* Chemical Reviews, 2017. **117**(17): p. 11302-11336.
84. Liu, S., et al., *Antibacterial Activity of Graphite, Graphite Oxide, Graphene Oxide, and Reduced Graphene Oxide: Membrane and Oxidative Stress.* ACS Nano, 2011. **5**(9): p. 6971-6980.
85. Carmel-Harel, O. and G. Storz, *Roles of the Glutathione- and Thioredoxin-Dependent Reduction Systems in the Escherichia Coli and Saccharomyces Cerevisiae Responses to Oxidative Stress.* Annual Review of Microbiology, 2000. **54**(1): p. 439-461.
86. Vecitis, C.D., et al., *Electronic-structure-dependent bacterial cytotoxicity of single-walled carbon nanotubes.* ACS Nano, 2010. **4**(9): p. 5471-9.
87. Allocati, N., et al., *Die for the community: an overview of programmed cell death in bacteria.* Cell Death & Disease, 2015. **6**(1): p. e1609-e1609.
88. Peeters, S.H. and M.I. de Jonge, *For the greater good: Programmed cell death in bacterial communities.* Microbiological Research, 2018. **207**: p. 161-169.
89. Durand, P.M. and G. Ramsey, *The Nature of Programmed Cell Death.* Biological Theory, 2019. **14**(1): p. 30-41.
90. Bright, R., et al., *In Vitro Bactericidal Efficacy of Nanostructured Ti6Al4V Surfaces is Bacterial Load Dependent.* ACS Appl Mater Interfaces, 2021. **13**(32): p. 38007-38017.
91. Singh, M.K. and L.J. Kenney, *Super-resolution imaging of bacterial pathogens and visualization of their secreted effectors.* FEMS Microbiology Reviews, 2020. **45**(2).
92. Casuso, I., L. Redondo-Morata, and F. Rico, *Biological physics by high-speed atomic force microscopy.* Philosophical Transactions of the Royal Society A: Mathematical, Physical and Engineering Sciences, 2020. **378**(2186): p. 20190604.
93. Ivanova, E.P., et al., *The multi-faceted mechano-bactericidal mechanism of nanostructured surfaces.* Proc Natl Acad Sci U S A, 2020. **117**(23): p. 12598-12605.
94. Mirzaali, M.J., et al., *In-silico quest for bactericidal but non-cytotoxic nanopatterns.* Nanotechnology, 2018. **29**(43): p. 43LT02.
95. Velic, A., et al., *Parametric Study on Nanopattern Bactericidal Activity.* Procedia Manufacturing, 2019. **30**: p. 514-521.
96. Linklater, D.P., et al., *High Aspect Ratio Nanostructures Kill Bacteria via Storage and Release of Mechanical Energy.* ACS Nano, 2018. **12**(7): p. 6657-6667.
97. Modaresifar, K., et al., *Bactericidal effects of nanopatterns: A systematic review.* Acta Biomaterialia, 2019. **83**: p. 29-36.
98. Mai-Prochnow, A., et al., *Gram positive and Gram negative bacteria differ in their sensitivity to cold plasma.* Scientific Reports, 2016. **6**(1): p. 38610.
99. Kim, E.-J., et al., *Thorn-like TiO2 nanoarrays with broad spectrum antimicrobial activity through physical puncture and photocatalytic action.* Scientific Reports, 2019. **9**(1): p. 13697.
100. Liu, T., et al., *Mechanism Study of Bacteria Killed on Nanostructures.* The Journal of Physical Chemistry B, 2019. **123**(41): p. 8686-8696.

101. Hizal, F., et al., *Impact of 3D Hierarchical Nanostructures on the Antibacterial Efficacy of a Bacteria-Triggered Self-Defensive Antibiotic Coating.* ACS Applied Materials & Interfaces, 2015. **7**(36): p. 20304-20313.
102. Xue, F., et al., *Theoretical study on the bactericidal nature of nanopatterned surfaces.* Journal of Theoretical Biology, 2015. **385**: p. 1-7.
103. Hori, K. and S. Matsumoto, *Bacterial adhesion: From mechanism to control.* Biochemical Engineering Journal, 2010. **48**(3): p. 424-434.
104. Labischinski, H., et al., *Direct proof of a "more-than-single-layered" peptidoglycan architecture of Escherichia coli W7: a neutron small-angle scattering study.* Journal of bacteriology, 1991. **173**(2): p. 751-756.
105. Vollmer, W. and J.-V. Höltje, *The Architecture of the Murein (Peptidoglycan) in Gram-Negative Bacteria: Vertical Scaffold or Horizontal Layer(s)?* Journal of Bacteriology, 2004. **186**(18): p. 5978.
106. Dickson, M.N., et al., *Nanopatterned polymer surfaces with bactericidal properties.* Biointerphases, 2015. **10**(2): p. 021010.
107. Tu, Y., et al., *Destructive extraction of phospholipids from Escherichia coli membranes by graphene nanosheets.* Nature Nanotechnology, 2013. **8**(8): p. 594-601.
108. Linklater, D.P., et al., *Comment on "Bactericidal Effects of Natural Nanotopography of Dragonfly Wing on Escherichia coli".* ACS Applied Materials & Interfaces, 2017. **9**(35): p. 29387-29393.
109. Semlitsch, M., F. Staub, and H. Weber, *Titanium-aluminium-niobium alloy, development for biocompatible, high strength surgical implants.* Biomed Tech (Berl), 1985. **30**(12): p. 334-9.
110. Long, M. and H.J. Rack, *Titanium alloys in total joint replacement—a materials science perspective.* Biomaterials, 1998. **19**(18): p. 1621-1639.
111. Kapat, K., et al., *Simultaneous hydrothermal bioactivation with nano-topographic modulation of porous titanium alloys towards enhanced osteogenic and antimicrobial responses.* J Mater Chem B, 2018. **6**(18): p. 2877-2893.
112. Auer, G.K. and D.B. Weibel, *Bacterial Cell Mechanics.* Biochemistry, 2017. **56**(29): p. 3710-3724.
113. Li, X., et al., *A nanostructured anti-biofilm surface widens the efficacy against spindle-shaped and chain-forming rod-like bacteria.* Nanoscale, 2020. **12**(36): p. 18864-18874.
114. Yang, D.C., K.M. Blair, and N.R. Salama, *Staying in Shape: the Impact of Cell Shape on Bacterial Survival in Diverse Environments.* Microbiology and Molecular Biology Reviews, 2016. **80**(1): p. 187.
115. Zapun, A., T. Vernet, and M.G. Pinho, *The different shapes of cocci.* FEMS Microbiol Rev, 2008. **32**(2): p. 345-60.
116. Pham, V.T.H., et al., *Nanotopography as a trigger for the microscale, autogenous and passive lysis of erythrocytes.* Journal of Materials Chemistry B, 2014. **2**(19): p. 2819-2826.
117. Hasan, J., et al., *Engineering a nanostructured "super surface" with superhydrophobic and superkilling properties.* RSC Advances, 2015. **5**(56): p. 44953-44959.
118. Pham, V.T.H., et al., *"Race for the Surface": Eukaryotic Cells Can Win.* ACS Applied Materials & Interfaces, 2016. **8**(34): p. 22025-22031.
119. Bhadra, C.M., et al., *Antibacterial titanium nano-patterned arrays inspired by dragonfly wings.* Sci Rep, 2015. **5**: p. 16817.
120. Wandiyanto, J.V., et al., *The Fate of Osteoblast-Like MG-63 Cells on Pre-Infected Bactericidal Nanostructured Titanium Surfaces.* Materials (Basel), 2019. **12**(10).
121. Hanson, L., et al., *Characterization of the cell-nanopillar interface by transmission electron microscopy.* Nano Lett, 2012. **12**(11): p. 5815-20.
122. Jagminas, A., et al., *Hydrothermal synthesis and characterization of nanostructured titanium monoxide films.* RSC Advances, 2019. **9**(69): p. 40727-40735.
123. Gao, Q., et al., *Antibacterial and hydroxyapatite-forming coating for biomedical implants based on polypeptide-functionalized titania nanospikes.* Biomaterials Science, 2020. **8**(1): p. 278-289.

GAPS IN KNOWLEDGE

Since Ivanova and colleagues first reported a mechano-bactericidal effect of sharp surface nanotopography features, there has been a substantial amount of focus on similar natural and synthetic surfaces. It is well established that these types of surfaces have a promising capacity to inactivate bacterial cells, but the relevant mechanisms of action are not fully understood. Numerous hypotheses have been put forth to explain the mechano-bactericidal effect of such nanostructured surfaces, with most ideas focused on membrane stress. Other potential mechanisms involve induced oxidative stress, and sheer forces generated by motile cells. While it has been shown that a subpopulation of cells persists on nanopatterned surfaces, there has been little research to determine whether these can form a biofilm as robust as that seen in clinical infections. It is possible that nanopatterned surfaces impede the expression of select virulence factors, such as proteins involved with adhesion and secretion of extracellular polymeric substance.

As nanopillar surfaces have repeatedly been demonstrated to penetrate bacterial cells, this opens possibilities of synergy with antibiotics and other antimicrobial compounds. Nanopillars penetrating the cell envelope will create pores, which may allow for the influx of a greater concentration of antibacterial compounds. Further, if induced oxidative stress is indeed a relevant mechanism of antibacterial action, it is reasonable to assume bactericidal antibiotics will be further enhanced. This is because it has been shown that all bactericidal antibiotics ultimately kill cells by a common mechanism of oxidative stress damage. It is plausible that the induced oxidative stress associated with the nanopillar surfaces will be synergistic with the oxidative stress associated with antibiotics, leading to a more thorough clearance of colonizing cells. There has been recent evidence that drug-resistant bacteria are susceptible to nanopatterned surfaces, but the potential synergy between antibiotics and nanotopography are yet to be explored.

Most publications in this field are focused on the capacity for mechano-bactericidal surfaces to inactivate bacterial pathogens relevant to orthopaedic implants. Conversely, there is very little knowledge about the interaction of these surfaces with fungal pathogens or anaerobic bacterial pathogens associated with periodontal disease. One paper has shown that some nanopillar surfaces can kill *Saccharomyces cerevisiae,* a form of yeast. However, *S. cerevisiae* is not a clinical pathogen, and focus should be directed toward more relevant species such as *Candida albicans* and *Candida parapsilosis.* One paper has demonstrated the ability for a nanopatterned surface to inactivate various anaerobic periodontal bacteria, but the surface used in this study was not titanium based. It remains to be seen whether hydrothermally etched titanium nanostructures can be utilized against fungal pathogens in a clinically relevant capacity. Further, little is known about the exact physiological changes that occur when bacteria attach to nanostructured surfaces.

RESEARCH QUESTIONS, AIMS AND EXPECTED OUTCOMES

Research Questions:

- Can a hydrothermally etched titanium surface eliminate fungal and anaerobic dental pathogens to a similar degree to that seen with orthopaedic pathogens?
- Do cells which persist on the antimicrobial nanostructure form biofilm comparable to cells incubated on a control surface, or are they phenotypically altered by the surface?
- What are the transcriptome-wide changes undergone by *S. aureus* once they attach to a nanostructured surface such as hydrothermally etched titanium?
- Does hydrothermally etched titanium modulate the expression profile of virulence factors relevant to adhesion and biofilm formation?
- Can hydrothermally etched titanium be combined with antibiotic treatment to a synergistic effect?

Project Aims:

This project will be aimed at further assessing the suitability of a nanopatterned surface to be implemented on titanium-based implants with the intention of minimizing implant-associated infection. This will be achieved by the following:

- Assess the capacity of the nanostructured surfaces to inactivate clinically relevant anaerobic bacteria and fungi
- Measure the changes in bacterial gene expression when interacting with nanostructured surfaces with particular focus on virulence factors to identify new mechanisms of action
- Investigate the potential for synergism between antibiotics and nanostructured surfaces

Expected outcomes:

- Determine the capacity for hydrothermally etched titanium to minimize the viability of pathogens relevant to both orthopaedic and periodontal implant infections, in aerobic and anaerobic settings
- Quantification of the expression of virulence genes, such as those related to adhesion and biofilm formation
- Determine the concentration and treatment duration of clinically relevant antibiotics required to eliminate an established bacterial biofilmy on the nanostructured surface compared to a flat control surface
- If synergism is detected between nanotopography and antibiotics, attempt to elucidate the mechanism of synergy

CHAPTER 1:

SPIKED NANOSTRUCTURES DISRUPT FUNGAL BIOFILM AND IMPART INCREASED SENSITIVITY TO ANTIFUNGAL TREATMENT

Andrew Hayles[1], Richard Bright[1], Jonathan Wood[1], Dennis Palms[1], Peter Zilm[2], Toby Brown[3], Dan Barker[3] and Krasimir Vasilev[1*]

[1]Academic Unit of STEM, University of South Australia, Mawson Lakes, Adelaide, 5095, South Australia, Australia.

[2]Adelaide Dental School, University of Adelaide, Adelaide, 5005, South Australia, Australia

[3]Corin Australia, Baulkham Hills, New South Wales 2153, Australia.

*Corresponding author email address: krasimir.vasilev@unisa.edu.au

Keywords: Mechano-bactericidal, morphogenesis, hydrothermal etched, implant, bioinspired, antifungal

Published in Advanced Materials Interfaces, vol. 9, issue 12, 4th February 2022

https://doi.org/10.1002/admi.202102353

Cover Page

Inside Front Cover, Advanced Materials Interfaces vol. 9, issue 12

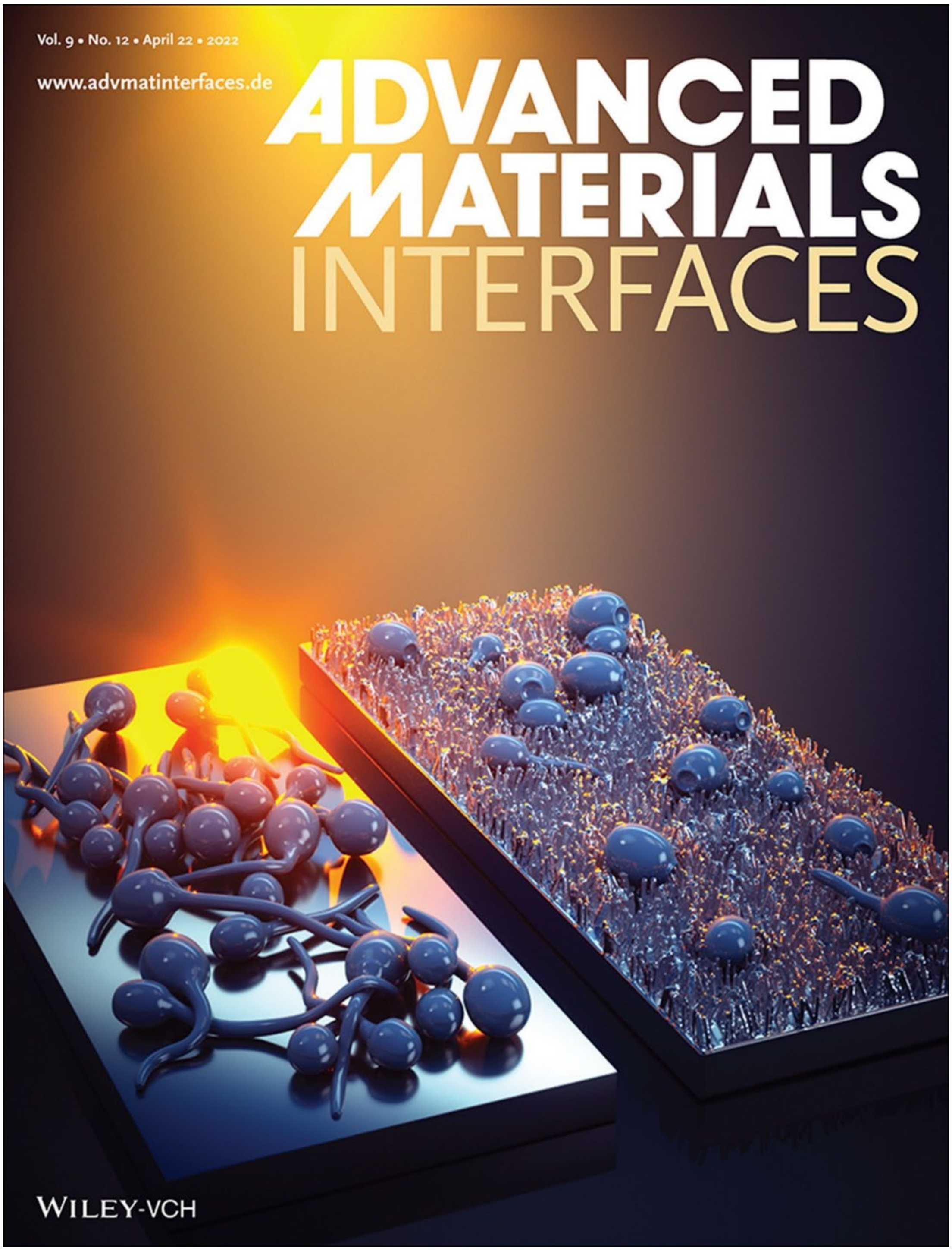

In article number 2102353, Andrew Hayles, Krasimir Vasilev, and co-workers demonstrate that fungal pathogens experience severe cell wall stress and impeded hyphae formation when incubated on nanostructured antimicrobial surfaces. This results in disrupted biofilms which are markedly more sensitive to antifungal drugs at subclinical concentrations. Amphotericin B entirely eradicates *C. albicans* on the nanostructured surface while failing to clear cells on the smooth control.

Abstract

There is a globally increasing demand for medically implanted devices, partly spurred by an aging population. In parallel, there is a proportionate increase in implant associated infection. Much focus has been directed toward development of techniques to fabricate nanostructured antimicrobial biomaterials to mitigate infection. The present study investigates the interaction of the fungal pathogen *Candida albicans* with an antimicrobial surface bearing nanoscale protrusions. *C. albicans* cells were observed to be affected by cell wall stress, which impeded its ability to switch to a hyphal phenotype. There were significant differences in the expression of *C. albicans* virulence-associated genes between the untreated and nanostructured surface. To determine whether the observed inhibition of *C. albicans* would also sensitize it to antifungal drugs, a culture was established for 3 days on the nanostructured surface before being treated with the antifungal drug amphotericin B. The drug was able to kill all cells on the nanostructured surface at sub-clinical concentrations, while remaining ineffective against cultures grown on a smooth control surface. These findings may eventually prove to be impactful in the clinic, as clinicians may be able to reduce antifungal drug dosages and minimize the effects of drug associated toxicity.

1. Introduction

Titanium-based biomaterials are commonly used as the material of choice for implants for orthopaedics, fracture fixation and the periodontal field [1]. The superiority of titanium as a biomaterial is reflected in its corrosion resistance, mechanical strength, biocompatibility and osseointegration capabilities [1a]. Although there is a high success rate associated with implanted devices, failure is not uncommon. One of the primary causes of implant failure is implant-associated infections (IAI) [2]. In the field of orthopaedics, approximately 1-2% of joint replacement arthroplasties result in IAI [3]. The IAI rate is significantly higher in the periodontal field, with peri-implantitis seen in as many as 1 in 3 patients [4]. Infections involving fungal pathogens are emerging in both of these clinical fields, and *Candida* species are detected in as many as 90% of fungal IAI cases [5]. *Candida albicans* represents the most common fungal threat, but other notable species include *Candida parapsilosis, Candida tropicalis* and *Candida glabrata* [5d]. In polymicrobial biofilms, *C. albicans* can protect *Porphyromonas gingivalis* from adverse conditions [6] and promote drug resistance in *Staphylococcus aureus* [7]. Its common occurrence in IAI can be attributed to the fact that *C. albicans* is found amongst the normal skin microbiota as a commensal microbe, and can occasionally translocate from the skin to the implanted device during surgery [8]. In a subset of the population, such as diabetics or those who have an otherwise compromised immune system, *C. albicans* can switch from its normal commensal state to an opportunistic pathogen. This is of particular concern because once a fungal infection becomes systemic, it is associated with a mortality rate of up to 50% [9]. In systemic candidiasis, the kidney is one of the primary organs to be affected, commonly leading to renal failure [10]. As a fungal pathogen, the virulence mechanisms of

C. albicans differs from bacterial pathogens. One striking difference is its ability of pathogenic fungi to reversibly switch between two alternate phenotypes – an ovoid-shaped yeast phenotype and a filamentous hyphal phenotype, referred to as morphogenesis [11]. The yeast phenotype is associated with initial surface colonization, and later dissemination. The hyphal phenotype acts as structural support and promotes tissue invasion [12]. Invasion of host tissue allows *C. albicans* to enter the bloodstream and translocate around the body. Within the bloodstream, the presence of serum and the slightly alkaline pH provides ideal conditions for hyphal cell growth, which then allows the pathogen to invade host tissue at sites distal to its initial colonization [8]. *C. albicans* is highly adaptive to a range of environmental niches which is why systemic candidiasis involves such aggressive pathogenesis, leading to high rates of morbidity and mortality.

When *C. albicans* colonizes an implanted device, it forms a biofilm with a sequence of stages [5a]. Yeast cells act as initial colonizers by attaching to the surface. Surface sensing mechanisms trigger *C. albicans* to switch to the hyphal phenotype, and the polymorphic surface colony begins to secrete an extracellular matrix containing hydrolytic enzymes aiding tissue invasion [13]. Compared to their planktonic counterparts, *C. albicans* biofilm displays enhanced virulence-associated characteristics and antifungal drug resistance [14]. Biofilm associated drug resistance is influenced by multiple factors, including the architecture of biofilm, the protective extracellular matrix and the induced expression of resistance genes such as drug efflux pumps [8]. Once biofilm cell density becomes greater than 10^6 colony forming units per mL (CFU mL^{-1}), yeast cells begin to disseminate and relocate to uninhabited surfaces [15].

As a fungal species, *C. albicans* is not susceptible to the antibacterial prophylaxis that is typically used during surgical implant placement [2b]. Furthermore, the eradication of bacteria by prophylactic antibiotics can promote the necessary conditions for *C. albicans* to switch from commensalism to opportunism [5d]. To complicate matters, the eukaryotic nature of *C. albicans* makes it exceedingly difficult to treat, as there are relatively few pathogen-specific targets for drugs to be developed against [9, 16].

Recently, there has been much attention to biomaterials with engineered surface topographies which can inhibit microbial colonization [17]. These types of biomaterials are particularly attractive due to the mechanical nature by which they passively kill pathogens [18] and can be described as 'mechano-bactericidal'. Depending on the fabrication method, antimicrobial nanostructured surfaces can be engineered to consist of highly ordered and geometrically defined features [17d], or randomly oriented and heterogenous features [19]. Typically, methods that generate highly ordered nanostructures are difficult to produce on large surface areas or on objects with complex geometry, making large scale manufacture challenging [20]. Hydrothermal etching is a highly scalable technique which generates randomly oriented nanoscale protrusions cost-effectively, with a total surface coverage irrespective of the geometric complexity of the object.

Nanostructured antimicrobial surfaces do not release any biocidal compounds, reducing the probability of cytotoxicity to surrounding tissue. Nanostructured surface modification can be emulated on common biomedical materials such as titanium and may reduce the need for prolonged drug usage and invasive revision surgeries. This is an attractive outcome because prolonged use of antifungal drugs is associated with substantial toxicity [21] and increased rates of drug resistance [22], while revision surgeries carry the added risk of morbidity and mortality, and further increase the susceptibility to infection [23]. There has been an abundance of in vitro data to show that biomimetic, nanostructured antimicrobial surfaces are effective at killing both Gram-negative and Gram-positive bacterial pathogens, but research into their antifungal capacity is lacking. A successful anti-infective implantable biomaterial will ideally be resistant to both bacterial and fungal pathogens. Therefore, the aim of the present study was to take an established biomimetic nanostructured antimicrobial surface [24] and investigate its antifungal potential. We also evaluate whether these surfaces affect the sensitivity of the pathogen to the antifungal drug amphotericin B (AmB).

2. Results and Discussion

2.1. Surface characterization of hydrothermally etched titanium (HTE-Ti)

To achieve the desired surface nanoarchitecture, Ti6Al4V alloy discs were processed by an alkaline hydrothermal treatment. This resulted in disordered, nanoscale protrusions (nanospikes) with high aspect ratio and an approximately perpendicular orientation. The as-received titanium (AR-Ti) and HTE-Ti surfaces were imaged at high magnification under a scanning electron microscope (SEM; Figure 1). The AR-Ti samples (Figure 1A-C) were observed to have some pits and marks at both the microscale and nanoscale, resultant from the machining and polishing processes undertaken during manufacturing. The higher magnification SEM images of the HTE-Ti surface (Figure 1D-F) revealed the presence of hierarchically ordered sharp nanospikes. The nanospikes had a mean height of 348 ± 152 nm and a mean width at mid-height of 98 ± 60 nm. The mean spacing between neighbouring spike tips was 437 ± 46 nm. Nanoscale roughness of the AR-Ti and HTE-Ti was analysed by AFM (Figure 1 G and H, respectively). The AR-Ti surface was relatively smooth with an average roughness value of $S_a = 4.15$ nm. By contrast, the HTE-Ti surface had an average roughness value of $S_a = 175.5$ nm, which reflects the change in surface topography generated by the hydrothermal etching process. The water contact angle of the AR-Ti and HRE-Ti surface was 61° ± 8° and below 10°, respectively (Figure 1 I and J). It is generally accepted that the increased wettability is an important property for titanium implants because it promotes protein adsorption, host cell attachment, proliferation and differentiation, all of which are precursors to bone formation [25].

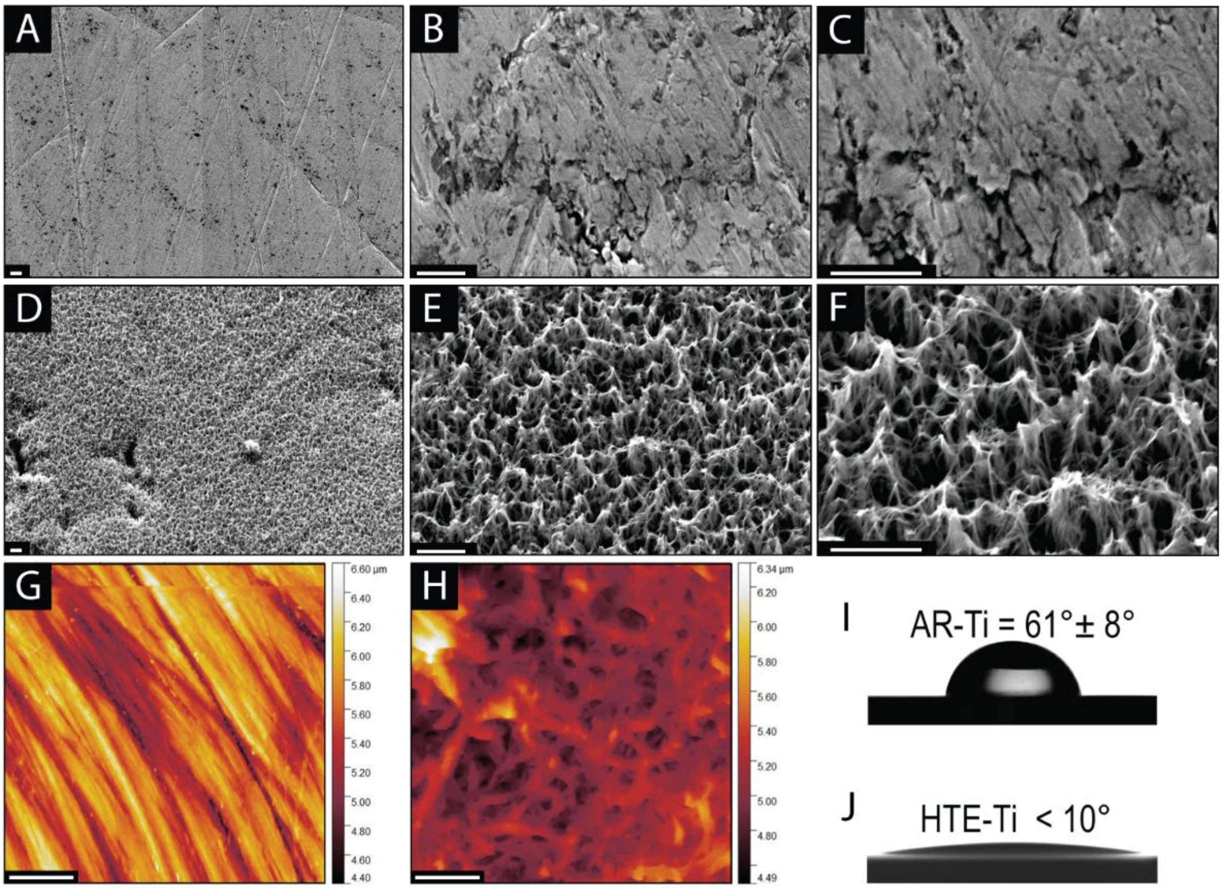

Figure 1. Representative SEM micrographs of AR-Ti (A-C) and HTE-Ti (D-F). Nanoscale roughness of AR-Ti (G) and HTE-Ti (H) measured by AFM. Static water contact angle of AR-Ti (I) and HTE-Ti (J) measured by the sessile drop method. Scale bars represent 1 µm.

2.2. SEM analysis of *C. albicans* on AR-Ti and HTE-Ti surfaces

To determine whether HTE-Ti nanostructures could disrupt the typical morphology of a fungal pathogen, *C. albicans* was incubated in hyphae-inducing conditions on both the AR-Ti and HTE-Ti surfaces (Figure 2). On the AR-Ti surface (Figure 2A-C), *C. albicans* was observed in both its yeast and hyphae forms, with typical dense hyphal networks containing clusters of yeast cells. In contrast, on the HTE-Ti surface (Figure 2D-F), *C. albicans* was primarily observed in its yeast cell phenotype. Where hyphae were observed, their morphology appeared disturbed, and their length was stunted. Figure 2E shows a hyphal apex sunken into the nanostructure, likely affecting its capacity to elongate. In Figure 2F, a hyphal cell appeared shrivelled and fragmented. These hyphae can be compared against the healthy hyphal cells shown in Figure 2A-C, which appear turgid, longer, and more networked. Despite the disturbed hyphal morphology on the HTE-Ti surface, yeast cells typically appeared healthy, however an exception to this was seen in Figure 2F which shows two atypical appearing yeast cells.

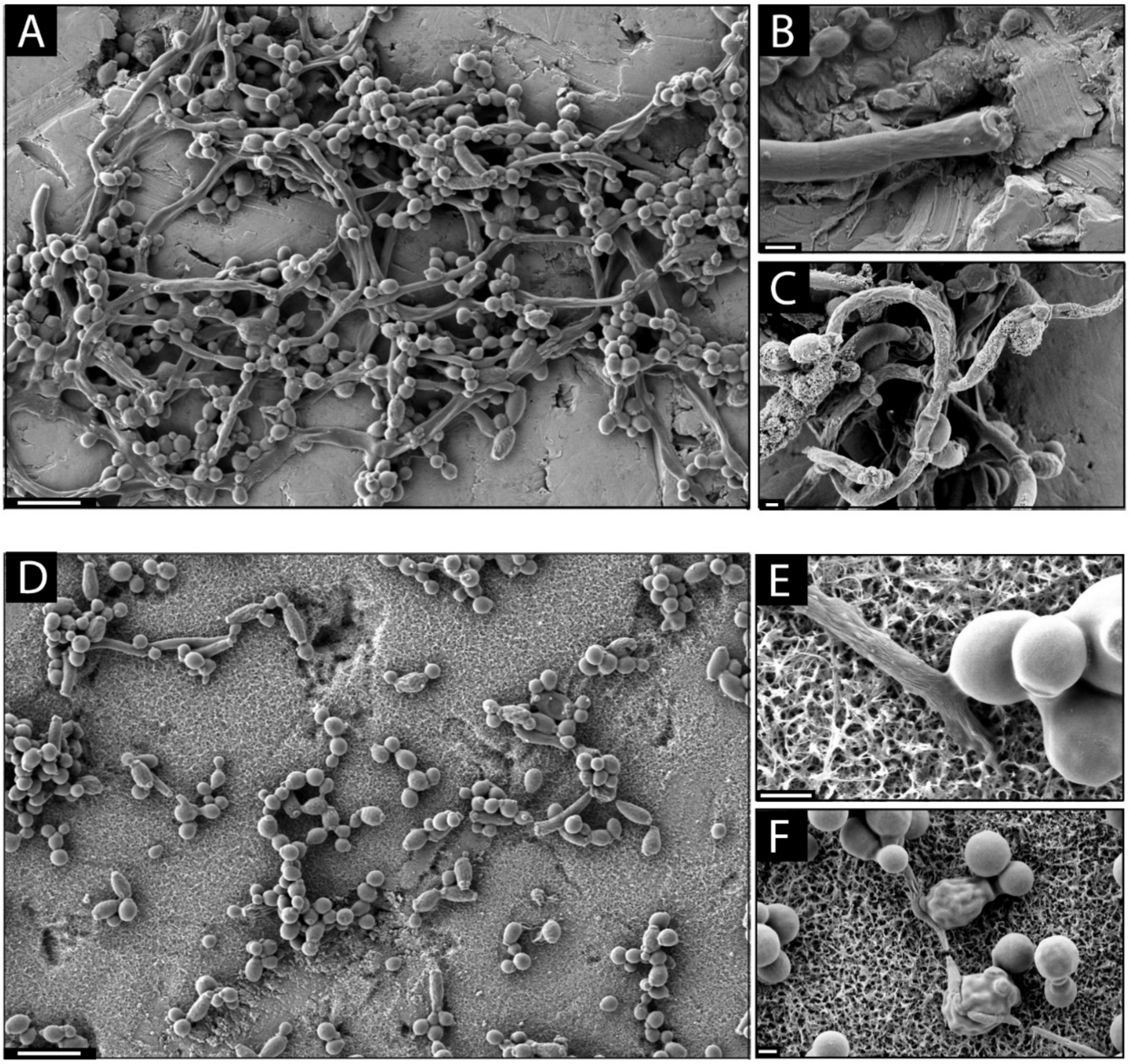

Figure 2. SEM micrographs showing *C. albicans* incubated on AR-Ti (A-C) and HTE-Ti (D-F). Scale bars represent 10 µm on A and D, and 1 µm for B, C, E, F.

2.3. *C. albicans* viability, morphogenesis, and growth rate on HTE-Ti

C. albicans cells attached to AR-Ti and HTE-Ti were stained with *Bac*Light™ LIVE/DEAD® and imaged with a CLSM following 48 h incubation (Figure 3). On the AR-Ti surface (Figure 3A) there was clear evidence of a dimorphic colony of cells, with networks of hyphae surrounded by yeast cells. On the HTE-Ti surface (Figure 3B), the cells were almost exclusively in the yeast form. Few hyphae were observed on the HTE-Ti surface (enlarged image), and they appeared stunted in length. The cells on both surfaces fluoresced green indicating that the cell membrane had not been ruptured by the HTE-Ti surface.

Vertically stacked fluorescence images were used to generate 3-D models of *C. albicans* on the AR-Ti and HTE-Ti surfaces to reveal the spatial arrangement of cells (Figure 3 C and D). Cells on the AR-Ti surface were more likely to aggregate vertically, particularly surrounding hyphal networks. Morphogenesis was compared across both surfaces (Figure 3E), and the mean hyphae percentage, length and network size on the HTE-Ti surface were plotted as a reduction from the values obtained on the AR-Ti surface. It was observed that there was a 91% reduction in hyphae percentage, a 30% reduction in hyphae length, and 85% reduction in hyphal network size on the HTE-Ti surface. By having smaller hyphal networks and an overall reduced presence of hyphae, it is likely that *C. albicans* colonizing the HTE-Ti surface is less structurally robust and potentially less resistant to antifungal drugs [26]. Consequently, the fungus may be more susceptible to host clearance and antifungal treatment. Furthermore, the reduced hyphal length is an important observation, as long hyphae are known to be better equipped to form multiple points of adhesion to host cells, increasing their capacity for invasion and systemic dissemination [27].

Biovolume was compared across both surfaces using 3-D fluorescence images (Figure 3F) following 48 h incubation. It was found that the biovolume on HTE-Ti was approximately 50% lower compared to the AR-Ti surface. To determine whether the nanostructured surface would also contribute to a reduced rate of growth over longer time periods, colony enumeration was performed at 4 timepoints over 10 days (Figure 3G). After 24 h, the cell density on the HTE-Ti surface was reduced by 1-log compared to the AR-Ti surface (approximately 10^6 and 10^7 CFU cm^{-2}, respectively). At this point during the incubation, the cell density was still relatively low, and cells must face the challenge of dividing laterally across the surface. The observed decrease in cell density at the early timepoints is likely a consequence of the mechanical interactions between cells and the nanostructured surface, which may have reduced the capacity for cell elongation. Over the following 10 days, the cell density on the AR-Ti surface remained relatively stable, only increasing slightly to $5.1\text{x}10^7$ CFU cm^{-2} at day 10. Over the same period, the cells on the HTE-Ti surface gradually accumulated up to a peak of $2.7\text{x}10^7$ CFU cm^{-2}. This was still a statistically significant reduction from the AR-Ti surface ($P < 0.001$). At these later timepoints, cells may be accumulating vertically such that the cells in the upper layers escape from the influence of the nanostructure. This could explain why the cell density on the HTE-Ti surface was able to approach similar values to the AR-Ti surface toward the end of the 10-day incubation period. Despite this, the reduced cell density on HTE-Ti at day 10 suggests that there are factors other than the mechanical interaction with the nanostructured surface which affect cell accumulation on the HTE-Ti surface. It has been shown that mutant *C. albicans* which cannot form hyphae are also unable to form a strong biofilm [12b]. Hyphal cells enable thicker biofilms, and they function as structural support for the surrounding yeast cells [27a]. The relative lack of hyphal cells observed on the HTE-Ti surface may consequently explain the reduced cell density, as it is likely that a robust biofilm could not be formed even after 10 days.

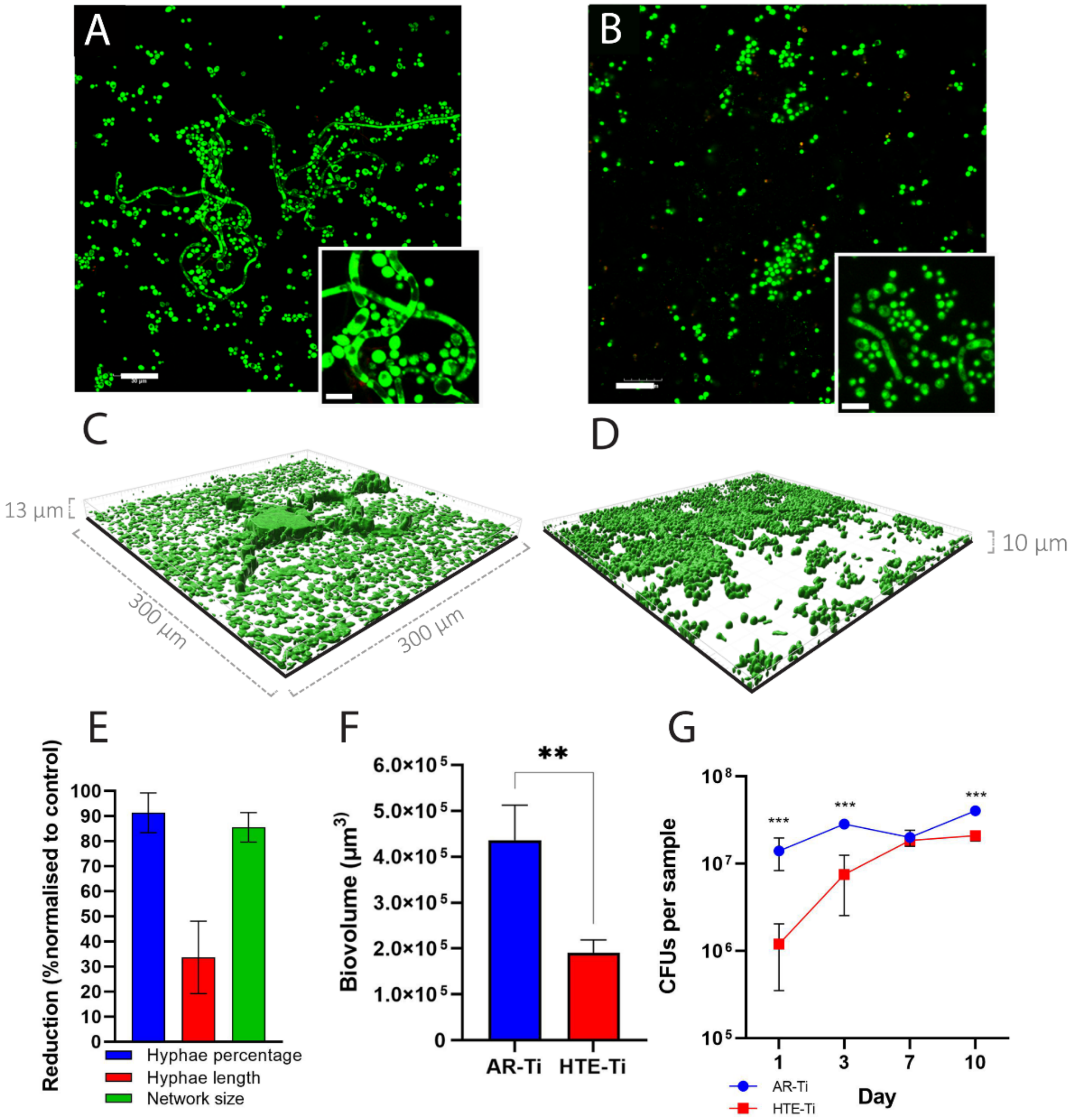

Figure 3. Single plane fluorescence micrographs showing differences in cell morphology on AR-Ti and HTE-Ti at the interface of the surface (A and B); 3-D representations of *C. albicans* cultured on AR-Ti and HTE-Ti (C and D); morphological statistics (E); biovolume (F) and longitudinal rate of surface colonization (G). Mean ± SD, n = 3, ** P < 0.01. *** P < 0.001

2.3. FIB-SEM cross-sectional analysis

To further characterize the mechanical interaction between *C. albicans* cells and HTE-Ti, FIB cross sections of the cell-surface interface were generated, which was then imaged by SEM (Figure 4). In Figure 4A, a typical yeast cell is shown attached to the smooth AR-Ti surface. The yeast cell appeared turgid, and its inner membrane appeared smooth. In Figure 4B, two yeast cells in the process of budding, are shown (labelled 1 and 2) attached to the HTE-Ti surface. Cell 1 had a typical appearance, and its morphology was smooth and turgid. Cell 2 had a shrivelled and flaccid appearance. A cross-section of these two cells is shown in Figure 4C. The dashed circles highlight points at which the nanostructure appeared to physically deform the cell wall. Both cells 1 and 2 had a rough, bumpy inner membrane surface which was strikingly different from the cell on the AR-Ti surface in Figure 4A. It is interesting to note that although cell 1 was turgid and superficially undisturbed, its inner membrane surface was still clearly deformed compared to the cell on the AR-Ti surface. Similar observations were made for hyphal cells. In Figure 4D, a hyphal cell is severely warped against the nanostructure beneath it. The cell membrane of the hyphal cell was observed to be much thinner in regions in direct contact with the nanostructure. This contrasts the hyphae on AR-Ti, which were shown to be resting flat against the surface without any obvious deformation (Figure 4E). Despite the membrane disturbances highlighted by cross sectional analysis, there was no evidence of membrane penetration or rupture by the HTE-Ti nanostructure.

C. albicans has an arsenal of responses which are triggered by various stressors, such as pH, temperature, or in this case, cell wall stress [28]. In particular, *C. albicans* attempts to remediate cell wall stress by fortifying its chitin layer (the structural component of the cell wall) [29]. Further, the same response results in a reduced ability for dividing *C. albicans* cells to separate, which may account for the reduction in viable cell counts presented in Figure 3. Cell wall stress also interferes with the localization of septin [30]. One of the functions of septin is to initiate and mediate proper hyphal morphogenesis and regulate their shape [31]. This therefore may be the key reason for the observed inhibition in hyphal morphogenesis.

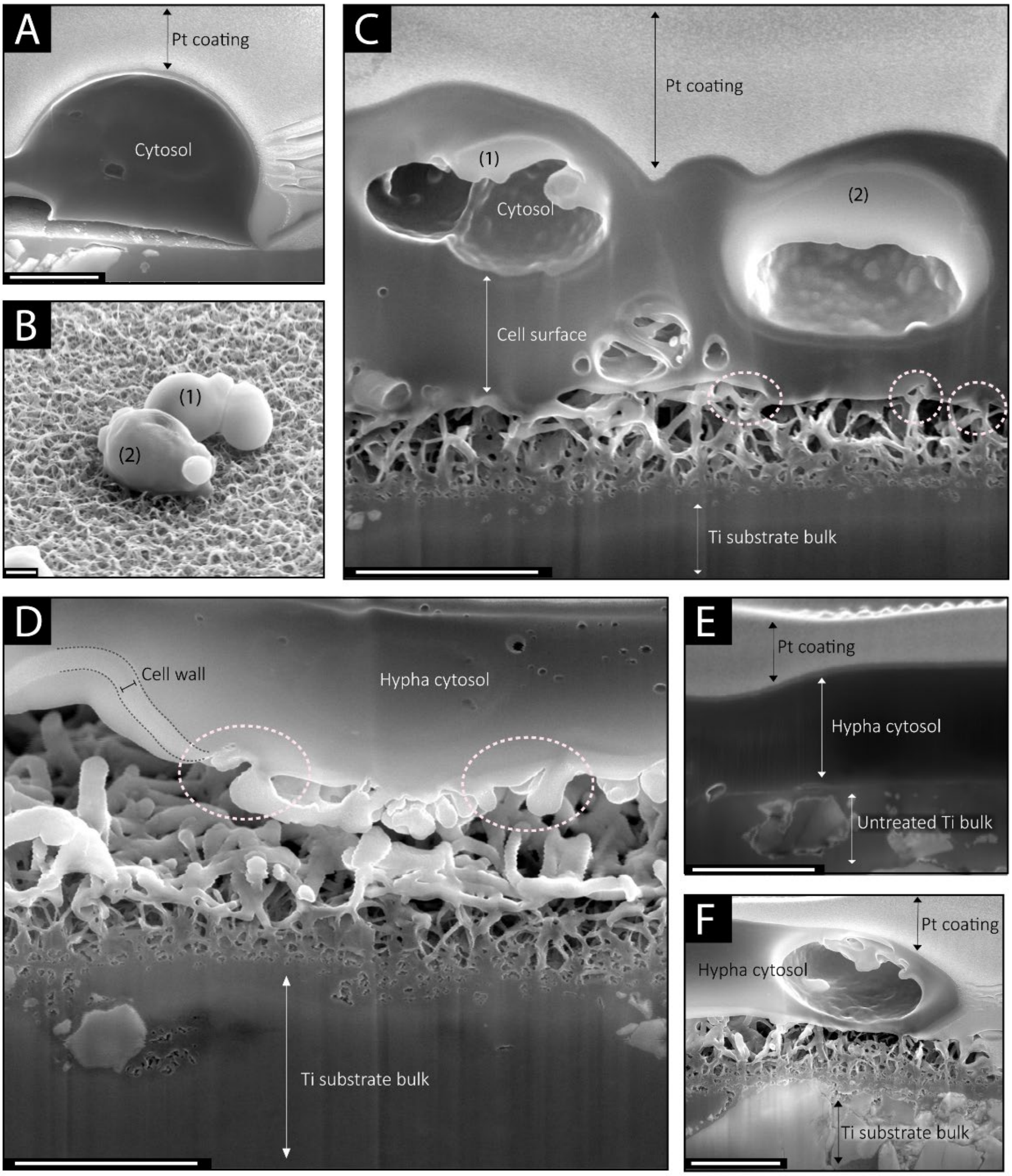

Figure 4. FIB-SEM analysis of *C. albicans* yeast cells on AR-Ti (A) and HTE-Ti (B and C), and hyphal cells on AR-Ti (E) and HTE-Ti (D and F). Dashed circles highlight points of cell wall deformation at the cell-nanostructure interface. Scale bars represent 1 µm.

2.4. Relative gene expression of hyphae-associated virulence factors

Based on the previous observations of inhibited morphogenesis, it was hypothesized that the expression of hyphae-associated virulence factors may also be altered on the HTE-Ti surface. To investigate this, HWP1, ALS3 and SAP5 were chosen as hyphae-associated genes of interest to be measured by qPCR (Figure 5). HWP1 encodes Hyphal wall protein 1 (Hwp1), a surface protein which has roles in cell wall assembly, development of hyphae, adhesion and invasion of host cells [32]. Hwp1 enables *C. albicans* hyphae to covalently bond with host cells, promoting strong adhesion prior to invasion [8]. It is also critical to biofilm formation, and Hwp1-null mutants are incapable of forming biofilm in vivo [12b, 33]. In an in vitro model, a Hwp1-deficient mutant formed a yeast-only biofilm while the surrounding media contained both yeast and hyphae [12b]. This emphasizes the hypha-specific adhesive role of Hwp1. Agglutinin-like sequence 3 (Als3), encoded by ALS3, is another hyphae-associated surface protein which has adhesin functions and is central to biofilm formation [6, 12b, 33-34]. However, unlike Hwp1, Als3 is not a requirement for biofilm formation in vivo [12b]. Als3 and Hwp1 are said to be complementary in function, and Als3 interacts with Hwp1 to contribute to biofilm formation [33b]. Secreted aspartyl proteinase 5 (Sap5) is a hyphae-associated protein, encoded by the SAP5 gene, which hydrolyses host proteins and enables invasion of host cells [6, 8, 35]. SAP5 is coregulated with hypha formation and is a requirement for hyphae to invade parenchymal organs [35b].

In the present study, we measured the relative mRNA transcription of hyphae-associated genes from *C. albicans* incubated on AR-Ti and HTE-Ti samples. Based on preliminary observations we noted that the hyphae phenotype was absent when *C. albicans* was cultured in media without serum supplementation – therefore we have included a no-serum group as a control to establish baseline levels of gene expression of the three genes. As the presence of serum is a contributing factor to hyphae formation, it was expected that the chosen genes would be upregulated when exposed to serum. Our observations support this assumption. However, the transcriptional response of *C. albicans* cultured on the HTE-Ti surface differed from that cultured on AR-Ti. For HWP1, serum treatment induced an upregulation 1040% on the AR-Ti surface, but only 380% on the HTE-Ti surface after 48 h. This correlates well with the observation that morphogenesis was substantially impeded on the HTE-Ti surface. For ALS3, the presence of serum did not result in a statistically different mRNA level between surfaces. However, the biofilm-promoting contribution of Als3 is likely impeded on the HTE-Ti surface because there is less Hwp1 for it to interact with [33b]. This interpretation would explain why the colony enumeration results yielded significantly fewer counts on HTE-Ti compared to the AR-Ti surface. For SAP5, serum supplementation resulted in a 260% increase in mRNA on the AR-Ti surface, and a 360% increase on the HTE-Ti surface. This could be interpreted as an adaptive response to mechanically induced stress. Other stressors are known to induce an upregulation of SAP5, such as antifungal treatment [36], or phagocytosis by macrophages [35b]. A common mechanism may be responsible for the increased SAP5 expression of *C. albicans* on HTE-Ti as well as within the phagosome of a macrophage. Within the phagosome, the macrophage attacks pathogens with reactive oxygen species (ROS) to generate lethal oxidative stress [37]. ROS has also been shown to be involved in the bactericidal activity of HTE-Ti,[38] and it is believed that ROS is generated intracellularly as a downstream effect of membrane perturbation [39]. It is plausible that *C. albicans* incubated on the HTE-Ti surface is induced to generate sublethal levels of ROS, and that this exposure triggers it to upregulate SAP5. It was also noted that in the absence of serum, ALS3 and SAP5 showed reduced expression on the HTE-Ti surface compared to AR-Ti. However, as the context of this study focuses on HTE-Ti as a prospective implantable biomaterial which would encounter serum, this observation bears little relevance. Overall, the expression profile of the targeted genes was indicative of a stressed fungal culture with reduced ability to form a typical biofilm.

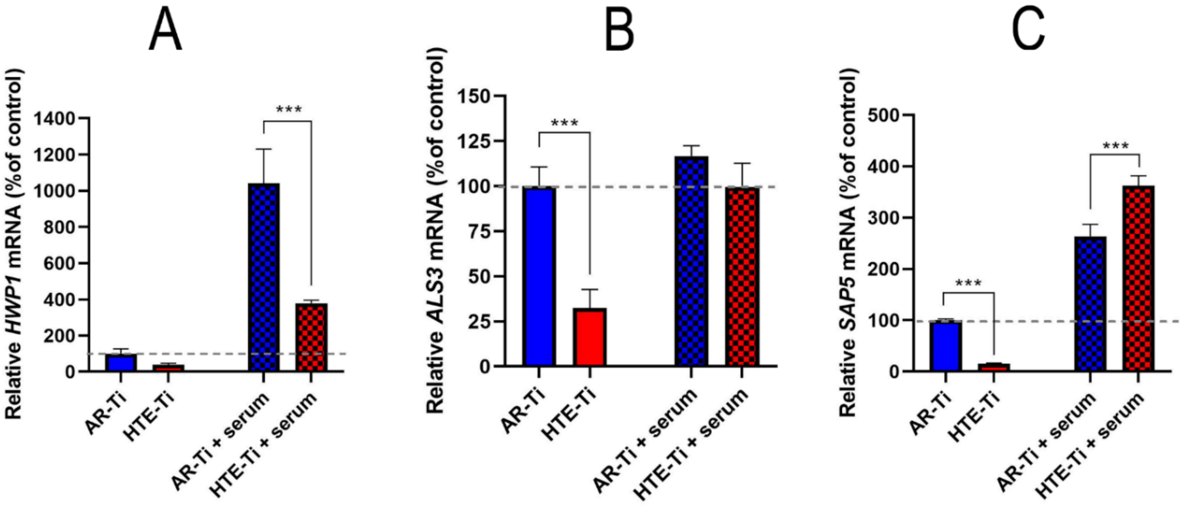

Figure 5: Relative mRNA levels of hyphae-associated virulence factors of *C. albicans* incubated on HTE-Ti at 48 h. (A) HWP1, (B) ALS3, (C) SAP5. Mean ± SD, n = 3. *** P < 0.001.

2.5. Antifungal sensitivity of *C. albicans* cultured on HTE-Ti

Spurred by the observed inhibition of morphogenesis, biofilm formation, and modulation in gene expression, we hypothesized that *C. albicans* cultured on HTE-Ti would be more susceptible to clearance by antifungal drugs. To investigate this, the fungicidal polyene, AmB, was administered daily at a concentration of 20 μg mL^{-1} for 7 days against 3-day established cultures of *C. albicans* on AR-Ti and HTE-Ti. By design, our experimental approach was to investigate substantially lower doses than what might be used clinically. When AmB is administered intravenously in a clinical setting, serum concentrations typically reach 250 μg mL^{-1} [40]. AmB is currently considered the gold-standard in antifungal treatment [41] and is therefore a highly relevant drug to gain insights into potential clinical outcomes. On the AR-Ti surface, AmB did not cause a reduction in biofilm thickness, but did decrease the overall biovolume by approximately 70% over the first 5 days. However, by day-7 the pathogen began to recover to almost the same biovolume at which it started (Figure 6 A and D). Supporting this observation, the proportion of dead biovolume was approximately 12-14% in the first 5 days, but on day 7 it was reduced to only 7% (Figure 6C). This suggests that the fungus had become somewhat resistant to the presence of AmB when cultured on the AR-Ti surface. *C. albicans* is known to be highly adaptive to hostile conditions, and acquired tolerance to antifungal drugs has been observed to occur in as little as 2 h [42]. When cultured on HTE-Ti, *C. albicans* was substantially more sensitive to AmB (Figure 6B), and after the first day of AmB treatment, the proportion of dead biovolume was 40%, which increased over the 7 days until the entire culture was eradicated (Figure

6C). This was met by a proportionate decline in thickness. Similarly, the total biovolume present on the HTE-Ti surface progressively dissipated over the 7 days of treatment and did not recover as it did on the AR-Ti surface (Figure 6D).

The dramatic difference in the sensitivity of *C. albicans* to AmB on AR-Ti and HTE-Ti resonates well with the observed morphological changes between cultures incubated on these two surfaces as well as the gene expression analysis. In general, microbial biofilms can increase antibiotic tolerance up to 1000x, in part due to the protective effects of EPS, expression and transmission of resistance genes and plasticity of metabolic state [43]. For *C. albicans* specifically, its tolerance to antifungals is granted by multiple factors. Firstly, Candida biofilms have a high cell density, and it has been shown that high cell densities increase the concentration of AmB required to inhibit growth, even in the planktonic form [44]. Beyond this, filamentous forms of *C. albicans* have been shown to be substantially more resistant to AmB-induced programmed cell death compared to their yeast counterparts [45]. It is unsurprising then that filamentous-defective mutants of *C. albicans* have been shown to be sensitized to AmB [44]. In the present study, *C. albicans* cultured on HTE-Ti was shown to have a lower cell density and substantially reduced filamentation, and these two factors likely explain the observed increase in sensitivity to AmB. Further, AmB functions by binding to ergosterol in the plasma membrane, thereby creating pores and disrupting membrane integrity [42]. It is plausible then that the membrane perforation induced by AmB acts synergistically with the cell wall perturbation which has been shown to be associated with nanostructured antimicrobial surfaces [46]. A similar occurrence has been reported, in which cell wall stress increases *C. albicans* sensitivity to the antifungal drug nikkomycin [47].

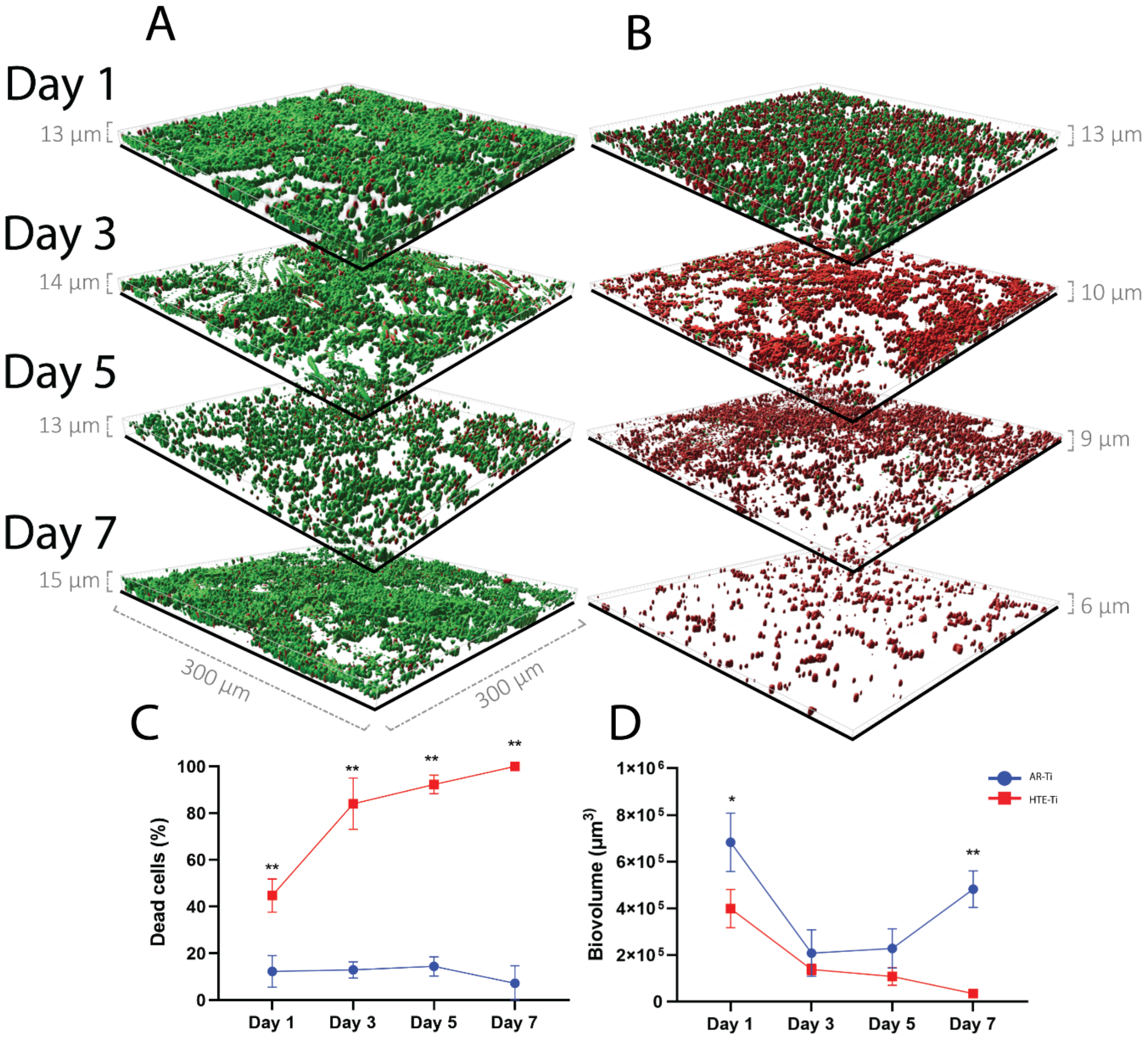

Figure 6: Fluorescence microscopy models of *C. albicans* treated with AmB and incubated on AR-Ti (A) and HTE-Ti (B). Proportions of live and dead cells over 7 days treatment (C). Progressive change in total measured biovolume (D). Mean ± SD, n = 3 ** = $P < 0.01$, * = $P < 0.05$

3. Outlook

Recently there has been a substantial focus directed toward fabrication of anti-infective biomaterials [48]. Biomaterials can be rendered anti-infective using two main fabrication strategies. One strategy involves the elution of antibacterial or antifungal drugs, including various metals such as silver. The benefit of this strategy is that it can eliminate pathogens not only on the surface of the device but also in the proximal tissue. However, there are always concerns associated with eluting materials and coatings associated with tissue toxicity. Furthermore, the reservoir of eluted compound would eventually be exhausted [49]. The alternative strategy involves generating a hostile surface which directly kills pathogens on contact. Nanostructured antimicrobial surfaces take the latter approach, and various laboratories have fabricated these biomaterials with impressive antibacterial efficacy [17d, 38, 50]. These surfaces kill bacteria through physical interaction rather than by a chemical eluting mechanism [18, 51], which means their efficacy should not decrease over time [52]. Further supporting this notion, we incubated *C. albicans* for 10 days on the HTE-Ti surface, then detached the cells by vortex and analysed the nanostructure by SEM (Figure S4). We noted that the long-term fungal culture did not affect the integrity of the nanoscale architecture, suggesting that the nanostructure could remain effective long-term. This is reassuring, as *Saccharomyces cerevisiae* yeast cells have been shown to shear off the nanopillars found on cicada wings [53].

Fungal pathogens are particularly difficult to treat. Due to their eukaryotic nature, it is difficult to develop drugs which target the pathogen and not the host. This has become increasingly complicated by the emergence of drug resistance against existing treatments. Furthermore, the ability of *C. albicans* to form a robust polymorphic biofilm allows it to better resist antifungal treatment [54]. Recently, attention has been directed toward targeting the virulence mechanisms of fungal pathogens [16, 55]. In this way, the aim is not to directly kill the fungal invader, but to limit its capacity to cause systemic infection. One such strategy is to impede *C. albicans* from switching phenotype and forming a polymorphic biofilm [55] In the case of implanted devices, *C. albicans* cannot form a strong biofilm if morphogenesis is impeded [12b]. This may limit its invasiveness and facilitate clearance of the pathogen by the host immune system.

Due to the hostile nature of HTE-Ti toward both bacteria and fungi, it is prudent to assess the cytocompatibility of the modified surface with mammalian cells before the technology can be elevated beyond in vitro studies. In a previous study, we have demonstrated that HTE-Ti does not reduce viability of human dermal fibroblasts [24]. Similarly, in the present study we showed that murine macrophages were able to grow unimpeded on HTE-Ti, without any loss in viability (Figure S5).

The aim of the present study was to take a biomimetic surface which has already been characterized as antibacterial and assess its capacity to inhibit a clinically relevant fungal pathogen. With that goal, we have determined that the HTE-Ti surface does not kill *C. albicans* outright like it kills bacteria, but instead mitigates its ability to form a robust polymorphic biofilm. This functionality is likely mediated by the mechanical interaction between the nanostructure and the fungal cell wall, which severely warps the cell but does penetrate the cytosol, as evidenced by cross-sectional analysis. In this way, the antifungal activity of HTE-Ti is distinct from the antifungal activity of the naturally occurring nanostructure found on the wing of *Neotibicen tibicen*, which ruptures fungal cells on contact [53, 56]. Ultimately, the varying mechanical interaction between a cell and a nanostructure depends on both the topographical parameters of the nanostructure (i.e. structure height, diameter, aspect ratio, spacing) and the biological properties of the cell (i.e. size, cell wall thickness, motility, mode of division). These interactions have been previously reviewed in detail [20]. Fabrication parameters may be tuned to generate nanostructures with defined geometric dimensions, which has been used as a method to optimize bactericidal efficacy [19c]. In this regard, a nanostructured surface may be tuned to specialize in killing either bacteria or fungal cells. It is presently unclear whether further tuning a nanostructured surface to penetrate and kill fungal cells would result in a trade-off in bactericidal efficacy, due to the different biological properties between bacteria and fungi. Nevertheless, it is highly encouraging that the results presented here are indicative of a broad-acting nanostructure, which both kills bacteria on contact, and inhibits polymorphic fungal biofilm. This is clinically important, as a sufficiently effective antimicrobial biomaterial must inhibit both fungal and bacterial pathogens.

By inhibiting fungal biofilm, the function of the HTE-Ti surface can be compared to the recent observations made by Ivanova and colleagues [57], who showed that the nanostructured wings of the Damselfly repel fungal cells. Although the biofilm inhibiting effect is similar between the Damselfly wing and HTE-Ti, their mechanisms are quite different. The Damselfly wing is a hydrophobic surface which entraps a layer of air between nanopillars, and this air layer reduces the propensity for fungal cells to attach to the surface [57]. The HTE-Ti surface is highly hydrophilic and thus there can be no trapped air to exert this effect. The biofilm inhibition observed on HTE-Ti is therefore more attributable to the mechanical interactions between the fungus and the nanostructures. Furthermore, we found that the reduced presence of robust biofilm enhances the capacity for fungicidal drugs to eliminate the surface culture in vitro. This suggests that HTE-Ti biomaterials could potentially reduce the burden of fungal pathogens by impeding them sufficiently for the host immune system and/or antifungal drugs to effectively clear them in a real clinical setting. While the results in this study are highly encouraging, they are limited by the constraints of the in vitro experiment. It is yet to be determined how effective the surface would be at inhibiting fungal biofilms within the dynamic biological environment of a mammalian host, and future in vivo studies will be of great importance in bringing this technology forward for clinical translation.

4. Conclusion

In the present study, we investigated the capacity of a nanostructured antimicrobial surface containing sharp nanostructures to inhibit the fungal pathogen *C. albicans*. SEM analysis revealed that morphogenesis was severely impeded, as primarily yeast cells were observed on the HTE-Ti surface. This contrasts with the AR-Ti surface, which showed high density networks of hyphae. Quantification of morphogenesis showed a significant reduction in hyphal percentage, length, and network size. Fluorescence images revealed that *C. albicans* had not been ruptured by the nanostructured surface, but cross-sectional analysis confirmed significant cell wall disturbance. 3-dimensional fluorescence analysis revealed a reduced biovolume on the HTE-Ti surface. A longitudinal incubation resulted in a decreased rate of surface colonization, and a reduced overall accumulation of cells on the HTE-Ti surface. Relative gene expression targeting virulence-associated genes provided molecular support to the morphology and colony enumeration analyses. An impeded expression of HWP1 supported the reduced presence of hyphae and reduced overall cell accumulation. An upregulation of SAP5 may reflect an adaptive response to the hostile conditions, as previously seen with antifungal drugs. A 7-day fungicide treatment at sub-clinical concentrations resulted in total clearance of *C. albicans* on HTE-Ti, while it was ineffective on the AR-Ti surface. Overall, the data presented in this study indicates that HTE-Ti inhibits the capacity of *C. albicans* to form a robust biofilm by imposing severe cell wall stress and subsequently inhibiting morphogenesis and cell proliferation. This inhibition weakened the antifungal drug resistance typically associated with biofilm formation. In an in vivo situation, this may facilitate clearance of the fungal pathogen by the host immune response, as well as make the pathogen more sensitive to orally administered antifungal drugs. These are major findings towards understanding the properties of such biomimetic nanostructures and applications on medical device surfaces.

5. Materials and Methods

5.1. Fabrication of nanostructure on Ti6Al4V

As-received polished Ti6Al4V discs had a diameter of 10 mm, height of 3 mm and a surface area of 0.78 cm^2. The AR-Ti discs were used as the control samples. An alkaline hydrothermal treatment was used to modify the AR-Ti discs, resulting in the hydrothermally etched titanium alloy surface. Treatment was carried out in a stainless-steel reactor (Parr Instrument Company, USA). 1M KOH was used as the alkaline solution for etching, which was heated to 165 °C for 5 h. Reaction vessel was cooled down with flowing water and samples were rinsed with ultrapure water. After 2 h of air drying at 70 °C, samples were annealed inside a tubular furnace at 450 °C for 4 h and cooled overnight. Samples were cleaned, placed in autoclave bags then autoclaved at 121 °C for 20 mins.

5.2. Surface characterization of HTE-Ti

HTE-Ti surface topography was analysed with a Zeiss Merlin FEG-SEM (Zeiss, Germany) equipped with a SE2 detector at 2KV with a 4 mm working distance, using magnifications between 5,000 and 50,000x, with a 45° stage tilt. SEM images were imported into ImageJ v1.53 (NIH, USA) to measure nanostructure topography. The nanostructures were observed to be composed of a network of spikes which coalesced at their apex, forming a basal pane which branched into an upper layer of spikes. Nanospike height was measured by the distance between the spike apex and the basal plane. Width was determined at mid-height, using a correction factor $\frac{x}{\cos 45°}$ where x equals the nanospike length, to compensate for dimensional distortion caused by the tilted stage during SEM imaging. Mean height and width of spikes were measured across 5 samples, by measuring 25 nanospikes per sample. Nanospike spacing was determined from four SEM images at 0-degree stage tilt, and the nanospike density was calculated in 25 μm^2 fields using ImageJ software v1.53a (NIH, USA). The mean spacing between nanospikes was calculated by $(\frac{[square\ root\ of\ density]}{25\ \mu m} \times 1000)$ to express the measurement in nm. Measurements were presented as mean and standard deviation. Atomic Force Microscopy (AFM) measurements were performed in air using a Bruker Dimension Icon. A NT-MDT NSG03 silicon nitride cantilever with a conical tip quoted by the manufacturer with a radius under 10 nm and a half side angle of 18° was used in PeakForce mode on the HTE-Ti surface. Initial calibration of the cantilever on a glass microscope slide derived a normal spring constant of 2.0 N m^{-1} and a deflection sensitivity of 94.4 nm V^{-1}. PeakForce amplitude over a 5 μm^2 image was set at 150 nm with a frequency of 2 kHz, a lift height of 34 nm, and a scan rate of 8.84 µm s^{-1}. Roughness values were calculated through Gwyddion data analysis software v2.54. Wettability was measured by contact angle (θ) using the sessile drop method, by a goniometer RD-SDM02 (RD Support, UK). Measurements were taken on 5 random areas over triplicate samples. Contact angle of 4 µl ultrapure water was measured by a tangent fitting method using the Contact_Angle.jar plugin for ImageJ v1.53 (NIH, USA).

5.3. Cultures and Conditions

Candida albicans (ATCC 10231) was retrieved from glycerol stock stored at -80 ˚C, and plated onto yeast extract peptone dextrose (YPD) agar plates containing 1% yeast extract, 2% bacteriological peptone, 2% sucrose and 1.5% agar, then incubated overnight at 37 °C. An isolated colony was transferred to YPD broth and incubated overnight at 37°C in static conditions. Following 18 h growth, the cell density was measured using a Nanodrop 2000 spectrophotometer (Thermo Scientific, MA, USA), using absorbance at 600nm (OD600). The OD600 was adjusted to 0.1, corresponding to approximately 1x107 CFU mL^{-1}.

5.4. Inoculation of *C. albicans* on titanium samples

HTE-Ti and AR-Ti discs were aseptically placed into individual wells of a 24-well plate. Diluted *C. albicans* culture was pelleted and resuspended in phosphate buffered saline (PBS) to the same volume. 50 µL containing approximately $5x10^5$ CFU was pipetted onto the surface of each disc and incubated for 3 h at 37˚C to allow for cells to attach. Subsequently, 1mL of Spider medium (1% nutrient broth, 1% peptone, 0.2% K_2HPO_4, adjusted to pH 7.2) supplemented with 20% fetal calf serum (FCS: Gibco, MA, USA), was pipetted into each well. Samples used for SEM, fluorescence microscopy and PCR were incubated for 48 h at 37 ˚C on an orbital shaker (Ratek Instruments Pty. Ltd., VIC, Australia) at 90 RPM, which was sufficient for the development of a mature polymorphic biofilm [58]. For the growth rate assay, samples were incubated under the same conditions for 10 days, with analysis undertaken at day 1, 3, 7 and 10, with daily replenishment of media. Samples for SEM analysis were fixed in 1.25% glutaraldehyde, 4% paraformaldehyde in PBS containing 4% sucrose. Samples for PCR analysis were immersed in 500 µl RNAlater® (Invitrogen, MA, USA) and stored at -80°C until required. Samples for fluorescence microscopy and colony enumeration were immediately analysed after incubation.

5.5. SEM analysis of *C. albicans* morphology

AR-Ti and HTE-Ti samples for SEM analysis were chemically dehydrated according to the following steps: PBS wash (5 minute), 50% ethanol (10 minutes), 70% ethanol (10 minutes), 100% ethanol (10 minutes), 1:1 ratio of 100% ethanol and hexamethyldisilazane (HMDS: Sigma-Aldrich, St. Louis, MO, USA) (20 minutes), 100% HMDS (20 minutes), air dry (2 h). Samples were then mounted on aluminium SEM stubs and sputter coated with 2nm platinum and imaged with a Zeiss Merlin FEG-SEM (Zeiss, Jena, Germany).

5.6. Focused ion beam (FIB) milling

Titanium samples were loaded into a FEI DualBeam FIB-SEM (Thermo Scientific, MA, USA) and the system was purged to create a vacuum. Prior to cross-sectional analysis, the stage was tilted by 52°, moving the titanium discs perpendicular to the gallium ion beam, with a working distance of 4 mm. Before milling, cells of interest were coated with 1 µm of platinum using an accelerated voltage of 10 kV and a 0.46 nA current to protect morphology. Following coating, cross sections were cut at a depth of 5 µm with an accelerated voltage of 10 kV and a 2.6 nA current, followed by a current of 0.46 nA for further refinement of cross sections. Images of cross section were acquired using electron beam accelerating voltages of 10 kV and current of 0.17 nA.

5.7. Live/Dead fluorescence and morphogenesis quantification

Samples were aseptically transferred from the incubation plate to a fresh 24-well plate and immersed in 1 mL of BacLight™ LIVE/DEAD® (Invitrogen, MA, USA) solution, containing equal proportions of propidium iodide and Syto9 at a concentration of 1.5 µl per mL of PBS. The plate was then incubated in the dark at room temperature for 15 minutes and imaged with an Olympus FV3000 confocal scanning laser microscope (CLSM; Olympus, Tokyo, Japan). Six random areas per disc were captured at 40x magnification. Fluorescence images were imported into ImageJ for quantification of the number of yeast cells and hyphal cells, and the lengths of hyphae. Percentage of hyphal cells on HTE-Ti and AR-Ti samples was calculated by (Total hyphal cells)/(Total cells)×100 [55a]. Hyphal length was measured from the yeast-hyphal junction to the apex of the hyphal filament [59]. A hyphal network was defined as all hyphal cells in physical contact, and the hyphal network size was counted as the number of hyphae per hyphal network. Morphogenesis metrics on the HTE-Ti surface were normalized to those on the AR-Ti surface by calculating a percentage reduction.

5.8. Colony enumeration

At timepoints of 1, 3, 7 and 10 days, samples were retrieved from the 24-well plate, gently rinsed in PBS, and transferred to sterile screwcap tubes containing 1 mL PBS. Cells were detached by sonication for 2 minutes followed by vortexing for 30 seconds. Serial 10-fold dilutions were performed and 10 µl aliquots from each dilution were dropped onto YPD agar plates, then incubated overnight at 37°C [60]. Colonies were counted after 24 h incubation and were used to calculate CFU per disc.

5.9. RNA extraction and purification

Samples previously immersed in RNA Later were sonicated for 2 minutes followed by vortexing for 30 seconds in 5 mL tubes to remove adhered cells from AR-Ti and HTE-Ti samples. The cell suspension was then centrifuged for 5 minutes at 12,000g to pellet the cells. The supernatant was discarded, and the pellet resuspended in lysis buffer provided with the RiboPure™ RNA Purification Kit (Invitrogen™, USA). The RNA extractions were carried out following the manufacturer's instructions, adapted to generate a final product of 50 µl. Quantification and purity of the extracted RNA was determined using a NanoDrop 2000c Spectrophotometer (ThermoFisher, MA, USA).

5.10. Quantitative PCR (qPCR)

PCR master mixes were assembled for each primer set using the SuperScript™ III Platinum™ One-Step qRT-PCR Kit (Invitrogen, CA, USA) according to the manufacturer's instructions. Primers were added at a concentration of 10 µM. RNA template (10ng) was added to each reaction tube in 1 µl aliquots. No-template controls (NTCs) received 1 µl of RNAse-free H2O instead. RNA was reverse transcribed to cDNA and amplified in 1 step in a Rotor-Gene Q Thermocycler (version 2.1.0, QIAGEN, Hilden, Germany) with the following program: 3 minutes hold at 50 ˚C; 5 minutes hold at 95 ˚C; 40x cycles of 95 ˚C for 15 seconds and 60 ˚C for 30 seconds. Fluorescent signal was acquired at 60 ˚C. A melting curve was generated between 72 and 95 ˚C at 1 ˚C increments. Amplification specificity was verified by melting curve analysis. qPCR data of target genes were normalized to the RPP2B data, which was chosen as a reference gene due to its stable expression observed on both AR-Ti and HTE-Ti surfaces. The normalized data were used to calculate relative gene expression ($2^{-\Delta Ct}$) and the data were plotted as a % change relative to the baseline (AR-Ti surface without serum supplementation). A list of the primers used in this study can be found in the supplementary information (Table S1).

5.11. Antifungal drug sensitivity

Amphotericin B (AmB: Sigma-Aldrich, St. Louis, MO, USA) was dissolved into a stock concentration of 1 mg mL^{-1} in DMSO. The minimum inhibitory concentration of AmB was determined following CLSI standard testing with the only adjustment being the media, which was Spider media supplemented with 20% FCS instead of Mueller-Hinton Broth. To determine the sensitivity of established cultures to AmB, AR-Ti and HTE-Ti discs were incubated with *C. albicans* for 3 days at 37°C with daily broth replenishment. After 3 days, samples were gently rinsed in PBS and transferred to a fresh a 24-well plate. Samples were immersed in 1mL of Spider media supplemented with 20% FCS and 20 µg mL^{-1} AmB. The media and AmB were replenished daily for 7 days. Samples were analysed for cell viability at days 1, 3, 5 and 7. Samples were stained with LIVE/DEAD™ BacLight™ Bacterial Viability Kit, containing equal proportions of Syto9 and Propidium Iodide at 1.5 µL mL^{-1} PBS, followed by 15 minutes of incubation in the dark at room temperature. Samples were inverted onto a glass coverslip, then imaged with an Olympus FV3000 CLSM, and full thickness biomass images were taken at 3 random locations per sample. Micrographs were analysed using Imaris 3D analysis software (Version 9.3.0, Bitplane, Zürich, CHE) implementing the 'surface' function to obtain total biovolume and dead biovolume.

5.12. Statistical analysis

All experiments were performed in biological triplicate. All data except PCR were analysed in GraphPad Prism v8.3.0 using a Student's T-test. Statistical analysis of qPCR data was performed in GraphPad Prism using a One-Way ANOVA using Tukey's multiple comparisons test, comparing % change in $2^{-\Delta Ct}$ relative to baseline. Statistical significance was defined as $P < 0.05$.

Author contributions

A.H, R.B, T.B, D.B and K.V designed the experiments. A.H, R.B, J.W, D.P and P.Z performed the experiments and analyzed the data. K.V supervised the study and revised the manuscript. All authors took part in drafting the manuscript.

Notes

The authors listed above declare no conflict of interest.

Supporting Information

The supporting information contains: an example fluorescence micrograph showing the bactericidal activity of HTE-Ti; an example of the quantification of hyphal networks; a list of primers used in this study; the measured MIC of AmB; the integrity of the HTE-Ti nanostructure following long-term fungal incubation; the cytocompatibility of murine macrophages on HTE-Ti.

Acknowledgements

This study was co-funded by the Department of Industry, Science, Energy and Resources (Innovative Manufacturing CRC Ltd) Global Orthopaedic Technology Pty Ltd (IMCRC/GOT/130318). The authors acknowledge the funding and in-kind support from Corin Australia and the University of South Australia. The authors would also like to acknowledge the instruments and scientific and technical assistance of Microscopy Australia at the University of South Australia, Mawson Lakes Campus, a facility that is funded by the University, and State and Federal Governments. KV thanks NHMRC for Fellowship GNT1194466.

6. References

[1] a) M. Geetha, A. K. Singh, R. Asokamani, A. K. Gogia, *Prog Mater Sci* **2009**, 54, 397; b) R. B. Osman, M. V. Swain, *Materials (Basel)* **2015**, 8, 932.

[2] a) J. Parvizi, T. Gehrke, *J Arthroplasty* **2014**, 29, 1331; b) J. Parvizi, T. Gehrke, A. F. Chen, *Bone Joint J* **2013**, 95-B, 1450; c) J. M. Schierholz, J. Beuth, *J Hosp Infect* **2001**, 49, 87.

[3] a) P. Stoodley, S. Kathju, F. Z. Hu, G. Erdos, J. E. Levenson, N. Mehta, B. Dice, S. Johnson, L. Hall-Stoodley, L. Nistico, N. Sotereanos, J. Sewecke, J. C. Post, G. D. Ehrlich, *Clin Orthop Relat Res* **2005**, DOI: 10.1097/01.blo.0000175129.83084.d531; b) M. A. Cataldo, N. Petrosillo, M. Cipriani, R. Cauda, E. Tacconelli, *J Infect* **2010**, 61, 443.

[4] K. Kordbacheh Changi, J. Finkelstein, P. N. Papapanou, *Clin Oral Implants Res* **2019**, 30, 306.

[5] a) G. Ramage, J. P. Martínez, J. L. López-Ribot, *FEMS Yeast Research* **2006**, 6, 979; b) C. Gökmenoglu, N. B. Kara, M. Beldüz, A. Kamburoğlu, I. Tosun, E. Sadik, C. Kara, *Niger J Clin Pract* **2018**, 21, 33; c) R. Bürgers, S. Hahnel, T. E. Reichert, M. Rosentritt, M. Behr, T. Gerlach, G. Handel, M. Gosau, *Acta Biomater* **2010**, 6, 2307; d) L. Escolà-Vergé, D. Rodríguez-Pardo, P. S. Corona, C. Pigrau, *Antibiotics (Basel)* **2021**, 10.

[6] E. Monroy-Pérez, R. M. Rodríguez-Bedolla, J. Garzón, F. Vaca-Paniagua, E. Arturo-Rojas Jiménez, G. L. Paniagua-Contreras, *Microbial Pathogenesis* **2020**, 148, 104436.

[7] M. M. Harriott, M. C. Noverr, *Antimicrob Agents Chemother* **2010**, 54, 3746.

[8] F. L. Mayer, D. Wilson, B. Hube, *Virulence* **2013**, 4, 119.

[9] G. D. Brown, D. W. Denning, N. A. R. Gow, S. M. Levitz, M. G. Netea, T. C. White, *Science Translational Medicine* **2012**, 4, 165rv13.

[10] L. Y. Ngo, S. Kasahara, D. K. Kumasaka, S. E. Knoblaugh, A. Jhingran, T. M. Hohl, *J Infect Dis* **2014**, 209, 109.

[11] M. Whiteway, C. Bachewich, *Annu Rev Microbiol* **2007**, 61, 529.

[12] a) P. E. Sudbery, *Nature Reviews Microbiology* **2011**, 9, 737; b) C. J. Nobile, J. E. Nett, D. R. Andes, A. P. Mitchell, *Eukaryot Cell* **2006**, 5, 1604.

[13] a) A. Correia, U. Lermann, L. Teixeira, F. Cerca, S. Botelho, R. M. Gil da Costa, P. Sampaio, F. Gärtner, J. Morschhäuser, M. Vilanova, C. Pais, *Infect Immun* **2010**, 78, 4839; b) M. Gulati, C. J. Nobile, *Microbes Infect* **2016**, 18, 310.

[14] J. Chandra, D. M. Kuhn, P. K. Mukherjee, L. L. Hoyer, T. McCormick, M. A. Ghannoum, *Journal of bacteriology* **2001**, 183, 5385.

[15] G. Ramage, S. P. Saville, B. L. Wickes, J. L. López-Ribot, *Appl Environ Microbiol* **2002**, 68, 5459.

[16] T. Vila, J. A. Romo, C. G. Pierce, S. F. McHardy, S. P. Saville, J. L. Lopez-Ribot, *Virulence* **2017**, 8, 150.

[17] a) C. M. Bhadra, V. K. Truong, V. T. Pham, M. Al Kobaisi, G. Seniutinas, J. Y. Wang, S. Juodkazis, R. J. Crawford, E. P. Ivanova, *Sci Rep* **2015**, 5, 16817; b) T. L. Clainche, D. Linklater, S. Wong, P. Le, S. Juodkazis, X. L. Guevel, J. L. Coll, E. P. Ivanova, V. Martel-Frachet, *ACS Appl Mater Interfaces* **2020**, 12, 48272; c) J. Hasan, R. J. Crawford, E. P. Ivanova, *Trends Biotechnol* **2013**, 31, 295; d) E. P. Ivanova, J. Hasan, H. K. Webb, G. Gervinskas, S. Juodkazis, V. K. Truong, A. H. Wu, R. N. Lamb, V. A. Baulin, G. S. Watson, J. A. Watson, D. E. Mainwaring, R. J. Crawford, *Nat Commun* **2013**, 4, 2838.

[18] D. P. Linklater, V. A. Baulin, S. Juodkazis, R. J. Crawford, P. Stoodley, E. P. Ivanova, *Nat Rev Microbiol* **2020**, DOI: 10.1038/s41579-020-0414-z.

[19] a) J. V. Wandiyanto, S. Cheeseman, V. K. Truong, M. A. Kobaisi, C. Bizet, S. Juodkazis, H. Thissen, R. J. Crawford, E. P. Ivanova, *Journal of Materials Chemistry B* **2019**, 7, 4424; b) R. Bright, D. Fernandes, J. Wood, D. Palms, A. Burzava, N. Ninan, T. Brown, D. Barker, K. Vasilev, *Materials Today Bio* **2022**, 13, 100176; c) J. V. Wandiyanto, T. Tamanna, D. P. Linklater, V. K. Truong, M. Al Kobaisi, V. A. Baulin, S. Joudkazis, H. Thissen, R. J. Crawford, E. P. Ivanova, *Journal of Colloid and Interface Science* **2020**, 560, 572.

[20] A. Hayles, J. Hasan, R. Bright, D. Palms, T. Brown, D. Barker, K. Vasilev, *Materials Today Chemistry* **2021**, 22, 100622.

[21] S. B. Girois, F. Chapuis, E. Decullier, B. G. P. Revol, *European Journal of Clinical Microbiology and Infectious Diseases* **2006**, 25, 138.

[22] L. E. Cowen, *Nat Rev Microbiol* **2008**, 6, 187.

[23] V. Boddapati, M. C. Fu, D. J. Mayman, E. P. Su, P. K. Sculco, A. S. McLawhorn, *J Arthroplasty* **2018**, 33, 521.

[24] R. Bright, A. Hayles, D. Fernandes, R. M. Visalakshan, N. Ninan, D. Palms, A. Burzava, D. Barker, T. Brown, K. Vasilev, *ACS Appl Mater Interfaces* **2021**, 13, 38007.

[25] a) B. D. Boyan, E. M. Lotz, Z. Schwartz, *Tissue Eng Part A* **2017**, 23, 1479; b) L. Lv, Y. Xie, K. Li, T. Hu, X. Lu, Y. Cao, X. Zheng, *Adv Healthc Mater* **2018**, 7, e1800675; c) S. M. Hamlet, R. S. B. Lee, H. J. Moon, M. A. Alfarsi, S. Ivanovski, *Clin Oral Implants Res* **2019**, 30, 1085.

[26] C. H. Kowalski, K. A. Morelli, D. Schultz, C. D. Nadell, R. A. Cramer, *Proc Natl Acad Sci U S A* **2020**, 117, 22473.

[27] a) A. Brand, *International Journal of Microbiology* **2012**, 2012, 517529; b) F. Mech, D. Wilson, T. Lehnert, B. Hube, M. Thilo Figge, *Cytometry Part A* **2014**, 85, 126.

[28] L. Popolo, T. Gualtieri, E. Ragni, *Med Mycol* **2001**, 39 Suppl 1, 111.

[29] C. J. Heilmann, A. G. Sorgo, S. Mohammadi, G. J. Sosinska, C. G. de Koster, S. Brul, L. J. de Koning, F. M. Klis, *Eukaryot Cell* **2013**, 12, 254.

[30] J. R. Blankenship, S. Fanning, J. J. Hamaker, A. P. Mitchell, *PLoS Pathog* **2010**, 6, e1000752.

[31] A. J. Warenda, J. B. Konopka, *Mol Biol Cell* **2002**, 13, 2732.

[32] J. Samot, M. Rouabhia, *Probiotics Antimicrob Proteins* **2021**, 13, 287.

[33] a) C. J. Nobile, D. R. Andes, J. E. Nett, F. J. Smith, F. Yue, Q. T. Phan, J. E. Edwards, S. G. Filler, A. P. Mitchell, *PLoS Pathog* **2006**, 2, e63; b) C. J. Nobile, H. A. Schneider, J. E. Nett, D. C. Sheppard, S. G. Filler, D. R. Andes, A. P. Mitchell, *Current Biology* **2008**, 18, 1017.

[34] a) Y. Liu, S. G. Filler, *Eukaryot Cell* **2011**, 10, 168; b) C. J. Nobile, A. P. Mitchell, *Curr Biol* **2005**, 15, 1150.

[35] a) R. Alves, C. Barata-Antunes, M. Casal, A. J. P. Brown, P. Van Dijck, S. Paiva, *PLOS Pathogens* **2020**, 16, e1008478; b) A. Felk, M. Kretschmar, A. Albrecht, M. Schaller, S. Beinhauer, T. Nichterlein, D. Sanglard, H. C. Korting, W. Schäfer, B. Hube, *Infect Immun* **2002**, 70, 3689.

[36] a) C. J. Barelle, V. M. Duncan, A. J. Brown, N. A. Gow, F. C. Odds, *J Antimicrob Chemother* **2008**, 61, 315; b) C. do Rosário Esteves Guimarães, H. F. de Freitas, T. F. Barros, *Molecular Biology Reports* **2019**, 46, 6147.

[37] J. M. Slauch, *Molecular microbiology* **2011**, 80, 580.

[38] J. Jenkins, J. Mantell, C. Neal, A. Gholinia, P. Verkade, A. H. Nobbs, B. Su, *Nat Commun* **2020**, 11, 1626.

[39] M. I. Ishak, X. Liu, J. Jenkins, A. H. Nobbs, B. Su, *Coatings* **2020**, 10.

[40] P. H. J. van der Voort, E. C. Boerma, J. P. Yska, *Journal of Antimicrobial Chemotherapy* **2007**, 59, 952.

[41] E. Grela, A. Zdybicka-Barabas, B. Pawlikowska-Pawlega, M. Cytrynska, M. Wlodarczyk, W. Grudzinski, R. Luchowski, W. I. Gruszecki, *Sci Rep* **2019**, 9, 17029.

[42] S. Costa-de-Oliveira, A. G. Rodrigues, *Microorganisms* **2020**, 8.

[43] a) M. A. Jabra-Rizk, W. A. Falkler, T. F. Meiller, *Emerg Infect Dis* **2004**, 10, 14; b) J. Yan, B. L. Bassler, *Cell Host & Microbe* **2019**, 26, 15; c) D. Sharma, L. Misba, A. U. Khan, *Antimicrobial Resistance & Infection Control* **2019**, 8, 76; d) C. W. Hall, T. F. Mah, *FEMS Microbiol Rev* **2017**, 41, 276.

[44] T. Watamoto, L. P. Samaranayake, J. A. Jayatilake, H. Egusa, H. Yatani, C. J. Seneviratne, *Int J Antimicrob Agents* **2009**, 34, 333.

[45] D. J. Laprade, M. S. Brown, M. L. McCarthy, J. J. Ritch, N. Austriaco, *Microb Cell* **2016**, 3, 285.

[46] a) A. Velic, J. Hasan, Z. Li, P. K. D. V. Yarlagadda, *Biophysical Journal* **2021**, 120, 217; b) S. Pogodin, J. Hasan, V. A. Baulin, H. K. Webb, V. K. Truong, T. H. Phong Nguyen, V. Boshkovikj, C. J. Fluke, G. S. Watson, J. A. Watson, R. J. Crawford, E. P. Ivanova, *Biophys J* **2013**, 104, 835.

[47] F. M. Klis, P. de Groot, K. Hellingwerf, *Med Mycol* **2001**, 39 Suppl 1, 1.

[48] a) A. Cavallaro, S. Taheri, K. Vasilev, *Biointerphases* **2014**, 9, 029005; b) K. Vasilev, J. Cook, H. J. Griesser, *Expert Rev Med Devices* **2009**, 6, 553; c) K. Vasilev, S. S. Griesser, H. J. Griesser, *Plasma Processes and Polymers* **2011**, 8, 1010.

[49] a) V. B. Damodaran, N. S. Murthy, *Biomaterials Research* **2016**, 20, 18; b) K. Vasilev, N. Poulter, P. Martinek, H. J. Griesser, *ACS Appl Mater Interfaces* **2011**, 3, 4831; c) S. Taheri, A. Cavallaro, S. N. Christo, P. Majewski, M. Barton, J. D. Hayball, K. Vasilev, *ACS Biomater Sci Eng* **2015**, 1, 1278; d) A. Bidossi, M. Bottagisio, N. Logoluso, E. De Vecchi, *Int J Mol Sci* **2020**, 21; e) M. Zilberman, A. Kraitzer, O. Grinberg, J. J. Elsner, *Handb Exp Pharmacol* **2010**, DOI: 10.1007/978-3-642-00477-3_11299.

[50] a) J. Hasan, S. Jain, K. Chatterjee, *Sci Rep* **2017**, 7, 41118; b) P. M. Tsimbouri, L. Fisher, N. Holloway, T. Sjostrom, A. H. Nobbs, R. M. Meek, B. Su, M. J. Dalby, *Sci Rep* **2016**, 6, 36857.

[51] E. P. Ivanova, J. Hasan, H. K. Webb, V. K. Truong, G. S. Watson, J. A. Watson, V. A. Baulin, S. Pogodin, J. Y. Wang, M. J. Tobin, C. Löbbe, R. J. Crawford, *Small* **2012**, 8, 2489.

[52] a) J. Meyer, G. Piller, C. A. Spiegel, S. Hetzel, M. Squire, *J Bone Joint Surg Am* **2011**, 93, 2049; b) V. J. Suhardi, D. A. Bichara, S. Kwok, A. A. Freiberg, H. Rubash, H. Malchau, S. H. Yun, O. K. Muratoglu, E. Oral, *Nat Biomed Eng* **2017**, 1, 0080.

[53] K. Nowlin, A. Boseman, A. Covell, D. LaJeunesse, *Journal of The Royal Society Interface* **2015**, 12, 20140999.

[54] a) S. Silva, C. F. Rodrigues, D. Araújo, M. E. Rodrigues, M. Henriques, *J Fungi (Basel)* **2017**, 3, 8; b) G. Vediyappan, T. Rossignol, C. d'Enfert, *Antimicrob Agents Chemother* **2010**, 54, 2096.

[55] a) L. Meng, H. Zhao, S. Zhao, X. Sun, M. Zhang, Y. Deng, *Antimicrobial Agents and Chemotherapy* **2019**, 63, e01891; b) F. Haque, M. Alfatah, K. Ganesan, M. S. Bhattacharyya, *Sci Rep* **2016**, 6, 23575; c) M. S. Ahmad Khan, F. Alshehrei, S. B. Al-Ghamdi, M. A. Bamaga, A. S. Al-Thubiani, M. Z. Alam, *Future Sci OA* **2020**, 6, FSO440.

[56] N. V. Kollu, D. R. LaJeunesse, *ACS Omega* **2021**, 6, 1361.

[57] E. P. Ivanova, D. P. Linklater, A. A. Medina, P. Le, V. A. Baulin, H. Khuong Duy Nguyen, R. Curtain, E. Hanssen, G. Gervinskas, S. Hock Ng, V. Khanh Truong, P. Luque, G. Ramm, H. A. B. Wösten, R. J. Crawford, S. Juodkazis, S. Maclaughlin, *Journal of Colloid and Interface Science* **2021**, DOI: https://doi.org/10.1016/j.jcis.2021.06.093.

[58] L. J. Douglas, *Trends Microbiol* **2003**, 11, 30.

[59] J. Westman, G. Moran, S. Mogavero, B. Hube, S. Grinstein, *mBio* **2018**, 9.

[60] S. Sieuwerts, F. A. M. De Bok, E. Mols, W. M. De Vos, J. E. T. Van Hylckama Vlieg, *Letters in Applied Microbiology* **2008**, 47, 275.

7.0. Supporting Information

7.1. Materials and Methods

Viability of *Staphylococcus aureus* on HTE-Ti

HTE-Ti and AR-Ti discs were aseptically placed in 24-well plates and the top surface was inoculated with 10^6 cfu *S. aureus* ATCC 25923 in 50 µl aliquots. The cells were given 3 hours to settle and attach to the surface, the discs were immersed in 1 ml TSB and incubated at 37°C for 18 hours on an orbital shaker at 90RPM. The discs were gently rinsed in PBS to remove non-adherent cells, then transferred to a fresh 24-well plate. Syto9 and Propidium Iodide were prepared in equal proportions in PBS at a final concentration of 1.5 µl / ml PBS, and the discs were immersed and incubated in the prepared reagent in the dark for 15 minutes. The samples were imaged on an Olympus FV3000 (Olympus, Tokyo, Japan), at 40x magnification, and triplicate images were taken on each sample.

Minimum inhibitory concentration (MIC) of AmB

The MIC was determined according to CLSI standards, with the only change being the media, which was Spider medium with 20% fetal calf serum instead of Mueller-Hinton broth. Briefly, a stock solution of AmB was prepared in DMSO at 30mg/ml. *C. albicans* was inoculated in triplicate in a 96-well plate at a final cell concentration of 5×10^5 cfu/ml in Spider medium with 20% fetal calf serum and AmB between concentrations of 4 and 0.002 µg/ml. The 96-well plate was incubated at 37°C for 24 h, and the absorbance (OD600) was read in a Synergy HTX plate reader. The assay was repeated 3 times.

Primer sets used in qPCR analysis

Table S1: Primer sets used for the quantitative PCR analysis.

Target			Reference
ALS3	Forward	AATGGTCCTTATGAATCACCATCTACTA	Green 2005
	Reverse	GAGTTTTCATCCATACTTGATTTCACAT	
HWP1	Forward	GACCGTCTACCTGTGGGACAGT	Nailis 2010
	Reverse	GCTCAACTTATTGCTATCGCTTATTACA	
SAP5	Forward	CCAGCATCTTCCCGCACTT	Nailis 2010
	Reverse	GCGTAAGAACCGTCACCATATTTAA	

RPP2B	Forward	TGCTTACTTATTGTTAGTTCAAGGTGGTA	Nailis 2010
	Reverse	CAACACCAACGGATTCCAATAAA	

Cytocompatibility of murine macrophages on HTE-Ti

RAW 264.7 cells macrophage-like cell line, derived from BALB/c mice were cultured in Dulbecco′s Modified Eagle′s Medium (DMEM; ThermoFisher Scientific, MA, USA) supplemented 10% with fetal calf serum (FCS: Gibco, MA, USA) and 1% v/v Penicillin-Streptomycin (ThermoFisher Scientific, MA, USA) at 37°C and 5% CO2. After the cells reached 80% confluency, they were removed using a cell scrapper and viable cell number was determined using a TC20 automated cell counter (Bio-Rad, CA, USA). Triplicate samples of AR-Ti and HTE-Ti were transferred into a 48-well plate, and 1×10^5 RAW 264.7 cells were added per well then incubated at 37°C and 5% CO2 for 48 h with daily replenishment of DMEM supplemented with 10% FCS and 1% Pen-Strep. After 48 h the supernatant was used to quantify LDH using LDH-Glo™ Cytotoxicity Assay (Promega, WI, USA), follow the manufacturer's instructions. The percentage viability was normalised to RAW 264.7 cells grown directly on the tissue culture plate. The cells attached to the AR-Ti and HTE-Ti samples were fluorescently stained with LIVE/DEAD® Viability/Cytotoxicity Kit for Mammalian Cells (Molecular Probes, OR, USA), following the manufacturer's instructions. Briefly, two dyes are utilised, calcein AM (excitation/emission 494/517 nm) will stain live cells green and ethidium homodimer-1 (excitation/emission 528/617 nm) will stain damaged/dead cells red. After a 30-minute incubation in the mixture of the two dyes, the samples were imaged with a Confocal Laser Scanning Microscope FV3000 (Olympus, Tokyo, Japan). Five randomised images were capture for each sample.

7.2. Results

Figure S1 is a representative fluorescence micrograph showing the proportion of live (green) and dead (red) *S. aureus* cells on the HTE-Ti surface after 18 hours incubation. The viability was determined to be approximately 40%.

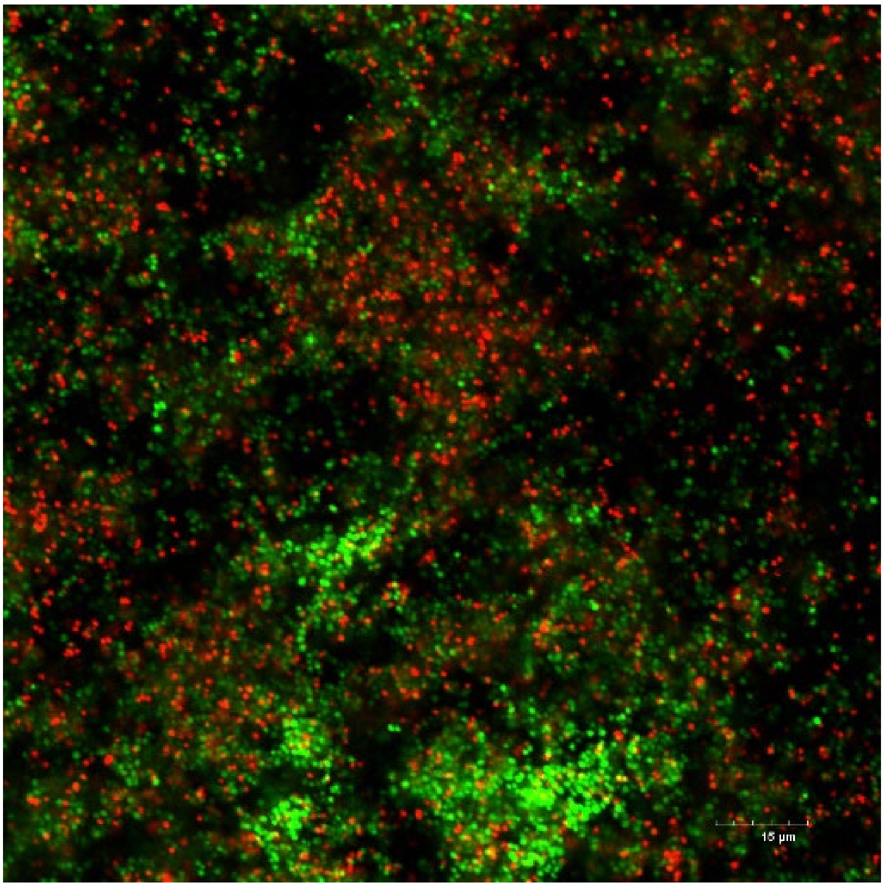

Figure S1. Live/Dead fluorescence images of *S. aureus* incubated on HTE-Ti.

Figure S2 describes the process by which hyphal networks were quantified on the HTE-Ti and AR-Ti surfaces. A network was defined as all hyphal cells which could be linked together by physical connection. In Figure S2 there were 2 separate networks and 1 lone hyphal cell.

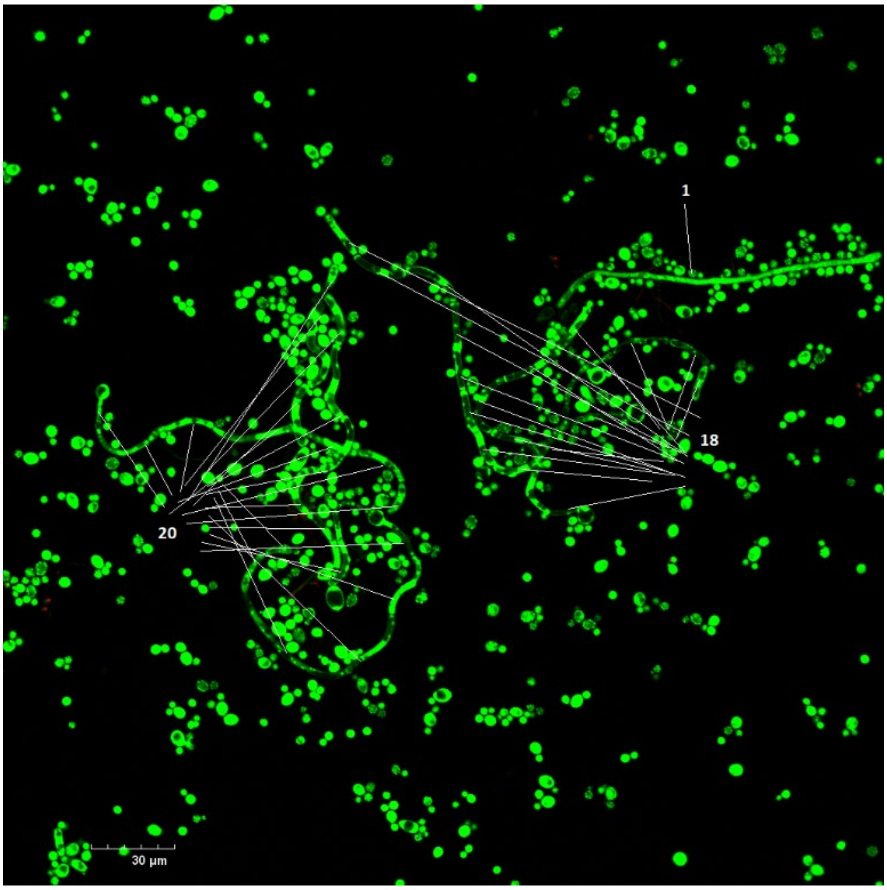

Figure S2. Method of quantifying hyphal network density on the AR-Ti surface.

Table S2: One-Way ANOVA statistical analysis of relative mRNA expression of 3 target genes, using ACT1 as an internal reference gene.

HWP1

Tukey's multiple comparisons test	Mean Diff.	95.00% CI of diff.	Significant?	Summary	Adjusted P Value	
AR-Ti vs. AR-Ti + serum	-941.1	-1191 to -691.0	Yes	****	<0.0001	A-B
AR-Ti vs. HTE-Ti	60.46	-189.7 to 310.6	No	ns	0.864	A-C
AR-Ti vs. HTE-Ti + serum	-278.2	-528.3 to -28.12	Yes	*	0.0302	A-D
AR-Ti + serum vs. HTE-Ti	1002	751.5 to 1252	Yes	****	<0.0001	B-C
AR-Ti + serum vs. HTE-Ti + serum	662.9	412.8 to 913.0	Yes	***	0.0001	B-D
HTE-Ti vs. HTE-Ti + serum	-338.7	-588.8 to -88.58	Yes	*	0.0107	C-D

ALS3

Tukey's multiple comparisons test	Mean Diff.	95.00% CI of diff.	Significant?	Summary	Adjusted P Value	
AR-Ti vs. AR-Ti + serum	-16.65	-43.47 to 10.17	No	ns	0.2683	A-B
AR-Ti vs. HTE-Ti	67.59	40.77 to 94.41	Yes	***	0.0002	A-C
AR-Ti vs. HTE-Ti + serum	0.2634	-26.56 to 27.09	No	ns	>0.9999	A-D
AR-Ti + serum vs. HTE-Ti	84.24	57.42 to 111.1	Yes	****	<0.0001	B-C
AR-Ti + serum vs. HTE-Ti + serum	16.91	-9.910 to 43.73	No	ns	0.2576	B-D
HTE-Ti vs. HTE-Ti + serum	-67.33	-94.15 to -40.51	Yes	***	0.0002	C-D

SAP5

Tukey's multiple comparisons test	Mean Diff.	95.00% CI of diff.	Significant?	Summary	Adjusted P Value	
AR-Ti vs. AR-Ti + serum	-163.1	-202.8 to -123.4	Yes	****	<0.0001	A-B
AR-Ti vs. HTE-Ti	84.98	45.31 to 124.7	Yes	***	0.0006	A-C
AR-Ti vs. HTE-Ti + serum	-262.2	-301.9 to -222.6	Yes	****	<0.0001	A-D
AR-Ti + serum vs. HTE-Ti	248.1	208.4 to 287.8	Yes	****	<0.0001	B-C
AR-Ti + serum vs. HTE-Ti + serum	-99.13	-138.8 to -59.46	Yes	***	0.0002	B-D
HTE-Ti vs. HTE-Ti + serum	-347.2	-386.9 to -307.6	Yes	****	<0.0001	C-D

The MIC of AmB against *C. albicans* was determined to be 0.5 µg/ml.

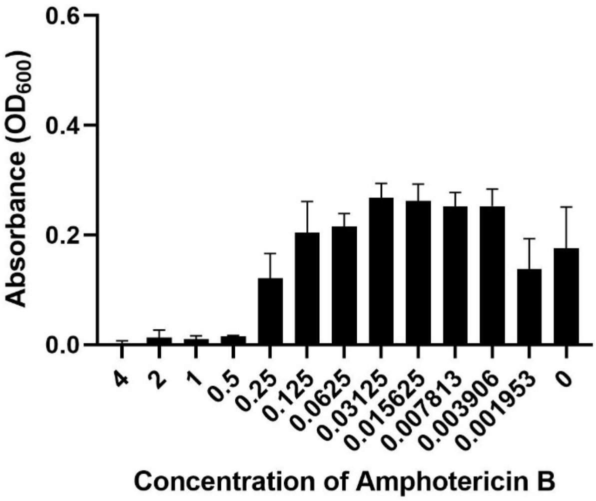

Figure S3. Minimum inhibitory concentration of AmB against *C. albicans* incubated in Spider medium supplemented with 20% fetal calf serum.

Following 10 days of incubation on the HTE-Ti surface, *C. albicans* was detached by vortex and imaged by SEM to assess the integrity of the nanostructure. The SEM image is displayed in Figure 4, and no evidence of nanostructure damage was observed.

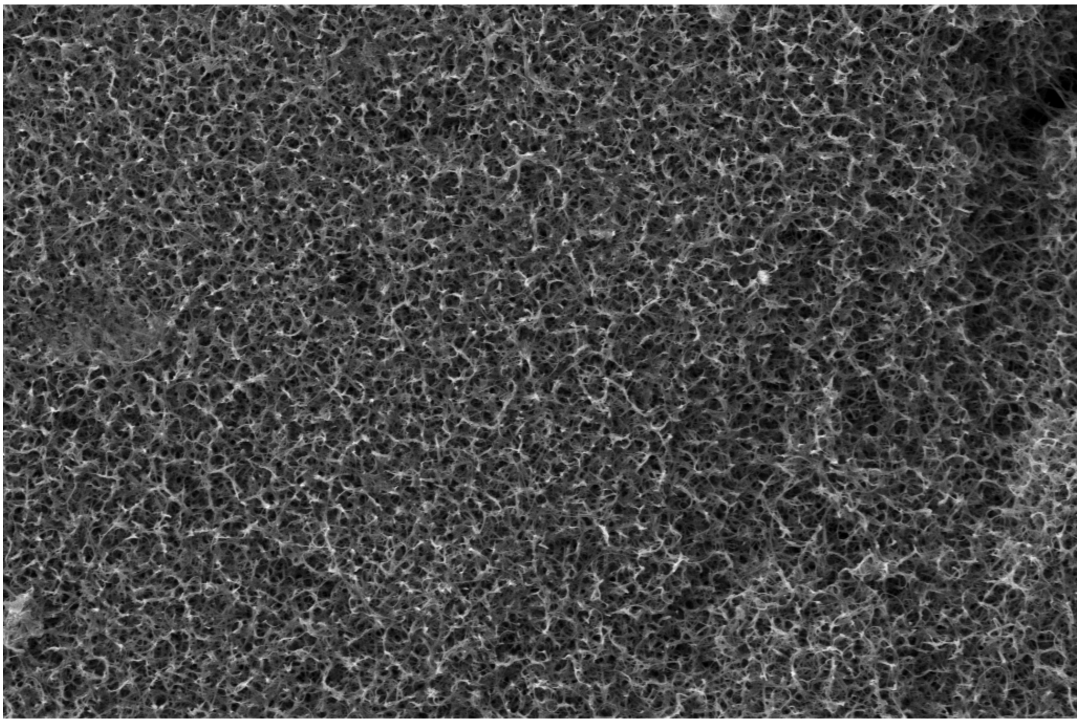

Figure S4. Integrity of nanostructure following removal of a 10-day *C. albicans* culture.

The cytocompatibility of RAW 264.7 murine macrophage cell line (Figure S5) was determined to be 97.73 ± 1.17% on AR-Ti and 95.80 ± 1.35% on HTE-Ti, which was not significantly different (P = 0.133). The viability and morphology were comparable between RAW 264.7 murine macrophage cell line incubated on AR-Ti and THE-Ti samples.

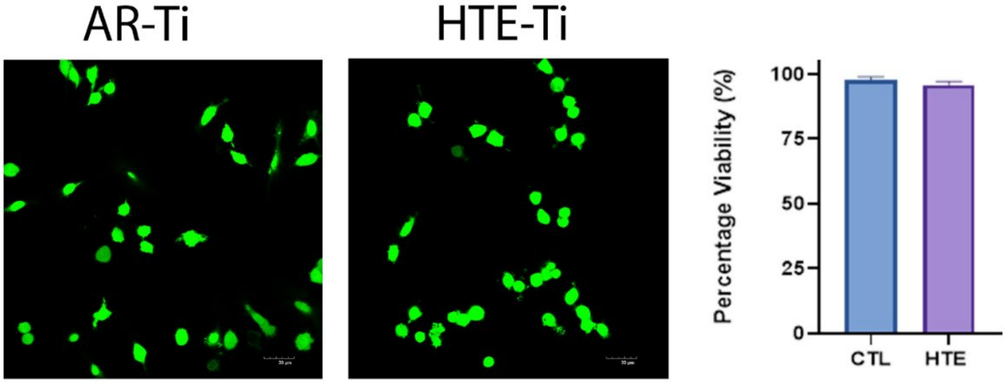

Figure S5. Viability of murine macrophages cultured on AR-Ti and HTE-Ti at 48 h. The first two panels show live dead staining to determine both viability and morphology of the RAW 264.7 murine macrophage cell line. The graph shows viability determined by LDH assay normalized to cells incubated on tissue culture plastic. Mean ± SD, P = 0.13 and n = 3.

CHAPTER 2:

SPIKED TITANIUM NANOSTRUCTURES THAT INHIBIT ANAEROBIC DENTAL PATHOGENS

Andrew Hayles[a], Jafar Hasan[a*], Richard Bright[a], Jonathan Wood[a], Dennis Palms[a], Peter Zilm[b], Dan Barker[c], Krasimir Vasilev[a*]

[a]Academic Unit of STEM, University of South Australia, Mawson Lakes, Adelaide, 5095, South Australia, Australia.

[b]Adelaide Dental School, University of Adelaide, Adelaide, 5005, South Australia, Australia

[c]ANISOP Holdings Pty Ltd, 101 Collins St, Melbourne VIC 3000

(*Corresponding author email: krasimir.vasilev@unisa.edu.au)

(*Co-corresponding author email: jafar.hasan@unisa.edu.au)

Keywords: biomimetic, mechano-bactericidal, nanostructure, implant, Fusobacterium nucleatum, Porphyromonas gingivalis

Published in ACS Applied Nano Materials, vol. 5, 27th January 2022

https://doi.org/10.1021/acsanm.1c04073

Abstract

Peri-implantitis is a devastating oral disease which gives rise to a demand for improved implantable dental biomaterials that can integrate well into the supporting bone as well as resist bacterial colonization. Recent research has demonstrated that nanostructured titanium may be well positioned to meet this demand. An abundance of literature has established the in vitro efficacy of nanostructured titanium against bacteria cultured aerobically, but its efficacy against anaerobic bacteria relevant to dental infections remains unknown. In the present study, we engineered sharp, spike-like nanostructures on commercially pure titanium surfaces using hydrothermal etching and challenged them with 3 clinically relevant, anaerobic dental pathogens: *Streptococcus mutans*, *Fusobacterium nucleatum*, and *Porphyromonas gingivalis*. Our results demonstrated that titanium nanostructured with sharp structures can be effective at eliminating bacteria in anaerobic conditions, in both single-species (up to ~94% cell death) and dual-species (up to ~70% cell death) models. Furthermore, the surface modification greatly enhanced the efficacy of azithromycin treatment against anaerobic dental pathogens, compared to a control titanium surface. At 2xMIC, azithromycin eliminated 99.4% ± 0.3% of *S. mutans* on the nanostructures surface within 10 days while only 26% of bacteria were killed on the control surface. A similar result was observed for *P. gingivalis*. The data presented here serve as a promising foundation of knowledge on which to build a greater understanding of how nanostructured biomaterials can be effective in anaerobic environments such as that found in the oral cavity.

1. Introduction

Beginning with the pioneering work of Brånemark in the 1970s, dental implantology has progressed substantively. Presently, the long-term success rate of dental implants is high, but still approximately 5-30% of patients experience peri-implant disease [1-2]. Peri-implant diseases are site-specific infections which share a common microbiological etiology with periodontal disease [3]. The term ‘peri-implant disease’ is a broad denominator which describes two distinct but related ailments; peri-implant mucositis and peri-implantitis. Peri-implant mucositis involves infection and inflammation of the gingival tissue surrounding the implant. Peri-implant mucositis is considered the precursor to the more severe peri-implantitis, which involves the progressive loss of supporting bone around the implant [2]. It is estimated that peri-implantitis represented a global economic burden of $710 million USD in 2019, and this is expected to expand [4]. Beyond the clinical symptoms of pain, swelling, bleeding, and bone loss, peri-implantitis often leads to implant failure and necessitates further surgical interventions [5].

Periodontal implants are frequently treated with processes such as sand blasting and acid etching in an effort to increase surface roughness, which is believed to facilitate improved osteointegration [6]. Unfortunately, an increase in surface roughness may also promote bacterial adhesion [7]. Preventing bacterial colonization of implant surfaces has been the focus of a substantial amount of recent research [8-10]. Various strategies have been devised to tackle this problem, including modifications that either reduce biofouling or inactivate bacterial cells [11-12]. In general, implant materials can be incorporated with antimicrobial agents, including alloying with inherent bactericidal elements such as copper or silver, and grafting with antimicrobial peptides, bioactive compounds, or silver nanoparticles [8-9, 13-14]. In the field of dental implantology specifically, much research into anti-infective surfaces is focused on coatings or alloying with inherent bactericidal agents such as copper or silver [15-16. An alternative strategy involves modifying the nanoscale architecture of the material surface to fabricate structures which mechanically eliminate adherent bacterial cells. This strategy was inspired by the mechanical disruption of cells caused by nanopillars naturally occurring on cicada wings [17], dragonfly wings [18] and gecko feet [19]. Similar nanotopographies have since been replicated on synthetic materials based on silicon and titanium [20-24]. The fabrication of mechano-bactericidal nanostructures on titanium is particularly attractive for the field of dental implantology because titanium is currently considered the gold-standard biomaterial for dental implants [25]. This is due to its strength, corrosion resistance, biocompatibility and elastic modulus which is similar to bone [26-27]. It is encouraging to note that titanium nanostructures have previously been reported to promote osteogenesis [28-30], therefore meeting one of the most important criteria for endosseous implants such as dental screws. Titanium nanostructures have shown promising bactericidal efficacy against a range of pathogens in aerobic conditions, particularly those relevant to orthopaedic implant associated infection [23, 31-32]. The most common model pathogens used in this area of research are the Gram-positive Staphylococcus aureus and the Gram-negative Pseudomonas aeruginosa [21-22, 33-34]. However, there is currently very little research addressing the capacity for nanostructured surfaces to inactivate anaerobic pathogens such as those found in peri-implantitis. A recent study by Jenkins and colleagues [31] has implicated oxidative stress as a contributing factor to nanostructure induced cell death. Oxidative stress is thought to be promoted by the intracellular generation of reactive oxygen species, occurring as a downstream effect of membrane perturbation [35]. Therefore, it is of interest to determine whether a bactericidal nanostructured surface will remain effective in an environment devoid of oxygen. At the time of writing, we are aware of only one study that investigates this, where the authors used a lithography based technique to engineer nanostructures on poly(methyl)-methacrylate (PMMA), and challenged them with anaerobic bacteria [36] Although this work is very elegant the method of preparation is difficult to apply to structures with complex shapes such as the screw of a dental implant.

In the present study, we generated sharp, spike-like nanostructures on medical grade titanium and challenged the surface with three common anaerobic dental pathogens; *Streptococcus mutans*, *Fusobacterium nucleatum* and *Porphyromonas gingivalis*. The Gram-positive *S. mutans* was chosen to represent the early colonizer role in oral biofilms. *F. nucleatum* is a Gram-negative (mid-colonizer) species. *F. nucleatum* is associated with both peri-implantitis and periodontal disease, and its presence has been implicated in multiple ailments such as rheumatoid arthritis, colorectal cancer, and abnormal pregnancy outcomes [37-38]. *P. gingivalis* is a Gram-negative late colonizer which has been referred to as a keystone pathogen in the oral microbiota for its ability to influence the microbial composition of its environment and the host immune response [39]. *P. gingivalis* has also been implicated in serious ailments at sites distal to the oral cavity, such as rheumatoid arthritis, gastrointestinal cancer, diabetes, preterm birth, stroke and cardiovascular disease [40-42]. By challenging our nanostructured titanium surface with 3 key dental pathogens in anaerobic conditions, we have generated foundational knowledge of how these materials may perform as implantable biomaterials in the oral cavity.

2. Materials and Methods

2.1. Fabrication of Hydrothermally Etched Nanospikes

Commercially pure titanium (grade 2, 10 mm diameter, 3 mm thickness) were procured from Hamagawa Industrial (M) SDN BHD (Kedah, Malaysia). The as-received titanium (AR-Ti) discs were subjected to alkaline hydrothermal etching as described previously [23]. Briefly, alkaline hydrothermal etching was performed using a 1 M KOH etchant, at 150 °C for 5 h, followed by rinsing in ultrapure water and annealing for 5 h.

2.2. Characterization of Hydrothermally Etched Titanium

Surface morphology of the AR-Ti and hydrothermally etched titanium (HTE-Ti) surfaces was observed using a scanning electron microscope (Zeiss Merlin FEG SEM, Zeiss, Jena, Germany) set at 2-3 kV and a 4.5mm working distance. A secondary or in-lens detector was used to image at magnifications ranging from 3,000x up to 50,000x at 0- and 45-degrees stage tilt angle. For nanopillar measurements, a correction factor for the tilt stage was applied to amend dimensional distortion during linear measurements. Analysis was performed using ImageJ software v1.53 (NIH, USA). A contact angle goniometer (RD-SDM02, RD Support, Scotland, UK) was used to measure the surface wettability of the AR-Ti and HTE-Ti surfaces. The measurements were taken from ultrapure water (4 µL) using the sessile drop method at a minimum of five different areas across triplicate samples. Atomic force microscopy (AFM) was used to acquire 5 µm² images in air using a Dimension Icon FastScan AFM with Nanoscope V controller in PeakForce with ScanAsyst mode on the AR-Ti and HTE-Ti surfaces. An NT-MDT NSG03 silicon nitride cantilever with conical tip (<10 nm radius), spring constant 2.0 N/m was used for both samples. Initial calibration of the cantilever on a glass microscope slide derived a normal spring constant of 1.9 N/m at the just off the first resonant frequency of 86.8 kHz. Roughness values were calculated through Gwyddion data analysis software (v2.54).

Further surface topography measurements were performed using an Olympus 3D measuring Laser Microscope (OLS5000, LEXT) with a dedicated objective of 100× lens over several scanning areas of 128 × 128 µm on control and nanostructured surfaces. To determine the surface values, a Gaussian filter was applied. Surface roughness measurements were also calculated using an inbuilt software (Olympus Stream image analysis software, Olympus IMS).

2.3. Culture of Human Gingival Fibroblasts (HGF)

Healthy human gingival tissue biopsies were obtained during gingivectomy in the third molar region, with informed consent (Human Research Ethics Committee of the University of Adelaide; Approval Number H-112-2008). Immediately after removal, the biopsies were stored in Hank's balanced salt solution (HBSS; ThermoFisher, MA, USA) until processed. The gingival tissue was cut into smaller pieces (~ 1 mm^3) and incubated in Dulbecco's modified Eagle medium (DMEM; ThermoFisher, MA, USA) supplemented with 10 % fetal calf serum (FCS; ThermoFisher, MA, USA) 1% W/V penicillin and streptomycin (ThermoFisher, MA, USA). The outgrowing cells were incubated at 37°C with 5% CO2 until 80% confluent. The human gingival fibroblasts (HGF) were further passaged to reach cell quantities required for storage in liquid nitrogen and short-term cytocompatibility experiments. AR-Ti and HTE-Ti samples were placed in 48-well plates in triplicate and seeded with 5 x 10^4 HGF cells per well, then incubated for 72 h at 37°C with 5% CO2.

2.4. Cell Morphology of HGF

To show cell spreading and the cytoskeleton structure of HGF cells on the AR-Ti and HTE-Ti surfaces after 72 h of incubation, cells were initially fixed with 4% paraformaldehyde for 3 h. HGF cells incubated on AR-Ti and HTE-Ti samples were then rinsed in phosphate buffered saline pH 7.4 (PBS), treated with 0.1% Triton-X (Sigma-Aldrich, MI, USA) to permeabilize the cells. F-actin cytoskeleton and nuclei were stained, respectively with TRITC-phalloidin (Ex/Em 540/565 nm, ThermoFisher Scientific, MA), and DAPI (Ex/Em 350/470 nm, 4′,6-diamidino-2-phenylindole, dihydrochloride, ThermoFisher Scientific, MA, USA). Samples were inverted onto a glass coverslip and imaged using an Olympus FV3000 confocal laser scanning microscope (CLSM; Olympus, Tokyo, Japan), acquiring 5 random images per sample.

2.5. Determination of Cytotoxicity

Short-term cytocompatibility of HGF incubated for 24 h and 72 h on AR-Ti and HTE-Ti was assessed using LDH-Glo™ Cytotoxicity Assay (Promega, WI, USA), following the manufactures instruction. The release of lactate dehydrogenase (LDH) into the surrounding medium upon disruption of the plasma membrane is a widely used marker to assess in vitro cytotoxicity [43-44]. Briefly, 50 µL of supernatant was added to 50 µL of LDH detection reagent in a 96-well opaque plate, mixed and incubated at room temperature for 30 min. The resulting luminescence was measured on a Synergy HTX multi-mode microplate reader (Biotek, VT, USA). To calculate viability, triplicate readings were normalized to HGF cells grown on tissue culture plates (TCP).

2.6. Bacterial Cultures and Conditions

S. mutans (ATCC 25175), *F. nucleatum* (ATCC 25586) and *P. gingivalis* ATCC 53978 (strain W50) were recovered from -80°C glycerol stocks and plated onto agar plates. For *S. mutans*, the plate contained tryptone soy agar (TSA; Thermo Scientific, MA, USA) and 20% (w/v) sucrose. For *F. nucleatum* and *P. gingivalis*, anaerobic blood agar plates (Thermo Fisher, MA, USA) were used to culture the bacteria at 37°C for 48 h in an anerobic jar (AnaeroJar 2.5L, Oxoid, ThermoFisher, MA, USA) containing an oxygen scavenging sachet (AnaeroGen 2.5L, Oxoid, ThermoFisher, MA, USA). For each species, a single colony was aseptically transferred to either tryptone soy broth supplemented with 5% (w/v) sucrose (for *S. mutans*), or heart infusion broth (HIB) supplemented with 5 µg/mL hemin (Sigma-Aldrich, MI, USA) and 1µg/mL vitamin K (Sigma-Aldrich, MI, USA). The broths were incubated anaerobically at 37°C for 48 h (*S. mutans*) or 5 days (*F. nucleatum* and *P. gingivalis*).

The preculture was Gram-stained to verify purity, and cell density was inferred by measuring the optical density at 600 nm (OD600) using a Nanodrop 2000 (Thermo Scientific, MA, USA). The preculture cell concentration was adjusted to 10^6 CFU/mL for *S. mutans* and 10^7 CFU/mL for *F. nucleatum* and *P. gingivalis*. AR-Ti and HTE-Ti samples were aseptically placed into individual wells of a 24-well tissue culture plate (Nunc, Thermo Scientific, MA, USA), and immersed in 1 mL of the diluted cell suspension. For the dual-species incubation containing *S. mutans* and *P. gingivalis*, 10^6 CFU/mL *S. mutans* was mixed with 10^7 CFU/mL of *P. gingivalis* in HIB supplemented with 5% (w/v) sucrose. The *P. gingivalis* inoculum was 10-fold higher than *S. mutans* to compensate for the slower growth rate of *P. gingivalis*. For the dual-species incubation containing *F. nucleatum* and *P. gingivalis*, 10^7 CFU/mL of each species were mixed. Single-species and dual-species cultures were all cultured for 5 days, with replenishment of the culture media every 48 h, by aspirating the spent media and replacing it with 1 mL of fresh sterile media.

2.7. Salivary Pellicle Formation

The study was approved by the Human Research Ethics Committees (Human Ethics Approval No: H-2020-198). Unstimulated human saliva was obtained from 5 healthy volunteers for 1 h per day over several days, at least 1.5 h after eating, drinking or tooth brushing.45 Pooled human saliva was centrifuged at 10,000 rpm for 20 minutes, diluted 1:3 in PBS and heated at 60 °C for 1 h. Further, the saliva was filter sterilized using 0.22 µm syringe filters. The sample discs were coated with the diluted saliva by immersion for 1 h to simulate salivary pellicle. The discs were then transferred to 24-well plates and washed with sterile culture media before inoculation with bacteria.

2.8. Live/Dead Viability Analysis

At each timepoint, the discs were retrieved from the 24-well plates, gently rinsed in PBS, and then transferred to a fresh plate. Each sample was immersed in 1 mL BacLight™ LIVE/DEAD® (Molecular Probes, OR, USA), with propidium iodide (PI) and Syto9 diluted in equal proportions to 1.5 µl/mL of PBS. The samples were incubated in the dark at room temperature for 15 minutes and then immediately imaged with an Olympus FV3000 confocal scanning laser microscope (CLSM; Olympus, Tokyo, Japan). Excitation and emission spectra for Syto9 was 483 nm and 503 nm, respectively. For PI, excitation and emission spectra were 535 nm and 617 nm, respectively. Micrographs were taken at 40x magnification in random areas on each of the replicate samples. For single-plane images, the numbers of red and green stained cells were quantified using ImageJ software to determine cell viability. For 3-dimensional biovolume analysis, fluorescence micrographs were captured in stacks with a step size of 0.5 µm. Stacked fluorescence images were analyzed using Imaris 3D software (Version 9.3.0, Bitplane AG, Zürich, Switzerland). The viability of cells in the 3-dimensional stacked micrographs was measured by taking the quantity of biovolume in the green channel compared to the total biovolume.

2.9. Colony Enumeration

Colony enumeration was performed at each timepoint. To achieve this, samples were retrieved from the tissue culture plate, gently rinsed in PBS, and transferred to a fresh 5 mL screwcap tube containing 1 mL sterile PBS. Bacteria were recovered from the discs with 2 minutes of sonication in a water bath, followed by a 30 second burst on a vortex. The cell suspension was diluted by serial 10-fold dilutions, and 10 µl drops of each dilution were plated in duplicate on TSA plates (for *S. mutans*) and anaerobic blood agar plates (for *F. nucleatum* and *P. gingivalis*).46 The log reduction in viable cell counts were calculated using the following formula: $\log_{10}\frac{CFU_{AR-Ti}}{CFU_{HTE-Ti}}$, where CFU_{AR-Ti} and CFU_{HTE-Ti} are the mean CFU/sample measured on the AR-Ti and HTE-Ti surfaces, respectively.

2.10. Minimum Inhibitory Concentration (MIC) of Azithromycin

The minimum inhibitory concentration of azithromycin was determined according to the standards proposed by the Clinical and Laboratory Standards Institute (CLSI),47 with the only adjustment being to the culture media, which was TSB supplemented with 5% sucrose (*S. mutans*) or HIB (*P. gingivalis*). Briefly, relevant culture media was dispensed into a 96-well microtiter plate (Thermo Scientific, MA, USA) and supplemented with azithromycin at two-fold decreasing concentrations starting from 1000 µg/mL. *S. mutans* or *P. gingivalis* were inoculated into wells at a concentration of 5×10^5 CFU/mL, and the plate was incubated at 37°C for 5 days in anaerobic conditions. Following incubation, the absorbance of the wells was read on a plate reader at 600 nm (OD600). The MIC was determined to be the lowest concentration at which the absorbance was not statistically different from the background measurement.

2.11. Azithromycin Treatment Assay

Titanium samples were incubated with representative Gram-positive *S. mutans* and Gram-negative *P. gingivalis* for 3 and 5 days, respectively, using the same procedure described above. Following this, the culture media was replaced daily with fresh media, supplemented with azithromycin at 1x and 2x MIC. MIC was 500 µg/mL for *S. mutans* and 64 µg/mL for *P. gingivalis*. Samples were taken after 1, 5 and 10 days of treatment, then stained with Live/Dead and imaged by CLSM to obtain 3-dimensional stacked fluorescence micrographs. Stacked micrographs were analyzed by Imaris, as described above.

2.12. Statistical Analysis

All experiments were performed in triplicates. Data in plots is presented as mean and standard deviation. Data ananlysis was performed using GraphPad Prism v8.3.0 (GraphPad Software, San Diego, California, USA). For Figure 2, 3 and 4, p- values were determined with a t-test using the two-stage linear step-up procedure of Benjamini, Krieger and Yekutieli to control for false discovery rate. For figure 5, a two-way ANOVA was used with Tukey’s multiple comparisons test. Significance was set at $p < 0.05$.

3. Results and Discussion

3.1. Materials and Cytocompatibility Characterization of HTE-Ti

Scanning electron microscopy (SEM) analysis was conducted to confirm the presence and characterize the surface morphology of the materials used in this study (Figure 1 A and B). The hydrothermal etching process resulted in a modified topography consisting of spiked protrusions branched at their base. The average measured height of the protrusions was 296 ± 48 nm which was determined by the vertical distance from the node of the branched network to the top of the nanopillar. The width of the protrusions was 62 ± 12 nm, which was measured at mid-height in parallel orientation with the basal plane. The orientation of the nanostructures was approximately perpendicular, and their arrangement was disordered. The nanostructure was observed to have total coverage across the entire surface. The atomic composition of HTE-Ti was analyzed using energy dispersive spectroscopy (EDS) (Figure 1E and F). Prior to hydrothermal etching, the atomic composition of the AR-Ti sample was typical of commercially pure titanium. After hydrothermal etching, there was a clear increase in the surface concentration of oxygen, indicative of a thickened oxide layer generated by the process. A minor presence of potassium was also noted on the HTE-Ti surface which is due to the formation of potassium titanates during hydrothermal treatment using a potassium hydroxide etchant [48]. Atomic force microscopy (AFM) analysis of the nanoscale roughness (Ra) of the AR-Ti surface showed a mean value of 28.8 ± 9.8 nm. After modification, the Ra measured on the HTE-Ti surface increased to 84.3 ± 8.2 nm (Table 1 and Figure S1). This approximate 3-fold increase in surface roughness reflects the generation of spike-like nanostructures on the HTE-Ti surface. This bodes well for dental implant applications, as these devices are often treated with varying processes to increase surface roughness for the enhancement of bone formation and osteointegration [49]. However, despite enhancing osteointegration, rough surfaces are thought to also facilitate adhesion of dental bacteria [7]. This underscores the need for implants which are rough enough to facilitate osteointegration, but which also possess antibacterial properties to mitigate the associated increase in bacterial adhesion. The water contact angle of HTE-Ti was measured at <10°, reflecting the substantially increased wettability compared to the AR-Ti surface, which had a water contact angle of 40° ± 2°. This increased wettability may benefit protein adsorption, which is an important first step in the osteointegration process following implantation [50]. To briefly assess the in vitro short-term cytocompatibility, human gingival fibroblasts (HGF) were cultured on AR-Ti and HTE-Ti surfaces for 72 h. Cytotoxicity was determined by a commercially bought LDH cytotoxicity assay (Figure 1I), which showed no statistically significant difference between surfaces ($p = 0.98$ at day 1 and 0.21 at day 3). Interestingly, HGF cells exhibited increased viability on both surfaces compared to the TCP control. To assess morphology, HGF cells were stained with DAPI and phalloidin (Figure 1 G and 1 H). The HGF cells were comparable between AR-Ti and HTE-Ti surfaces, with normal actin distribution, cell number, and attachment. To confirm the osteogenic potential of the HTE-Ti surface modification, MG-63 osteoblast-like cells were cultured on AR-Ti and HTE-Ti surfaces (Figure S2). The morphology of MG-63 cells was similar on both surfaces, however they appeared slightly more spread on the HTE-Ti surface. Osteoblast spreading is a prerequisite to osteointegration [51], therefore our observations are encouraging. The LDH-based viability of MG-63 cells was similar on AR-Ti and HTE-Ti samples (95.7 ± 7.1% and 91.6 ± 9.7% respectively, p = 0.58), indicating that there were no short-term cytotoxic effects against MG-63 cells.

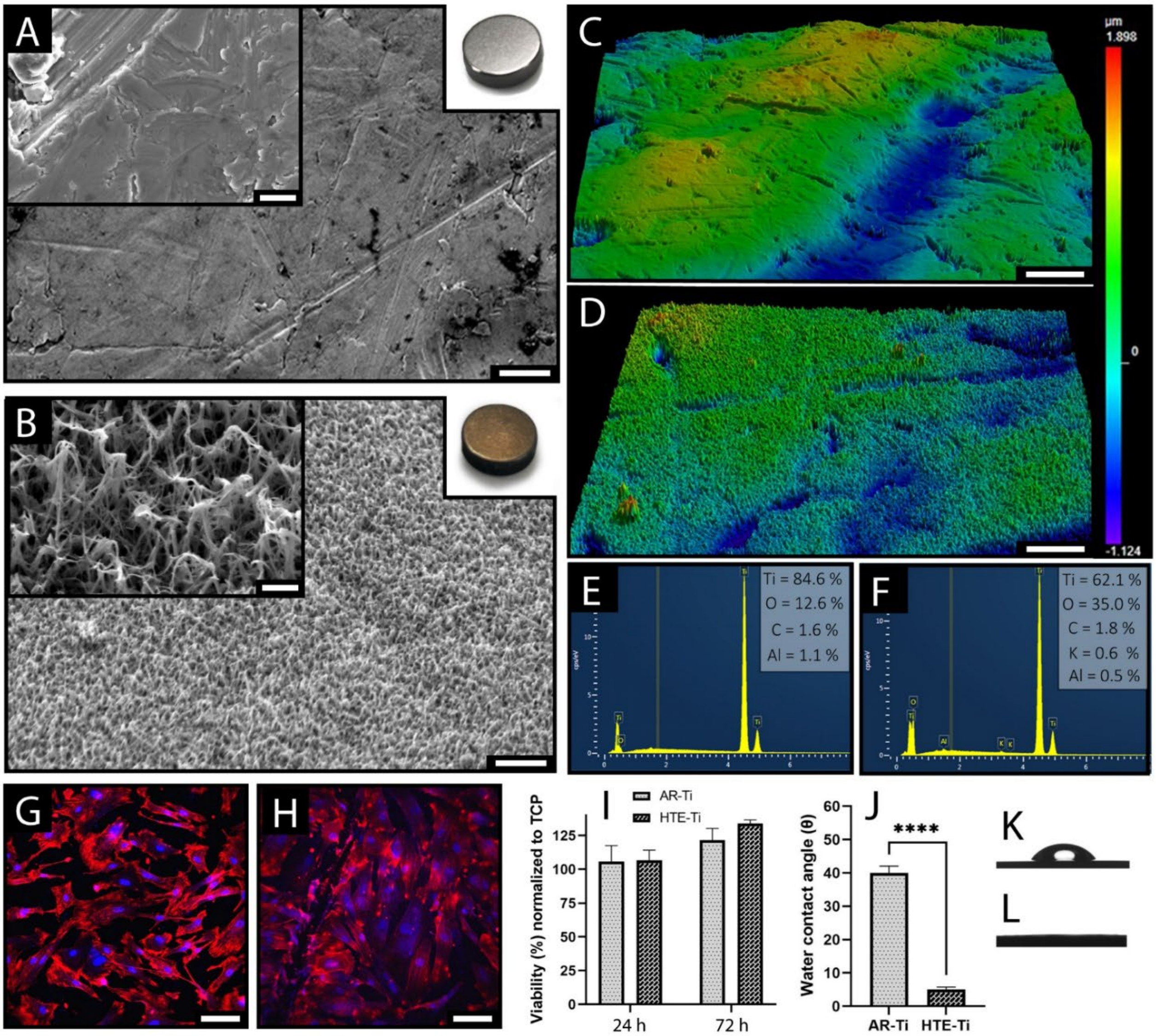

Figure 1. Material and Cytocompatibility characterization of HTE-Ti. SEM of AR-Ti (A) and HTE-Ti (B). Optical profilometry analysis of AR-Ti (C) and HTE-Ti (D). EDS analysis of AR-Ti (E) and HTE-Ti (F). HGF cells on AR-Ti (G) and HTE-Ti (H), stained with DAPI and phalloidin. LDH viability analysis of HGF on AR-Ti and HTE-Ti at 24 hand 72h (I). Water contact angle of AR-Ti and HTE-Ti (J). Images of water droplet spreading on AR-Ti (K) and HTE-Ti (L). Photographs of AR-Ti and HTE-Ti samples are inset into the SEM images. Scale bars are 2 µm for A and B, 200 nm for B inset, 15 µm for C and D and 100 µm for G and H. n = 3, Mean ± SD, **** $p < 0.0001$

Table 1. Surface roughness analysis using AFM images. n = 3, Mean ± SD

Surface type	Average roughness (R_a, nm)	Root-mean-squared roughness (R_q, nm)	Skewness	Kurtosis	Increase in Surface to projected area (%)
AR-Ti	28.8 ± 9.8	39.6 ± 9.5	-0.6 ± 0.5	2.1 ± 2.5	3.1 ± 0.5
HTE-Ti	84.3 ± 8.2 (*p* = 0.0017)	106.8 ± 9.9 (*p* = 0.0001)	0.4 ± 0.2 (*p* = 0.0324)	0.5 ± 0.4 (*p* = 0.3352)	101.6 ± 7.2 (*p* = 0.0001)

3.2. Mechanical Disruption of Anaerobic Dental Pathogens Incubated as Single-Species Cultures

To investigate the interaction between the three anaerobic dental pathogens used in this study and the nanostructured HTE-Ti surface, bacteria were incubated on AR-Ti and HTE-Ti surfaces for 5 days, then analyzed by SEM (Figure 2 A-F). On the AR-Ti surface, *S. mutans* formed thick biofilms with geometric three-dimensional complexity. However, on the HTE-Ti surface, *S. mutans* cells were primarily observed in small monolayer aggregations, with many cells appearing perturbed or flattened against the nanostructure. Similar observations were noted for *F. nucleatum*, but this species appeared to produce more turgid cells compared to *S. mutans* on the HTE-Ti surface. On both AR-Ti and HTE-Ti surfaces, there was a low abundance of *P. gingivalis*, likely reflecting its status as a late colonizer which prefers to attach to cells of early colonizer species [52]. It should be noted that different species of the *P. gingivalis fimA* genotype may have a different capacity to attach to surfaces. The *P. gingivalis* (ATCC 53978) strain used in the present study has a type IV fimA genotype, and this strain was chosen due to its predominance in advanced periodontal diseases [53].

To further interrogate the interaction between the three dental pathogens and the nanostructured surface, cells were stained with BacLight Live/Dead reagent to reveal the cell viability (Figure 2 G-L). *S. mutans* appeared densely populated on the AR-Ti surface compared to the HTE-Ti surface, with 97.4% ± 3.5% of cells appearing viable. This contrasts with *S. mutans* on the HTE-Ti surface, which had an approximate viability of only 6% ± 7.3% ($p < 0.00001$) and a sparser population. This provides support to our SEM observations which showed many disrupted and flattened *S. mutans* cells. When *F. nucleatum* was incubated on the AR-Ti surface, it had a high viability of 99.8% ± 0.1%, but on the HTE-Ti surface its viability was 30% ± 5.4% ($p < 0.00001$). This also aligns with the qualitative SEM analysis. The Live/Dead results were similar for *P. gingivalis*, which was 95.5% ± 3.1% viable on the AR-Ti surface and 37.2% ± 12.7% on the HTE-Ti surface ($p < 0.00001$). On both surfaces, *S. mutans* appeared in a larger abundance than *F. nucleatum*, and both species were much more abundant than *P. gingivalis*. It should be noted here that the degree of cell attachment was improved by preconditioning the samples with diluted human saliva to form a pellicle layer of salivary glycoproteins to which the bacteria can more strongly adhere [54]. Prior experiments without the introduction of a pellicle layer resulted in far fewer attached cells, making it more difficult to draw meaningful comparisons between AR-Ti and HTE-Ti (Figure S3). To further interrogate these results, colony enumeration was performed to assess the quantity of viable cells retrieved from HTE-Ti and AR-Ti surfaces. The relative reductions in CFU counts between the three species (Figure 2N) was consistent with the viability measurements drawn from the microscopy analyses (Figure 2M). *S. mutans* showed a 1.2 log reduction of viable cells on the HTE-Ti surface, whereas *F. nucleatum* and *P. gingivalis* had their viable counts reduced by 0.6 and 0.5 logs, respectively.

The relatively higher bactericidal efficacy against Gram-positive *S. mutans* compared to Gram-negative *F. nucleatum* and *P. gingivalis* was unexpected due to the commonly held belief that Gram-positive species are more resistant to mechanical rupture [55-56]. For example, *Staphylococcus aureus* incubated on HTE-Ti was shown to have a viability of approximately 40%, but only 1% of Pseudomonas aeruginosa cells were viable [23]. It is well understood that peptidoglycan is the primary structural support for bacteria, which grants a degree of rigidity and confers load-bearing properties to the cell [43]. While the peptidoglycan layer in Gram-negative cells is only a few nm thick, Gram-positive cells have multi-layered peptidoglycan in the range of 30-100 nm thick [57]. The results presented here suggest that cell rigidity is not the only factor which influences susceptibility to mechanical rupture on nanostructured surfaces. As *S. mutans* and *S. aureus* are both Gram-positive cocci, their differing susceptibility to protruding nanostructures must be explained by factors other than peptidoglycan thickness. One plausible explanation for this discrepancy may be found in their contrasting modes of cell division (Figure S4)[24]. *S. aureus* cells divide along 3 geometric planes, which causes them to replicate in clusters expanding in all directions. This allows *S. aureus* cells to form layers upon themselves to therefore escape the mechanically disruptive interactions occurring at the nanostructured surface. By contrast, *S. mutans* cells divide along a single geometric plane, which causes cells to form long chains [58]. It is therefore likely that *S. mutans* must face the challenge of dividing laterally across the nanostructured surface becoming exposed to a larger surface area, potentially incurring high degrees of membrane stress. This interpretation is somewhat similar to the motility hypothesis, in which motile cells are thought to be more susceptible to mechanical rupture as they move along the hostile topography of nanostructured surfaces [33].

The relatively higher viability of *F. nucleatum* and *P. gingivalis*, in comparison to *S. mutans*, was also unexpected, as our own data as well as data published by other groups suggests the Gram-negative status of these bacteria should predispose them to higher rates of cell death. Again, factors other than cell rigidity must be considered to interpret this result. One potential explanation may involve their rates of cell division. During cell division, the bacterial cell must continuously dismantle and remodel its peptidoglycan layer to accommodate the newly forming daughter cell [59-60]. This may present a window of weakness during which the dividing cell is more prone to mechanical rupture. If this is the case, then it stands to reason that as the rate of division increases, so too must the rate of mechanically induced cell death. The doubling time of *P. aeruginosa* is often cited in the range of 1-2 h [61], which is faster than what is observed for *F. nucleatum* (3.5-7 h) [62-63] and *P. gingivalis* (3-9 h). [64-65]. The slower growth rate of *F. nucleatum* and *P. gingivalis* could be one of the underlying mechanisms that explains why these bacteria appear more resistant to killing by the nanostructured surface compared to *P. aeruginosa*.

At the time of writing, a literature search involving anerobic pathogens and bactericidal nanostructured surfaces only yielded a single report [36]. In this study, the authors incubated *S. mutans*, *F. nucleatum* and *P. gingivalis* on nanostructured PMMA, a polymer commonly used to manufacture dentures [66]. Although the surface architecture of the various PMMA nanostructures was somewhat different to the HTE-Ti used in this study, the trend in bactericidal activity against *F. nucleatum* and *P. gingivalis* was comparable. On the PMMA surfaces, however, *S. mutans* was killed at a lower rate of approximately 50% after 7 days. This may be attributed to the varying structural sharpness and topography of nanostructured PMMA and HTE-Ti. The nanostructured PMMA surface had a patterned topography with 500 nm separating each peak, which may have provided the nesting space for *S. mutans* cells. In contrast, the HTE surface in this study had randomly oriented nanostructures with irregular spacing which would have not allowed the cells to settle or divide.

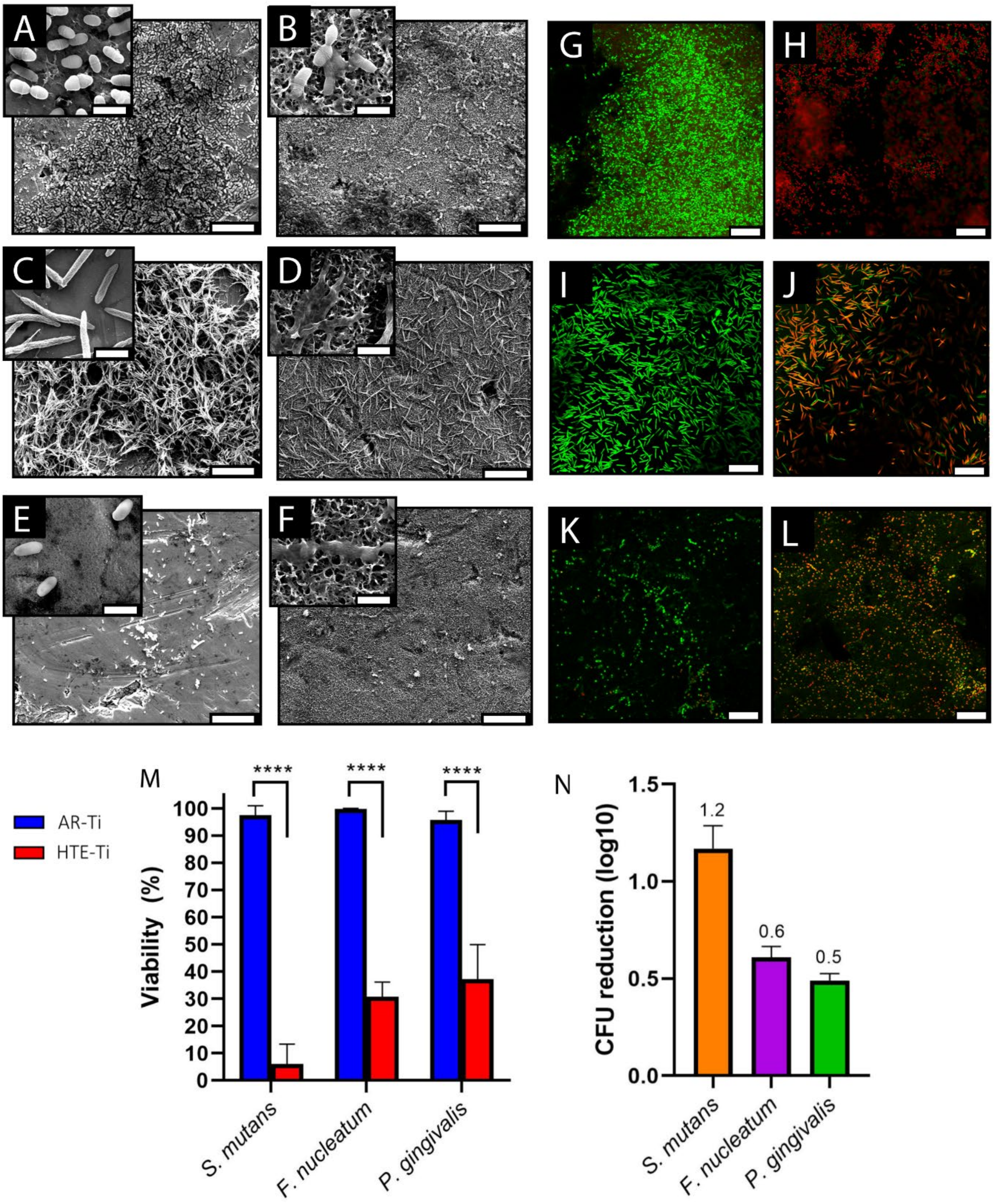

Figure 2. Bactericidal efficacy of HTE-Ti against 3 anaerobic dental pathogens. *S. mutans* incubated on AR-Ti (A and G) and HTE-Ti (B and H). *F. nucleatum* incubated on AR-Ti (C and I) and HTE-Ti (D and J). *P. gingivalis* incubated on AR-TI (E and K) and HTE-Ti (F and L). Cell viability of each species on AR-Ti and HTE-Ti (M). Log reduction based on colony enumeration (N). Scale bars represent 15μm in CLSM images, 10 μm in SEM images and 1 μm in SEM insets. n = 3, Mean ± SD **** $p < 0.0001$

3.3. Mechano-bactericidal Susceptibility of Anaerobic Dental Pathogens Incubated in Mixed Cultures

The oral cavity is host to a broad diversity of microbial organisms, with an estimated number of up to 700 individual species [67]. While it is useful to assess the bactericidal efficacy of titanium nanostructures against anaerobic pathogens individually, it is also important to build on this by acknowledging that there are complex cross-species interactions in the oral cavity. Therefore, to further assess the suitability for HTE-Ti to be used in dental implants, two groups, consisting of dual-species were carried out.

Firstly, *S. mutans* and *P. gingivalis* (SmPg) were incubated as a dual-species culture on the HTE-Ti surface to determine the effect on a culture containing both Gram-positive and Gram-negative species. The presence of *S. mutans* also had the added benefit of acting as an early colonizer promoting the adhesion of *P. gingivalis*. After a 5-day incubation, SmPg had a combined viability of 33.7% ± 6.4% on the HTE-Ti surface compared to 96.7% ± 0.8% on the AR-Ti surface ($p < 0.0001$) (Figure 3E). This result makes intuitive sense because it should be expected that the viability of the mixed culture might fall somewhere between the values observed for the individual cultures of *S. mutans* (6%) and *P. gingivalis* (37%). On the AR-Ti surface, the mean biovolume of SmPg was 4.34 x 106 µm3/mm2, while on the HTE-Ti surface it was only 1.37 x 106 µm3/mm2 ($p < 0.01$) (Figure 3F). This is approximately a 68% significant reduction in biovolume, which is highly consistent with the rate of cell death on HTE-Ti (~67%).

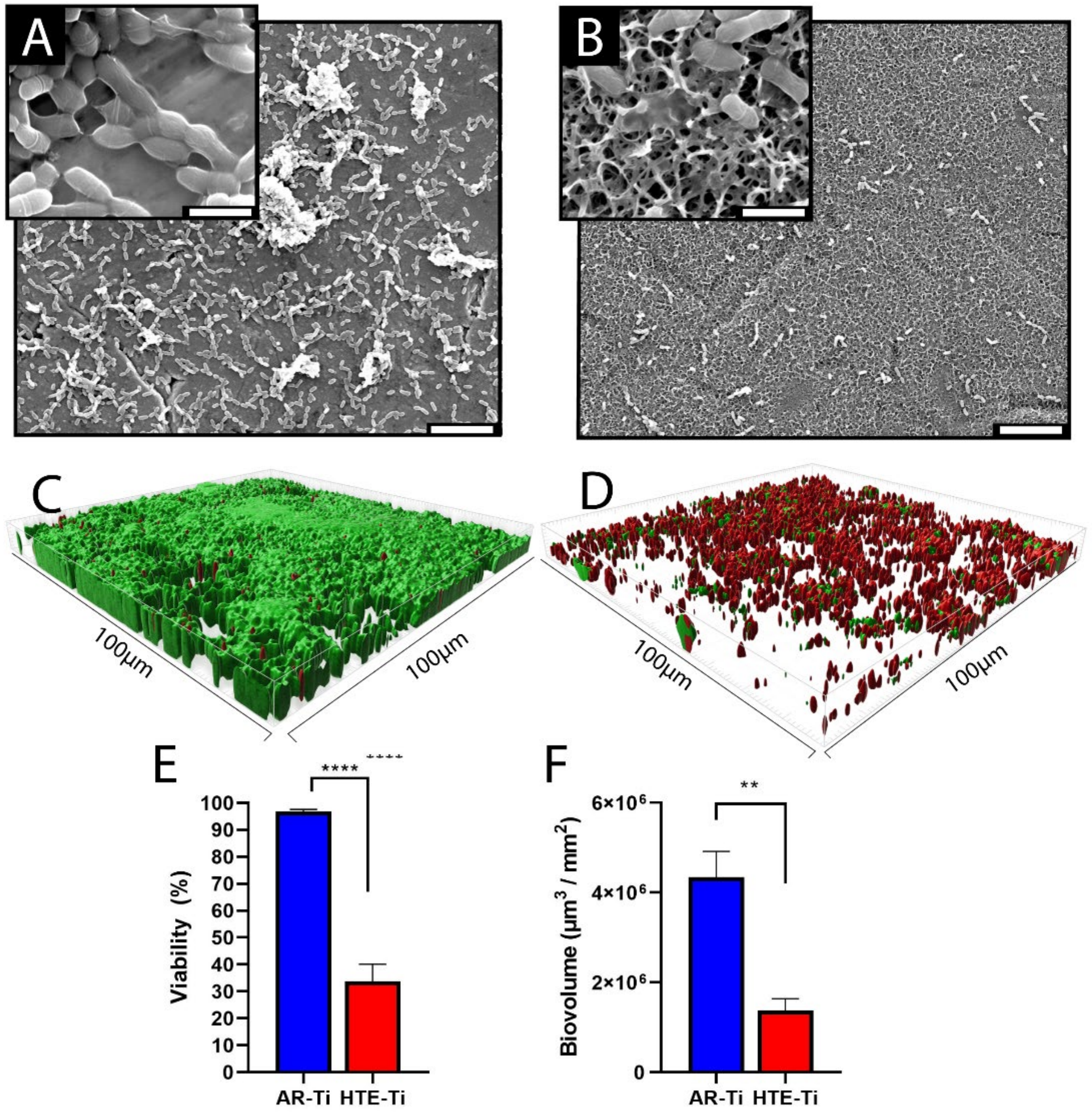

Figure 3. Dual-species incubation of *S. mutans* and *P. gingivalis*. SEM of SmPg on AR-TI (A) and HTE-Ti (B). 3-D biovolume reconstructed from fluorescence stacks on AR-Ti (C) and HTE-Ti (D). Proportion of viable biovolume (E) and total measured biovolume (F). n = 3, Mean ± SD, **** $p < 0.0001$, **$p < 0.01$

Secondly and more importantly, *F. nucleatum* and *P. gingivalis* (FnPg) were incubated as a dual-species culture on the HTE-Ti surface (Figure 4). *F. nucleatum* and *P. gingivalis* share a mutually beneficial relationship, and it has been shown that their combined presence results in a thicker and more robust biofilm compared to the individually cultured species [68-69]. The synergy shared between *F. nucleatum* and *P. gingivalis* may lead to enhanced pathogenesis, and for this reason they are commonly used in models relevant to peri-implantitis and periodontitis [70-71]. Therefore, we mimicked their mutual relationship in the oral environment in an in vitro model. As *F. nucleatum* and *P. gingivalis* are frequently co-localized in oral biofilms [72], it is of particular interest to determine how their synergistic nature would affect their susceptibility to nanostructured surfaces. The FnPg dual-species incubation had a combined viability of 30.5% ± 7.2% on the HTE-Ti surface, compared to 79.4% ± 7.4% on the AR-Ti surface ($p < 0.01$). The viability of FnPg on HTE-Ti is consistent with the viabilities observed for the two species incubated separately. This indicates that their cooperative existence could not assist them to overcome the hostile nature of the nanostructured surface. The total biovolume of FnPg measured on AR-Ti was 2.41×10^6 µm^3/mm^2, while on HTE-Ti it was only 8.45×10^5 µm^3/mm^2 ($p < 0.05$). The reduction in FnPg biovolume is highly consistent with the measured viability and this presents a highly promising result for eventual clinical implementation as it suggests that cross-species synergy may not be a relevant factor in nanostructure sensitivity.

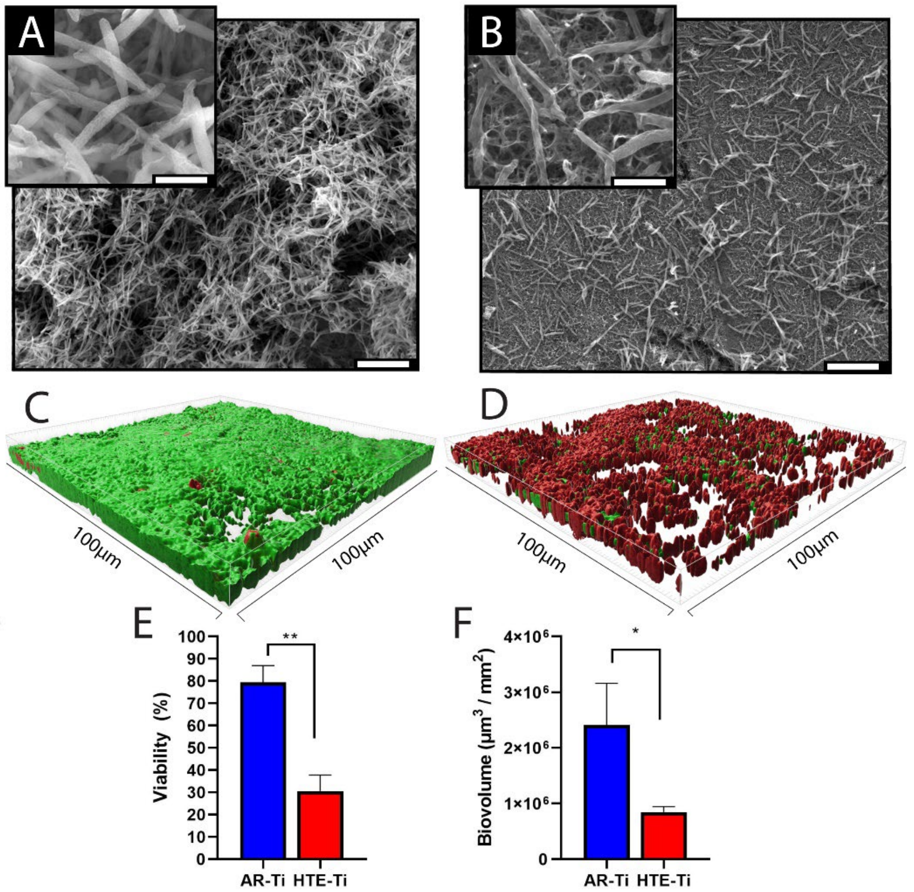

Figure 4. Dual-species incubation of *F. nucleatum* and *P. gingivalis*. SEM of FnPg on AR-TI (A) and HTE-Ti (B). 3-dimensional biovolume reconstructed from fluorescence stacks on AR-Ti (C) and HTE-Ti (D). Proportion of viable biovolume (E) and total measured biovolume (F). n = 3, Mean ± SD ** $p < 0.01$, * $p < 0.05$

3.4. Antibiotic Treatment of Dental Pathogens on HTE-Ti

When bacteria are in a biofilm state, they have a dramatically increased tolerance to antibiotics, and in some cases are up to 1000-fold more resistant to treatment [73]. Due to the observation of biovolume inhibition and decreased viability for all 3 bacteria on HTE-Ti, we hypothesized that there would be an increased sensitivity to antibiotic treatment when bacteria were cultured on HTE-Ti. To investigate this, azithromycin was administered daily to single-species cultures of *S. mutans* (Figure 5) on both AR-Ti and HTE-Ti surfaces for 10 days. Azithromycin was the chosen antibiotic due to its wide usage in the treatment of periodontitis [74]. Azithromycin was administered at 500 and 1000 µg/mL (equivalent to 1 and 2x MIC) to both surfaces. Over the 10 days of treatment, both antibiotic concentrations resulted in a moderate decrease in viability on the AR-Ti surface, to a low of 64.2% ± 9.4%. On the HTE-Ti surface, azithromycin brought *S. mutans* viability down to 1.5% ± 0.6% at 500 µg/mL and 0.6% ± 0.3% at 1000 µg/mL over 10 days. One likely explanation for this increased efficacy of azithromycin may be a reduction in the capacity for bacteria to form biofilm [75]. To expand our azithromycin assay across both Gram-positive and Gram-negative species, the experiment was repeated with *P. gingivalis* (Figure S6 and 7) which produced similar results, but it was slightly less effective than the combined treatment against *S. mutans*. These results are highly encouraging because they suggest that surviving bacteria colonizing the nanostructured surface can be more easily cleared by antibiotic treatment. In contrast, the same concentrations of azithromycin are not a viable outcome on the smooth titanium surface. As patients are typically administered antibiotics both prophylactically and post-surgically, the synergistic relationship between azithromycin treatment and the antibacterial HTE-Ti surface bodes well for clinical implementation.

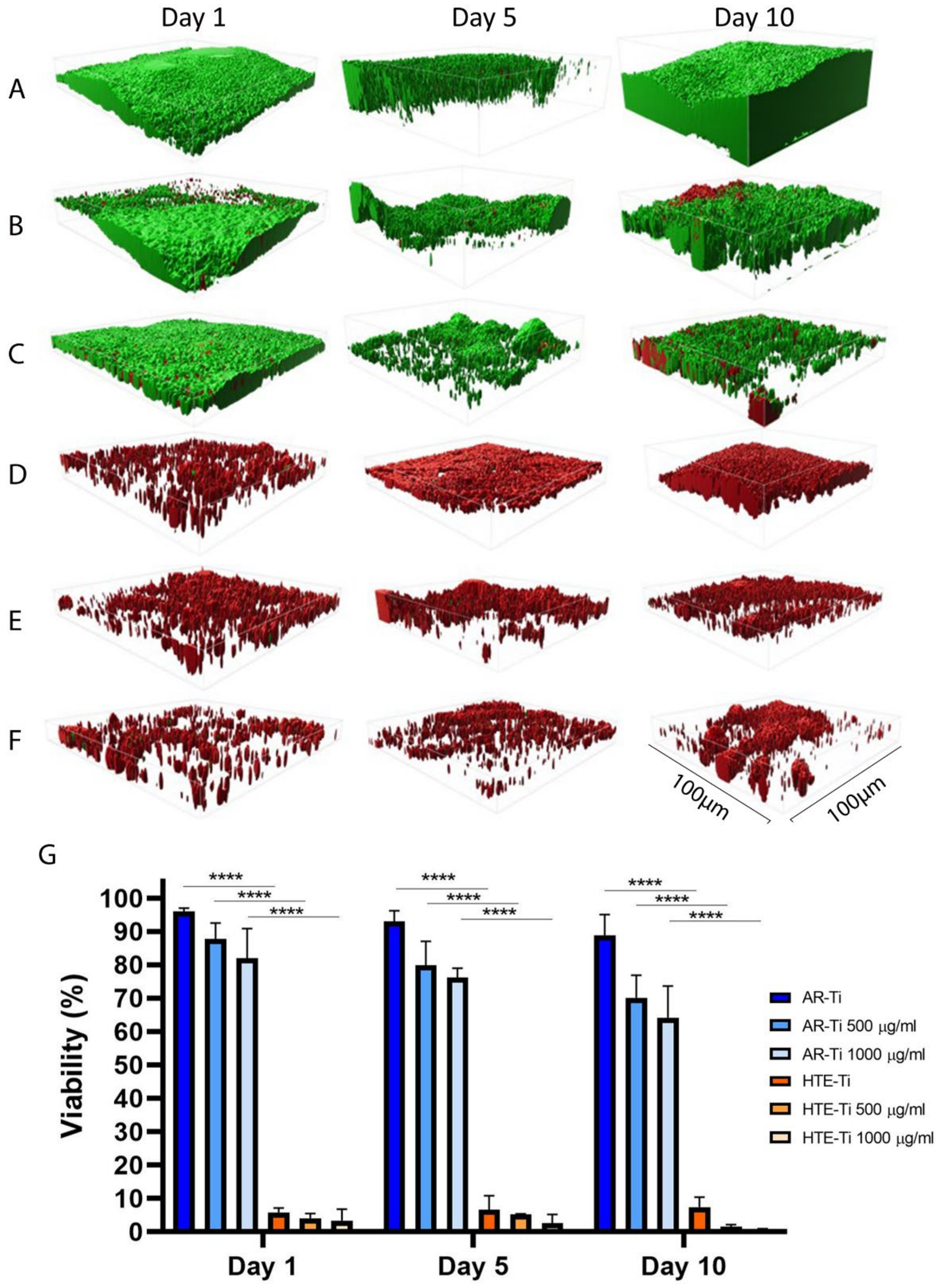

Figure 5. Sensitivity of *S. mutans* to azithromycin when incubated on HTE-Ti. (A) AR-Ti without antibiotics, (B) AR-Ti with 500 µg/mL azithromycin, (C) AR-Ti with 1000 µg/mL azithromycin. (D) HTE-Ti without antibiotics, (E) HTE-Ti with 500 µg/mL azithromycin, (F) HTE-Ti with 1000 µg/mL azithromycin. (G) Longitudinal viability of *S. mutans* in each condition over 10 days. n = 3, Mean ± SD, **** $p < 0.0001$. Full statistical analysis is presented in Figure S5.

Since the discovery of the mechano-bactericidal effect on cicada wings, the mechanism of action of these nanostructured surfaces has been actively interrogated [56, 76-78]. In general, there is consensus that the primary factor involves membrane perturbation or penetration. Recent models suggest this occurs at the point of contact between the nanostructure tip and cell membrane [79-80].

Beyond this primary mechanical interaction, the presence of reactive oxygen species (ROS) has been detected in bacteria cultured on nanostructured titanium [31]. In parallel to this observation, antioxidant proteins and DNA repair proteins were detected with high abundance, implicating oxidative stress as a contributing factor to bacterial cell death. However, it is unclear how much of the bactericidal effect can be attributed to oxidative stress, and how much is purely based on mechanical disruption. In the present study we have cultured dental pathogens in an anaerobic environment, and thus ROS-induced oxidative stress cannot be attributed to the bactericidal effect observed herein. This is encouraging because it refutes any potential skepticism that nanostructures would be effective in the absence of oxygen. The results presented here provide the foundation for further research into the implementation of nanostructured titanium in dental implantology. To build upon this, future studies may benefit from challenging nanostructured surfaces with complex oral microbiome samples, and in vivo animal peri-implantitis model.

Despite decades of advancements in implant design and surgical practices, the rate of peri-implantitis remains at an unacceptably high level. As the pathogenesis of peri-implantitis is strongly linked with the presence of oral bacteria, the development of implantable biomaterials with bactericidal properties is direly needed. The fabrication of mechano-bactericidal nanostructures is one recent strategy which has shown promise in facilitating the inhibition of bacterial colonization.

4. Conclusion

In the present study, we have demonstrated that nanostructured titanium engineered with sharp, spike-like surface structures can indeed be effective in anaerobic conditions against clinically relevant dental pathogens in single-species and dual-species models. Single-species models showed up to 94% cell death, and dual-species models showed up to 70% cell death. An encouraging highlight of this work is that the mutually beneficial relationship typically shared between *F. nucleatum* and *P. gingivalis* was not sufficient to enable them to overcome the hostile nature of the sharp nanostructured surface. Beyond this, our results suggest that the passive bactericidal activity of nanostructured titanium can be complemented with antibiotic treatment to enact a substantially higher rate of bacterial clearance (up to 99.4% killed *S. mutans* cells on azithromycin + spiked surfaces). This may allow clinicians to prescribe lower antibiotic doses for shorter periods of time, and thereby reduce the toxicity associated with antibiotic treatment. The results presented here provide a solid foundation on which to build a greater understanding of how nanostructured titanium biomaterials can be used to reduce the failure rate of dental implants.

Author contributions

A.H, J.H, R.B, J.W, D.B, P.Z and K.V designed the experiments. A.H, J.H, R.B and J.W and D.P performed the experiments and analyzed the data. K.V supervised the study and revised the manuscript. All authors took part in drafting the manuscript.

Notes

The authors listed above declare no conflict of interest.

Supporting Information

The supporting information contains: S1) The images obtained from AFM scans; S2) The morphology and viability of MG-63 cells on HTE-Ti; S3) SEM images of the degree of cell attachment to titanium without saliva pre-coating; S4) a schematic illustrating the differing modes of cell division between *S. aureus* and *S. mutans*; S5) Full statistical analysis for *S. mutans* azithromycin assay; S6) 10-day azithromycin of *P. gingivalis* on HTE-Ti; S7) Full statistical analysis for *P. gingivalis* azithromycin assay.

Acknowledgements

The authors would like to thank Dr. Daniel Fernandes for technical assistance in obtaining the optical profilometry images in Figure 1. This project was funded by MTPConnect Grant (BMTH3_65) under the BioMedtech Horizons Program. KV thanks NHMRC for Fellowship GNT1194466.

5. References

(1) Smeets, R.; Stadlinger, B.; Schwarz, F.; Beck-Broichsitter, B.; Jung, O.; Precht, C.; Kloss, F.; Gröbe, A.; Heiland, M.; Ebker, T. Impact of Dental Implant Surface Modifications on Osseointegration. *Biomed Res Int* **2016,** *2016*, 6285620, DOI: 10.1155/2016/6285620.
(2) Derks, J.; Schaller, D.; Håkansson, J.; Wennström, J. L.; Tomasi, C.; Berglundh, T. Peri-implantitis - onset and pattern of progression. *J Clin Periodontol* **2016,** *43* (4), 383-8, DOI: 10.1111/jcpe.12535.
(3) Salvi, G. E.; Cosgarea, R.; Sculean, A. Prevalence and Mechanisms of Peri-implant Diseases. *J Dent Res* **2017,** *96* (1), 31-37, DOI: 10.1177/0022034516667484.
(4) Research, G. V. Research Report - Peri-implantitis Market. https://www.grandviewresearch.com/industry-analysis/peri-implantitis-market.
(5) Prathapachandran, J.; Suresh, N. Management of peri-implantitis. *Dent Res J (Isfahan)* **2012,** *9* (5), 516-21, DOI: 10.4103/1735-3327.104867.
(6) Yurttutan, M. E.; Keskin, A. Evaluation of the effects of different sand particles that used in dental implant roughened for osseointegration. *BMC Oral Health* **2018,** *18* (1), 47, DOI: 10.1186/s12903-018-0509-3.
(7) McConnell, M. D.; Liu, Y.; Nowak, A. P.; Pilch, S.; Masters, J. G.; Composto, R. J. Bacterial plaque retention on oral hard materials: effect of surface roughness, surface composition, and physisorbed polycarboxylate. *J Biomed Mater Res A* **2010,** *92* (4), 1518-27, DOI: 10.1002/jbm.a.32493.
(8) Vasilev, K.; Cook, J.; Griesser, H. J. Antibacterial surfaces for biomedical devices. *Expert Rev Med Devices* **2009,** *6* (5), 553-67, DOI: 10.1586/erd.09.36.
(9) Vasilev, K.; Griesser, S. S.; Griesser, H. J. Antibacterial Surfaces and Coatings Produced by Plasma Techniques. *Plasma Processes and Polymers* **2011,** *8* (11), 1010-1023, DOI: https://doi.org/10.1002/ppap.201100097.
(10) Maan, A. M. C.; Hofman, A. H.; de Vos, W. M.; Kamperman, M. Recent Developments and Practical Feasibility of Polymer-Based Antifouling Coatings. *Advanced Functional Materials* **2020,** *30* (32), 2000936, DOI: https://doi.org/10.1002/adfm.202000936.
(11) Hasan, J.; Crawford, R. J.; Ivanova, E. P. Antibacterial surfaces: the quest for a new generation of biomaterials. *Trends Biotechnol* **2013,** *31* (5), 295-304, DOI: 10.1016/j.tibtech.2013.01.017.

(12) Wu, S.; Xu, J.; Zou, L.; Luo, S.; Yao, R.; Zheng, B.; Liang, G.; Wu, D.; Li, Y. Long-lasting renewable antibacterial porous polymeric coatings enable titanium biomaterials to prevent and treat peri-implant infection. *Nature Communications* **2021,** *12* (1), 3303, DOI: 10.1038/s41467-021-23069-0.
(13) Griesser, S. S.; Jasieniak, M.; Vasilev, K.; Griesser, H. J. Antimicrobial Peptides Grafted onto a Plasma Polymer Interlayer Platform: Performance upon Extended Bacterial Challenge. *Coatings* **2021,** *11* (1), DOI: 10.3390/coatings11010068.
(14) Vasilev, K. Nanoengineered Antibacterial Coatings and Materials: A Perspective. *Coatings* **2019,** *9* (10), 654.
(15) Liu, R.; Tang, Y.; Zeng, L.; Zhao, Y.; Ma, Z.; Sun, Z.; Xiang, L.; Ren, L.; Yang, K. In vitro and in vivo studies of anti-bacterial copper-bearing titanium alloy for dental application. *Dental Materials* **2018,** *34* (8), 1112-1126, DOI: https://doi.org/10.1016/j.dental.2018.04.007.
(16) Kim, S.; Park, C.; Cheon, K.-H.; Jung, H.-D.; Song, J.; Kim, H.-E.; Jang, T.-S. Antibacterial and bioactive properties of stabilized silver on titanium with a nanostructured surface for dental applications. *Applied Surface Science* **2018,** *451*, 232-240, DOI: https://doi.org/10.1016/j.apsusc.2018.04.270.
(17) Ivanova, E. P.; Hasan, J.; Webb, H. K.; Truong, V. K.; Watson, G. S.; Watson, J. A.; Baulin, V. A.; Pogodin, S.; Wang, J. Y.; Tobin, M. J.; Löbbe, C.; Crawford, R. J. Natural bactericidal surfaces: mechanical rupture of Pseudomonas aeruginosa cells by cicada wings. *Small* **2012,** *8* (16), 2489-94, DOI: 10.1002/smll.201200528.
(18) Bandara, C. D.; Singh, S.; Afara, I. O.; Wolff, A.; Tesfamichael, T.; Ostrikov, K.; Oloyede, A. Bactericidal Effects of Natural Nanotopography of Dragonfly Wing on Escherichia coli. *ACS Appl Mater Interfaces* **2017,** *9* (8), 6746-6760, DOI: 10.1021/acsami.6b13666.
(19) Li, X.; Cheung, G. S.; Watson, G. S.; Watson, J. A.; Lin, S.; Schwarzkopf, L.; Green, D. W. The nanotipped hairs of gecko skin and biotemplated replicas impair and/or kill pathogenic bacteria with high efficiency. *Nanoscale* **2016,** *8* (45), 18860-18869, DOI: 10.1039/C6NR05046H.
(20) Ivanova, E. P.; Hasan, J.; Webb, H. K.; Gervinskas, G.; Juodkazis, S.; Truong, V. K.; Wu, A. H.; Lamb, R. N.; Baulin, V. A.; Watson, G. S.; Watson, J. A.; Mainwaring, D. E.; Crawford, R. J. Bactericidal activity of black silicon. *Nat Commun* **2013,** *4*, 2838, DOI: 10.1038/ncomms3838.
(21) Hasan, J.; Jain, S.; Chatterjee, K. Nanoscale Topography on Black Titanium Imparts Multi-biofunctional Properties for Orthopedic Applications. *Sci Rep* **2017,** *7*, 41118, DOI: 10.1038/srep41118.
(22) Bhadra, C. M.; Truong, V. K.; Pham, V. T.; Al Kobaisi, M.; Seniutinas, G.; Wang, J. Y.; Juodkazis, S.; Crawford, R. J.; Ivanova, E. P. Antibacterial titanium nano-patterned arrays inspired by dragonfly wings. *Sci Rep* **2015,** *5*, 16817, DOI: 10.1038/srep16817.
(23) Bright, R.; Hayles, A.; Fernandes, D.; Visalakshan, R. M.; Ninan, N.; Palms, D.; Burzava, A.; Barker, D.; Brown, T.; Vasilev, K. In Vitro Bactericidal Efficacy of Nanostructured Ti6Al4V Surfaces is Bacterial Load Dependent. *ACS Appl Mater Interfaces* **2021,** *13* (32), 38007-38017, DOI: 10.1021/acsami.1c06919.
(24) Hayles, A.; Hasan, J.; Bright, R.; Palms, D.; Brown, T.; Barker, D.; Vasilev, K. Hydrothermally etched titanium: a review on a promising mechano-bactericidal surface for implant applications. *Materials Today Chemistry* **2021,** *22*, 100622, DOI: https://doi.org/10.1016/j.mtchem.2021.100622.
(25) Osman, R. B.; Swain, M. V. A Critical Review of Dental Implant Materials with an Emphasis on Titanium versus Zirconia. *Materials (Basel)* **2015,** *8* (3), 932-958, DOI: 10.3390/ma8030932.
(26) Hanawa, T. Titanium–Tissue Interface Reaction and Its Control With Surface Treatment. *Frontiers in Bioengineering and Biotechnology* **2019,** *7* (170), DOI: 10.3389/fbioe.2019.00170.
(27) Niinomi, M.; Liu, Y.; Nakai, M.; Liu, H.; Li, H. Biomedical titanium alloys with Young's moduli close to that of cortical bone. *Regen Biomater* **2016,** *3* (3), 173-185, DOI: 10.1093/rb/rbw016.
(28) Clainche, T. L.; Linklater, D.; Wong, S.; Le, P.; Juodkazis, S.; Guevel, X. L.; Coll, J. L.; Ivanova, E. P.; Martel-Frachet, V. Mechano-Bactericidal Titanium Surfaces for Bone Tissue Engineering. *ACS Appl Mater Interfaces* **2020,** *12* (43), 48272-48283, DOI: 10.1021/acsami.0c11502.
(29) Tsimbouri, P. M.; Fisher, L.; Holloway, N.; Sjostrom, T.; Nobbs, A. H.; Meek, R. M.; Su, B.; Dalby, M. J. Osteogenic and bactericidal surfaces from hydrothermal titania nanowires on titanium substrates. *Sci Rep* **2016,** *6*, 36857, DOI: 10.1038/srep36857.
(30) Goriainov, V.; Hulsart-Billstrom, G.; Sjostrom, T.; Dunlop, D. G.; Su, B.; Oreffo, R. O. C. Harnessing Nanotopography to Enhance Osseointegration of Clinical Orthopedic Titanium Implants—An in Vitro and in Vivo Analysis. *Frontiers in Bioengineering and Biotechnology* **2018,** *6* (44), DOI: 10.3389/fbioe.2018.00044.

(31) Jenkins, J.; Mantell, J.; Neal, C.; Gholinia, A.; Verkade, P.; Nobbs, A. H.; Su, B. Antibacterial effects of nanopillar surfaces are mediated by cell impedance, penetration and induction of oxidative stress. *Nat Commun* **2020,** *11* (1), 1626, DOI: 10.1038/s41467-020-15471-x.
(32) Jaggessar, A.; Shahali, H.; Mathew, A.; Yarlagadda, P. Bio-mimicking nano and micro-structured surface fabrication for antibacterial properties in medical implants. *J Nanobiotechnology* **2017,** *15* (1), 64, DOI: 10.1186/s12951-017-0306-1.
(33) Diu, T.; Faruqui, N.; Sjöström, T.; Lamarre, B.; Jenkinson, H. F.; Su, B.; Ryadnov, M. G. Cicada-inspired cell-instructive nanopatterned arrays. *Sci Rep* **2014,** *4*, 7122, DOI: 10.1038/srep07122.
(34) Jaggessar, A.; Mathew, A.; Tesfamichael, T.; Wang, H.; Yan, C.; Yarlagadda, P. K. Bacteria Death and Osteoblast Metabolic Activity Correlated to Hydrothermally Synthesised TiO(2) Surface Properties. *Molecules* **2019,** *24* (7), DOI: 10.3390/molecules24071201.
(35) Ishak, M. I.; Liu, X.; Jenkins, J.; Nobbs, A. H.; Su, B. Protruding Nanostructured Surfaces for Antimicrobial and Osteogenic Titanium Implants. *Coatings* **2020,** *10* (8), DOI: 10.3390/coatings10080756.
(36) Li, X.; Tsui, K.-H.; Tsoi, J. K. H.; Green, D. W.; Jin, X.-z.; Deng, Y. Q.; Zhu, Y. M.; Li, X. G.; Fan, Z.; Cheung, G. S.-p. A nanostructured anti-biofilm surface widens the efficacy against spindle-shaped and chain-forming rod-like bacteria. *Nanoscale* **2020,** *12* (36), 18864-18874, DOI: 10.1039/D0NR03809A.
(37) Stockham, S.; Stamford, J. E.; Roberts, C. T.; Fitzsimmons, T. R.; Marchant, C.; Bartold, P. M.; Zilm, P. S. Abnormal Pregnancy Outcomes in Mice Using an Induced Periodontitis Model and the Haematogenous Migration of Fusobacterium nucleatum Sub-Species to the Murine Placenta. *PLOS ONE* **2015,** *10* (3), e0120050, DOI: 10.1371/journal.pone.0120050.
(38) Kaur, S.; Bright, R.; Proudman, S. M.; Bartold, P. M. Does periodontal treatment influence clinical and biochemical measures for rheumatoid arthritis? A systematic review and meta-analysis. *Semin Arthritis Rheum* **2014,** *44* (2), 113-22, DOI: 10.1016/j.semarthrit.2014.04.009.
(39) Darveau, R. P.; Hajishengallis, G.; Curtis, M. A. Porphyromonas gingivalis as a potential community activist for disease. *J Dent Res* **2012,** *91* (9), 816-20, DOI: 10.1177/0022034512453589.
(40) Fiorillo, L.; Cervino, G.; Laino, L.; D'Amico, C.; Mauceri, R.; Tozum, T. F.; Gaeta, M.; Cicciù, M. Porphyromonas gingivalis, Periodontal and Systemic Implications: A Systematic Review. *Dent J (Basel)* **2019,** *7* (4), DOI: 10.3390/dj7040114.
(41) Liu, X.-b.; Gao, Z.-y.; Sun, C.-t.; Wen, H.; Gao, B.; Li, S.-b.; Tong, Q. The potential role of P.gingivalis in gastrointestinal cancer: a mini review. *Infectious Agents and Cancer* **2019,** *14* (1), 23, DOI: 10.1186/s13027-019-0239-4.
(42) Gully, N.; Bright, R.; Marino, V.; Marchant, C.; Cantley, M.; Haynes, D.; Butler, C.; Dashper, S.; Reynolds, E.; Bartold, M. Porphyromonas gingivalis peptidylarginine deiminase, a key contributor in the pathogenesis of experimental periodontal disease and experimental arthritis. *PLoS One* **2014,** *9* (6), e100838, DOI: 10.1371/journal.pone.0100838.
(43) Auer, G. K.; Weibel, D. B. Bacterial Cell Mechanics. *Biochemistry* **2017,** *56* (29), 3710-3724, DOI: 10.1021/acs.biochem.7b00346.
(44) Kumar, P.; Nagarajan, A.; Uchil, P. D. Analysis of Cell Viability by the Lactate Dehydrogenase Assay. *Cold Spring Harb Protoc* **2018,** *2018* (6), DOI: 10.1101/pdb.prot095497.
(45) Guggenheim, B.; Giertsen, E.; Schüpbach, P.; Shapiro, S. Validation of an in vitro biofilm model of supragingival plaque. *J Dent Res* **2001,** *80* (1), 363-70, DOI: 10.1177/00220345010800011201.
(46) Sieuwerts, S.; De Bok, F. A. M.; Mols, E.; De Vos, W. M.; Van Hylckama Vlieg, J. E. T. A simple and fast method for determining colony forming units. *Letters in Applied Microbiology* **2008,** *47* (4), 275-278, DOI: https://doi.org/10.1111/j.1472-765X.2008.02417.x.
(47) CLSI. Performance Standards for Antimicrobial Susceptibility Testing; Twenty-Fourth Informational Supplement. *Clinical and Laboratory Standards Institute* **2014**.
(48) Yuan, Z. Y.; Zhang, X. B.; Su, B. L. Moderate hydrothermal synthesis of potassium titanate nanowires. *Applied Physics A* **2004,** *78* (7), 1063-1066, DOI: 10.1007/s00339-003-2165-x.
(49) Wennerberg, A.; Albrektsson, T. Effects of titanium surface topography on bone integration: a systematic review. *Clinical Oral Implants Research* **2009,** *20* (s4), 172-184, DOI: https://doi.org/10.1111/j.1600-0501.2009.01775.x.
(50) Buser, D.; Broggini, N.; Wieland, M.; Schenk, R. K.; Denzer, A. J.; Cochran, D. L.; Hoffmann, B.; Lussi, A.; Steinemann, S. G. Enhanced Bone Apposition to a Chemically Modified SLA Titanium Surface. *Journal of Dental Research* **2004,** *83* (7), 529-533, DOI: 10.1177/154405910408300704.

(51) Rabel, K.; Kohal, R.-J.; Steinberg, T.; Tomakidi, P.; Rolauffs, B.; Adolfsson, E.; Palmero, P.; Fürderer, T.; Altmann, B. Controlling osteoblast morphology and proliferation via surface micro-topographies of implant biomaterials. *Scientific Reports* **2020,** *10* (1), 12810, DOI: 10.1038/s41598-020-69685-6.
(52) Periasamy, S.; Kolenbrander, P. E. Mutualistic biofilm communities develop with Porphyromonas gingivalis and initial, early, and late colonizers of enamel. *J Bacteriol* **2009,** *191* (22), 6804-11, DOI: 10.1128/jb.01006-09.
(53) Mendez, K. N.; Hoare, A.; Soto, C.; Bugueño, I.; Olivera, M.; Meneses, C.; Pérez-Donoso, J. M.; Castro-Nallar, E.; Bravo, D. Variability in Genomic and Virulent Properties of Porphyromonas gingivalis Strains Isolated From Healthy and Severe Chronic Periodontitis Individuals. *Frontiers in Cellular and Infection Microbiology* **2019,** *9* (246), DOI: 10.3389/fcimb.2019.00246.
(54) Chawhuaveang, D. D.; Yu, O. Y.; Yin, I. X.; Lam, W. Y.; Mei, M. L.; Chu, C. H. Acquired salivary pellicle and oral diseases: A literature review. *J Dent Sci* **2021,** *16* (1), 523-529, DOI: 10.1016/j.jds.2020.10.007.
(55) Xue, F.; Liu, J.; Guo, L.; Zhang, L.; Li, Q. Theoretical study on the bactericidal nature of nanopatterned surfaces. *J Theor Biol* **2015,** *385*, 1-7, DOI: 10.1016/j.jtbi.2015.08.011.
(56) Pogodin, S.; Hasan, J.; Baulin, V. A.; Webb, H. K.; Truong, V. K.; Phong Nguyen, T. H.; Boshkovikj, V.; Fluke, C. J.; Watson, G. S.; Watson, J. A.; Crawford, R. J.; Ivanova, E. P. Biophysical model of bacterial cell interactions with nanopatterned cicada wing surfaces. *Biophys J* **2013,** *104* (4), 835-40, DOI: 10.1016/j.bpj.2012.12.046.
(57) Silhavy, T. J.; Kahne, D.; Walker, S. The bacterial cell envelope. *Cold Spring Harb Perspect Biol* **2010,** *2* (5), a000414, DOI: 10.1101/cshperspect.a000414.
(58) Zapun, A.; Vernet, T.; Pinho, M. G. The different shapes of cocci. *FEMS Microbiol Rev* **2008,** *32* (2), 345-60, DOI: 10.1111/j.1574-6976.2007.00098.x.
(59) Egan, A. J. F.; Errington, J.; Vollmer, W. Regulation of peptidoglycan synthesis and remodelling. *Nature Reviews Microbiology* **2020,** *18* (8), 446-460, DOI: 10.1038/s41579-020-0366-3.
(60) Truong, T. T.; Vettiger, A.; Bernhardt, T. G. Cell division is antagonized by the activity of peptidoglycan endopeptidases that promote cell elongation. *Molecular Microbiology* **2020,** *114* (6), 966-978, DOI: https://doi.org/10.1111/mmi.14587.
(61) Yin, N.; Santos, T. M.; Auer, G. K.; Crooks, J. A.; Oliver, P. M.; Weibel, D. B. Bacterial cellulose as a substrate for microbial cell culture. *Appl Environ Microbiol* **2014,** *80* (6), 1926-32, DOI: 10.1128/aem.03452-13.
(62) Rogers, A. H.; Zilm, P. S.; Gully, N. J.; Pfennig, A. L.; Marsh, P. D. Aspects of the growth and metabolism of Fusobacterium nucleatum ATCC 10953 in continuous culture. *Oral Microbiol Immunol* **1991,** *6* (4), 250-5, DOI: 10.1111/j.1399-302x.1991.tb00486.x.
(63) Bradshaw, D. J.; Marsh, P. D.; Watson, G. K.; Allison, C. Role of Fusobacterium nucleatum and coaggregation in anaerobe survival in planktonic and biofilm oral microbial communities during aeration. *Infect Immun* **1998,** *66* (10), 4729-32, DOI: 10.1128/iai.66.10.4729-4732.1998.
(64) Grenier, D.; Imbeault, S.; Plamondon, P.; Grenier, G.; Nakayama, K.; Mayrand, D. Role of gingipains in growth of Porphyromonas gingivalis in the presence of human serum albumin. *Infect Immun* **2001,** *69* (8), 5166-72, DOI: 10.1128/iai.69.8.5166-5172.2001.
(65) Lo, A. W.; Seers, C. A.; Boyce, J. D.; Dashper, S. G.; Slakeski, N.; Lissel, J. P.; Reynolds, E. C. Comparative transcriptomic analysis of Porphyromonas gingivalis biofilm and planktonic cells. *BMC Microbiol* **2009,** *9*, 18, DOI: 10.1186/1471-2180-9-18.
(66) Frazer, R. Q.; Byron, R. T.; Osborne, P. B.; West, K. P. PMMA: an essential material in medicine and dentistry. *J Long Term Eff Med Implants* **2005,** *15* (6), 629-39, DOI: 10.1615/jlongtermeffmedimplants.v15.i6.60.
(67) Kilian, M.; Chapple, I. L. C.; Hannig, M.; Marsh, P. D.; Meuric, V.; Pedersen, A. M. L.; Tonetti, M. S.; Wade, W. G.; Zaura, E. The oral microbiome – an update for oral healthcare professionals. *British Dental Journal* **2016,** *221* (10), 657-666, DOI: 10.1038/sj.bdj.2016.865.
(68) Tavares, L. J.; Klein, M. I.; Panariello, B. H. D.; Dorigatti de Avila, E.; Pavarina, A. C. An in vitro model of Fusobacterium nucleatum and Porphyromonas gingivalis in single- and dual-species biofilms. *J Periodontal Implant Sci* **2018,** *48* (1), 12-21, DOI: 10.5051/jpis.2018.48.1.12.
(69) Diaz, P. I.; Zilm, P. S.; Rogers, A. H. Fusobacterium nucleatum supports the growth of Porphyromonas gingivalis in oxygenated and carbon-dioxide-depleted environments. *Microbiology (Reading)* **2002,** *148* (Pt 2), 467-472, DOI: 10.1099/00221287-148-2-467.

(70) Sun, X.; Sun, J.; Sun, Y.; Li, C.; Fang, J.; Zhang, T.; Wan, Y.; Xu, L.; Zhou, Y.; Wang, L.; Dong, B. Oxygen Self-Sufficient Nanoplatform for Enhanced and Selective Antibacterial Photodynamic Therapy against Anaerobe-Induced Periodontal Disease. *Advanced Functional Materials* **2021,** *31* (20), 2101040, DOI: https://doi.org/10.1002/adfm.202101040.

(71) Li, X.; Qi, M.; Sun, X.; Weir, M. D.; Tay, F. R.; Oates, T. W.; Dong, B.; Zhou, Y.; Wang, L.; Xu, H. H. K. Surface treatments on titanium implants via nanostructured ceria for antibacterial and anti-inflammatory capabilities. *Acta Biomater* **2019,** *94*, 627-643, DOI: 10.1016/j.actbio.2019.06.023.

(72) Rosen, G.; Sela, M. N. Coaggregation of Porphyromonas gingivalis and Fusobacterium nucleatum PK 1594 is mediated by capsular polysaccharide and lipopolysaccharide. *FEMS Microbiology Letters* **2006,** *256* (2), 304-310, DOI: 10.1111/j.1574-6968.2006.00131.x.

(73) Olson, M. E.; Ceri, H.; Morck, D. W.; Buret, A. G.; Read, R. R. Biofilm bacteria: formation and comparative susceptibility to antibiotics. *Can J Vet Res* **2002,** *66* (2), 86-92.

(74) Hirsch, R. Periodontal healing and bone regeneration in response to azithromycin. *Australian Dental Journal* **2010,** *55* (2), 193-199, DOI: https://doi.org/10.1111/j.1834-7819.2010.01227.x.

(75) Bright, R.; Fernandes, D.; Wood, J.; Palms, D.; Burzava, A.; Ninan, N.; Brown, T.; Barker, D.; Vasilev, K. Long-term antibacterial properties of a nanostructured titanium alloy surface: An in vitro study. *Materials Today Bio* **2022,** *13*, 100176, DOI: https://doi.org/10.1016/j.mtbio.2021.100176.

(76) Watson, G. S.; Green, D. W.; Watson, J. A.; Zhou, Z.; Li, X.; Cheung, G. S. P.; Gellender, M. A Simple Model for Binding and Rupture of Bacterial Cells on Nanopillar Surfaces. *Advanced Materials Interfaces* **2019,** *6* (10), 1801646, DOI: https://doi.org/10.1002/admi.201801646.

(77) Ivanova, E. P.; Linklater, D. P.; Werner, M.; Baulin, V. A.; Xu, X.; Vrancken, N.; Rubanov, S.; Hanssen, E.; Wandiyanto, J.; Truong, V. K.; Elbourne, A.; Maclaughlin, S.; Juodkazis, S.; Crawford, R. J. The multi-faceted mechano-bactericidal mechanism of nanostructured surfaces. *Proc Natl Acad Sci U S A* **2020,** *117* (23), 12598-12605, DOI: 10.1073/pnas.1916680117.

(78) Linklater, D. P.; Baulin, V. A.; Juodkazis, S.; Crawford, R. J.; Stoodley, P.; Ivanova, E. P. Mechano-bactericidal actions of nanostructured surfaces. *Nat Rev Microbiol* **2021,** *19* (1), 8-22, DOI: 10.1038/s41579-020-0414-z.

(79) Velic, A.; Hasan, J.; Li, Z.; Yarlagadda, P. Mechanics of Bacterial Interaction and Death on Nanopatterned Surfaces. *Biophysical Journal* **2020**, DOI: 10.1016/j.bpj.2020.12.003.

(80) Cui, Q.; Liu, T.; Li, X.; Zhao, L.; Wu, Q.; Wang, X.; Song, K.; Ge, D. Validation of the mechano-bactericidal mechanism of nanostructured surfaces with finite element simulation. *Colloids and Surfaces B: Biointerfaces* **2021,** *206*, 111929, DOI: https://doi.org/10.1016/j.colsurfb.2021.111929.

6. Supporting Information

6.1. Results

Figure S1 shows the images acquired by AFM which were used to determine the nanoscale roughness.

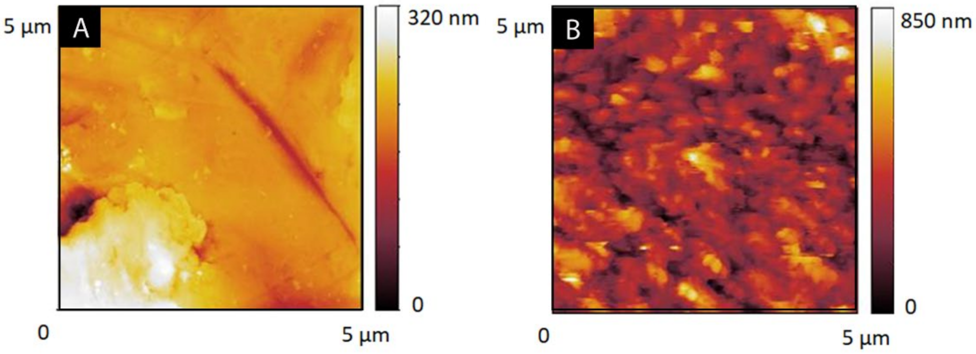

Figure S1. The nanoscale roughness of AR-Ti and HTE-Ti as measured by AFM using a 5 μm^2 scan size. (A) The smooth AR-Ti and (B) the rough HTE-Ti.

Figure S2 shows the initial incubation experiment using *S. mutans*, *F. nucleatum*, and *P. gingivalis* without pre-treating the titanium surfaces with saliva to generate a pellicle layer. The degree of cell attachment was considered too low to be used in further studies, and optimizations were made by coating the titanium samples in saliva.

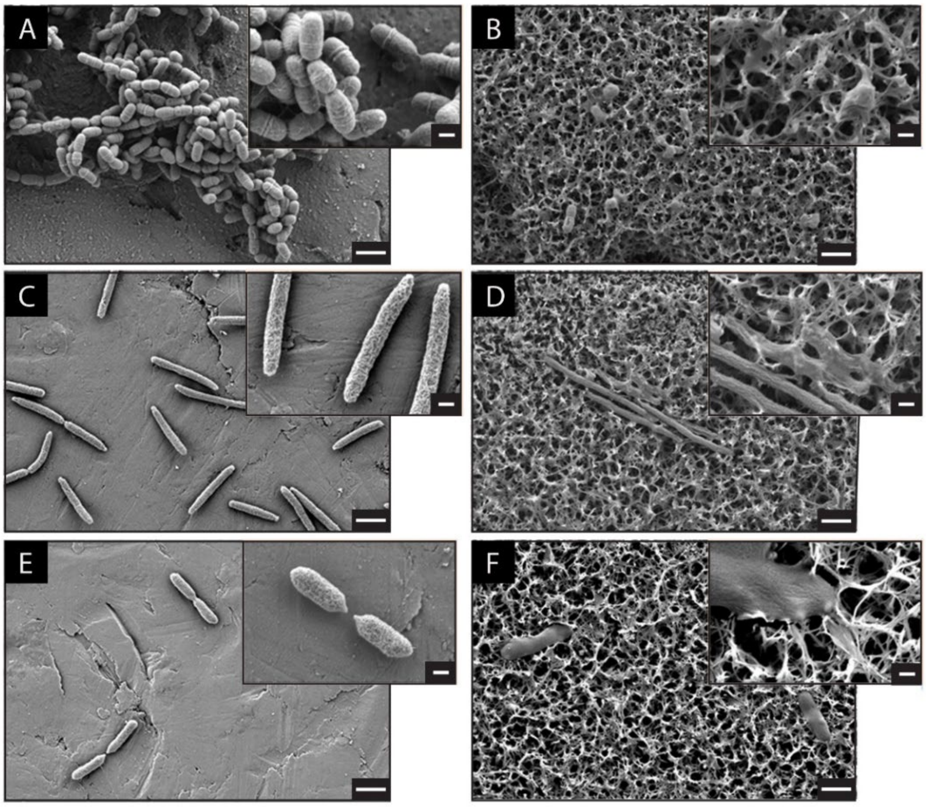

Figure S2. Cell attachment of anaerobic oral pathogens to titanium surfaces without a saliva pre-coating. *S. mutans* on AR-Ti (A) and HTE-Ti (B). *F. nucleatum* on AR-Ti (C) and HTE-Ti (D). *P. gingivalis* on AR-Ti (E) and HTE-Ti (F).

Figure S3 shows the different modes of cell division between *S. aureus* and *S. mutans*. *S. aureus* has 3 planes of division and can therefore expand across all 3 dimensions. This may allow *S. aureus* to escape the hostile effects of the nanostructure by dividing 'away' from the surface. *S. mutans* divides along a single plane, and therefore must divide laterally across the nanostructured surface. As *S. aureus* and *S. mutans* are both Gram-positive cells with a comparably thick peptidoglycan layer, this difference in cell division is proposed to account for the increased sensitivity of *S. mutans* to mechanically induced cell death.

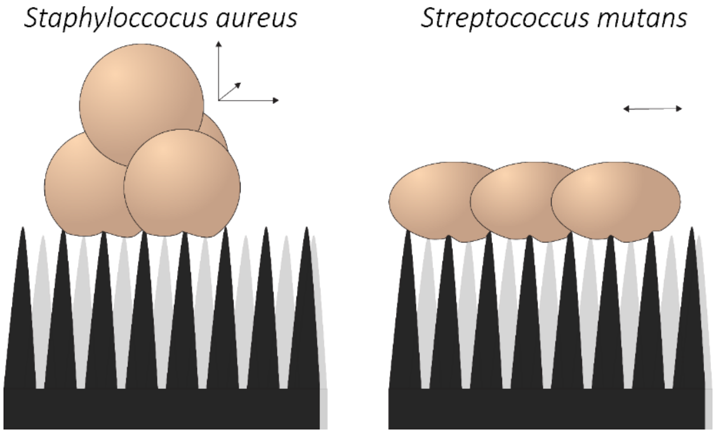

Figure S3. The differing modes of cell division between *S. aureus* and *S. mutans*.

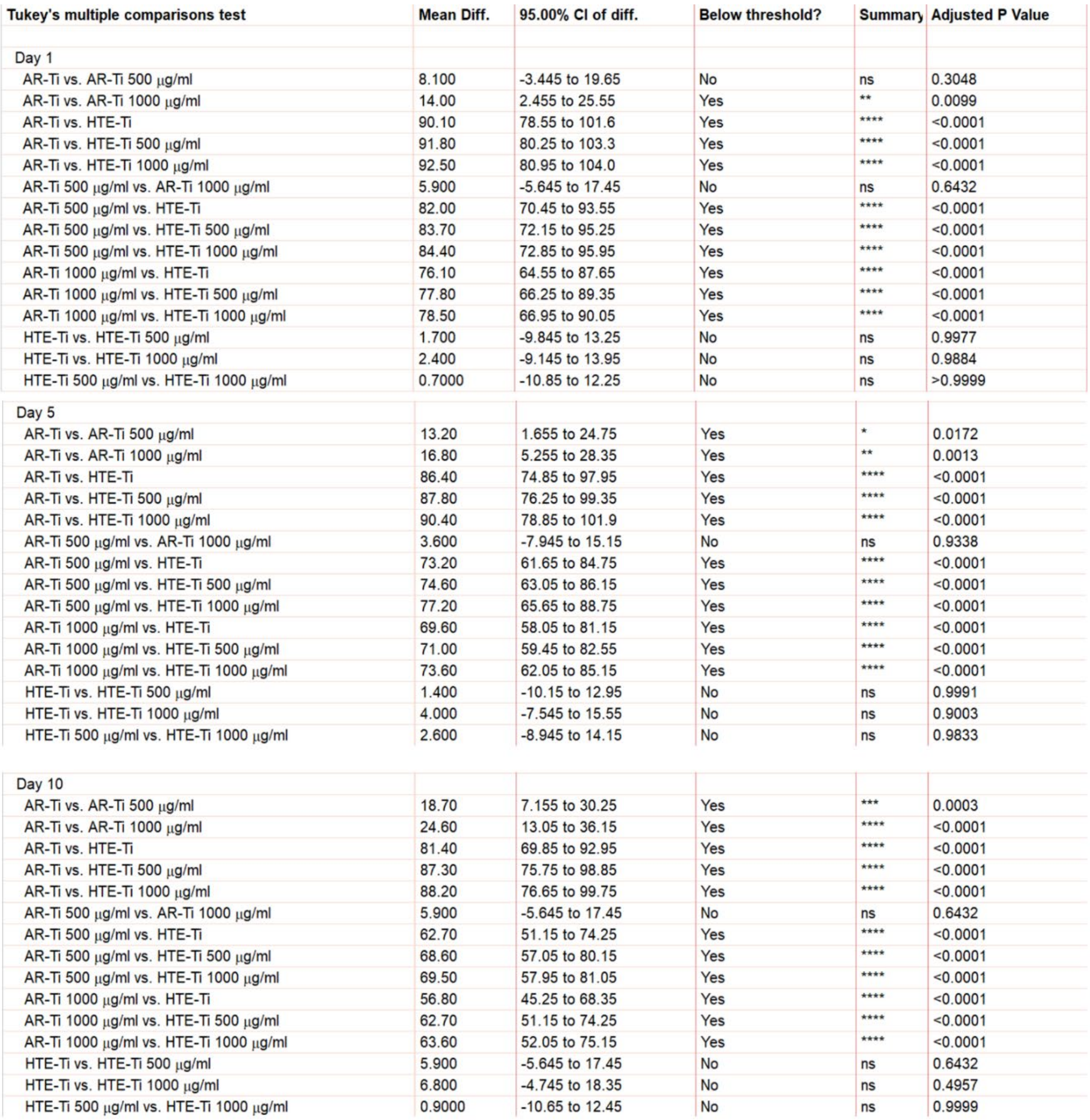

Tukey's multiple comparisons test	Mean Diff.	95.00% CI of diff.	Below threshold?	Summary	Adjusted P Value
Day 1					
AR-Ti vs. AR-Ti 500 μg/ml	8.100	-3.445 to 19.65	No	ns	0.3048
AR-Ti vs. AR-Ti 1000 μg/ml	14.00	2.455 to 25.55	Yes	**	0.0099
AR-Ti vs. HTE-Ti	90.10	78.55 to 101.6	Yes	****	<0.0001
AR-Ti vs. HTE-Ti 500 μg/ml	91.80	80.25 to 103.3	Yes	****	<0.0001
AR-Ti vs. HTE-Ti 1000 μg/ml	92.50	80.95 to 104.0	Yes	****	<0.0001
AR-Ti 500 μg/ml vs. AR-Ti 1000 μg/ml	5.900	-5.645 to 17.45	No	ns	0.6432
AR-Ti 500 μg/ml vs. HTE-Ti	82.00	70.45 to 93.55	Yes	****	<0.0001
AR-Ti 500 μg/ml vs. HTE-Ti 500 μg/ml	83.70	72.15 to 95.25	Yes	****	<0.0001
AR-Ti 500 μg/ml vs. HTE-Ti 1000 μg/ml	84.40	72.85 to 95.95	Yes	****	<0.0001
AR-Ti 1000 μg/ml vs. HTE-Ti	76.10	64.55 to 87.65	Yes	****	<0.0001
AR-Ti 1000 μg/ml vs. HTE-Ti 500 μg/ml	77.80	66.25 to 89.35	Yes	****	<0.0001
AR-Ti 1000 μg/ml vs. HTE-Ti 1000 μg/ml	78.50	66.95 to 90.05	Yes	****	<0.0001
HTE-Ti vs. HTE-Ti 500 μg/ml	1.700	-9.845 to 13.25	No	ns	0.9977
HTE-Ti vs. HTE-Ti 1000 μg/ml	2.400	-9.145 to 13.95	No	ns	0.9884
HTE-Ti 500 μg/ml vs. HTE-Ti 1000 μg/ml	0.7000	-10.85 to 12.25	No	ns	>0.9999
Day 5					
AR-Ti vs. AR-Ti 500 μg/ml	13.20	1.655 to 24.75	Yes	*	0.0172
AR-Ti vs. AR-Ti 1000 μg/ml	16.80	5.255 to 28.35	Yes	**	0.0013
AR-Ti vs. HTE-Ti	86.40	74.85 to 97.95	Yes	****	<0.0001
AR-Ti vs. HTE-Ti 500 μg/ml	87.80	76.25 to 99.35	Yes	****	<0.0001
AR-Ti vs. HTE-Ti 1000 μg/ml	90.40	78.85 to 101.9	Yes	****	<0.0001
AR-Ti 500 μg/ml vs. AR-Ti 1000 μg/ml	3.600	-7.945 to 15.15	No	ns	0.9338
AR-Ti 500 μg/ml vs. HTE-Ti	73.20	61.65 to 84.75	Yes	****	<0.0001
AR-Ti 500 μg/ml vs. HTE-Ti 500 μg/ml	74.60	63.05 to 86.15	Yes	****	<0.0001
AR-Ti 500 μg/ml vs. HTE-Ti 1000 μg/ml	77.20	65.65 to 88.75	Yes	****	<0.0001
AR-Ti 1000 μg/ml vs. HTE-Ti	69.60	58.05 to 81.15	Yes	****	<0.0001
AR-Ti 1000 μg/ml vs. HTE-Ti 500 μg/ml	71.00	59.45 to 82.55	Yes	****	<0.0001
AR-Ti 1000 μg/ml vs. HTE-Ti 1000 μg/ml	73.60	62.05 to 85.15	Yes	****	<0.0001
HTE-Ti vs. HTE-Ti 500 μg/ml	1.400	-10.15 to 12.95	No	ns	0.9991
HTE-Ti vs. HTE-Ti 1000 μg/ml	4.000	-7.545 to 15.55	No	ns	0.9003
HTE-Ti 500 μg/ml vs. HTE-Ti 1000 μg/ml	2.600	-8.945 to 14.15	No	ns	0.9833
Day 10					
AR-Ti vs. AR-Ti 500 μg/ml	18.70	7.155 to 30.25	Yes	***	0.0003
AR-Ti vs. AR-Ti 1000 μg/ml	24.60	13.05 to 36.15	Yes	****	<0.0001
AR-Ti vs. HTE-Ti	81.40	69.85 to 92.95	Yes	****	<0.0001
AR-Ti vs. HTE-Ti 500 μg/ml	87.30	75.75 to 98.85	Yes	****	<0.0001
AR-Ti vs. HTE-Ti 1000 μg/ml	88.20	76.65 to 99.75	Yes	****	<0.0001
AR-Ti 500 μg/ml vs. AR-Ti 1000 μg/ml	5.900	-5.645 to 17.45	No	ns	0.6432
AR-Ti 500 μg/ml vs. HTE-Ti	62.70	51.15 to 74.25	Yes	****	<0.0001
AR-Ti 500 μg/ml vs. HTE-Ti 500 μg/ml	68.60	57.05 to 80.15	Yes	****	<0.0001
AR-Ti 500 μg/ml vs. HTE-Ti 1000 μg/ml	69.50	57.95 to 81.05	Yes	****	<0.0001
AR-Ti 1000 μg/ml vs. HTE-Ti	56.80	45.25 to 68.35	Yes	****	<0.0001
AR-Ti 1000 μg/ml vs. HTE-Ti 500 μg/ml	62.70	51.15 to 74.25	Yes	****	<0.0001
AR-Ti 1000 μg/ml vs. HTE-Ti 1000 μg/ml	63.60	52.05 to 75.15	Yes	****	<0.0001
HTE-Ti vs. HTE-Ti 500 μg/ml	5.900	-5.645 to 17.45	No	ns	0.6432
HTE-Ti vs. HTE-Ti 1000 μg/ml	6.800	-4.745 to 18.35	No	ns	0.4957
HTE-Ti 500 μg/ml vs. HTE-Ti 1000 μg/ml	0.9000	-10.65 to 12.45	No	ns	0.9999

Figure S4. The full set of statistical analyses for the azithromycin treatment assay using *S. mutans*.

Figure S5 shows the increased the antibiotic/nanostructure dual-treatment strategy against *P. gingivalis*. Following 10 days of daily azithromycin treatment at 64 µg/mL and 128 µg/mL (representing 1x and 2x MIC, respectively), *P. gingivalis* on the AR-Ti surface was only reduced to a viability of approximately 60%. On the HTE-Ti, when *P. gingivalis* was treated with 2x MIC, the pre-established culture was brought down to a viability of approximately 7.5%.

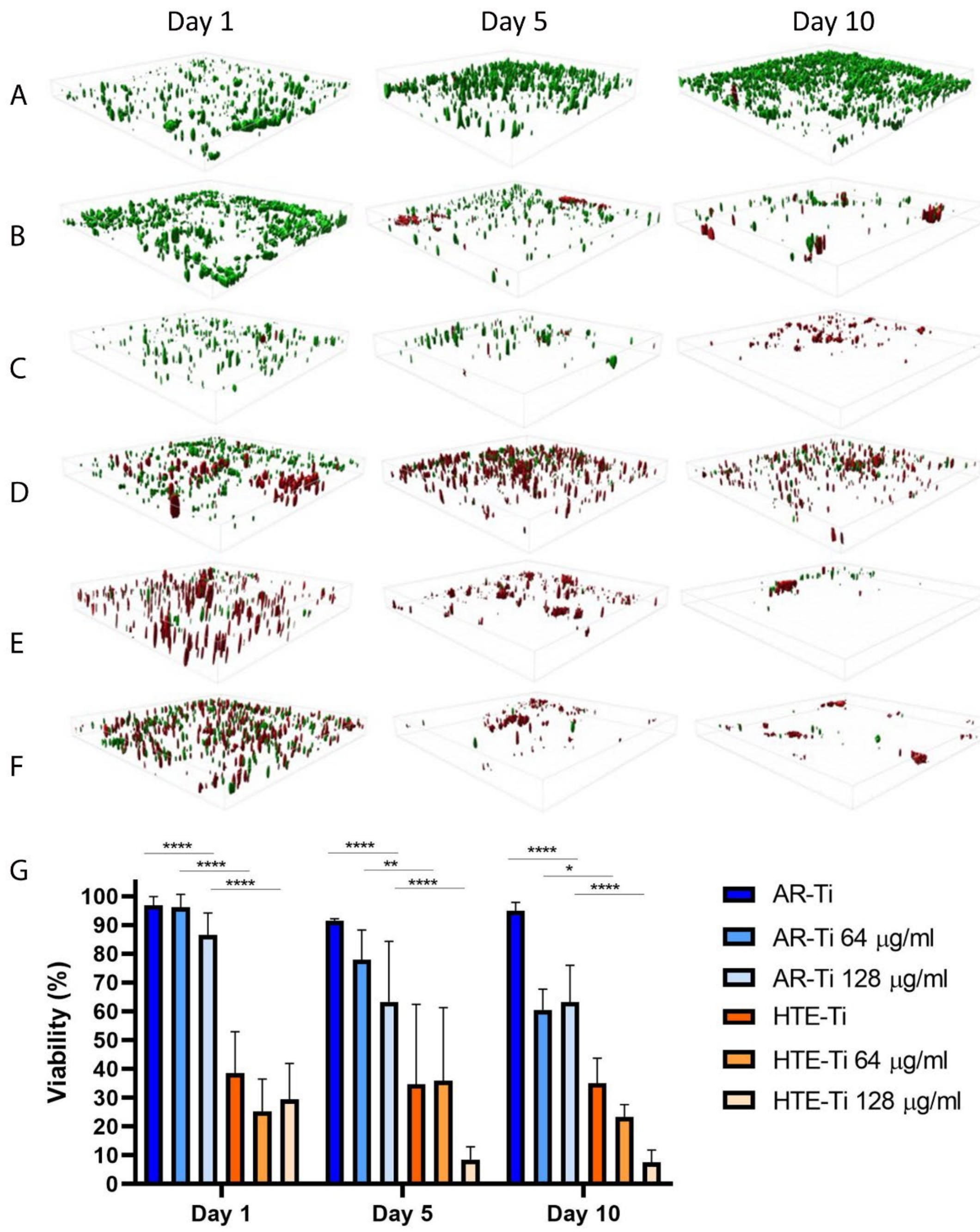

Figure S5. Azithromycin treatment of pre-established *P. gingivalis* on HTE-Ti. (A) AR-Ti with no azithromycin, (B) AR-Ti with 64 μg/mL, (C) AR-Ti with 128 μg/mL. (D) HTE-Ti with no azithromycin, (E) HTE-Ti with 64 μg/mL, (F) HTE-Ti with 128 μg/mL. (G) Viabilities of *P. gingivalis* treated with azithromycin over 10 days.

Figure S6 shows the full set of statistical analyses for the azithromycin treatment assay using *P. gingivalis*.

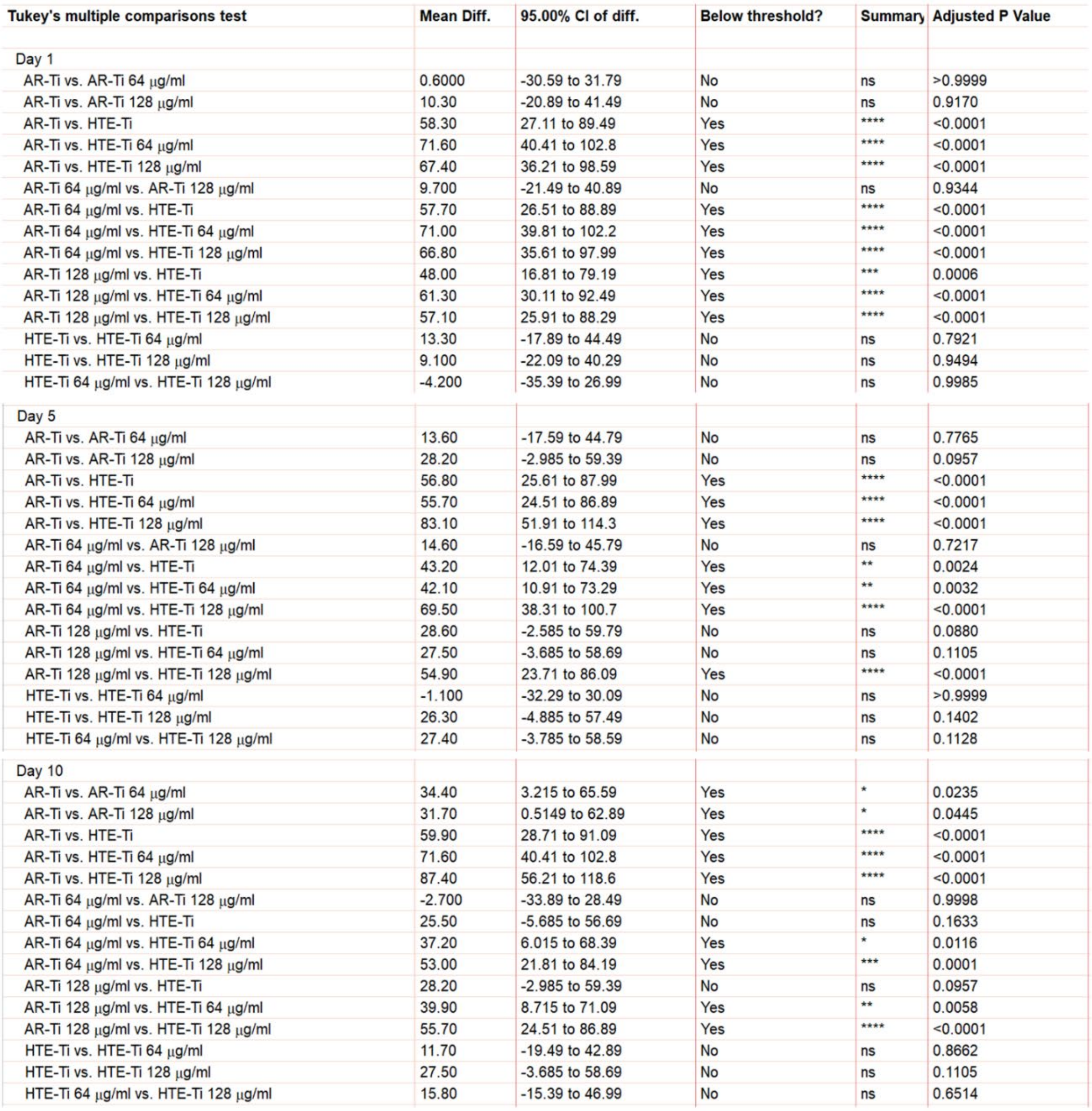

Tukey's multiple comparisons test	Mean Diff.	95.00% CI of diff.	Below threshold?	Summary	Adjusted P Value
Day 1					
AR-Ti vs. AR-Ti 64 µg/ml	0.6000	-30.59 to 31.79	No	ns	>0.9999
AR-Ti vs. AR-Ti 128 µg/ml	10.30	-20.89 to 41.49	No	ns	0.9170
AR-Ti vs. HTE-Ti	58.30	27.11 to 89.49	Yes	****	<0.0001
AR-Ti vs. HTE-Ti 64 µg/ml	71.60	40.41 to 102.8	Yes	****	<0.0001
AR-Ti vs. HTE-Ti 128 µg/ml	67.40	36.21 to 98.59	Yes	****	<0.0001
AR-Ti 64 µg/ml vs. AR-Ti 128 µg/ml	9.700	-21.49 to 40.89	No	ns	0.9344
AR-Ti 64 µg/ml vs. HTE-Ti	57.70	26.51 to 88.89	Yes	****	<0.0001
AR-Ti 64 µg/ml vs. HTE-Ti 64 µg/ml	71.00	39.81 to 102.2	Yes	****	<0.0001
AR-Ti 64 µg/ml vs. HTE-Ti 128 µg/ml	66.80	35.61 to 97.99	Yes	****	<0.0001
AR-Ti 128 µg/ml vs. HTE-Ti	48.00	16.81 to 79.19	Yes	***	0.0006
AR-Ti 128 µg/ml vs. HTE-Ti 64 µg/ml	61.30	30.11 to 92.49	Yes	****	<0.0001
AR-Ti 128 µg/ml vs. HTE-Ti 128 µg/ml	57.10	25.91 to 88.29	Yes	****	<0.0001
HTE-Ti vs. HTE-Ti 64 µg/ml	13.30	-17.89 to 44.49	No	ns	0.7921
HTE-Ti vs. HTE-Ti 128 µg/ml	9.100	-22.09 to 40.29	No	ns	0.9494
HTE-Ti 64 µg/ml vs. HTE-Ti 128 µg/ml	-4.200	-35.39 to 26.99	No	ns	0.9985
Day 5					
AR-Ti vs. AR-Ti 64 µg/ml	13.60	-17.59 to 44.79	No	ns	0.7765
AR-Ti vs. AR-Ti 128 µg/ml	28.20	-2.985 to 59.39	No	ns	0.0957
AR-Ti vs. HTE-Ti	56.80	25.61 to 87.99	Yes	****	<0.0001
AR-Ti vs. HTE-Ti 64 µg/ml	55.70	24.51 to 86.89	Yes	****	<0.0001
AR-Ti vs. HTE-Ti 128 µg/ml	83.10	51.91 to 114.3	Yes	****	<0.0001
AR-Ti 64 µg/ml vs. AR-Ti 128 µg/ml	14.60	-16.59 to 45.79	No	ns	0.7217
AR-Ti 64 µg/ml vs. HTE-Ti	43.20	12.01 to 74.39	Yes	**	0.0024
AR-Ti 64 µg/ml vs. HTE-Ti 64 µg/ml	42.10	10.91 to 73.29	Yes	**	0.0032
AR-Ti 64 µg/ml vs. HTE-Ti 128 µg/ml	69.50	38.31 to 100.7	Yes	****	<0.0001
AR-Ti 128 µg/ml vs. HTE-Ti	28.60	-2.585 to 59.79	No	ns	0.0880
AR-Ti 128 µg/ml vs. HTE-Ti 64 µg/ml	27.50	-3.685 to 58.69	No	ns	0.1105
AR-Ti 128 µg/ml vs. HTE-Ti 128 µg/ml	54.90	23.71 to 86.09	Yes	****	<0.0001
HTE-Ti vs. HTE-Ti 64 µg/ml	-1.100	-32.29 to 30.09	No	ns	>0.9999
HTE-Ti vs. HTE-Ti 128 µg/ml	26.30	-4.885 to 57.49	No	ns	0.1402
HTE-Ti 64 µg/ml vs. HTE-Ti 128 µg/ml	27.40	-3.785 to 58.59	No	ns	0.1128
Day 10					
AR-Ti vs. AR-Ti 64 µg/ml	34.40	3.215 to 65.59	Yes	*	0.0235
AR-Ti vs. AR-Ti 128 µg/ml	31.70	0.5149 to 62.89	Yes	*	0.0445
AR-Ti vs. HTE-Ti	59.90	28.71 to 91.09	Yes	****	<0.0001
AR-Ti vs. HTE-Ti 64 µg/ml	71.60	40.41 to 102.8	Yes	****	<0.0001
AR-Ti vs. HTE-Ti 128 µg/ml	87.40	56.21 to 118.6	Yes	****	<0.0001
AR-Ti 64 µg/ml vs. AR-Ti 128 µg/ml	-2.700	-33.89 to 28.49	No	ns	0.9998
AR-Ti 64 µg/ml vs. HTE-Ti	25.50	-5.685 to 56.69	No	ns	0.1633
AR-Ti 64 µg/ml vs. HTE-Ti 64 µg/ml	37.20	6.015 to 68.39	Yes	*	0.0116
AR-Ti 64 µg/ml vs. HTE-Ti 128 µg/ml	53.00	21.81 to 84.19	Yes	***	0.0001
AR-Ti 128 µg/ml vs. HTE-Ti	28.20	-2.985 to 59.39	No	ns	0.0957
AR-Ti 128 µg/ml vs. HTE-Ti 64 µg/ml	39.90	8.715 to 71.09	Yes	**	0.0058
AR-Ti 128 µg/ml vs. HTE-Ti 128 µg/ml	55.70	24.51 to 86.89	Yes	****	<0.0001
HTE-Ti vs. HTE-Ti 64 µg/ml	11.70	-19.49 to 42.89	No	ns	0.8662
HTE-Ti vs. HTE-Ti 128 µg/ml	27.50	-3.685 to 58.69	No	ns	0.1105
HTE-Ti 64 µg/ml vs. HTE-Ti 128 µg/ml	15.80	-15.39 to 46.99	No	ns	0.6514

Figure S6. Two-Way ANOVA of *P. gingivalis* azithromycin treatment assay on HTE-Ti

CHAPTER 3:

DUAL SPECIES BACTERIAL CHALLENGE OF A BIOMIMETIC NANOSTRUCTURED SURFACE

Andrew Hayles[1,2], Richard Bright[1,2], Jafar Hasan[1], Jonathan Wood[1], Dennis Palms[1,2], Dan Barker[3], Krasimir Vasilev[2*]

1 Academic Unit of STEM, University of South Australia, Mawson Lakes, Adelaide, 5095, South Australia, Australia.

2 College of Medicine and Public Health, Flinders, University, Bedford Park 5042, South Australia, Australia

3 Corin Australia, Sydney, NSW 2153, Australia

(* Corresponding author: Krasimir.vasilev@flinders.edu.au)

Published in Advanced Materials Interfaces, vol. 9, issue 32, 14th November 2022

https://doi.org/10.1002/admi.202201583

Abstract

An ever-present risk of medical device associated infection has driven a significant body of research towards development of novel anti-infective materials. Surfaces bearing sharp nanostructures are an emerging technology to address this concern. The in vitro efficacy of antimicrobial nanostructures has previously been verified using single species cultures, but there remains a paucity of data to address the threat of multi-species infections. Polymicrobial infections are a concerning threat because they can complicate treatment, promote drug resistance, and harshen patient prognosis. In the present study we employed dual-species cultures to challenge the mechano-bactericidal properties of nanostructured surfaces. We used Escherichia coli with either *Staphylococcus aureus* or *Enterococcus faecalis* due to their clinical relevance in implant associated infection. Despite the presence of multiple species, we found a high rate of bactericidal activity. Interestingly, in the mixed culture containing *Escherichia coli* with *Enterococcus faecalis*, the nanostructured surface triggered a shift in species distribution to favour Enterococcus faecalis. Overall, this study highlights the potential for mechano-bactericidal surfaces to minimize the burden of multi-species bacterial infection. It also serves as an enticing foundation for further research into more complex biointerfacial interactions.

1. Introduction

There is an increasing global demand for biomedical implants to remedy the various health issues associated with an aging population. Despite decades worth of improvements and innovations in biomedical engineering, there continues to be an ever-present threat of implant-associated infection

(IAI) [1]. The occurrence of IAI is predominately triggered during surgery, when bacteria from the surgical site transfer to the implant surface and initiate a sequence of attachment, proliferation and maturation [2]. This sequence leads to the establishment of a biofilm, which is characterized by an aggregation of bacterial cells attached to the implant surface and embedded in a matrix of extracellular polymeric substance (EPS) [3]. The biofilm state affords bacteria an improved ability to avoid clearance by the host immune system and antibacterial drugs [4]. It is well established that bacterial biofilms enhance antibiotic resistance by up to 1000-fold [5], and in most cases, antibiotics alone are insufficient to eliminate IAI [6].

Further, complications arise when multiple pathogenic species co-aggregate, as biofilm formation can be enhanced depending on the species composition [7]. This is concerning because polymicrobial infections account for a considerable proportion of IAI. For example, approximately 15-19% of orthopaedic implant infections involve more than one pathogenic species [2, 8]. *Staphylococcus aureus* is the most common pathogen identified in IAI [9], among other culprits such as *Pseudomonas aeruginosa*, *Escherichia coli*, *Enterococcus faecalis*, *Klebsiella pneumoniae* and *Candida albicans*, among others [8b].

Mixed species biofilms can also promote the emergence of drug resistant bacteria, as biofilm-associated cells share genetic elements through horizontal gene transfer.[10] Beyond this, cross-species interactions can benefit one or more species within the composition by mitigating unfavourable environmental conditions [11]. An example of this is seen during infection, when the host limits iron availability as a defence mechanism [12]. When *E. faecalis* is co-localized with Escherichia coli, these iron limiting conditions trigger *E. faecalis* to induce the upregulation of siderophore biosynthesis by *E. coli*, enhancing its iron uptake, and supporting it to overcome the host defence mechanism [13]. This seemingly altruistic behaviour of *E. faecalis* may ultimately cycle back to a realized benefit for itself if the *E. coli* isolate in the composition is carbapenemase-producing, as *E. faecalis* benefits from the presence of this drug resistance enzyme [14]. These mutually beneficial interactions lead to a concerning outcome, as co-infections of *E. faecalis* and *E. coli* have been shown to be significantly more virulent than their single-species counterparts [15].

Within the bioengineering and biomaterials fields there has been considerable focus on developing infection-resistant surface modifications for implant applications to minimize the rate of IAI, utilizing varying strategies. For instance, surfaces have been functionalized with antimicrobial peptides, antifouling compounds, or inherently antibacterial metals [16]. An enticing alternative strategy involves fabrication of nanoscale protrusions, or nanostructures, which passively kill bacteria on contact by inducing lethal membrane stretching and subsequent cell rupture [17]. These surfaces are often referred to as ‘mechano-bactericidal’ [18] and their efficacy has been well established against Gram-positive and Gram-negative bacteria inoculated as single species cultures [19] as well as against the pathogenic fungus *Candida albicans* [20].

Despite the growing wealth of literature focusing on mechano-bactericidal surfaces, there has been relatively little attention on how cross-species interaction might influence the bactericidal efficacy of such surfaces. In a previous study, we investigated the efficacy of a hydrothermally etched titanium surface against a dual-species inoculation of the dental pathogens *Fusobacterium nucleatum* and *Porphyromonas gingivalis* [21]. In the present study, we aim to investigate the efficacy of the antimicrobial nanostructured titanium surface against bacterial compositions involving species typically associated with hospital acquired and implant associated infections, namely *E. coli*, *S. aureus* and *E. faecalis* [22].

2. Results and Discussion

2.2 Surface Topographical and Chemical Characterization

To characterize the change in surface parameters induced by hydrothermal etching, hydrothermally etched titanium (HTE-Ti) and as-received titanium (AR-Ti) samples were imaged by high magnification scanning electron microscopy (SEM; Figures 1 A and B). The AR-Ti samples appeared mostly smooth at the micro scale, with occasional pits and scratches observed, likely resulting from the machining and polishing process. Contrasting this, the HTE-Ti surface was observed to have a total coverage of disordered, randomly oriented nanoscale protrusions which bore resemblance to the nanoscale topography of the dragonfly wing [23]. The nanoscale protrusions measured at a mean height of 348 ± 152 nm, and the diameter measured at 98 ± 60 nm. The mean spacing between nanoscale protrusions was measured at 437 ± 46 nm, which equates to a density of approximately 5 protrusions per μm^2, and this value is consistent with previously reported measurements for KOH-based titanium nanostructures [24]. Structures with comparable dimensions have previously been shown to be effective at eliminating *S. aureus* and *P. aeruginosa* with seeding densities up to 105 and 10^6 cfu/mL, respectively [19b, 25]. Atomic force microscopy (AFM) analysis supported the topography observed by SEM imaging, as machining marks were present on the otherwise smooth AR-Ti, while nanoscale protrusions were clearly visualised on the HTE-Ti surface. The nanoscale roughness (Ra) of the AR-Ti and HTE-Ti surfaces was determined from 5x5 μm AFM scans, which measured 42 nm on the AR-Ti and 175 nm on the HTE-Ti surface. Height profiles for the two surfaces were generated using optical profilometry (128x128 μm scan size), which revealed micron scale height variations on the AR-Ti surface (likely resulting from the polishing process), and high frequency nanoscale height variations on the HTE-Ti, representing the nanostructures (Figures 1 F and G). The colour scale maps from which these measurements were derived are found in the supplementary information (Figure S1)

There was a significant decrease in the water contact angle associated with the HTE-Ti surface, indicating improved hydrophilicity. This is a beneficial trait for implantable biomaterials, as the improved hydrophilicity facilitates protein adsorption and subsequent osseointegration [26]. The enhanced roughness of the HTE-Ti surface is a beneficial property for biomaterials which integrate into bone, as rough surface topography provides a suitable substrate for bone on-growth and osteoblast differentiation [27]. To characterize the atomic composition of the nanostructured surface, energy-dispersive X-ray spectroscopy (EDS) analysis was performed on both the AR-Ti and HTE-Ti surfaces. The atomic composition measured on the AR-Ti surface confirmed the presence of alloying elements (aluminium and vanadium) of a typical grade-5 Ti6Al4V alloy (Figure 1 J). Following hydrothermal etching, we observed an increase in the presence of oxygen, which is attributable to a thickening of the surface oxide layer (Figure 1 K) [28]. We also observed a minor presence of potassium after hydrothermal etching, which is expected due to the use of KOH as the alkaline etchant [29].

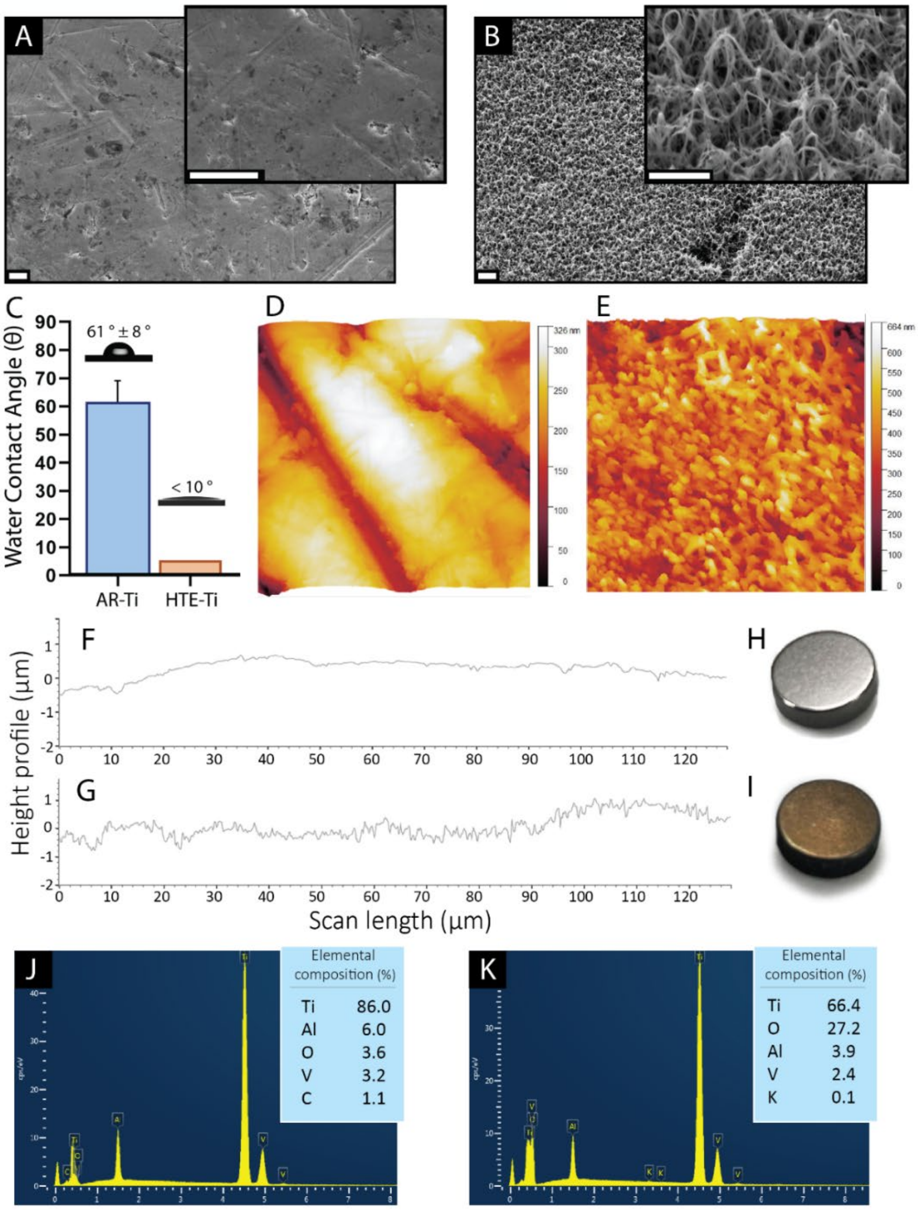

Figure 1. Topographical and chemical characterization of HTE-Ti. High magnification SEM images of AR-Ti (A) and HTE-Ti (B). Water contact angle measured on both AR-Ti and HTE-Ti samples (C). AFM images of AR-Ti (D) and HTE-Ti (E) captured with a scanning size of 5x5 µm. Height profiles of AR-Ti (F) and HTE-Ti (G) generated using surface profilometry. Photographs of titanium coupons prior to (H) and following HTE treatment (I). EDS spectra of AR-Ti (J) and HTE-Ti (K).

Scale bars of SEM images are 1 µm. The HTE-Ti inset SEM image is from a 45° tilted perspective, to better capture the geometry of the nanostructures.

To assess the bactericidal efficacy of HTE-Ti against polymicrobial challenges, two different mixed culture models were investigated. Both mixed culture models were designed to consist of a mixture of both Gram-positive and Gram-negative species which have been clinically reported to co-colonize medical implants [30]. The two mixed cultures were *E. coli* combined with *S. aureus* (Figures 2 and 3), and *E. coli* combined with *E. faecalis* (Figures 4 and 5).

2.3 *E. coli* and *S. aureus* (EcSa) Mixed Culture

Prior to investigating the efficacy of HTE-Ti against a mixed culture of *E. coli* and *S. aureus*, single species cultures were first analysed to determine a baseline bactericidal efficacy of the surface. *S. aureus* on the HTE-Ti surface was observed to have a viability of 34.0 ± 4.4 %, compared to 94.4 ± 0.1 % on the control AR-Ti surface ($P < 0.0001$, Figure 2 D). Further, the colony forming units (cfu) of *S. aureus* on the HTE-Ti surface decreased by 2 logarithms, and its biovolume was reduced from 7.81 x 10^6 to 1.15 x10^5 $\mu m^3/mm^2$ ($P < 0.0001$, Figures 2 F and E, respectively). These values closely match the single species HTE-Ti bactericidal efficacy reported previously [19a, 19b]. Similarly, when *E. coli* was incubated on the HTE-Ti surface, its viability was measured at 26.8 ± 10.9%, compared to 96.6 ± 0.4% on the AR-Ti surface ($P < 0.0001$). Additionally, *E. coli* saw a cfu reduction of 1.8 logarithms when incubated as a single species on the HTE-Ti surface. The biovolume of *E. coli* was reduced from 6.83 x 10^5 to 2.36 x 10^5 $\mu m^3/mm^2$ ($P < 0.0001$).

When *S. aureus* and *E. coli* were incubated as a mixed culture (EcSa), the viability measured on HTE-Ti was 24.2 ± 1.6%, while the same parameter was 90.5 ± 0.6% ($P < 0.0001$) on the AR-Ti control. Thus, the efficacy of HTE-Ti against EcSa is comparable to the efficacy against the species incubated individually. The high viability of the mixed EcSa culture on the AR-Ti surface is evidence that there were no overt antagonistic interactions between the two species. The SEM images on the HTE-Ti surface (Figure 2 C) revealed morphologically disturbed cells from both species in the EcSa study, where *E. coli* cells appeared flattened or deflated, and *S. aureus* appeared wrinkled and less turgid than their counterparts on the AR-Ti surface. Colony enumeration was also performed for the two species individually from the mixed EcSa culture (Figure 2 F). The logarithmic reduction in cfu count for *S. aureus*, incubated on HTE-Ti, was 1.8 in the mixed EcSa culture, which is comparable to the reduction observed for *S. aureus* incubated as a single species. Interestingly, the logarithmic cfu reduction for *E. coli*, incubated on HTE-Ti, was 2.6 in the mixed EcSa culture, compared to 1.8 when it was incubated as a single species culture ($P < 0.0001$). This is likely due to the poor adhesion of *E. coli* (single species) observed on the AR-Ti surface. This interpretation is supported by the 3D fluorescence biofilm reconstruction in Figure 2A, in which *E. coli* appears to form a sparser biomass compared to *S. aureus* on the AR-Ti surface. When the two species were combined, their biomass appeared much thicker than *E. coli* incubated as a single species, indicating that *S. aureus* was able to promote *E. coli* adhesion. As the mixed culture facilitated *E. coli* to better adhere to the AR-Ti surface, this explains the relatively higher cfu reduction of *E. coli* in the mixed culture compared to the single species culture.

Fluorescence in situ hybridization (FISH) analysis was performed to differentially stain the dual species in the EcSa mixed culture and map their spatial distribution throughout the biomass on both AR-Ti and HTE-Ti surfaces (Figures 3). The biomass was then divided into 3 layers along the Z-axis, to quantify the proportions of *S. aureus* and *E. coli* as a function of the distance from the cells to the titanium surface. In this case, the proportions of the two species in EcSa were approximately equal and their distribution was comparable throughout the biomass, regardless of which surface they were incubated on. This indicated that although the HTE-Ti surface did substantially reduce bacterial cell viability and biomass, it did not shift the species distribution away from an equally representative polymicrobial culture. These results were also supported by qualitative analysis using SEM (Figures 2 B and C), which revealed an approximately equal proportion of *E. coli* and *S. aureus* cells.

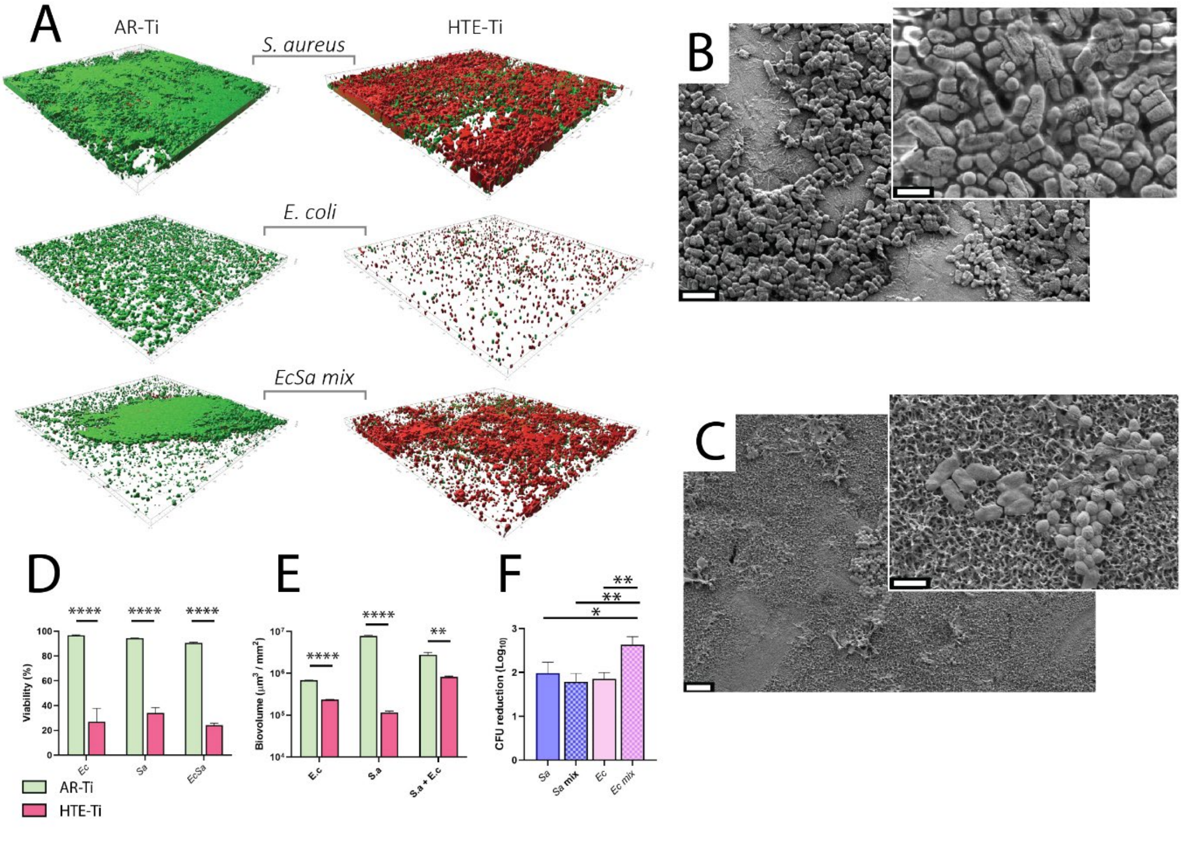

Figure 2. The viability of *E. coli* and *S. aureus* on HTE-Ti. 3D fluorescence reconstruction of single and mixed species bacteria stained with Live/Dead fluorescence viability kit (A). SEM images showing mixed species *E. coli* with *S. aureus* on AR-Ti (B) and HTE-Ti (C). Quantification of fluorescence-based viability (D) and biovolume (E) of single and mixed species cultures. Log reduction of cfu counts for both species as either single or mixed culture (F). * P < 0.05,** P < 0.01, *** P < 0.001, **** P < 0.0001, Mean ± SD, n = 3

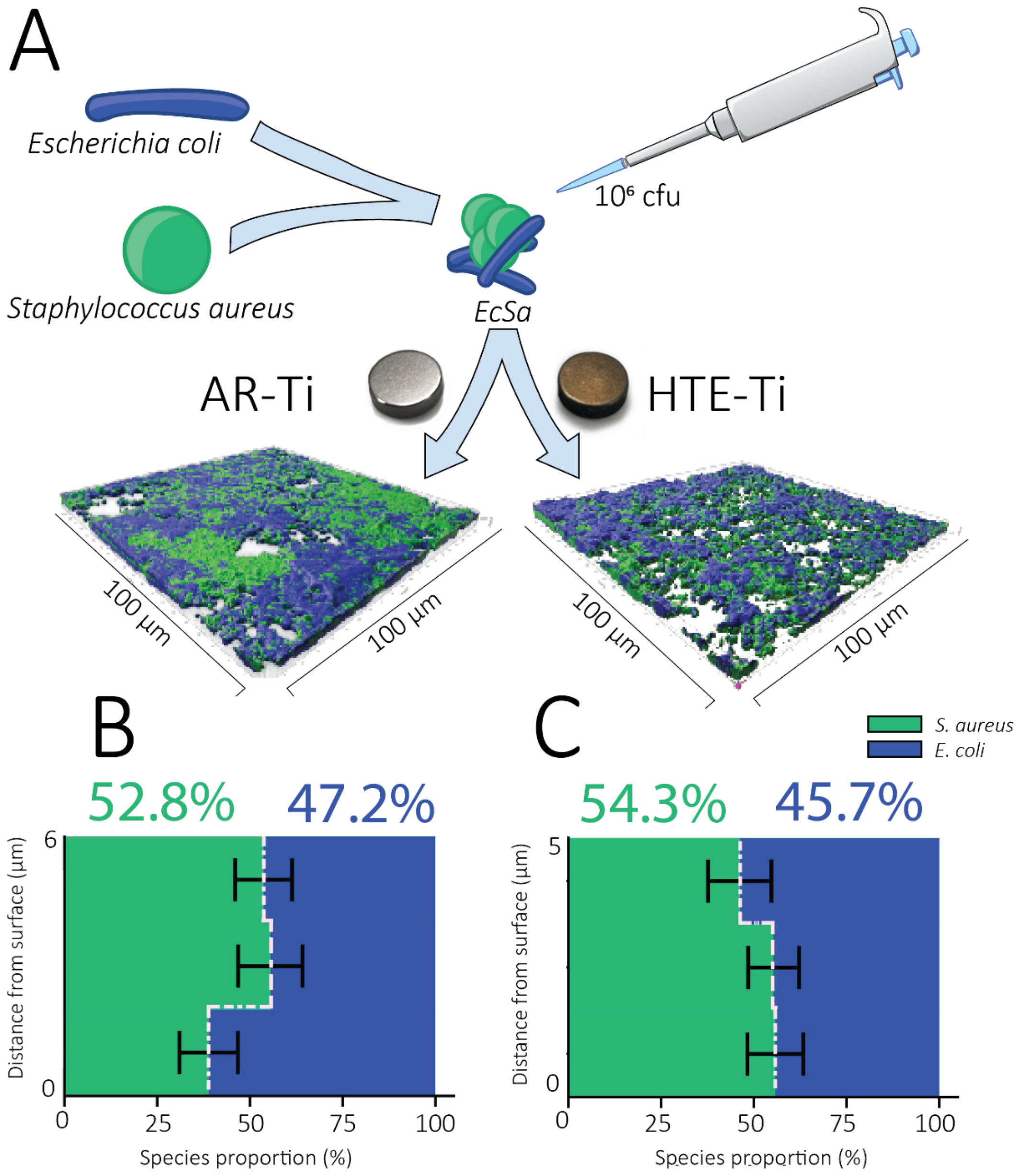

Figure 3. Species distribution of *E. coli* and *S. aureus* generated by FISH. A schematic of the inoculation process (A). Quantification of *E. coli* and *S. aureus* species distribution throughout the biovolume measured on AR-Ti (B) and HTE-Ti (C). The entire biovolume of each sample was divided into 3 segments along the Z-axis and species proportions were determined by the relative intensity of each species-specific fluorescent probe.

2.4 *E. coli* and *E. faecalis* (EcEF) Mixed Culture

In the second mixed culture study, we incubated *E. faecalis* as a single species culture, as well as in a mixed culture with *E. coli* (Figure 4). The fluorescence-based viability results were similar to that observed with EcSa. On the HTE-Ti surface, *E. faecalis* incubated as a single species culture had a viability of 29.8 ± 7.1%, while on the AR-Ti surface it was measured at 89.9 ± 1.3% ($P < 0.0001$). The biovolume of *E. faecalis* was reduced from 6.46 x 10^6 to 3.06 x 106 $\mu m^3/mm^2$ ($P < 0.05$), and its cfu quantity was reduced by 0.6 logarithms. When *E. faecalis* was combined with *E. coli* in a mixed culture (EfEc), its viability was observed to be 22.3 ± 3.9% on the HTE-Ti surface, and 92.9 ± 3.1% on the AR-Ti surface ($P < 0.0001$). The cfu counts of the two species in mixed culture were individually measured, and both species were observed to have their cfu quantities reduced by 0.2 logarithms on the HTE-Ti surface. As *E. coli* and *E. faecalis* both had higher logarithmic reductions when incubated as single species cultures compared to the mixed species culture, suggesting that the EcEf combination is more resilient than either species individually.

FISH analysis was also performed to observe the spatial distribution of the two individual species within the biomass on the HTE-Ti and AR-Ti surfaces (Figure 5). Interestingly, incubation on the HTE-Ti surface caused a shift in the species distribution and cell arrangement. Whereas *E. faecalis* occupied 54.8% of the bacterial biomass on AR-Ti, it occupied 79.1% of the biomass on HTE-Ti. Further, the shift in species distribution was most prominent in the areas of biomass in close contact with the nanostructured surface. This suggests that *E. faecalis* is more resilient than *E. coli* to the mechano-bactericidal effect of the nanostructured HTE-Ti surface and will therefore occupy more of the interface, while *E. coli* preferentially proliferated in the biomass not in direct contact with the surface.

The results of the present study are encouraging for multiple reasons. Firstly, it is reassuring to observe that the colonisation of pathogenic polymicrobial cultures can be effectively inhibited by the HTE-Ti surface. Secondly, depending on the species composition, HTE-Ti may be effective at reducing the species diversity in a polymicrobial culture, potentially allowing conventional drugs to more easily clear the remaining bacteria. This was most evident when using the EcEf mixed culture, as *E. faecalis* was able to occupy most of the surface area on the nanostructured titanium sample, outcompeting *E. coli* and reducing its overall presence. However, this was not the case when *S. aureus* was used instead of *E. faecalis*. As both *E. faecalis* and *S. aureus* are Gram-positive cocci, the differing outcomes of EcSa and EcEf are interesting. On one hand, both Gram-positive species have a rigid peptidoglycan layer which grants them a degree of resilience against the nanostructured surface, and this is reflected in their comparable viability when incubated as single species cultures (approximately 30% as observed in this study). Based on these observations, it would be logical to presume that they would occupy a similar surface area when each are co-incubated with *E. coli*. As this was not the case, factors other than cell rigidity must be at play. Perhaps one important and relevant difference between *E. faecalis* and *S. aureus* is their mode of cell division. *S. aureus* has 3 planes of division, and therefore dividing cells tend to form a cluster expanding through all dimensions [17a, 31]. Thus, there may be more opportunity for *E. coli* to establish itself on the titanium surface when it is competing with *S. aureus*, as *S. aureus* will readily proliferate vertically, leaving more room on the surface for *E. coli*. In contrast, *E. faecalis* divides along a single plane of division, which results in chains of cells expanding in one dimension. As *E. faecalis* only divides along one dimension, it must expand laterally across the surface, and therefore *E. faecalis* represents a stronger competition for surface area. Although *E. coli* also divides along one dimension, its structure is comparatively delicate due to its Gram-negative nature, and this may be a key factor which causes it to lose the battle for surface area with *E. faecalis*. Further, *E. coli* cells are approximately twice the length of *E. faecalis*, which ensures they interact with approximately twice the number of nanostructure tips, incurring a greater amount of membrane stress.

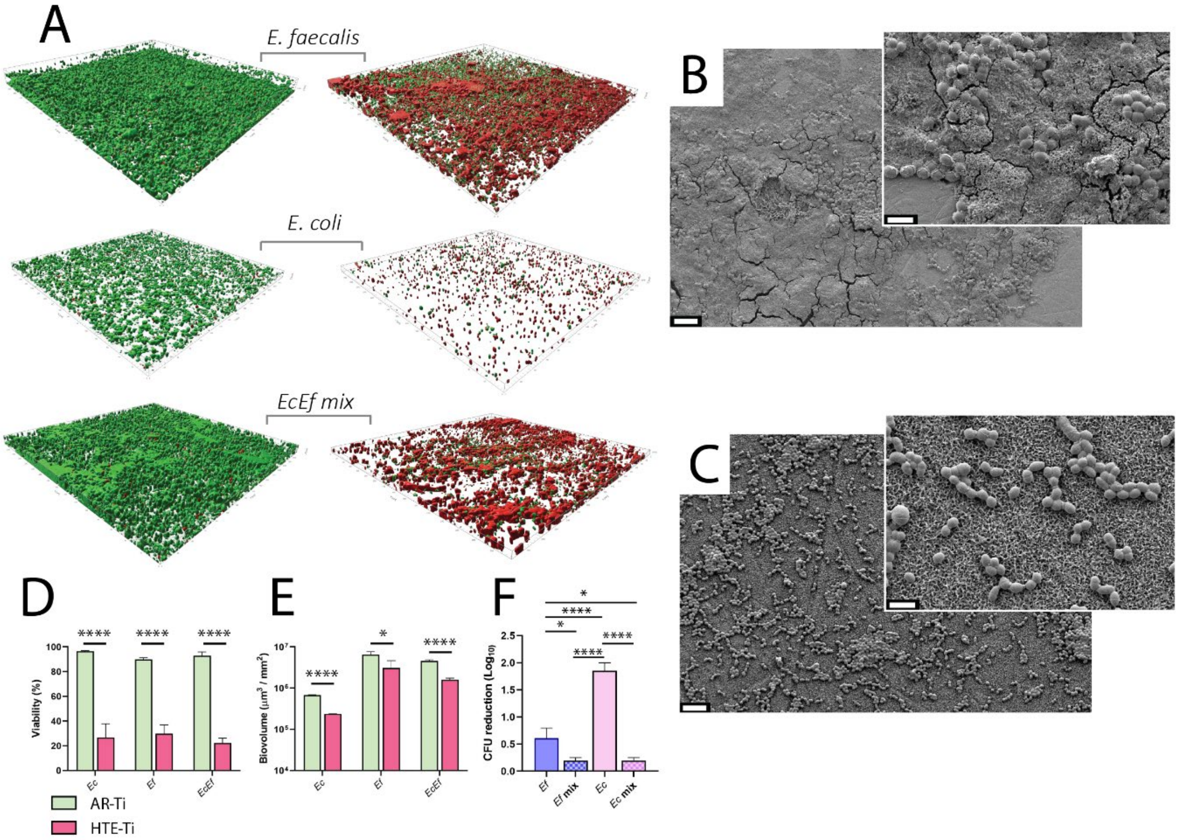

Figure 4. The viability of *E. coli* and *E. faecalis* on HTE-Ti. 3D fluorescence models of single and mixed species bacteria stained with Live/Dead fluorescence viability kit (A). SEM images showing mixed species *E. coli* with *E. faecalis* on AR-Ti (B) and HTE-Ti (C). Quantification of fluorescence-based viability (D) and biovolume (E) of single and mixed species cultures. Log reduction of cfu counts for both species as either single or mixed culture (F). * $P < 0.05$,** $P < 0.01$, *** $P < 0.001$, **** $P < 0.0001$, Mean ± SD, n = 3

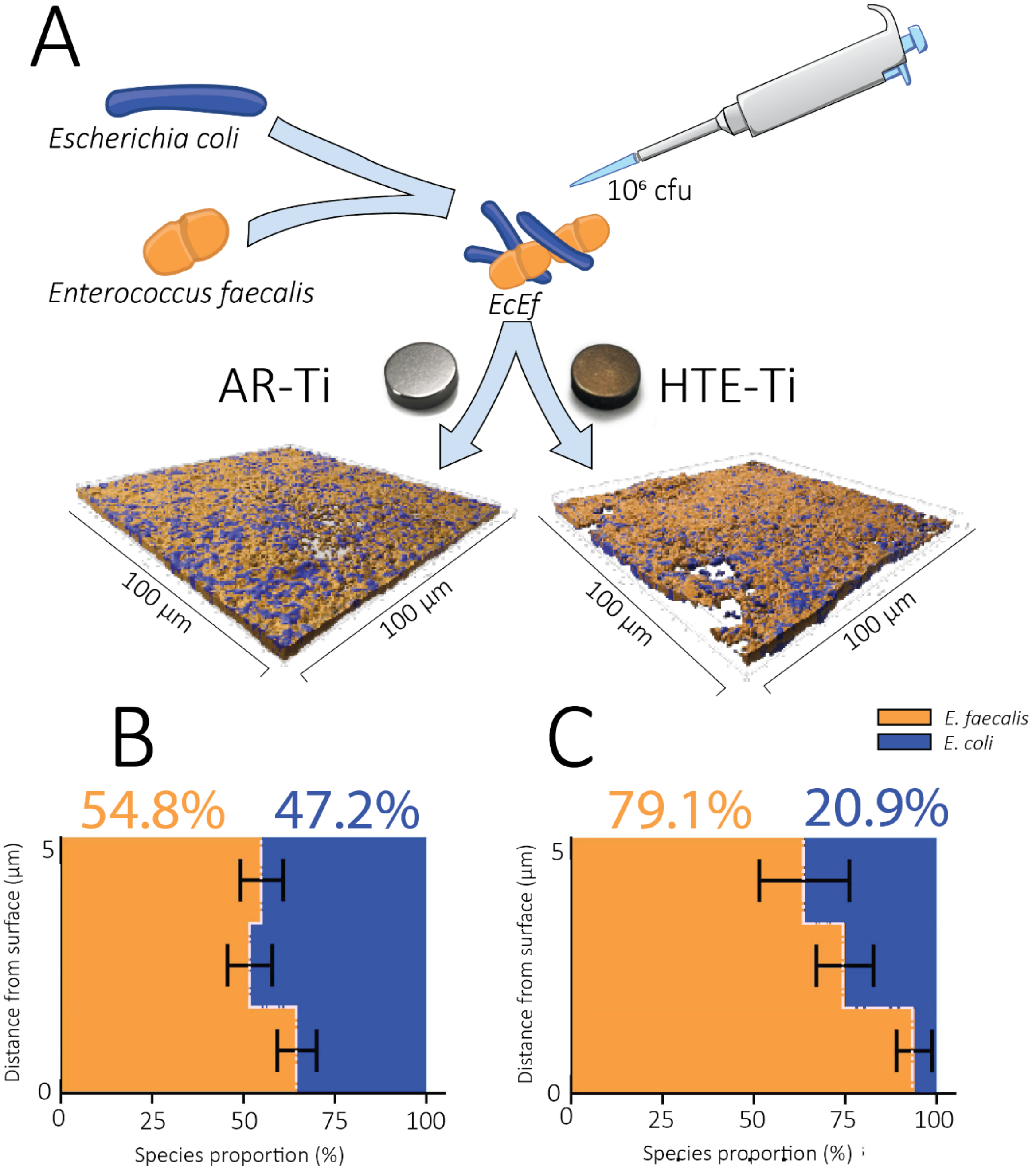

Figure 5. Species distribution of *E. coli* and *E. faecalis* generated by FISH. A schematic of the inoculation process (A). Quantification of *E. coli* and *E. faecalis* species distribution throughout the biovolume measured on AR-Ti (B) and HTE-Ti (C). The entire biovolume of each sample was divided into 3 segments along the Z-axis and species proportions were determined by the relative intensity of each species-specific fluorescent probe.

Despite decades of research into novel materials and surgical practices, implant infection remains a difficult problem to overcome. In an effort to improve the situation, considerable research has been focused on development of materials which can both promote osteogenesis and resist bacterial colonization. Over the last few years, many researchers have directed their attention toward bioinspired nanoscale surface topographies resembling those found on the wings of insects such as the dragonfly and cicada [17a, 19b, 19c, 32]. The benefit of such nanoscale surface modifications is two-fold. Firstly, the surface roughness introduced by topography modification can facilitate an enhanced osteointegration as reported for endosseous implants [27a]. Secondly, nanoscale protrusions with appropriate dimensions and shapes have been shown to effectively inhibit microbial growth, either through direct contact killing or inhibition of biofilm formation. While this is highly encouraging, most studies on antibacterial materials only focus on single species cultures. This is problematic because a sizeable proportion of IAI cases involve more than one species, with estimates of polymicrobial infection occurring in 15-19% of prosthetic joint infection cases [8]. Polymicrobial infections represent a novel threat for multiple reasons. For instance, multi-species bacterial infections can promote cross-species horizontal gene transfer of antibiotic resistance genes, accelerating the emergence of “superbugs” [33]. In addition, the presence of more than one species of pathogen may lead to interactions which can unilaterally or mutually enhance cell attachment, biofilm formation, and metabolism [34].

In the present study, we have demonstrated that HTE-Ti may help reduce the burden of polymicrobial infections. We have shown that HTE-Ti is able to reduce the viability of EcSa and EcEf down to approximately 20%. Beyond this, we have shown that the species distribution of EcEf shifts towards predominately *E. faecalis* when incubated on the HTE-Ti surface, while no shifts in species distribution were noted with EcSa. As antimicrobial therapy is complicated by the presence of multi-species infection, HTE-Ti may help to mitigate this issue by reducing species diversity and inhibiting viability of the remaining bacteria, thus limiting horizontal gene transfer. Without a doubt, these in vitro results are encouraging, and they lay a foundation for further investigation. More complex in vitro models, including more the two bacterial species, should be developed and supported by in vivo experiments to fully understand the true capacity of such nanostructured surfaces to stop polymicrobial infections.

3. Conclusion

In the present paper, we have built on previous findings regarding the efficacy of antimicrobial nanostructured surfaces by expanding beyond the typical single species culture assays and into a multi-species mode of investigation. As drug resistance genes are shared across species, polymicrobial infections threaten to accelerate the global decline in antibiotic efficacy. Hence, their threat is not just toward the individual patient, but extends throughout the entire of society. Our study employed two dual-species cultures involving *E. coli* with *S. aureus* and *E. coli* with *E. faecalis*. Our results suggest that in some cases, when multiple species are present on a mechano-bactericidal surface, species diversity is minimized by the disparate bactericidal effect against different species. The effect of this is multi-factorial, as a reduction in species diversity may limit the occurrence of horizontal gene transfer of drug resistance genes, as well as simplify drug therapy by reducing the need for broad-spectrum antibiotics.

4. Materials and Methods

4.1. Fabrication of Titanium Nanostructures

As-received (AR-Ti) polished Ti6Al4V coupons, with 10 mm diameter and 3 mm thickness were obtained by Hamagawa Industrial SDN BHD (Kedah, Malaysia). The AR-Ti samples were treated with a hydrothermal etching process previously described [19b, 21]. Briefly, samples were immersed in 1M KOH, sealed in a cylindrical steel vessel, and heated to 150 °C for 5 h, rinsed in ultrapure water, and then annealed for 5 h.

4.2. Surface Characterization of Titanium Nanostructures

Dimensions of protrusions present on HTE-Ti samples was measured using high magnification images obtained on an SEM (Zeiss Merlin FEG-SEM, Jena, Germany) using a 45° stage tilt. SEM images were imported into ImageJ v1.53 (NIH, USA) for measurements. The EDS spectra were obtained on the AR-Ti and HTE-Ti surfaces at 15 kV using X-ray spectrometer (AZtec v3.1, Oxford Instruments, MA, USA) interfaced with the SEM. AFM measurements were performed in air using a Bruker Dimension Icon. An NT-MDT NSG03 silicon nitride cantilever with a conical tip quoted by the manufacturer with a radius under 10 nm and a half side angle of 18° was used in PeakForce mode on the HTE-Ti surface. Initial calibration of the cantilever on a glass microscope slide derived a normal spring constant of 2.0 N m^{-1} and a deflection sensitivity of 94.4 nm V^{-1}. PeakForce amplitude over a 5 μm^2 image was set at 150 nm with a frequency of 2 kHz, a lift height of 34 nm, and a scan rate of 8.84 µm s–1. Roughness values were calculated through Gwyddion data analysis software v2.54. Surface wettability was measured by the sessile contact angle using a goniometer RD-SDM02 (RD Support, UK). Surface profilometry was measured using an Olympus 3D measuring Laser Microscope (OLS5000, LEXT) with a dedicated objective of 100× lens over several scanning areas of 128×128 µm on AR-Ti and HTE-Ti surfaces.

4.3. Cultures and Conditions

E. coli (ATCC 11303), Staphylococcus aureus (ATCC 25923) and *E. faecalis* (ATCC 29212) were retrieved from glycerol stocks stored at -80 °C, plated onto Tryptone Soy Agar (TSA; Oxoid, ThermoFisher, MA), and incubated overnight at 37 °C. Isolate colonies of each bacteria were separately inoculated into Tryptone Soy Broth (TSB; Oxoid, ThermoFisher, MA, USA) supplemented with 5% fetal bovine serum (FBS; Life Technologies California) and incubated overnight at 37 °C. Cell concentration was measured by absorbance at 600 nm, using a Nanodrop 2000 spectrophotometer (Thermo Scientific, MA, USA), and diluted to reach an optical density of 1 (approximately equal to 10^9 cfu/mL).

4.4. Inoculation of Titanium Samples

AR-Ti and HTE-Ti samples were aseptically placed in 24-well plates. Overnight cultures of *E. coli*, *E. faecalis* and *S. aureus* were further diluted to a final cell concentration of 10^6 cfu/mL in TSB +

FBS. 1 mL of bacterial cell suspension was transferred to AR-Ti and HTE-Ti samples, fully immersing them. For mixed bacterial cultures, *E. coli* and *S. aureus* or *E. coli* and *E. faecalis* were mixed at a 1:1 ratio of 10^6 cfu/mL. Samples were incubated at 37 °C for 18 h in a box with a damp paper towel to maintain humidity.

4.5. Live/Dead Analysis

Samples were transferred from the inoculation plate to a fresh 24-well plate, with each well containing 1 mL of BacLight Live/Dead (Invitrogen, ThermoFisher, MA, USA) prepared with equal proportions of Syto9 and Propidium Iodide to a final concentration of 1.5 µl / mL in phosphate-buffered saline (PBS). Samples were incubated in the dark at room temperature for 15 minutes and then immediately imaged with an Olympus FV3000 confocal laser scanning microscope (CLSM; Olympus, Tokyo). Excitation and emission spectra for PI was set to 490/635 nm, and for Syto9 they were set to 480/500 nm. 3-D vertically aligned fluorescence image stacks were acquired at random locations on each sample. 3-D fluorescence stacks were imported into Imaris 3-D analysis (version 9.3.0, Bitplane AG, Zürich, Switzerland)

4.6. Colony Enumeration

Samples were retrieved from the overnight incubation plate and gently rinsed in PBS (pH 7.4) to remove non-adhered cells. Samples were then individually transferred to 5 mL screwcap tubes filled with 1 mL PBS. Bacterial cells were detached from the samples using a 15 second vortex burst, sonication for 2 minutes, followed by a second vortex burst for 15 seconds. The resulting bacterial cell suspension was serially diluted in 10-fold increments down to a dilution factor of 10^7, and 10 µL drops from each dilution were plated in triplicate on TSA plates [35]. Colony counts were used to calculate the cell density present on the titanium samples, and the logarithmic difference in bacterial cell density was calculated using the formula $\log_{10}\left(\frac{CFU_{AR-Ti}}{CFU_{HTE-Ti}}\right)$,, where CFU_{AR-Ti}refers to the mean quantity of CFUs measured on the AR-Ti samples, and CFU_{HTE-Ti} is the corresponding measurement on HTE-Ti. To confirm that all cells were retrieved from titanium samples, SEM analysis was performed on titanium discs after sonication (Figure S2).

4.7. Bacterial Morphology by Scanning Electron Microscope (SEM)

Samples were retrieved from the overnight incubation plate and fixed for 2 h using 1.25% glutaraldehyde and 4% paraformaldehyde in PBS containing 4% sucrose. Samples were gently rinsed in PBS and dehydrated using increasing concentrations of ethanol (50, 70 and 100%) for 10 minutes each, followed by a 1:1 mixture of pure ethanol and hexamethyldisilazane (HMDS) for 20 minutes, and finally 100% HMDS for 20 minutes. Samples were air dried and mounted on aluminium SEM stubs using carbon tape, then sputter coated with 2 nm platinum. Samples were imaged using a Zeiss Merlin FEG-SEM.

4.8 Fluorescence in Situ Hybridization (FISH) Analysis

Mixed cultures of SaEc and EfEc were incubated on AR-Ti and HTE-Ti as previously described, for 18 hours. Samples were gently rinsed in PBS and then immersed in fixative solution (1.25% glutaraldehyde, 4% paraformaldehyde and 4% sucrose in PBS) for 3 hours. Fixative solution was removed and replaced with ice-cold PBS, and the PBS was replaced a further 2 times to remove residual fixative. Samples were dried at 46 °C until all moisture was evaporated. Samples were immersed in lysozyme (1mg/mL) for 10 minutes. The samples were then progressively dehydrated in ethanol in a series of increasing concentrations (50%, 80% and 100%, v/v) for 3 minutes each. The samples were dried again at 46 °C. Samples were immersed in hybridization buffer (composed of 900 mM NaCl, 20 mM Tris/HCl, 30% formamide (v/v), and 0.01% SDS, prepared in distilled H2O. Hybridization buffer was prepared with fluorophore-tagged oligonucleotides with sequences complementary to a 16S rDNA or rRNA region from each species (probe sequences are listed in supplementary information, Table S1), at a final concentration of 5 ng/µL. Samples were incubated in hybridization buffer for 5 hours at 46 °C. Samples were washed with pre-warmed wash buffer (composed of 112 mM NaCl, 20mM Tris/HCl, 5 mM EDTA, 0.01% SDS, prepared in distilled water). Washing was performed by gently dipping the samples into pre-warmed wash buffer for 5 seconds, then transferring each sample to a sterile 24-well plate containing 1 mL wash buffer in each well and incubating the samples at 46 °C for 15 minutes. Samples were then gently dipped into ice-cold distilled H2O for 3 seconds and then rapidly air dried with compressed air.

4.9. Species distribution imaging and quantification

Samples stained with FISH probes were inverted on a glass slide with a drop of mounting oil provided with the BacLight Live/Dead stain kit, and the glass slide was placed over the 40x objective in an Olympus FV3000 CLSM. Excitation and emission spectra were configured according to the fluorophores used for each of the 3 species (fluorophores and spectra listed in supplementary information, Table S1). 3-dimensional stacked fluorescence images were acquired at random locations on each sample. Stacked images were imported into Imaris 3D analysis software package and the spots analysis tool were used to quantify the differentially stained cells. The quantified spots were divided into 3 layers ascending on the z-axis, to capture the species proportions as a function of their distance from the nanostructured surface.

Acknowledgements

The authors acknowledge the funding and in-kind support from Corin Australia and the University of South Australia. The authors would also like to acknowledge the instruments and scientific and technical assistance of Microscopy Australia at the University of South Australia, Mawson Lakes Campus, a facility that is funded by the University, and State and Federal Governments. The authors would also like to acknowledge the South Australian node of the Australian National Fabrication Facility under the National Collaborative Research Infrastructure Strategy. K.V. thanks NHMRC for Fellowship GNT1194466 and ARC for grant DP180101254.

Supplementary information

Colour scale topography maps generated by laser microscopy (Figure S1), SEM images of titanium samples following sonication of bacterial cultures (Figure S2), Table of oligonucleotides used in FISH analysis (Table S1).

5. References

1. a) Kurtz, S. M., Lau, E. C., Son, M. S., Chang, E. T., Zimmerli, W.,Parvizi, J., *J Arthroplasty* **2018**, *33*: p. 3238; b) Parvizi, J., Gehrke, T.,Chen, A. F., *Bone Joint J* **2013**, *95-B*: p. 1450
2. Tande, A. J.,Patel, R., *Clin Microbiol Rev* **2014**, *27*: p. 302
3. Kumar, A., Alam, A., Rani, M., Ehtesham, N. Z.,Hasnain, S. E., *Int J Med Microbiol* **2017**, *307*: p. 481
4. Roilides, E., Simitsopoulou, M., Katragkou, A.,Walsh, T. J., *Microbiol Spectr* **2015**, *3*: p.
5. Olson, M. E., Ceri, H., Morck, D. W., Buret, A. G.,Read, R. R., *Can J Vet Res* **2002**, *66*: p. 86
6. a) Argenson, J. N., Arndt, M., Babis, G., Battenberg, A., Budhiparama, N., Catani, F., Chen, F., de Beaubien, B., Ebied, A., Esposito, S., Ferry, C., Flores, H., Giorgini, A., Hansen, E., Hernugrahanto, K. D., Hyonmin, C., Kim, T. K., Koh, I. J., Komnos, G., Lausmann, C., Loloi, J., Lora-Tamayo, J., Lumban-Gaol, I., Mahyudin, F., Mancheno-Losa, M., Marculescu, C., Marei, S., Martin, K. E., Meshram, P., Paprosky, W. G., Poultsides, L., Saxena, A., Schwechter, E., Shah, J., Shohat, N., Sierra, R. J., Soriano, A., Stefansdottir, A., Suleiman, L. I., Taylor, A., Triantafyllopoulos, G. K., Utomo, D. N., Warren, D., Whiteside, L., Wouthuyzen-Bakker, M., Yombi, J.,Zmistowski, B., *J Arthroplasty* **2019**, *34*: p. S399; b) Cobo, J.,Del Pozo, J. L., *Expert Rev Anti Infect Ther* **2011**, *9*: p. 787
7. Røder, H. L., Sørensen, S. J.,Burmølle, M., *Trends Microbiol* **2016**, *24*: p. 503
8. a) Marculescu, C. E.,Cantey, J. R., *Clinical orthopaedics and related research* **2008**, *466*: p. 1397; b) Flurin, L., Greenwood-Quaintance, K. E.,Patel, R., *Diagn Microbiol Infect Dis* **2019**, *94*: p. 255
9. a) Wildeman, P., Tevell, S., Eriksson, C., Lagos, A. C., Söderquist, B.,Stenmark, B., *Sci Rep* **2020**, *10*: p. 5938; b) Arduino, J. M., Kaye, K. S., Reed, S. D., Peter, S. A., Sexton, D. J., Chen, L. F., Hardy, N. C., Tong, S. Y. C., Smugar, S. S., Fowler, V. G.,Anderson, D. J., *Antimicrobial Resistance and Infection Control* **2015**, *4*: p. 13
10. a) Li, B., Qiu, Y., Zhang, J., Huang, X., Shi, H.,Yin, H., *Environmental Science & Technology* **2018**, *52*: p. 11132; b) Lécuyer, F., Bourassa, J.-S., Gélinas, M., Charron-Lamoureux, V., Burrus, V., Beauregard, P. B.,Ellermeier, C. D., *mSphere* **2018**, *3*: p. e00473
11. Gabrilska, R. A.,Rumbaugh, K. P., *Future Microbiology* **2015**, *10*: p. 1997
12. Hood, M. I.,Skaar, E. P., *Nat Rev Microbiol* **2012**, *10*: p. 525
13. a) Keogh, D., Tay, W. H., Ho, Y. Y., Dale, J. L., Chen, S., Umashankar, S., Williams, R. B. H., Chen, S. L., Dunny, G. M.,Kline, K. A., *Cell Host Microbe* **2016**, *20*: p. 493; b) Hughes, Elizabeth R.,Winter, Sebastian E., *Cell Host & Microbe* **2016**, *20*: p. 411
14. Sevillano, D., Aguilar, L., Alou, L., Giménez, M. J., Cafini, F., González, N.,Prieto, J., *Rev Esp Quimioter* **2013**, *26*: p. 220
15. Lavigne, J. P., Nicolas-Chanoine, M. H., Bourg, G., Moreau, J.,Sotto, A., *PLoS One* **2008**, *3*: p. e3370
16. a) Cavallaro, A. A., Macgregor-Ramiasa, M. N.,Vasilev, K., *ACS Applied Materials & Interfaces* **2016**, *8*: p. 6354; b) Vasilev, K., Griesser, S. S.,Griesser, H. J., *Plasma Processes and Polymers* **2011**, *8*: p. 1010; c) Vasilev, K., Cook, J.,Griesser, H. J., *Expert Rev Med Devices* **2009**, *6*: p. 553; d) Vasilev, K., *Coatings* **2019**, *9*: p. 654
17. a) Hayles, A., Hasan, J., Bright, R., Palms, D., Brown, T., Barker, D.,Vasilev, K., *Materials Today Chemistry* **2021**, *22*: p. 100622; b) Elbourne, A., Crawford, R. J.,Ivanova, E. P., *J Colloid Interface Sci* **2017**, *508*: p. 603

18. Linklater, D. P., Baulin, V. A., Juodkazis, S., Crawford, R. J., Stoodley, P.,Ivanova, E. P., *Nature Reviews Microbiology* **2021**, *19*: p. 8
19. a) Bright, R., Fernandes, D., Wood, J., Palms, D., Burzava, A., Ninan, N., Brown, T., Barker, D.,Vasilev, K., *Materials Today Bio* **2022**, *13*: p. 100176; b) Bright, R., Hayles, A., Fernandes, D., Visalakshan, R. M., Ninan, N., Palms, D., Burzava, A., Barker, D., Brown, T.,Vasilev, K., *ACS Applied Materials & Interfaces* **2021**, *13*: p. 38007; c) Bhadra, C. M., Truong, V. K., Pham, V. T., Al Kobaisi, M., Seniutinas, G., Wang, J. Y., Juodkazis, S., Crawford, R. J.,Ivanova, E. P., *Sci Rep* **2015**, *5*: p. 16817; d) Tsimbouri, P. M., Fisher, L., Holloway, N., Sjostrom, T., Nobbs, A. H., Meek, R. M., Su, B.,Dalby, M. J., *Sci Rep* **2016**, *6*: p. 36857
20. Hayles, A., Bright, R., Wood, J., Palms, D., Zilm, P., Brown, T., Barker, D.,Vasilev, K., *Advanced Materials Interfaces n/a*: p. 2102353
21. Hayles, A., Hasan, J., Bright, R., Wood, J., Palms, D., Zilm, P., Barker, D.,Vasilev, K., *ACS Applied Nano Materials* **2022**,
22. a) Peleg, A. Y.,Hooper, D. C., *N Engl J Med* **2010**, *362*: p. 1804; b) Khan, H. A., Baig, F. K.,Mehboob, R., *Asian Pacific Journal of Tropical Biomedicine* **2017**, *7*: p. 478; c) Osmon, D. R., Berbari, E. F., Berendt, A. R., Lew, D., Zimmerli, W., Steckelberg, J. M., Rao, N., Hanssen, A., Wilson, W. R.,Infectious Diseases Society of, A., *Clin Infect Dis* **2013**, *56*: p. e1; d) Zimmerli, W., *J Intern Med* **2014**, *276*: p. 111
23. Bandara, C. D., Singh, S., Afara, I. O., Wolff, A., Tesfamichael, T., Ostrikov, K.,Oloyede, A., *ACS Applied Materials & Interfaces* **2017**, *9*: p. 6746
24. Wood, J., Hayles, A., Bright, R., Palms, D., Vasilev, K.,Hasan, J., *Colloids and Surfaces B: Biointerfaces* **2022**, *217*: p. 112600
25. Bright, R., Hayles, A., Wood, J., Ninan, N., Palms, D., Visalakshan, R. M., Burzava, A., Brown, T., Barker, D.,Vasilev, K., *Nanomaterials* **2022**, *12*: p.
26. Buser, D., Broggini, N., Wieland, M., Schenk, R. K., Denzer, A. J., Cochran, D. L., Hoffmann, B., Lussi, A.,Steinemann, S. G., *J Dent Res* **2004**, *83*: p. 529
27. a) Wu, Y., Zitelli, J. P., TenHuisen, K. S., Yu, X.,Libera, M. R., *Biomaterials* **2011**, *32*: p. 951; b) Marinucci, L., Balloni, S., Becchetti, E., Belcastro, S., Guerra, M., Calvitti, M., Lilli, C., Calvi, E. M.,Locci, P., *Int J Oral Maxillofac Implants* **2006**, *21*: p. 719; c) Hasegawa, M., Saruta, J., Hirota, M., Taniyama, T., Sugita, Y., Kubo, K., Ishijima, M., Ikeda, T., Maeda, H.,Ogawa, T., *Int J Mol Sci* **2020**, *21*: p. 783
28. Anitha, V. C., Banerjee, A. N., Joo, S. W.,Min, B. K., *Nanotechnology* **2015**, *26*: p. 355705
29. Yuan, Z. Y., Zhang, X. B.,Su, B. L., *Applied Physics A* **2004**, *78*: p. 1063
30. Flurin, L., Greenwood-Quaintance, K. E.,Patel, R., *Diagnostic Microbiology and Infectious Disease* **2019**, *94*: p. 255
31. Zapun, A., Vernet, T.,Pinho, M. G., *FEMS Microbiol Rev* **2008**, *32*: p. 345
32. a) Hasan, J., Crawford, R. J.,Ivanova, E. P., *Trends Biotechnol* **2013**, *31*: p. 295; b) Ivanova, E. P., Hasan, J., Webb, H. K., Gervinskas, G., Juodkazis, S., Truong, V. K., Wu, A. H., Lamb, R. N., Baulin, V. A., Watson, G. S., Watson, J. A., Mainwaring, D. E.,Crawford, R. J., *Nat Commun* **2013**, *4*: p. 2838
33. a) Sun, D., Jeannot, K., Xiao, Y.,Knapp, C. W., *Frontiers in Microbiology* **2019**, *10*: p. ; b) Evans, D. R., Griffith, M. P., Sundermann, A. J., Shutt, K. A., Saul, M. I., Mustapha, M. M., Marsh, J. W., Cooper, V. S., Harrison, L. H.,Van Tyne, D., *eLife* **2020**, *9*: p. e53886; c) Ochman, H., Lawrence, J. G.,Groisman, E. A., *Nature* **2000**, *405*: p. 299; d) Lerminiaux, N. A.,Cameron, A. D. S., *Can J Microbiol* **2019**, *65*: p. 34
34. a) Peters, B. M., Jabra-Rizk, M. A., O'May, G. A., Costerton, J. W.,Shirtliff, M. E., *Clinical microbiology reviews* **2012**, *25*: p. 193; b) Elias, S.,Banin, E., *FEMS Microbiol Rev* **2012**, *36*: p. 990; c) Raghupathi, P. K., Liu, W., Sabbe, K., Houf, K., Burmølle, M.,Sørensen, S. J., *Frontiers in Microbiology* **2018**, *8*: p. ; d) Vila, T., Kong, E. F., Montelongo-Jauregui, D., Van Dijck, P., Shetty, A. C., McCracken, C., Bruno, V. M.,Jabra-Rizk, M. A., *Virulence* **2021**, *12*: p. 835
35. Bankier, C., Cheong, Y., Mahalingam, S., Edirisinghe, M., Ren, G., Cloutman-Green, E.,Ciric, L., *PLOS ONE* **2018**, *13*: p. e0192093

6. Supplementary Information

6.1. Results

Surface profilometry was measured using an Olympus 3D measuring Laser Microscope to generate a height profile of the nanostructures across a relatively large 128x128 µm scan size. The height profile showed that the HTE-Ti surface had the micron scale height variations observed on the AR-Ti surface, as well as high frequency nanoscale height variations representing the densely packed nanostructures. In supplementary Figure S1, the scan pathway is shown on AR-Ti (C) and HTE-Ti (D).

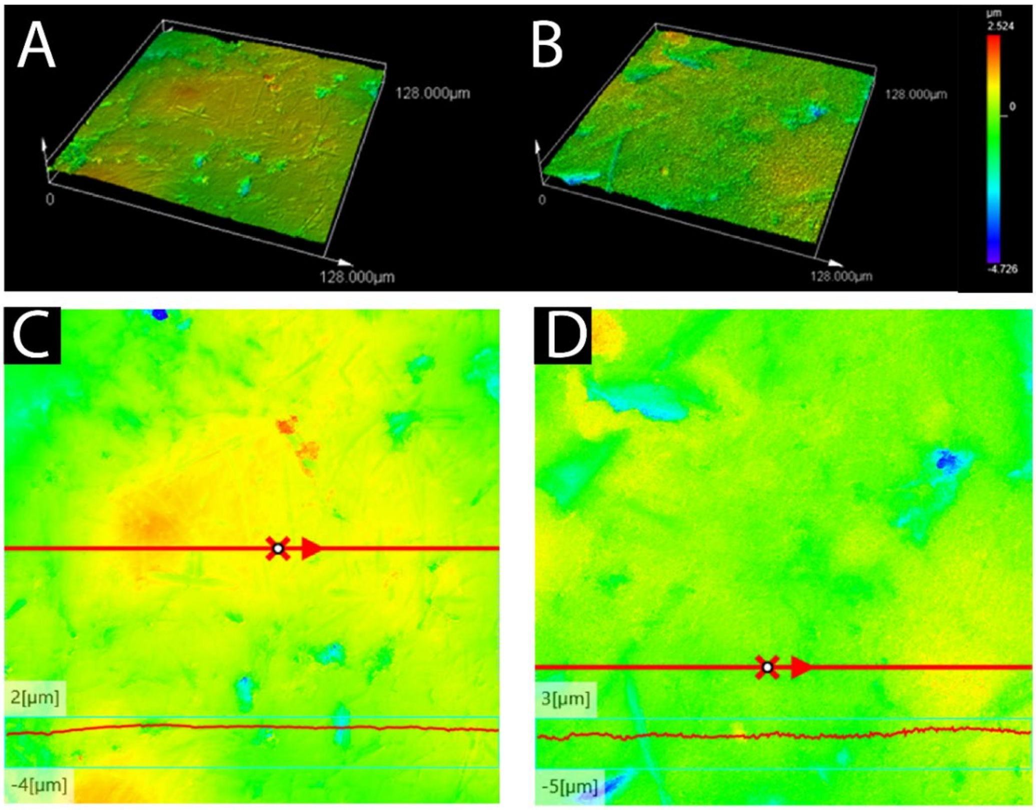

Figure S1. Surface profilometry of AR-Ti (A and C) and HTE-Ti (B and D). Colour scale maps of the 128x128 µm scans of AR-Ti (A) and HTE-Ti (B). Height profiles of randomly chosen 1-dimensional scan paths across the surface profile of AR-Ti (C) and HTE-Ti (D).

Table S1. Oligonucleotide sequences used for probes in FISH analysis. All probe sequences are complementary to the 16S rRNA sequence of their respective species.

Species	16s probe sequence	rRNA type	Reference
Escherichia coli	5’ – TATTAACTTTACTCCCTTCCTCCCC GCTGAA – 3’	16s rDNA	[1]
Staphylococcus aureus	5’ – GAAGCAAGCTTCTCGTCCG – 3’	16S rRNA	[2]
Enterococcus faecalis	5’ – CCCCTTCTGATGGGCAGG – 3’	23S rRNA	[2]

To ensure that colony enumeration measurements were representative of the entire population of viable cells on a given sample, the AR-Ti and HTE-Ti discs were imaged by SEM after cell detachment by sonication in PBS (Figure S1). No cells were observed to remain attached to the surface following sonication.

When performing the colony enumeration assay using cells detached from the titanium samples, it was important to validate the sonication method to determine whether all cells were being detached. Figure S2 presents the SEM images obtained following sonication of bacterial cells, and these images suggest that there was a total retrieval of the bacteria incubated on these titanium samples.

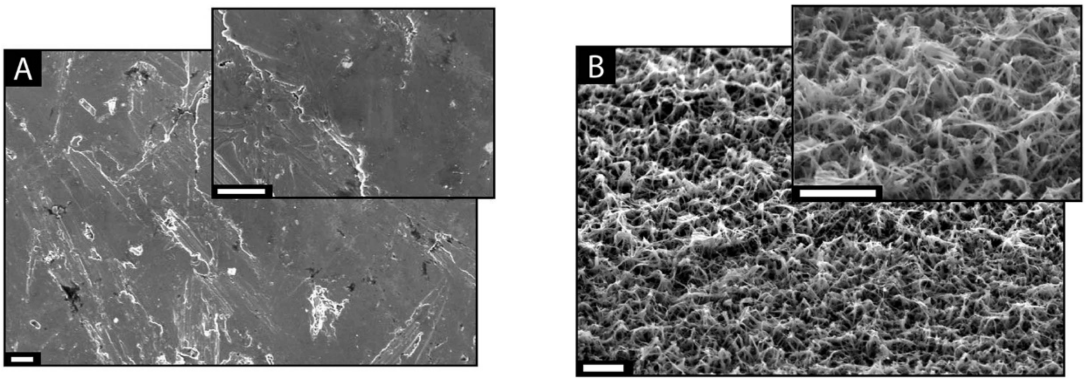

Figure S2. HTE-Ti sample following sonication to remove attached bacteria. A) AR-Ti surface, B) HTE-Ti surface. Scale bars are 1 µm.

References

1. Wang, I.-K., et al., *Real-Time PCR Analysis of the Intestinal Microbiotas in Peritoneal Dialysis Patients.* Applied and Environmental Microbiology, 2012. **78**(4): p. 1107-1112.
2. Kempf, V.A.J., K. Trebesius, and I.B. Autenrieth, *Fluorescent In Situ Hybridization Allows Rapid Identification of Microorganisms in Blood Cultures.* Journal of Clinical Microbiology, 2000. **38**(2): p. 830-838.

CHAPTER 4:
VANCOMYCIN TOLERANCE OF ADHERENT *STAPHYLOCOCCUS AUREUS* IS IMPEDED BY SPIKED-NANOSTRUCTURE-INDUCED PHYSIOLOGICAL CHANGES

Andrew Hayles[1], Richard Bright[1], Ngoc Nguyen[1], Vi Khanh Truong[1], Jonathan Wood[2], Dennis Palms[1], Jitraporn Pimm Vongsvivut[3], Dan Barker[4], Krasimir Vasilev[1*]

[1] College of Medicine and Public Health, Flinders, University, Bedford Park 5042, South Australia, Australia

[2] Academic Unit of STEM, University of South Australia, Mawson Lakes, Adelaide, 5095, South Australia, Australia.

[3] Infrared Microspectroscopy Beamline, ANSTO Australian Synchrotron, Clayton, Victoria 3168, Australia

[4] Corin Australia, Baulkham Hills, New South Wales 2153, Australia

(* Corresponding author: Krasimir.vasilev@flinders.edu.au)

Keywords: gene expression, FTIR, nanospikes, biofilm, biomaterials, transcriptomics, synchrotron,

Abstract

Bacterial colonization of implantable biomaterials is an ever-pervasive threat that causes devastating infections but continues to elude resolution. In the present study, we investigate how a rationally designed nanostructured antibacterial surface can enhance the susceptibility of pathogenic bacteria to antibiotics used in prophylactic procedures. We show that tolerance to vancomycin of *Staphylococcus aureus* rapidly increases following attachment to a medical-grade titanium alloy, but this effect does not occur when bacteria are in contact with a surface modified with sharp nanostructures. Analysis of differential gene expression implicated a set of genes involved with the modification of cell surface charge. In particular, genes involved in the D-alanylation of teichoic acids, and the lysylation of phosphatidylglycerol were uniquely upregulated on cells attached to the unmodified titanium surface. We supported these findings using synchrotron macro attenuated Fourier-transform infrared microspectroscopy. By inhibiting the ability of the pathogen to reduce its net negative charge, the nanoengineered surface renders *S. aureus* more susceptible to positively charged antimicrobials such as vancomycin. This finding highlights the opportunity for nanostructured antibacterial surfaces to enhance the potency of prophylactic antibiotic treatments during implant placement surgery.

1. Introduction

Biomedical implants are increasingly being used to treat a broad range of pathologies, with device types ranging from orthopaedic joint replacements to stents and catheters. These biomaterials successfully reduce the rate of mortality and improve the quality of patient lives. Unfortunately, these benefits are often outweighed by detrimental bacterial infections.[1] Despite stringent hygiene practices and prophylactic administration of antibiotics, the threat of implant infection stubbornly remains. Bacterial colonization of an implanted material results in the formation of biofilm on the foreign surface. Biofilm enables the pathogen to evade the host immune system[2] and persist through antibiotic treatment.[3] It is well established that biofilms increase the drug tolerance of pathogens by as much as 1000-fold.[4] Due to this, implant infections typically require further invasive revision surgeries to clear the infection, as antibiotics alone are insufficient. The results can be disastrous for patients, often resulting in total limb amputation[5] and even death.[6] Various biofilm-associated factors are purported to contribute to the increased antibiotic tolerance of adherent pathogens. Some of these include the secretion of extracellular polymeric substance (EPS)[7], reduced metabolic activity[8], and modification of cell surface structures.[9] In a recent report, we demonstrated that vancomycin tolerance of *S. aureus* in an established biofilm is inhibited when the cells are attached to a bactericidal nanospiked titanium surface.[10] This finding is highly relevant to an infection situation when bacteria have already established a biofilm on the device surface prior to treatment. However, how are bacteria affected by antibiotics on a nanostructured surface during the initial stages of attachment? This is the most likely scenario for the initiation of infection since the greatest probability of bacteria contaminating the device occurs at the time of implantation.[11] To counteract that and mitigate implant infection, patients are often prophylactically administered antibiotics.[12] In the present study, we address this typical scenario and investigate the capacity of a nanostructured antibacterial surface to work synergistically with antibiotics to eliminate invading pathogens. We used titanium as the material substrate for our study because titanium is often considered the gold standard for implant applications such as orthopaedics and dentistry.[13] We used *Staphylococcus aureus* as the bacterium due to the prevalence of these species in medical device-associated infections.[14] We selected vancomycin as an antibiotic often used in prophylactic treatment procedures.[15] We used a combination of microscopy, differential gene expression, and synchrotron macro-attenuated total reflection Fourier-transform infrared microspectroscopy (ATR-FTIR) to provide a detailed description of the influence of the combination of the nanospiked antibacterial surface and the antibiotic on the physiological characteristics of *S. aureus*.

2. Results

2.1. The influence of nanospikes on adherent S. aureus. We fabricated sharp spike-like nanostructures on Ti surfaces (called nanospiked throughout this report) using a hydrothermal etching process.[16] SEM images show the sharp, branching and stochastically oriented features that extend from the titanium surface after modification (Fig. 1C), while the original surface is completely featureless containing only a few cracks and defects (Fig. 1D). Comprehensive characterisation of the morphological, chemical and physical properties of the nanospiked and unmodified Ti samples are reported in Fig. S1. We investigated the early stages of *S. aureus* attachment and colonisation on unmodified and nanospiked surfaces using electron and fluorescence microscopy (Fig. 1 E-H). After 24 h, *S. aureus* cells appeared shrivelled and frequently lysed on the nanospiked surface (Fig. 1F). In comparison, the cells showed a typical turgid morphology on the unmodified surface (Fig. 1E). Live/Dead staining showed that the bactericidal effect of the nanospikes was cumulative over 24 h, where approximately 35% of cells were killed after 3 h and 65% of cells were killed after 24 h. In parallel, the biovolume of *S. aureus* on the nanospiked surface did not significantly increase over 24 h, while the biovolume on the unmodified counterpart was two-fold greater by 24 h. We measured the rate of EPS secretion using the FilmTracer™ SYPRO™ Ruby Biofilm Matrix stain, which revealed approximately equal mean fluorescence intensities on both surfaces over the 24 h of incubation. The FilmTracer fluorescence images revealed that EPS tended to accumulate in cell clusters on the unmodified Ti surface, while on the nanospiked Ti surface, it was more homogenously distributed across the surface.

The bactericidal efficacy of the nanospikes presented here is comparable to other reported nanostructured surfaces.[17] When Gram-positive cells are exposed to bactericidal nanostructured surfaces, most cells are killed, while a smaller subset of the population persists. This is particularly evident in Fig. 1F, where approximately half of the cells appear turgid while the other half appear severely deformed. Next, we tested our hypothesis that nanospiked surfaces induce molecular and biochemical changes in *S. aureus* which simultaneously allow a subset of cells to persist and also sensitize them to antibiotic treatment.

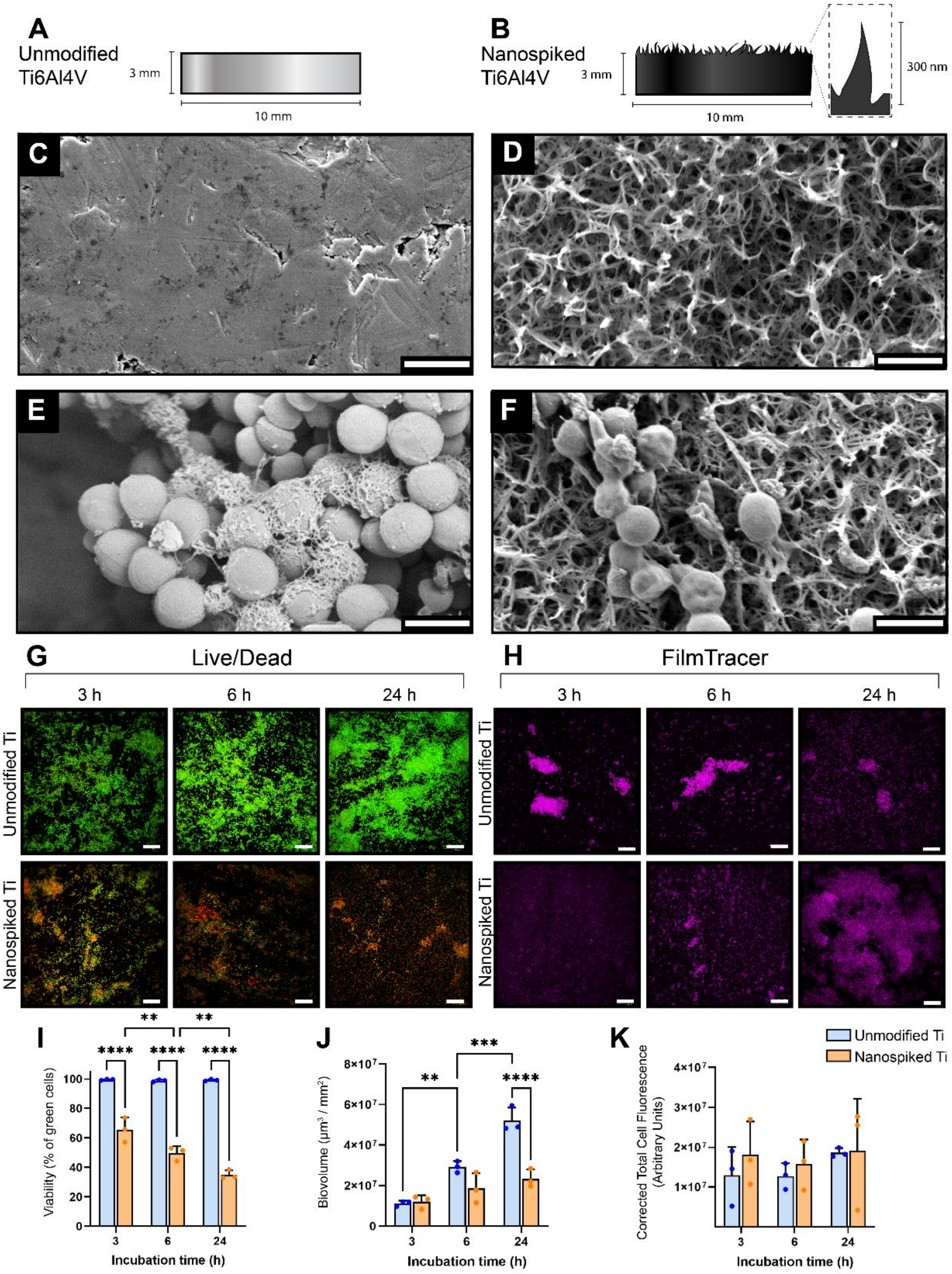

Fig. 1. The antibacterial effect of nanospiked titanium against *S. aureus* over 24 h. A and B) Schematic illustration of unmodified and nanospiked Ti samples. C and D) The Ti surfaces before and after hydrothermal treatment, respectively. E and F) *S. aureus* morphology following attachment to unmodified and nanospiked Ti surfaces, respectively. G) Live/Dead fluorescence micrographs showing the accumulation of bacterial cell death on nanospiked Ti over 24 h. H) FilmTracer™ SYPRO™ Ruby fluorescence micrographs showing the secretion of EPS over 24 h. I) Quantified bacterial cell viability. J) Biovolume generated from 3D z-stack fluorescence micrographs. K) Quantification of EPS secretion using fluorescence intensity acquired from FilmTracer micrographs. ** $P < 0.01$, *** $P < 0.001$ **** $P < 0.0001$, n=3, mean ± *SD*. Statistical tests were performed with Two-way ANOVA using Tukey's multiple comparisons test. Scale bars represent 1 µm for SEM images and 30 µm for fluorescence micrographs.

2.2. The influence of early-stage surface attachment on the antibiotic tolerance of S. aureus. It is commonly understood that bacteria are substantially more tolerant to antibiotics when they establish a biofilm.8 In the present study we set out to examine the change in vancomycin tolerance of S. aureus cells attaching to either unmodified or nanospiked Ti surfaces (Fig. 2). Vancomycin has a molecular mass of 1449.3 g/mol and a net charge of (+)0.9 at physiological pH (Fig. S2) and is an antibiotic regularly used for prophylaxis prior to surgery. Since the goal of this study is to reveal the susceptibility of bacteria to antibiotics at early stages of surface attachment and colonisation, we treated S. aureus with vancomycin at its MIC, for 24 h, either at the same time as inoculation or following surface attachment for 3 and 6 h. For both surfaces, when the drug was administered at the same time as inoculation, all cells were observed dead following treatment. When the cells were attached to the unmodified Ti for 3 h before vancomycin treatment, the post-treatment viability climbed to 57% and subsequently increased to 81% when the cells were attached for 6 h before vancomycin treatment. On the nanospiked Ti surface, attaching the cells to the surface for 3h and 6 h did not increase the post-treatment viability, and the entire culture was observed to be dead.

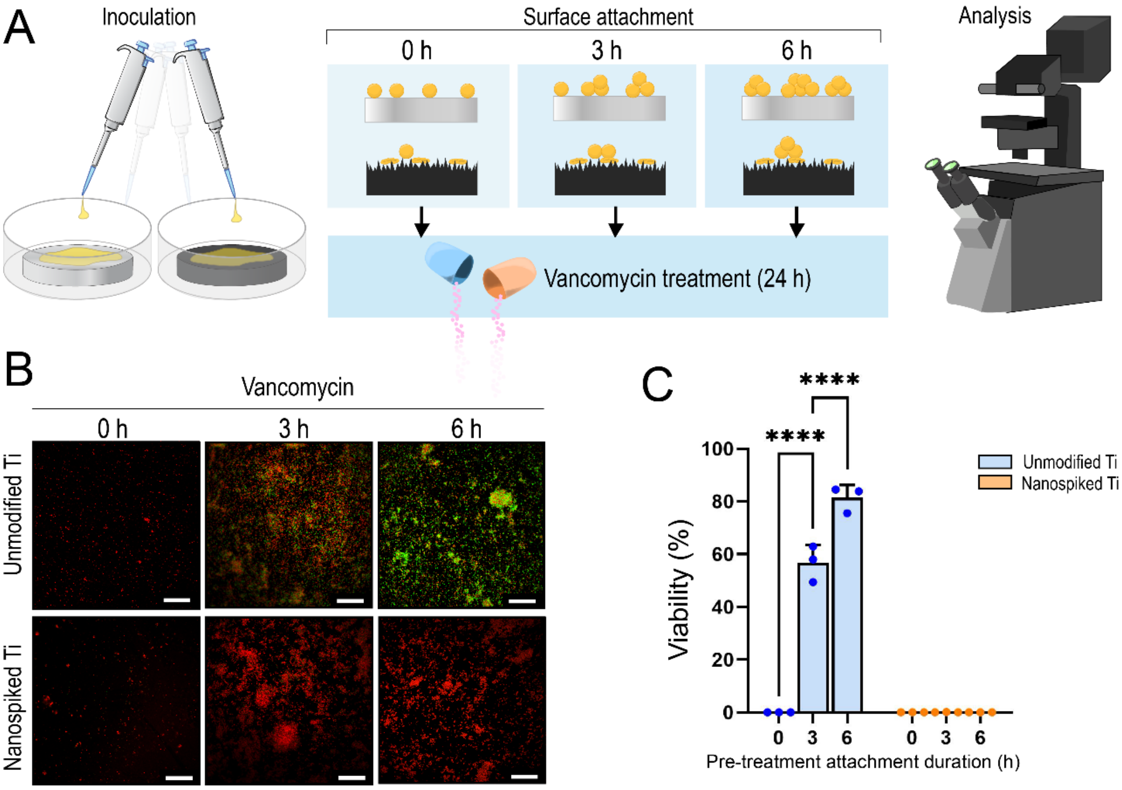

Fig. 2. The antibiotic defences associated with surface-attached bacteria are inhibited by the nanospiked surface. A) A flow schematic showing the attachment and treatment of *S. aureus* using vancomycin and nanospiked or unmodified surfaces. B) Fluorescence micrographs obtained using Live/Dead staining reagent. Scale bars represent 30 µm. C) Viability of *S. aureus* quantified from fluorescence images at 1x MIC. **** $P < 0.0001$, n=3, mean ± *SD*

2.3. Differential expression of genes related to formation and modification of S. aureus cell wall and associated structures. To begin to understand how adherent S. aureus persists through vancomycin treatment (or fails to, as on the nanospiked surface), we performed a genome-wide differential expression analysis. Our experimental design aimed to compare free-floating planktonic cells to adherent cells attached to either the unmodified or nanospiked Ti surfaces (Fig. 3). We identified 246 differentially expressed genes (DEGs) common to both comparisons (Table S2), indicative of the phenotype switch from planktonic to adherent cells. More importantly, we identified a set of 87 DEGs unique to the comparison between unmodified Ti and planktonic cells (henceforth referred to as the unmodified Ti comparison), and a further 78 unique DEGs in the nanospiked Ti comparison (Tables S3 and S4, respectively). From our differential gene expression analysis of S. aureus on the nanospiked and unmodified surfaces, we identified a set of uniquely upregulated genes associated with the biosynthesis of peptidoglycan and the modification of cell surface structures on the unmodified Ti surface (Table 1).

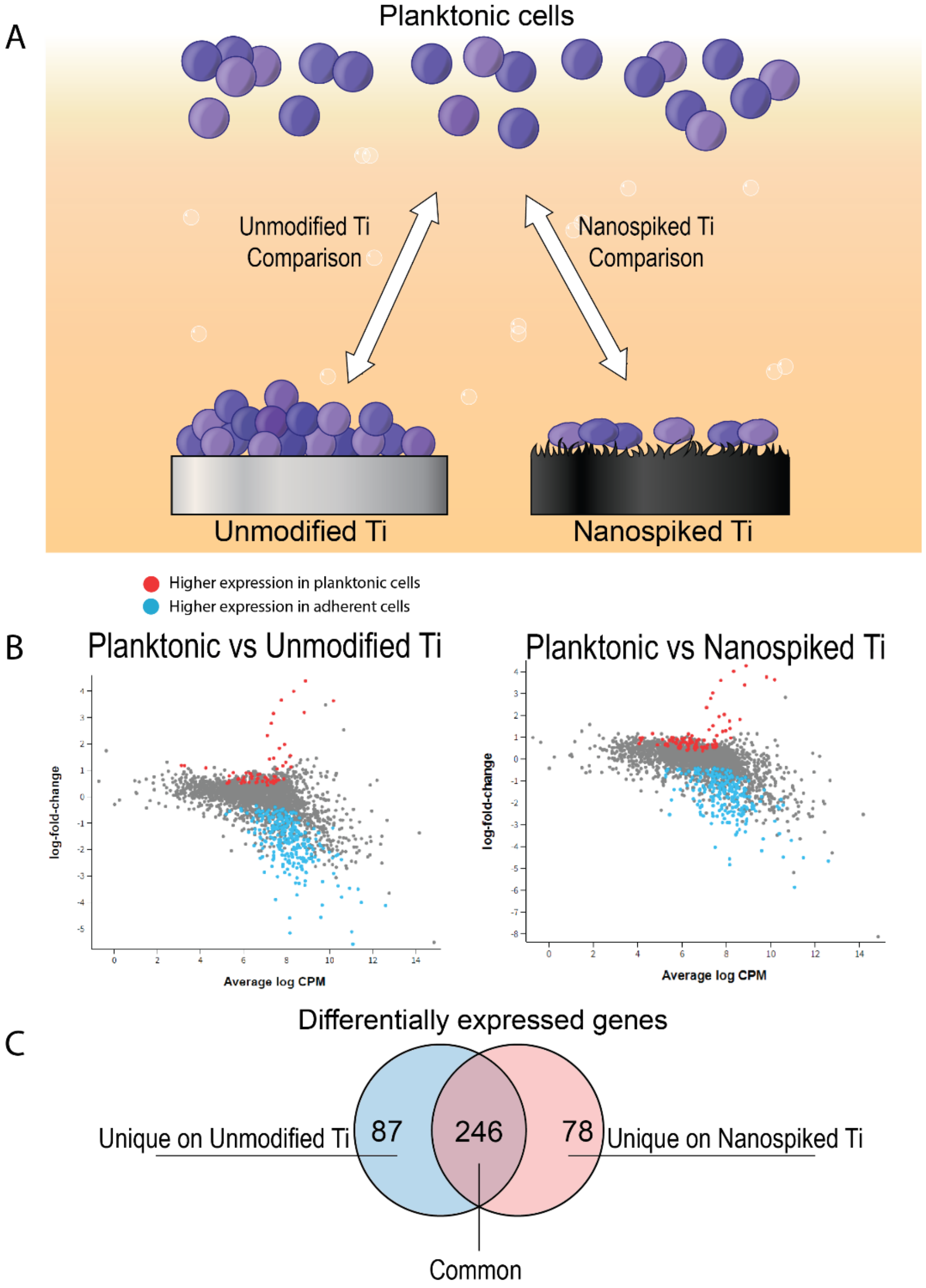

Fig. 3. Differential gene expression analysis of planktonic and adherent *S. aureus* on nanospiked Ti. A) A schematic of the experimental design of the differential gene expression analysis. B) Volcano plots of differentially expressed *S. aureus* genes comparing planktonic and adherent cells on both surface types. C) Venn diagram showing the number of common and unique differentially expressed genes from the two comparisons.

Table 1. Uniquely upregulated genes, from the unmodified Ti comparison, involved in the cell wall assembly, growth and division. All genes in the table were uniquely upregulated on the unmodified Ti surface, but not the nanospiked surface. The table includes gene symbols where available (italics), product name (as described by NCBI), GeneID (unique to NCBI reference genome database), and functional description.

Genes associated with cell surface assembly and modification

*Gene symbol**, product	GeneID	Functional description	*P*
Dat D-amino-acid transaminase	KQ76_RS08950	Catalyses synthesis of D-glutamate and D-alanine for peptidoglycan synthesis	0.023
murD UDP-N-acetylmuramoyl-L-alanine--D-glutamate ligase	KQ76_RS05595	Catalyses the formation of the peptide bond between UDP-N-acetylehyl-l-alanine and d-glutamic acid	0.024
alr Alanine racemase	KQ76_RS06790	Converts between L-alanine to D-alanine	0.028
polysaccharide biosynthesis protein	KQ76_RS08970	Biosynthesis of polysaccharides for peptidoglycan and capsule formation	0.046
undecaprenyl/decaprenyl-phosphate alpha-N-acetylglucosaminyl 1-phosphate transferase	KQ76_RS03675	Involved in biosynthesis and organisation of cell wall	0.036
isaA lytic transglycosylase IsaA	KQ76_RS13190	Hydrolysis of peptidoglycan during cell growth and division	0.042
lytM glycine-glycine endopeptidase LytM	KQ76_RS01125	Hydrolysis of peptidoglycan during cell growth and division	0.029
amidase domain-containing protein	KQ76_RS13615	Hydrolysis of peptidoglycan during cell growth and division	0.024

CHAP domain-containing protein	KQ76_RS01150	Hydrolysis of peptidoglycan during cell growth and division	0.038
amidohydrolase family protein	KQ76_RS13245	Hydrolysis of peptidoglycan during cell growth and division	0.049
hom homoserine dehydrogenase	KQ76_RS06420	Coordination of a metabolic pathway that leads to the synthesis of cell-wall components such as L-lysine and m-DAP, as well as other amino acids such as L-threonine, L-methionine, L-isoleucine	0.030
dltB PG: teichoic acid D-alanyltransferase DltB	KQ76_RS04160	D-alanylation of teichoic acids	0.020
dltD D-alanyl-lipoteichoic acid biosynthesis protein DltD	KQ76_RS04170	D-alanylation of teichoic acids	0.032
tarS poly(ribitol-phosphate) beta-N-acetylglucosaminyltransferase	KQ76_RS01020	β-O-GlcNAcylation of teichoic acids	0.034
mprF bifunctional lysylphosphatidylglycerol flippase/synthetase MprF	KQ76_RS06595	Lysylation of phosphatidylglycerol	0.023

---

*Gene symbols are provided for those which are specifically labelled in the reference genome of ATCC25923 on NCBI.

From the DEGs listed in Table 1, we identified a group of genes associated with the modification of cell surface charge (Fig. 4). Expression of these genes was upregulated on the unmodified Ti surface in comparison to the nanospiked surface.

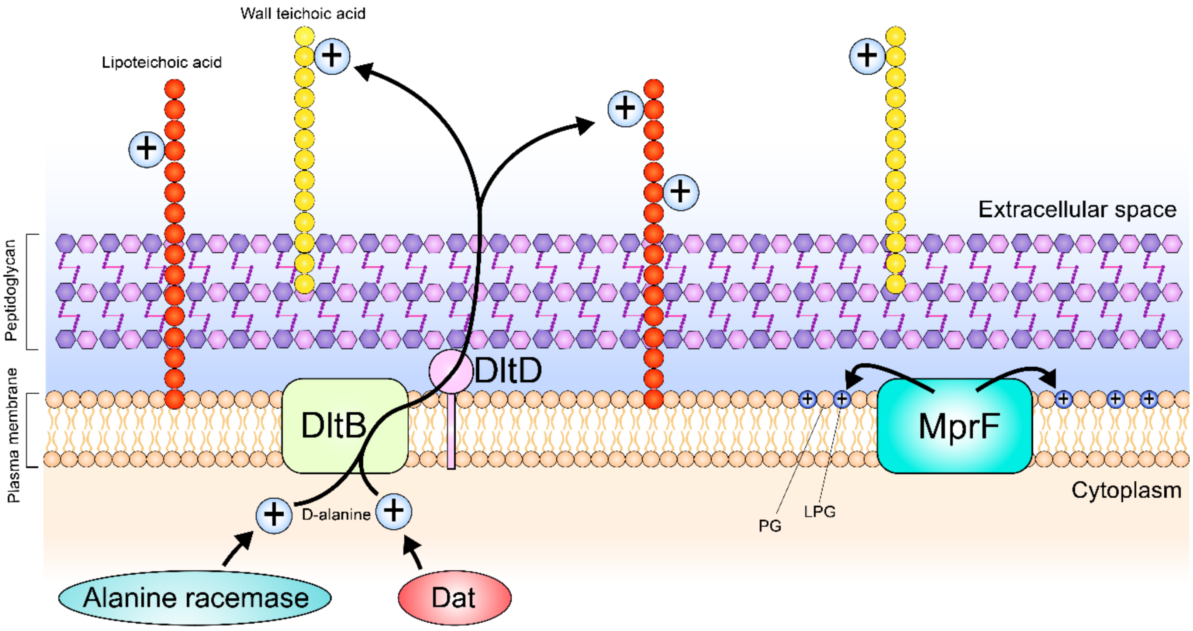

Fig. 4. Genes involved with the modification of cell wall surface charge of S. aureus, which were uniquely upregulated on the unmodified Ti surface. The positively charged D-alanine is generated in the cytoplasm by the actions of D-amino acid transferase (Dat) and alanine racemase. The newly synthesized D-alanine is then brought across the plasma membrane and covalently attached to teichoic acids by the two membrane-bound proteins DltB and DltD. This modification reduces the overall negative charge associated with teichoic acids. Another membrane-bound protein, multiple peptide resistance factor (MprF), converts phosphatidylglycerol (PG) into lysyl-phosphatidylglycerol (LPG) and then orients the modified phospholipid to sit within the outer leaflet of the phospholipid bilayer using its flippase activity.18 Through this bifunctional activity, MprF also contributes to the reduction of the overall negative charge of the S. aureus cell surface.

2.4. Nanospike-induced changes in S. aureus cell biochemistry. To further investigate the biochemical changes in S. aureus induced by the titanium nanospikes, we utilised synchrotron ATR-FTIR microspectroscopy to analyse changes in biochemical interactions between S. aureus cells and the surfaces (Fig. 4). Three regions of interest were captured and analysed. A flowchart of the analysis is presented in Fig. S4. The C-H region, mostly representing lipids, was captured in the 3000-2850 cm-1 spectral range; the amide I and II regions, largely representing proteins, was captured in the 1700-1450 cm-1 range; and the fingerprint region, mostly representing polysaccharides and nucleic acids, was captured in the 1150-1000 cm-1 range.19 The heatmaps presented in Fig. 4A show the absorption intensity of these 3 spectral regions and provide information on their spatial distribution. 3D maps were generated for the heatmaps (Fig. S5), which reveal a spatial distribution of the signatures of the 3 regions of interest. Differences in all 3 regions were observed. While the differences observed in the spectral maps are qualitatively overt, their statistical significance was confirmed using hierarchical cluster analysis (HCA) to group similar spectra. Following this, variations in chemical interactions of cells on unmodified and nanospiked Ti were assessed by principal component analysis (PCA) using principal component (PC)-1 and PC-2 (Fig. 5B and S3). The differences between the unmodified and nanospiked Ti groups were largely described by PC-1 (76%), compared to 24% in PC-2 (Fig. S6). The clustering and distribution of scores between unmodified and nanospiked samples in the PCA plot indicate an unambiguous difference between the two sample types. The loading curve of PC-1 (Fig. 4C) was chosen in this study to represent the major biochemical changes of S. aureus which were influenced by the nanospiked Ti. This enabled the identification of wavenumbers with outstanding peaks, representing significant chemical differences. To appreciate the overall magnitude of difference in the chemical signatures identified in the PCA loading peaks, average spectra were generated for the 3 regions (3000-2850 cm-1, 1700-1450 cm-1, and 1150-1000 cm-1) indicating a significant biochemical change in lipids, protein, and polysaccharides/carbohydrates, respectively (Fig. 4 D-F).

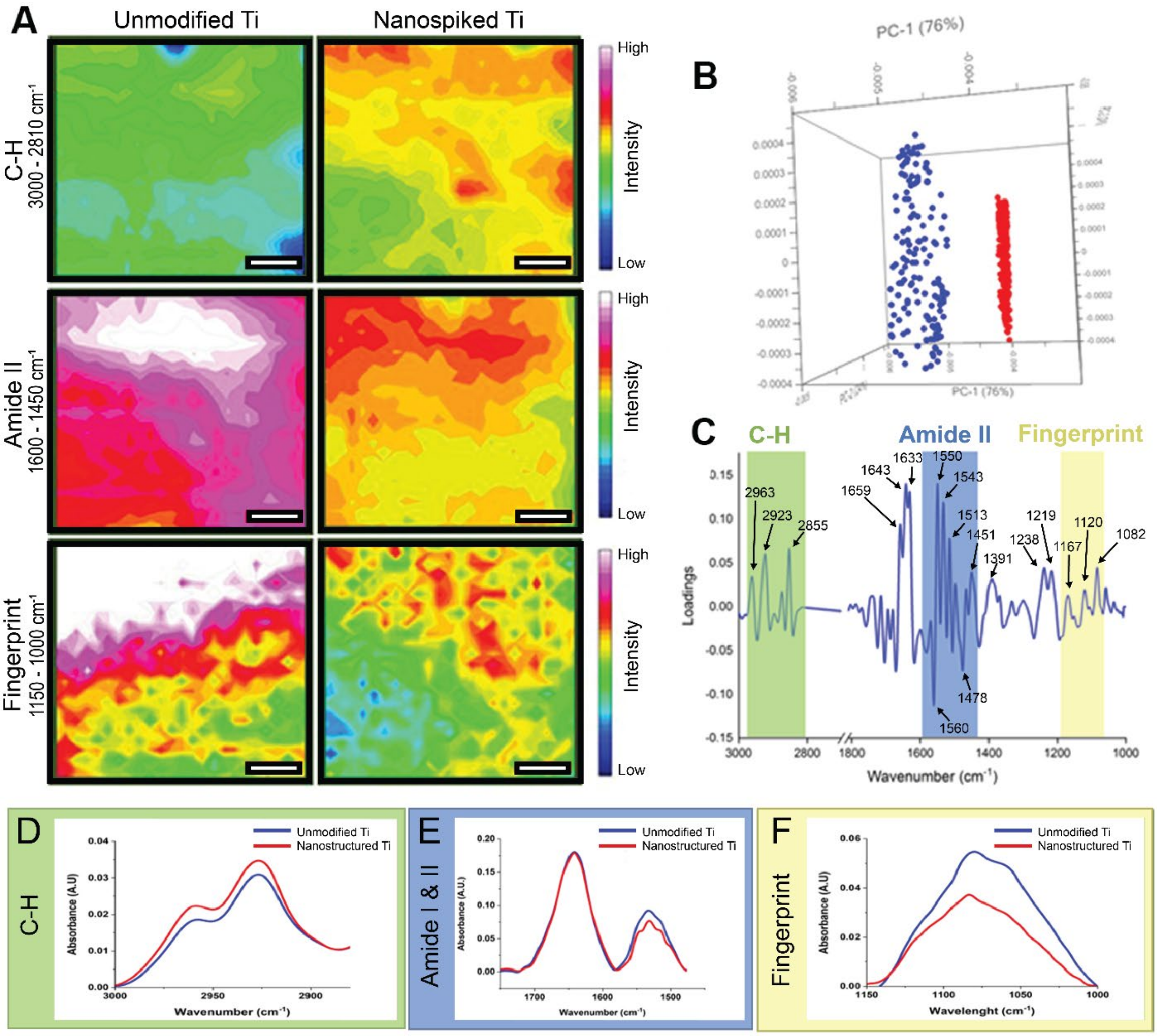

Fig. 5. Synchrotron ATR-FTIR microspectroscopy of *S. aureus* attached to a nanospiked titanium surface. A) heat maps showing the intensity of absorption of wavelength ranges corresponding to 3 regions of interest (C-H, Amide and

Fingerprint). Scale bars are 5 µm. B) The PCA score plots of *S. aureus* cells incubated on unmodified and nanospiked samples. Blue points represent cells on unmodified Ti and red points represent cells on nanospiked Ti. C) The PCA loading spectra of *S. aureus* incubated on unmodified and nanospiked Ti samples. D-F) Comparisons of the average spectra from hierarchical cluster analysis for *S. aureus* C-H bonds, Amide I & II and the fingerprint region, respectively.

3. Discussion

We set out to perform an in-depth molecular and biochemical characterization of *S. aureus* on a nanospiked surface and elucidate potential mechanisms underpinning surface-induced antibiotic sensitization. The nanospiked surface was prepared by hydrothermal etching[20] as previously described,[21] due to well-established bactericidal efficacy.[22] Material and chemical characterisation of the nanospiked Ti surface is presented in the supplementary information (Fig. S1, Table S1). In the present study, we noted that the bactericidal activity of the nanospikes is not an instantaneous process but instead occurs cumulatively over time. The rate of *S. aureus* biovolume growth on the nanospiked surface was impeded, but the rate of EPS secretion was approximately equal between both sample types. However, while the EPS on the unmodified Ti surface tended to accumulate around cell clusters, it was more homogenously distributed across the entire surface of the nanospiked Ti. This is plausibly a stress response effect, considering that *S. aureus* has been reported to manipulate its EPS secretions as a response to mechanical stress.[23] We aimed to investigate the change in vancomycin tolerance of early-adherent *S. aureus* cells on both surface types. Interestingly, a mere 3 h of attachment to the unmodified surface was sufficient to enable *S. aureus* to persist through vancomycin treatment, and this effect was strengthened with 6 h of pre-treatment attachment. Conversely, on the nanospiked Ti surface, *S. aureus* was not able to persist through vancomycin treatment irrespective of pre-treatment attachment duration. Interestingly, the summative bactericidal effect of the nanospikes and vancomycin led to total clearance of *S. aureus* even when the vancomycin concentration was reduced to 0.5×MIC (Fig. S3). This indicates that the synergistic effects of vancomycin and the nanospikes provide a comparatively greater bactericidal effect than the antibiotic alone. This raises the question, how does the nanospiked Ti surface influence the antibiotic tolerance of *S. aureus*? Previous reports have identified various mechanisms of antibiotic defence in adherent bacterial cells, but this concept is usually discussed in the context of established biofilms.[7, 8] A commonly cited drug tolerance factor related to biofilms is the secretion of EPS and an associated restriction of antibiotic penetration.[24] From our measurements, EPS secretions were equal between surface types throughout the duration of the study. Due to this, the degree of EPS secretion can be reliably ruled out as the differentiating factor, however, there was a difference in EPS organisation. EPS was concentrated around adhered bacterial cell clusters on the unmodified Ti surface, potentially providing some protection from the antibiotic. On the contrary, EPS was equally distributed across the entire surface of the nanospiked sample. Although there was an overall increase in biovolume on the unmodified Ti surface over 24 h, in the first 6 h of attachment, there was no significant difference between surface types. As we see a substantial difference in antibiotic tolerance during the first 6 h, the evidence suggests that biovolume is not the differentiating factor between sample types. To further investigate differences in factors associated with antibiotic defence, we performed a differential gene expression between planktonic cells and cells attached to either the unmodified or nanospiked surface. Broadly, the cells incubated on the unmodified surface showed an expression profile that reflects a comparatively greater aptitude to assemble and remodel peptidoglycan and its associated surface structures. The upregulation of *dltB* and *dltD* on *S. aureus* cells incubated on the unmodified Ti promote the D-alanylation of teichoic acids to reduce the net negative charge of the cell surface.[25] In parallel, the upregulation of *dat*[26] and alanine racemase[27] fuels the production of D-alanine required for this modification. Similarly, the increased expression of *mprF* enables the cells on the unmodified surface to produce the positively charged phospholipid LPG[28], to further reduce the net negative charge on the outer surface of the cell. To obtain further insight, we used ATR-FTIR to compare the biochemical signatures of cells attached to both types of surfaces. Supporting evidence for differences in D-alanylation of teichoic acids and lysylation of PG was found by identifying spectral peaks (Table S5) associated with primary amines (present in LPG) or esters (present in D-alanylated teichoic acids). The FTIR spectra for both chemical markers were higher in cells on the unmodified Ti surface. Interestingly, on the unmodified surface, we observed a large increase of the bands in the region of 1180-1000 cm^{-1}, which captures the signature of polysaccharides, including precursors of peptidoglycan.[29] These data suggest that cells on the unmodified surface have a greater capacity to form peptidoglycan and modify the charge-bearing structures on both the cell wall and membrane bilayer. The modification of cell surface charge via D-alanylation of teichoic acids[30] and lysylation of PG[31] has been recognized as an important virulence factor in *S. aureus.*[32] We propose that the modification of cell surface charge is the primary differentiating factor that enables *S. aureus* to persist through vancomycin treatment on an unmodified Ti surface. This is because a reduction in net negative surface charge enables the cell to repel positively charged compounds, such as cationic antimicrobial peptides and some antibiotics including daptomycin and vancomycin.[33] In this way, the nanospikes nullify one of the main mechanisms of vancomycin tolerance in *S. aureus*. It is presently unclear exactly what triggers the differential expression of genes associated with cell surface structures, but a clue for this may be found in the accumulation of inorganic phosphate (P_i). It has previously been shown that when *S. aureus* accumulates P_i, the *dlt* operon becomes upregulated, leading to increased D-alanylation of teichoic acids and a greater tolerance to the antibiotic daptomycin.[34] Our results showed an increased expression of a P_i transporter (KQ76_RS03230, Table S3) on the unmodified Ti surface, enabling *S. aureus* to better accumulate P_i from its surroundings.

Our findings have major implications for the biomedical field for multiple reasons. Firstly, we have provided a detailed mechanistic insight into how nanospiked surfaces can sensitize bacteria to the positively charged antibiotic vancomycin. This occurs in the very early stages of cell attachment. These findings are relevant to many implant surgical procedures, where a prophylactic dose of vancomycin is administered to the patient prior to implant placement.[15] This is impactful because the majority of implant infections arise from contamination during surgical placement.[35] As the hostile effects of the nanospiked surface are mediated by mechanical forces[36] rather than chemical ones, this synergy can be considered substrate-ambivalent. As such, similar nanoengineered structures can be translated beyond titanium and its alloys, to many other material types such as silicon[37] or PMMA[38], meaning this synergistic interaction can be harnessed in many more implant applications. These findings support and further explain our previous finding, related to a late-onset infection scenario, that established biofilms could be completely eradicated with sub-clinical concentrations of antibiotics when incubated on a nanospiked surface.[10] It is now evident that the synergy between mechanical stress and antibiotic treatment could benefit patients at the time of implant placement thus preventing biofilm formation and infection from occurring. Furthermore, as we observed a similar synergistic effect at 0.5× MIC, this suggests that clinicians may be able to reduce antibiotic dosages administered to patients to curb the rate of nephrotoxicity.[39]

4. Methods

4.1. Cultures and conditions

Staphylococcus aureus ATCC 25923 was retrieved from glycerol stocks kept at -80°C, and incubated on Tryptone Soy Agar (TSA, Oxoid, ThermoFisher, MA) overnight at 37°C. A single colony was aseptically transferred to a 5 mL tube containing Tryptone Soy Broth (TSB, Oxoid, ThermoFisher, MA) and incubated until late log phase. Cell density was determined by optical density at 600nm (OD_{600}) using the cuvette reader of a Nanodrop 2000 (Thermo Scientific, MA, USA).

4.2. Surface inoculation

S. aureus pre-culture was diluted to $OD_{600} = 0.1$, which is equivalent to approximately 10^8 cfu/mL. Titanium samples were placed into sterile 24-well plates and immersed in 1 mL of the diluted *S. aureus* culture. The plates were incubated in an opaque humid chamber (a sealed plastic box with a damp paper towel) at 37°C on an orbital shaker (Ratek Instruments Pty. Ltd., VIC, Australia) at 90 RPM.

4.3. Live/Dead and biovolume analysis

Following incubation, samples were transferred to sterile 24-well plates and immersed in BacLight Live/Dead reagent (Invitrogen, MA, USA), prepared with equal concentrations of SYTO9 and Propidium Iodide at 1.5 µL/mL phosphate-buffered saline (PBS). The samples were incubated for 15 minutes in the dark and then imaged with an Olympus FV3000 confocal laser scanning microscope (CLSM, Olympus, Tokyo, Japan). Excitation and emission spectra were set to 480/500 for SYTO9 and 490/635 for Propidium Iodide, as instructed by the manufacturer. Micrographs were taken at 40x magnification at 3 random locations per sample. For viability analysis, proportions of green and red cells were counted in ImageJ v1.53a (NIH, Bethesda, MD, USA). For biovolume measurements, 3D Z-stack images were taken in triplicate and analysed using the 'surface' function in Imaris 3D analysis software v9.3.0 (Bitplane, Zürich, CHE).

4.4. EPS staining with FilmTracer™ SYPRO™ Ruby

Samples were immersed in SYPRO Ruby (Invitrogen, MA, USA) as directed by the manufacturer. Following incubation, samples were imaged with an Olympus FV3000 CLSM, using the excitation and emission spectra of 450/610. Triplicate micrographs were taken at 40x magnification. The fluorescence intensity of EPS was quantified in ImageJ v1.53 and normalized and the corrected total cell fluorescence was determined using the following formula:

$$CTCF = Integrated\ Intesity - (Area\ selcted\ \times\ Mean\ background\ fluorescence).$$

4.5. Vancomycin tolerance of surface attached S. aureus

To determine the tolerance of adherent *S. aureus* to vancomycin (Merck, NJ, USA), we cultured *S. aureus* on the samples according to the inoculation procedure described above, for either 3 or 6 h. Following culture, we rinsed non-adherent cells from the Ti samples by gently dipping them in sterile PBS 3 times. We then immersed the Ti samples in TSB supplemented with vancomycin at a concentration equal to its MIC (1 µg/mL, Fig. S7) for 24 h in a humid box at 37°C on an orbital shaker set to rotate at 90 RPM. Post-treatment viability was determined following the BacLight LIVE/DEAD Bacterial Viability Kit (ThermoFisher, MA, USA) protocol described above.

4.6. RNA extraction

S. aureus was cultured on titanium samples as previously described for 24 h, then cells were retrieved by vortex for 30 s followed by ultrasonication for 2 mins. Cells were pelleted and resuspended in the lysis buffer provided in the RiboPure Bacterial RNA extraction kit (Invitrogen, MA, USA), and RNA was extracted and isolated following the directions of the manufacturer. The purity of RNA was verified using a Nanodrop 2000.

4.7. RNA sequencing

An MGI DNBSEQ G400 was equipped with a PE100 flow cell (MGI Tech Co., Ltd, Shenzhen, China), and used for high throughput sequencing of *S. aureus* RNA samples. PolyA libraries were prepared using Tecan Universal Prokaryotic RNA-seq (Tecan Group Ltd, Männedorf, Switzerland). Conversion from Illumina to MGI Library was performed with MGIEasy Universal Library Conversion Kit (Part No. MGI1000004155, MGI Tech Co., Ltd, Shenzhen, China). RNA-seq data pre-processing was done with an in-house pre-processing workflow, using MultiQC for quality reporting, STAR for alignment to the *S. aureus* genome assembly (GCA_000756205.1), and FeatureCounts for quantification of gene expression. There was an 85% alignment and library sizes were over 12M/sample, ensuring their suitability for downstream analysis in R. Limma-Voom (v.3.52.0) was used for the analysis of differential gene expression. Two different comparisons were used to observe the differential expression of genes (DEG) across three conditions (free-floating planktonic cells vs cells adherent to either unmodified or nanospiked Ti. Significant DEGs were identified for each comparison (FDR-adjusted p-value < 0.05).

4.8. ATR-FTIR

S. aureus ATCC25923 cells were grown in TSB until late-log phase and diluted to OD_{600} = 0.1 (10^8 CFU/mL). The cells were analysed at the interface of the nanospiked surface using Synchrotron ATR-FTIR microspectroscopy at the Australian Synchrotron's Infrared Microspectroscopy (IRM) beamline with a Bruker Hyperion 2000 FTIR microscope equipped with a liquid nitrogen-cooled narrow-band mercury cadmium telluride (MCT) detector coupled to a VERTEX V80v FTIR spectrometer (Bruker Optik GmbH, Ettlingen, Germany). Macro-ATR-FTIR device equipped with a 100 mm diameter facet germanium (Ge) ATR crystal (nGe = 4.0) and a 20x IR objective (NA = 0.60; Bruker Optik GmbH, Ettlingen, Germany) was used. The unique combination of the high refractive index of the Ge ATR crystal and the high NA objective used in this device, when coupled to the synchrotron-IR beam, allowed the surface characterisation of the concentrated microbial cell samples to be performed at a high spatial resolution <1 µm. The samples were then drop cast onto BF_4, airdried and placed into the sample stage of the macro ATR-FTIR unit. The Ge ATR crystal was brought to the focus of the synchrotron-IR beam, and a background spectrum was recorded in air using 4 cm^{-1} spectral resolution and 256 co-added scans. The samples were then brought into contact with the sensing facet of the Ge ATR crystal, and a synchrotron macro ATR-FTIR spectral map was acquired. Chemical maps were generated from the embedded spectra by integrating the area under the relevant peaks using the OPUS 8.0 software. Multivariate data analysis was performed using CytoSpec v. 1.4.02 (Cytospec Inc., Boston, MA, USA) and the Unscrambler X 11.1 software package (CAMO Software AS, Oslo, Norway). HCA was carried out with Ward's algorithm, and cluster imaging was carried out with the processed second derivative spectra by assigning five clusters to be generated. Spectral wavenumbers covering 1000–1080 cm^{-1} and 2080–3004 cm^{-1} were chosen for analysis as these regions contain the molecular information most relevant to the microbial samples, in particular, the protein, lipid, polysaccharide and nucleic acid signals. The selected clustering from HCA was imported into Unscrambler software to perform principal component analysis (PCA). The second (2nd) derivative was performed using the Unscrambler software. The Savitzky–Golay algorithm removed the broad baseline offset and curvature. In addition, the final spectra were further analysed by the extended multiplicative scatter correction (EMSC). The EMSC algorithm removes light scattering artefacts and normalises the spectra accounting for pathlength differences. After the EMSC correction, the PCA was performed using the Unscrambler X 11.1 software package. The first three principal components (PCs) were used to compare the unmodified and nanospiked Ti samples.

4.9. Statistics

Graphical data is represented with mean and standard deviation and plotted with GraphPad Prism v9.0.0 (GraphPad Software, CA, USA). A two-way ANOVA with post hoc analysis using the Bonferroni method of multiple comparisons was used to measure statistical significance, where a *P* value ≤ 0.05 was deemed significant. All experiments were performed in triplicate, except for the RNA sequencing experiment in which we used four replicates.

Acknowledgements

The authors acknowledge the funding and in-kind support from Corin Australia and the University of South Australia. The authors would also like to acknowledge the instruments assistance of Microscopy Australia, a facility that is funded by the University, and State and Federal Governments. We would also like to acknowledge the contribution of the South Australian Genomics Centre (SAGC) in the generation of data used in this publication. K.V. thanks NHMRC for Fellowship GNT1194466 and ARC for grant DP180101254.

Author contributions

A.H, experimental design, data generation and analysis, manuscript drafting and revision. **R.B**, experimental design, data generation, manuscript revision. **N.N**, data generation and analysis, manuscript revision. **V.K.T**, data analysis, manuscript revision, supervision. **J.W**, data generation and analysis, manuscript revision. **D.P**, data generation and analysis, manuscript revision. **J.P.V**, technical help with synchrotron, data analysis. **D.B**, manuscript revision K.**V**, supervision, funding, manuscript revision

Competing interests

The authors declare no competing interests.

5. References

1. Arciola, C.R., Campoccia, D., and Montanaro, L. Implant infections: adhesion, biofilm formation and immune evasion. *Nat Rev Microbiol*, 16(7): p. 397-409 (2018).
2. Edwards, A.M. Silence is golden for Staphylococcus. *Nature Microbiology*, 4(7): p. 1073-1074 (2019).
3. Sharma, D., Misba, L., and Khan, A.U. Antibiotics versus biofilm: an emerging battleground in microbial communities. *Antimicrob Resist Infect Control*, 8: p. 76 (2019).
4. Olsen, I. Biofilm-specific antibiotic tolerance and resistance. *European Journal of Clinical Microbiology & Infectious Diseases*, 34(5): p. 877-886 (2015).
5. Ribeiro, M., Monteiro, F.J., and Ferraz, M.P. Infection of orthopedic implants with emphasis on bacterial adhesion process and techniques used in studying bacterial-material interactions. *Biomatter*, 2(4): p. 176-194 (2012).
6. Teterycz, D., Ferry, T., Lew, D., Stern, R., Assal, M., Hoffmeyer, P., Bernard, L., and Uçkay, I. Outcome of orthopedic implant infections due to different staphylococci. *International Journal of Infectious Diseases*, 14(10): p. e913-e918 (2010).
7. Ciofu, O., Moser, C., Jensen, P.Ø., and Høiby, N. Tolerance and resistance of microbial biofilms. *Nature Reviews Microbiology*, 20(10): p. 621-635 (2022).
8. Hall, C.W. and Mah, T.-F. Molecular mechanisms of biofilm-based antibiotic resistance and tolerance in pathogenic bacteria. *FEMS Microbiology Reviews*, 41(3): p. 276-301 (2017).

9. Nilsson, M., Rybtke, M., Givskov, M., Høiby, N., Twetman, S., and Tolker-Nielsen, T. The dlt genes play a role in antimicrobial tolerance of Streptococcus mutans biofilms. *Int J Antimicrob Agents*, 48(3): p. 298-304 (2016).
10. Bright, R., Hayles, A., Wood, J., Palms, D., Brown, T., Barker, D., and Vasilev, K. Surfaces Containing Sharp Nanostructures Enhance Antibiotic Efficacy. *Nano Letters*, (2022).
11. Kok, T.W., Agrawal, N., Sathappan, S.S., and Chen, W.K. Risk factors for early implant-related surgical site infection. *J Orthop Surg (Hong Kong)*, 24(1): p. 72-6 (2016).
12. Enzler, M.J., Berbari, E., and Osmon, D.R. Antimicrobial prophylaxis in adults. *Mayo Clin Proc*, 86(7): p. 686-701 (2011).
13. Geetha, M., Singh, A.K., Asokamani, R., and Gogia, A.K. Ti based biomaterials, the ultimate choice for orthopaedic implants - A review. *Progress in Materials Science*, 54(3): p. 397-425 (2009).
14. Montanaro, L., Speziale, P., Campoccia, D., Ravaioli, S., Cangini, I., Pietrocola, G., Giannini, S., and Arciola, C.R. Scenery of Staphylococcus implant infections in orthopedics. *Future Microbiol*, 6(11): p. 1329-49 (2011).
15. Parvizi, J., Gehrke, T., and Chen, A.F. Proceedings of the International Consensus on Periprosthetic Joint Infection. *Bone Joint J*, 95-b(11): p. 1450-2 (2013).
16. Bright, R., Hayles, A., Wood, J., Ninan, N., Palms, D., Visalakshan, R.M., Burzava, A., Brown, T., Barker, D., and Vasilev, K. Bio-Inspired Nanostructured Ti-6Al-4V Alloy: The Role of Two Alkaline Etchants and the Hydrothermal Processing Duration on Antibacterial Activity. *Nanomaterials*, 12(7) (2022).
17. Ivanova, E.P., Linklater, D.P., Werner, M., Baulin, V.A., Xu, X., Vrancken, N., Rubanov, S., Hanssen, E., Wandiyanto, J., Truong, V.K., Elbourne, A., Maclaughlin, S., Juodkazis, S., and Crawford, R.J. The multi-faceted mechano-bactericidal mechanism of nanostructured surfaces. *Proceedings of the National Academy of Sciences*, 117(23): p. 12598-12605 (2020).
18. Ernst, C.M., Slavetinsky, C.J., Kuhn, S., Hauser, J.N., Nega, M., Mishra, N.N., Gekeler, C., Bayer, A.S., and Peschel, A. Gain-of-Function Mutations in the Phospholipid Flippase MprF Confer Specific Daptomycin Resistance. *mBio*, 9(6) (2018).
19. Di Martino, P. Extracellular polymeric substances, a key element in understanding biofilm phenotype. *AIMS Microbiol*, 4(2): p. 274-288 (2018).
20. Hayles, A., Hasan, J., Bright, R., Palms, D., Brown, T., Barker, D., and Vasilev, K. Hydrothermally etched titanium: a review on a promising mechano-bactericidal surface for implant applications. *Materials Today Chemistry*, 22: p. 100622 (2021).
21. Bright, R., Hayles, A., Fernandes, D., Visalakshan, R.M., Ninan, N., Palms, D., Burzava, A., Barker, D., Brown, T., and Vasilev, K. In Vitro Bactericidal Efficacy of Nanostructured Ti6Al4V Surfaces is Bacterial Load Dependent. *ACS Applied Materials & Interfaces*, 13(32): p. 38007-38017 (2021).
22. Hayles, A., Bright, R., Hasan, J., Wood, J., Palms, D., Barker, D., and Vasilev, K. Dual Species Bacterial Challenge of a Biomimetic Nanostructured Surface. *Advanced Materials Interfaces*, n/a(n/a): p. 2201583 (2022).
23. Peterson, B.W., van der Mei, H.C., Sjollema, J., Busscher, H.J., and Sharma, P.K. A distinguishable role of eDNA in the viscoelastic relaxation of biofilms. *mBio*, 4(5): p. e00497-13 (2013).
24. Singh, R., Sahore, S., Kaur, P., Rani, A., and Ray, P. Penetration barrier contributes to bacterial biofilm-associated resistance against only select antibiotics, and exhibits genus-, strain- and antibiotic-specific differences. *Pathogens and Disease*, 74(6): p. ftw056 (2016).
25. McBride, S.M. and Sonenshein, A.L. The dlt operon confers resistance to cationic antimicrobial peptides in Clostridium difficile. *Microbiology (Reading)*, 157(Pt 5): p. 1457-1465 (2011).
26. Manning, J.M. *Studies on the mechanism of action of D-amino acid transaminase*. in *Biochemistry of Vitamin B6 and PQQ*. 1994. Basel: Birkhäuser Basel.
27. Azam, M.A. and Jayaram, U. Inhibitors of alanine racemase enzyme: a review. *J Enzyme Inhib Med Chem*, 31(4): p. 517-26 (2016).
28. Ernst, C.M., Staubitz, P., Mishra, N.N., Yang, S.-J., Hornig, G., Kalbacher, H., Bayer, A.S., Kraus, D., and Peschel, A. The Bacterial Defensin Resistance Protein MprF Consists of Separable Domains for Lipid Lysinylation and Antimicrobial Peptide Repulsion. *PLOS Pathogens*, 5(11): p. e1000660 (2009).

29. Kochan, K., Nethercott, C., Taghavimoghaddam, J., Richardson, Z., Lai, E., Crawford, S.A., Peleg, A.Y., Wood, B.R., and Heraud, P. Rapid Approach for Detection of Antibiotic Resistance in Bacteria Using Vibrational Spectroscopy. *Analytical Chemistry*, 92(12): p. 8235-8243 (2020).
30. Cox, K.H., Ruiz-Bustos, E., Courtney, H.S., Dale, J.B., Pence, M.A., Nizet, V., Aziz, R.K., Gerling, I., Price, S.M., and Hasty, D.L. Inactivation of DltA Modulates Virulence Factor Expression in Streptococcus pyogenes. *PLOS ONE*, 4(4): p. e5366 (2009).
31. Ernst, C.M. and Peschel, A. Broad-spectrum antimicrobial peptide resistance by MprF-mediated aminoacylation and flipping of phospholipids. *Molecular Microbiology*, 80(2): p. 290-299 (2011).
32. Weidenmaier, C., Peschel, A., Kempf, V.A., Lucindo, N., Yeaman, M.R., and Bayer, A.S. DltABCD- and MprF-mediated cell envelope modifications of Staphylococcus aureus confer resistance to platelet microbicidal proteins and contribute to virulence in a rabbit endocarditis model. *Infect Immun*, 73(12): p. 8033-8 (2005).
33. Thitiananpakorn, K., Aiba, Y., Tan, X.-E., Watanabe, S., Kiga, K., Sato'o, Y., Boonsiri, T., Li, F.-Y., Sasahara, T., Taki, Y., Azam, A.H., Zhang, Y., and Cui, L. Association of mprF mutations with cross-resistance to daptomycin and vancomycin in methicillin-resistant Staphylococcus aureus (MRSA). *Scientific Reports*, 10(1): p. 16107 (2020).
34. Mechler, L., Bonetti, E.J., Reichert, S., Flötenmeyer, M., Schrenzel, J., Bertram, R., François, P., and Götz, F. Daptomycin Tolerance in the Staphylococcus aureus pitA6 Mutant Is Due to Upregulation of the dlt Operon. *Antimicrob Agents Chemother*, 60(5): p. 2684-91 (2016).
35. Izakovicova, P., Borens, O., and Trampuz, A. Periprosthetic joint infection: current concepts and outlook. *EFORT Open Rev*, 4(7): p. 482-494 (2019).
36. Linklater, D.P., Baulin, V.A., Juodkazis, S., Crawford, R.J., Stoodley, P., and Ivanova, E.P. Mechano-bactericidal actions of nanostructured surfaces. *Nature Reviews Microbiology*, 19(1): p. 8-22 (2021).
37. Ivanova, E.P., Hasan, J., Webb, H.K., Gervinskas, G., Juodkazis, S., Truong, V.K., Wu, A.H., Lamb, R.N., Baulin, V.A., Watson, G.S., Watson, J.A., Mainwaring, D.E., and Crawford, R.J. Bactericidal activity of black silicon. *Nat Commun*, 4: p. 2838 (2013).
38. Li, X., Tsui, K.-H., Tsoi, J.K.H., Green, D.W., Jin, X.-z., Deng, Y.Q., Zhu, Y.M., Li, X.G., Fan, Z., and Cheung, G.S.-p. A nanostructured anti-biofilm surface widens the efficacy against spindle-shaped and chain-forming rod-like bacteria. *Nanoscale*, 12(36): p. 18864-18874 (2020).
39. Elyasi, S., Khalili, H., Dashti-Khavidaki, S., and Mohammadpour, A. Vancomycin-induced nephrotoxicity: mechanism, incidence, risk factors and special populations. A literature review. *Eur J Clin Pharmacol*, 68(9): p. 1243-55 (2012).

6. Supplementary Information

Results

Characterization of nanostructured titanium

We fabricated the nanospiked Ti surface using an alkaline hydrothermal etching method previously described.[1] Material characterization was carried out to verify the consistency of the method (Fig. S1 and Table S1). We found a mean spike height of 306 ± 78 nm, and width of 75 ± 21 nm, which is consistent with previously published results. The mean roughness, as measured by arithmetic average (Ra) was 10.1 nm on the unmodified Ti, and 61.5 nm on the nanospiked Ti surface. EDS analysis showed a decrease in the proportion of Ti and an increase in O on the nanospiked surface, reflecting the oxidation of Ti resulting from the hydrothermal procedure. The change in surface wettability was measured using water contact angle, which showed a decrease from 40° to <10° on the nanospiked Ti surface. This indicates a substantial increase in the hydrophilicity of the surface.

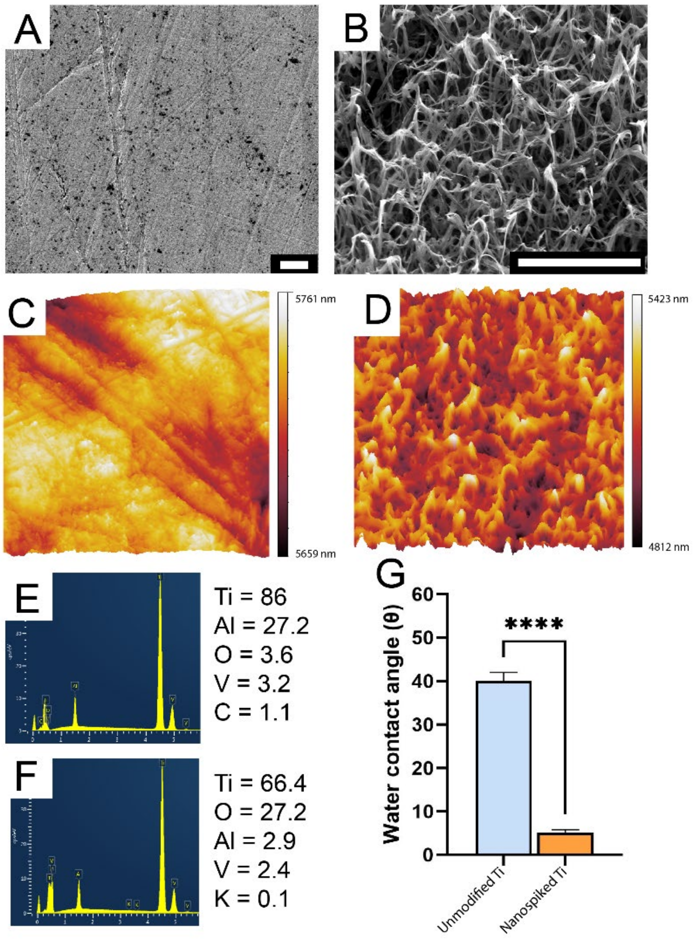

Fig. S1. Physical and Chemical Characterization of nanostructured titanium. A and B) SEM micrographs of the unmodified and nanospiked Ti surfaces, respectively. C and D) AFM images of unmodified and nanospiked Ti surfaces, show a degree of roughness. E and F) EDS measurements of the surface of unmodified and nanospiked Ti. G)

Table S1. Surface roughness and area measurements of unmodified and nanospiked titanium.

Measurement	Unmodified Ti	Nanospiked Ti
Arithmetic average (Ra), nm	10.1	61.5
Root mean square (RMS), nm	6.6	88.5
Surface Area, μm^2	25.2	50.3

Molecular properties of vancomycin

We aimed to measure the influence of the molecular charge of vancomycin on its efficacy against adherent *S. aureus* attached to both surface types. Vancomycin is a glycopeptide antibiotic that binds to the D-Ala-D-Ala residues on newly forming peptidoglycan sheets, preventing crosslinking from occurring.[2] Vancomycin was chosen due to its clinical relevance in prophylactic treatments during implant placement (Fig S2). The charge of vancomycin at physiological pH was calculated using the Henderson-Hasselbalch equation, with pKa values for titratable functional groups of vancomycin obtained in the relevant literature.[3]

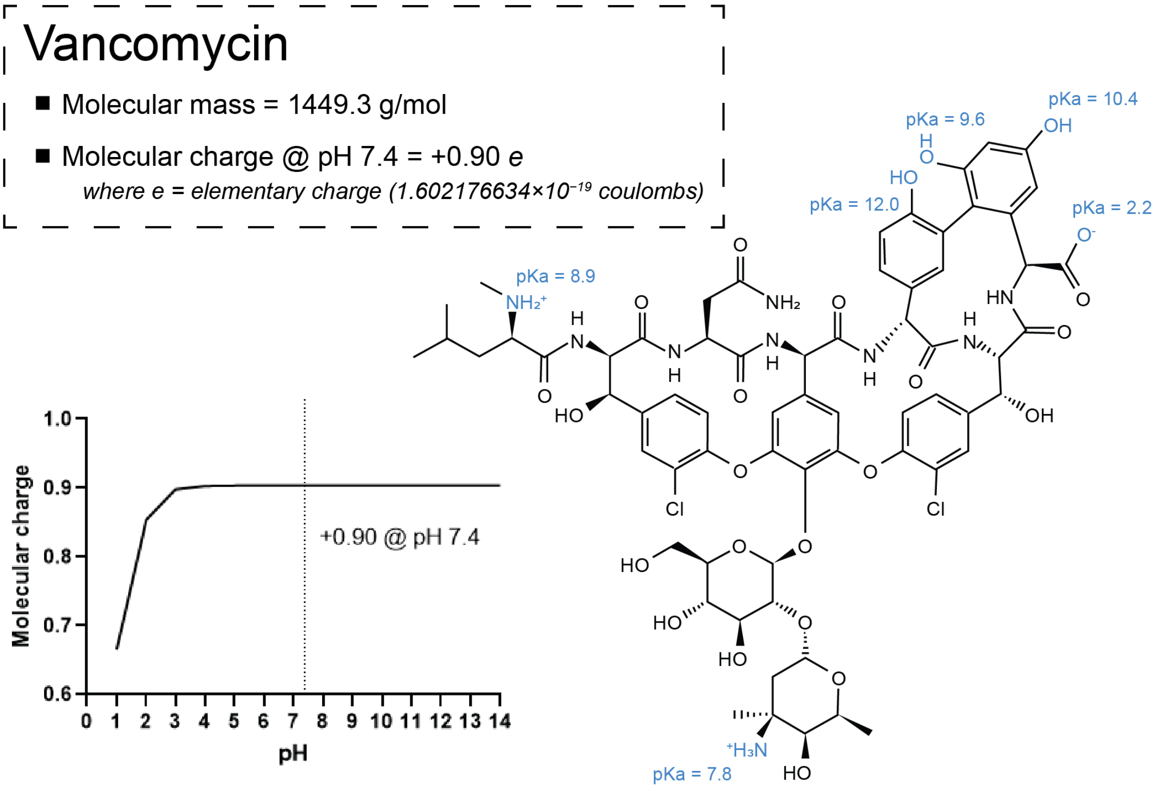

Fig. S2. The chemical structure, molecular mass and formal molecular charge of vancomycin at physiological pH.

Calculating the molecular charge of vancomycin

The charge of both antibiotics was calculated as a function of pH, using the Henderson-Hasselbalch equation, with pKa values for the titratable groups obtained from relevant literature.[3]

$$pH = pKa + \log_{10}\frac{[A-]}{[HA]}$$

Equation 1. The Henderson-Hasselbalch equation. K_a is the dissociation constant of the weak acid, $pK_a = -\log K_a$ and $[HA]$ and $[A-]$ are the molar concentrations of the weak acid and its conjugate base.[4]

For each of the empirically determined titratable groups on the antibiotics, the degree of dissociation was calculated by inputting the pK_a and pH values. To determine the overall molecular charge at each pH level, the degrees of dissociation for each titratable group, along with their contribution to charge, were combined to generate a net molecular charge. An arbitrary example is given below for two titratable groups at pH 10:

Titratable group	*pKa*	*Degree of dissociation*	*Contribution to charge*
R-COOH	1.9	0.9999	0 → –
$R\text{-}NH3^+$	8.35	0.9781	+ → 0

In this arbitrary example, the overall molecular charge at pH 10 would be calculated by the following:

$$\text{Charge} = (-1 \times 0.9999) + (1 \times [1 - 0.9781]) = -0.978$$

Equation 2. An example of the calculation used to obtain molecular charge values using the degree of dissociation of each titratable group in a molecule.

The activity of sub-MIC vancomycin

We investigated whether the synergy between nanospikes and vancomycin would persist if the vancomycin dosage was reduced to half its MIC value (Fig. S3). On the unmodified surface, the attachment of *S. aureus* for 3 h resulted in 80% post-treatment viability. With 6 h attachment, the post-treatment viability was approximately 95%. Contrasting this, attachment to the nanospiked surface was associated with a decrease in post-treatment viability. With a 6 h attachment, *S. aureus* had a viability of <1%.

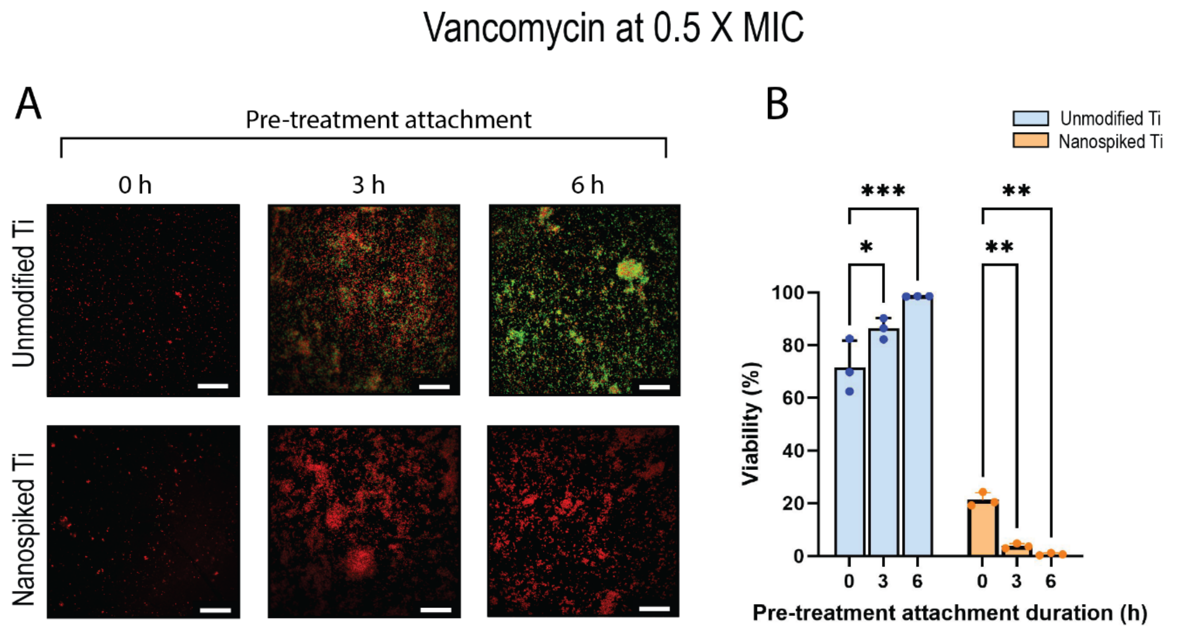

Fig. S3. Activity of sub-MIC dose vancomycin against *S. aureus* attached to the nanospiked surfaces for the increasing duration. A) The Live/Dead fluorescence micrographs obtained following attachment and subsequent vancomycin treatment. B) The mean post-treatment viability of *S. aureus* quantified from fluorescence micrographs. Scale bars represent 30 µm. * $P < 0.05$, ** $P < 0.01$, *** $P < 0.001$ mean ± SD

Differential gene expression of S. aureus adherent on unmodified or nanospiked Ti

Table S2. Common DEGs identified in both the planktonic vs AR-Ti and HTE-Ti comparisons. GeneIDs are specific to the *S. aureus* ATCC25923 reference genome, as listed on the NCBI database. Gene symbols are provided where available and were acquired from the annotated reference genome. DEGs are sorted by log fold-change, where a positive value corresponds to an upregulation on HTE-Ti compared to planktonic.

GeneID	Symbol	Product Description	Log FC
KQ76_RS04860	sspB	cysteine protease staphopain B	5.875099
KQ76_RS01800		hypothetical protein	4.838287
KQ76_RS00865		3-hydroxyacyl-CoA dehydrogenase/enoyl-CoA hydratase family protein	4.677278
KQ76_RS04855	sspC	staphostatin B	4.58259
KQ76_RS00870		acyl-CoA dehydrogenase family protein	4.510791
KQ76_RS13580	aur	zinc metalloproteinase aureolysin	4.488095
KQ76_RS04300		argininosuccinate synthase	4.20662
KQ76_RS10335		cyclic lactone autoinducer peptide	4.038172
KQ76_RS00875		acyl--CoA ligase	3.728256
KQ76_RS04295	argH	argininosuccinate lyase	3.667964
KQ76_RS05000	purN	phosphoribosylglycinamide formyltransferase	3.470311
KQ76_RS00860		thiolase family protein	3.424063
KQ76_RS09170		excalibur calcium-binding domain-containing protein	3.362537
KQ76_RS07605		hypothetical protein	3.342676
KQ76_RS11430	rplX	50S ribosomal protein L24	3.234334
KQ76_RS08440		DUF4930 family protein	3.012092
KQ76_RS04440		ATP-binding cassette domain-containing protein	2.975198
KQ76_RS07600		hypothetical protein	2.956842

KQ76_RS11440	rpsQ	30S ribosomal protein S17	2.918199
KQ76_RS11475	rplW	50S ribosomal protein L23	2.914579
KQ76_RS06235		MerR family transcriptional regulator	2.913718
KQ76_RS01795		L-cystine transporter	2.84513
KQ76_RS06785		amidohydrolase	2.83644
KQ76_RS11435	rplN	50S ribosomal protein L14	2.796281
KQ76_RS11425	rplE	50S ribosomal protein L5	2.760127
KQ76_RS04400		MAP domain-containing protein	2.734562
KQ76_RS01155	esxA	WXG100 family type VII secretion effector EsxA	2.622365
KQ76_RS10750	atpE	F0F1 ATP synthase subunit C	2.618355
KQ76_RS09985		staphostatin A	2.612195
KQ76_RS13925		S8 family serine peptidase	2.606231
KQ76_RS13920		SAR2788 family putative toxin	2.597913
KQ76_RS06770	dapA	4-hydroxy-tetrahydrodipicolinate synthase	2.593283
KQ76_RS11465	rpsS	30S ribosomal protein S19	2.563046
KQ76_RS10185		hypothetical protein	2.550667
KQ76_RS11450	rplP	50S ribosomal protein L16	2.531738
KQ76_RS04995	purM	phosphoribosylformylglycinamidine cyclo-ligase	2.527018
KQ76_RS08790		alanine--glyoxylate aminotransferase family protein	2.493834
KQ76_RS11445	rpmC	50S ribosomal protein L29	2.481996
KQ76_RS06780	dapD	2,3,4,5-tetrahydropyridine-2,6-dicarboxylate N-acetyltransferase	2.479461
KQ76_RS11460	rplV	50S ribosomal protein L22	2.440601
KQ76_RS05625		cell division protein SepF	2.430133
KQ76_RS06455		catalase	2.399397
KQ76_RS05955	hslV	ATP-dependent protease subunit HslV	2.397299
KQ76_RS11115		YjiH family protein	2.389067
KQ76_RS05680		aspartate carbamoyltransferase catalytic subunit	2.363472
KQ76_RS06925		PTS glucose transporter subunit IIA	2.359194
KQ76_RS05685		dihydroorotase	2.34079
KQ76_RS07290	lukS-PV	Panton-Valentine bi-component leukocidin subunit S	2.288209
KQ76_RS04445		peptide ABC transporter substrate-binding protein	2.286407
KQ76_RS04965	purK	5-(carboxyamino)imidazole ribonucleotide synthase	2.28384
KQ76_RS02780		hypothetical protein	2.273974
KQ76_RS07020		dynamin family protein	2.261298
KQ76_RS04435		ABC transporter ATP-binding protein	2.25412
KQ76_RS11480	rplD	50S ribosomal protein L4	2.25045
KQ76_RS05965	codY	GTP-sensing pleiotropic transcriptional regulator codY	2.224011
KQ76_RS08795	serA	phosphoglycerate dehydrogenase	2.217932
KQ76_RS10755	atpB	F0F1 ATP synthase subunit A	2.197726
KQ76_RS11455	rpsC	30S ribosomal protein S3	2.185476
KQ76_RS05690		carbamoyl phosphate synthase small subunit	2.174814
KQ76_RS06540	acnA	aconitate hydratase AcnA	2.174178
KQ76_RS11420		type Z 30S ribosomal protein S14	2.17299
KQ76_RS11415	rpsH	30S ribosomal protein S8	2.170202
KQ76_RS04280		ornithine--oxo-acid transaminase	2.149646
KQ76_RS06680		Cof-type HAD-IIB family hydrolase	2.126842
KQ76_RS06820		acylphosphatase	2.122783

KQ76_RS13750	lip1	YSIRK domain-containing triacylglycerol lipase Lip1	2.119379
KQ76_RS04030		methionine ABC transporter ATP-binding protein	2.105125
KQ76_RS07685	proC	pyrroline-5-carboxylate reductase	2.095534
KQ76_RS08640	icd	NADP-dependent isocitrate dehydrogenase	2.036681
KQ76_RS08965		rRNA pseudouridine synthase	2.025482
KQ76_RS07970		deoxyribonuclease IV	1.970027
KQ76_RS11485	rplC	50S ribosomal protein L3	1.96629
KQ76_RS10770	upp	uracil phosphoribosyltransferase	1.963157
KQ76_RS11690	ureC	urease subunit alpha	1.953105
KQ76_RS07805	nusB	transcription antitermination factor NusB	1.940483
KQ76_RS11395	rpmD	50S ribosomal protein L30	1.928253
KQ76_RS04550		NAD kinase	1.890976
KQ76_RS05640		DivIVA domain-containing protein	1.86845
KQ76_RS11375	infA	translation initiation factor IF-1	1.847728
KQ76_RS00620		DUF2294 domain-containing protein	1.829735
KQ76_RS06930	msrB	peptide-methionine (R)-S-oxide reductase MsrB	1.828725
KQ76_RS08645		citrate synthase	1.769368
KQ76_RS04430		ABC transporter permease	1.760555
KQ76_RS06425	thrC	threonine synthase	1.756772
KQ76_RS06765		aspartate-semialdehyde dehydrogenase	1.737707
KQ76_RS10090		thioredoxin family protein	1.734299
KQ76_RS13450		CitMHS family transporter	1.734107
KQ76_RS04035		ABC transporter permease	1.7303
KQ76_RS08210	pxpA	5-oxoprolinase subunit PxpA	1.72953
KQ76_RS08675		NAD-dependent malic enzyme 4	1.725404
KQ76_RS05695	carB	carbamoyl-phosphate synthase large subunit	1.724676
KQ76_RS10450	leuB	3-isopropylmalate dehydrogenase	1.72296
KQ76_RS10445		2-isopropylmalate synthase	1.71414
KQ76_RS05945	trmFO	methylenetetrahydrofolate--tRNA-(uracil(54)- C(5))-methyltransferase (FADH(2)-oxidizing) TrmFO	1.711381
KQ76_RS08855	acsA	acetate--CoA ligase	1.677067
KQ76_RS06775	dapB	4-hydroxy-tetrahydrodipicolinate reductase	1.676859
KQ76_RS06240	glnA	type I glutamate--ammonia ligase	1.652739
KQ76_RS08890		hypothetical protein	1.634379
KQ76_RS01010		ribitol-5-phosphate dehydrogenase	1.61297
KQ76_RS08010		glycine--tRNA ligase	1.594851
KQ76_RS13590		hypothetical protein	1.593444
KQ76_RS11390	rplO	50S ribosomal protein L15	1.567387
KQ76_RS11400	rpsE	30S ribosomal protein S5	1.56473
KQ76_RS09095		CPBP family intramembrane metalloprotease	1.525028
KQ76_RS05675		NCS2 family nucleobase:cation symporter	1.504702
KQ76_RS08585	dnaI	primosomal protein DnaI	1.498073
KQ76_RS08665		acetyl-CoA carboxylase carboxyltransferase subunit alpha	1.481138
KQ76_RS07230	ebpS	elastin-binding protein EbpS	1.477509
KQ76_RS11410	rplF	50S ribosomal protein L6	1.464961
KQ76_RS08205		divalent metal cation transporter	1.45291
KQ76_RS07125		YpiB family protein	1.43023
KQ76_RS01185		TIGR04197 family type VII secretion effector	1.429717

KQ76_RS06370	cls	cardiolipin synthase	1.422521
KQ76_RS01160	esaA	type VII secretion protein EsaA	1.422495
KQ76_RS05610	ftsZ	cell division protein FtsZ	1.405476
KQ76_RS01165	essA	type VII secretion protein EssA	1.404665
KQ76_RS03105		glycosyltransferase family 2 protein	1.39927
KQ76_RS10130		aminotransferase class I/II-fold pyridoxal phosphate-dependent enzyme	1.38947
KQ76_RS08420	rplU	50S ribosomal protein L21	1.38866
KQ76_RS05950	xerC	tyrosine recombinase XerC	1.383844
KQ76_RS06430	thrB	homoserine kinase	1.380716
KQ76_RS07790		polyprenyl synthetase family protein	1.360145
KQ76_RS01450	glpT	glycerol-3-phosphate transporter	1.358195
KQ76_RS11380		adenylate kinase	1.35682
KQ76_RS07680		SDR family oxidoreductase	1.347439
KQ76_RS10425	ilvD	dihydroxy-acid dehydratase	1.329832
KQ76_RS02765		AMP-binding protein	1.314837
KQ76_RS06415		aspartate kinase	1.304811
KQ76_RS08215		acetyl-CoA carboxylase biotin carboxylase subunit	1.296582
KQ76_RS05670	pyrR	bifunctional pyr operon transcriptional regulator/uracil phosphoribosyltransferase PyrR	1.293504
KQ76_RS09930	gatB	Asp-tRNA(Asn)/Glu-tRNA(Gln) amidotransferase	1.281921
KQ76_RS07235		ATP-dependent DNA helicase	1.275003
KQ76_RS03350	mgrA	HTH-type transcriptional regulator MgrA	1.272681
KQ76_RS08865		acetoin utilization protein AcuC	1.253553
KQ76_RS04660		competence protein ComK	1.234448
KQ76_RS06435		Cof-type HAD-IIB family hydrolase	1.232642
KQ76_RS11775		2-hydroxyacid dehydrogenase family protein	1.232146
KQ76_RS07140	aroB	3-dehydroquinate synthase	1.223334
KQ76_RS10945	czrA	Zn(II)-responsive metalloregulatory transcriptional repressor CzrA	1.218973
KQ76_RS11405	rplR	50S ribosomal protein L18	1.216407
KQ76_RS05105	def	peptide deformylase	1.202483
KQ76_RS03825	gap	type I glyceraldehyde-3-phosphate dehydrogenase	1.201252
KQ76_RS05825	plsX	phosphate acyltransferase PlsX	1.193764
KQ76_RS02770		thiolase family protein	1.178227
KQ76_RS04955	folD	bifunctional methylenetetrahydrofolate dehydrogenase/methenyltetrahydrofolate cyclohydrolase FolD	1.173907
KQ76_RS06225	hflX	GTPase HflX	1.162707
KQ76_RS11685		urease subunit beta	1.155727
KQ76_RS05920	sucD	succinate--CoA ligase subunit alpha	1.126213
KQ76_RS07620		DUF1672 domain-containing protein	1.115425
KQ76_RS02975		hypothetical protein	1.108119
KQ76_RS05665		RluA family pseudouridine synthase	1.093772
KQ76_RS07975		DEAD/DEAH box helicase	1.087345
KQ76_RS11365	rpsM	30S ribosomal protein S13	1.082828
KQ76_RS10430	ilvB	biosynthetic-type acetolactate synthase large subunit	1.075309
KQ76_RS07670		aldo/keto reductase	1.06602
KQ76_RS07145	aroC	chorismate synthase	1.063711

KQ76_RS01790		NADPH-dependent oxidoreductase	1.049088
KQ76_RS08960		YtxH domain-containing protein	0.998704
KQ76_RS07570		hypothetical protein	0.997274
KQ76_RS04985	purL	phosphoribosylformylglycinamidine synthase subunit PurL	0.996956
KQ76_RS03670		GGDEF domain-containing protein	0.988453
KQ76_RS09805		aminopeptidase	0.983619
KQ76_RS04040		MetQ/NlpA family ABC transporter substrate-binding protein	0.960481
KQ76_RS00285		L-lactate permease	0.945314
KQ76_RS08050	floA	flotillin-like protein FloA	0.874902
KQ76_RS02595	rplL	50S ribosomal protein L7/L12	0.869492
KQ76_RS12715		AbgT family transporter	0.86198
KQ76_RS05830	fabD	ACP S-malonyltransferase	0.861921
KQ76_RS06555	plsY	glycerol-3-phosphate 1-O-acyltransferase PlsY	0.855538
KQ76_RS12230		NarK/NasA family nitrate transporter	0.846675
KQ76_RS07375		phage major capsid protein	0.844868
KQ76_RS06755		ATP-binding cassette domain-containing protein	0.808771
KQ76_RS02580	rplK	50S ribosomal protein L11	0.801481
KQ76_RS07325		phage tail family protein	0.777179
KQ76_RS03210	graS	histidine kinase GraS/ApsS	0.770472
KQ76_RS09175		DUF4352 domain-containing protein	0.76621
KQ76_RS02590	rplJ	50S ribosomal protein L10	0.762473
KQ76_RS05605	ftsA	cell division protein FtsA	0.758464
KQ76_RS05745		hypothetical protein	0.713196
KQ76_RS03215	vraF	ABC transporter ATP-binding protein VraF	0.703157
KQ76_RS07610		site-specific integrase	0.701294
KQ76_RS10640	cls	cardiolipin synthase	0.699256
KQ76_RS08860		hypothetical protein	0.676057
KQ76_RS07700		AraC family transcriptional regulator	0.638272
KQ76_RS12190		YbgA family protein	0.624883
KQ76_RS01145		hypothetical protein	0.623133
KQ76_RS05305	isdA	LPXTG-anchored heme-scavenging protein IsdA	0.563751
KQ76_RS06195	glpK	glycerol kinase GlpK	0.556582
KQ76_RS05820	fapR	transcription factor FapR	0.546234
KQ76_RS10645		HD domain-containing protein	0.526614
KQ76_RS06100		SDR family NAD(P)-dependent oxidoreductase	0.500085
KQ76_RS08715	ald	alanine dehydrogenase	0.495937
KQ76_RS11320	rpsI	30S ribosomal protein S9	0.494267
KQ76_RS07280		hypothetical protein	0.477356
KQ76_RS04415	fabF	beta-ketoacyl-ACP synthase II	0.471705
KQ76_RS07460		DUF1024 family protein	0.469275
KQ76_RS05770	rlmN	23S rRNA (adenine(2503)-C(2))-methyltransferase RlmN	0.454999
KQ76_RS02745	hxlA	3-hexulose-6-phosphate synthase	0.446456
KQ76_RS06705		ABC transporter permease	0.43506
KQ76_RS06230		aminotransferase class I/II-fold pyridoxal phosphate-dependent enzyme	0.423676
KQ76_RS12695	cntL	D-histidine (S)-2-aminobutanoyltransferase CntL	-0.48559

KQ76_RS11100		UDPGP type 1 family protein	-0.51493
KQ76_RS02485	pdxT	pyridoxal 5'-phosphate synthase glutaminase subunit PdxT	-0.51761
KQ76_RS01875		superantigen-like protein SSL1	-0.52909
KQ76_RS10360		LacI family DNA-binding transcriptional regulator	-0.55212
KQ76_RS11585	moaA	GTP 3',8-cyclase MoaA	-0.57951
KQ76_RS11590	mobA	molybdenum cofactor guanylyltransferase MobA	-0.58293
KQ76_RS09335	sei	staphylococcal enterotoxin type I	-0.62108
KQ76_RS00805		response regulator transcription factor	-0.63308
KQ76_RS01930		restriction endonuclease subunit S	-0.64915
KQ76_RS00280		DUF1648 domain-containing protein	-0.65494
KQ76_RS00645		YagU family protein	-0.67155
KQ76_RS11550		hypothetical protein	-0.67641
KQ76_RS00480		XRE family transcriptional regulator	-0.69019
KQ76_RS03890		hypothetical protein	-0.69421
KQ76_RS13325		aspartate 1-decarboxylase	-0.71437
KQ76_RS13940		DUF3147 family protein	-0.72246
KQ76_RS01530		ABC-2 transporter permease	-0.75301
KQ76_RS01275		DUF4467 domain-containing protein	-0.78786
KQ76_RS13605	manA	mannose-6-phosphate isomerase, class I	-0.81023
KQ76_RS01910		superantigen-like protein SSL9	-0.81606
KQ76_RS12425		6-carboxyhexanoate--CoA ligase	-0.84205
KQ76_RS10190		TDT family transporter	-0.84813
KQ76_RS12215		DUF3139 domain-containing protein	-0.88081
KQ76_RS01915		superantigen-like protein SSL10	-0.89397
KQ76_RS15025		transposase	-0.93004
KQ76_RS12320	adcA	zinc ABC transporter substrate-binding lipoprotein AdcA	-0.95414
KQ76_RS00795		isoprenylcysteine carboxyl methyltransferase family protein	-0.9687
KQ76_RS12285	nirD	nitrite reductase small subunit NirD	-0.98992
KQ76_RS12415	hlgB	bi-component gamma-hemolysin HlgAB/HlgCB subunit B	-1.06645
KQ76_RS13440	nrdG	anaerobic ribonucleoside-triphosphate reductase activating protein	-1.14315
KQ76_RS05525		YfcC family protein	-1.2518
KQ76_RS11300	alsS	acetolactate synthase AlsS	-1.28025

Table S3. Unique DEGs identified in the planktonic vs unmodified Ti comparison. GeneIDs are specific to *S. aureus* ATCC25923 reference genome, as listed on the NCBI database. Gene symbols are provided where available and were acquired from the annotated reference genome. DEGs are sorted by log fold-change, where a positive value corresponds to an upregulation on AR-Ti compared to planktonic.

GeneID	Symbol	Product Description	Log FC
KQ76_RS09980	scpA	cysteine protease staphopain A	5.113875
KQ76_RS00880		acyl CoA:acetate/3-ketoacid CoA transferase	3.502256
KQ76_RS06420		homoserine dehydrogenase	3.212019
KQ76_RS06825		5-bromo-4-chloroindolyl phosphate hydrolysis family protein	2.758667
KQ76_RS02615		ribosomal L7Ae/L30e/S12e/Gadd45 family protein	2.517145

KQ76_RS07285	lukF-PV	Panton-Valentine bi-component leukocidin subunit F	2.402489
KQ76_RS07950		superoxide dismutase	2.351649
KQ76_RS08670	accD	acetyl-CoA carboxylase, carboxyltransferase subunit beta	2.334499
KQ76_RS05960	hslU	ATP-dependent protease ATPase subunit HslU	2.320309
KQ76_RS02620	rpsL	30S ribosomal protein S12	2.314879
KQ76_RS01090	rbsD	D-ribose pyranase	2.256099
KQ76_RS06935	msrA	peptide-methionine (S)-S-oxide reductase MsrA	2.156539
KQ76_RS02625	rpsG	30S ribosomal protein S7	2.103091
KQ76_RS13615		amidase domain-containing protein	2.10054
KQ76_RS01150		CHAP domain-containing protein	2.023817
KQ76_RS13980	rpmH	50S ribosomal protein L34	1.851371
KQ76_RS07810		Asp23/Gls24 family envelope stress response protein	1.776191
KQ76_RS10655	yidC	membrane protein insertase YidC	1.68573
KQ76_RS10910	deoD	purine-nucleoside phosphorylase	1.684355
KQ76_RS12810		Hypothetical protein	1.671551
KQ76_RS13190	isaA	lytic transglycosylase IsaA	1.65213
KQ76_RS08590		replication initiation and membrane attachment family protein	1.614407
KQ76_RS01805		Hypothetical protein	1.605025
KQ76_RS04510	mecA	adaptor protein MecA	1.584948
KQ76_RS03555		5'-3'-deoxyribonucleotidase	1.57959
KQ76_RS11490	rpsJ	30S ribosomal protein S10	1.451716
KQ76_RS08950	dat	D-amino-acid transaminase	1.375269
KQ76_RS01020	tarS	poly(ribitol-phosphate) beta-N-acetylglucosaminyltransferase	1.368601
KQ76_RS12220		MarR family transcriptional regulator	1.318169
KQ76_RS07655	xerD	site-specific tyrosine recombinase XerD	1.29262
KQ76_RS11715	sarR	HTH-type transcriptional regulator SarR	1.232636
KQ76_RS06045	infB	translation initiation factor IF-2	1.213806
KQ76_RS08765		GAF domain-containing protein	1.20107
KQ76_RS01655		primase alpha helix C-terminal domain-containing protein	1.198253
KQ76_RS08595	nrdR	transcriptional regulator NrdR	1.189821
KQ76_RS07130		Hypothetical protein	1.185884
KQ76_RS01180	essC	type VII secretion protein EssC	1.185822
KQ76_RS13245		amidohydrolase family protein	1.150507
KQ76_RS01125	lytM	glycine-glycine endopeptidase LytM	1.150078
KQ76_RS03675		undecaprenyl/decaprenyl-phosphate alpha-N-acetylglucosaminyl 1-phosphate transferase	1.132165
KQ76_RS10440	ilvC	ketol-acid reductoisomerase	1.032815
KQ76_RS01005		D-ribitol-5-phosphate cytidylyltransferase	1.003806
KQ76_RS03120		ABC transporter ATP-binding protein/permease	0.994827
KQ76_RS05595	murD	UDP-N-acetylmuramoyl-L-alanine--D-glutamate ligase	0.984699
KQ76_RS08970		polysaccharide biosynthesis protein	0.984495
KQ76_RS10955		Hypothetical protein	0.974307
KQ76_RS05175		Nramp family divalent metal transporter	0.972957
KQ76_RS08055		Hypothetical protein	0.94747
KQ76_RS07015		5'-3' exonuclease	0.946654

KQ76_RS06010	rseP	RIP metalloprotease RseP	0.910551
KQ76_RS10025		SLC13 family permease	0.888286
KQ76_RS10290		site-specific integrase	0.841203
KQ76_RS13910		IS30 family transposase	0.835257
KQ76_RS11360	rpsK	30S ribosomal protein S11	0.832859
KQ76_RS01345		ROK family protein	0.781308
KQ76_RS07990	rpoD	RNA polymerase sigma factor RpoD	0.752628
KQ76_RS04160	dltB	PG:teichoic acid D-alanyltransferase DltB	0.747144
KQ76_RS11350	rplQ	50S ribosomal protein L17	0.728976
KQ76_RS03330		Hypothetical protein	0.715446
KQ76_RS09045	ribD	bifunctional diaminohydroxyphosphoribosylaminopyrimidine deaminase/5-amino-6-(5-phosphoribosylamino)uracil reductase RibD	0.701207
KQ76_RS07580		DUF739 family protein	0.659698
KQ76_RS11820		YafY family transcriptional regulator	0.653243
KQ76_RS11355		DNA-directed RNA polymerase subunit alpha	0.650514
KQ76_RS07135	aroA	3-phosphoshikimate 1-carboxyvinyltransferase	0.647774
KQ76_RS06595	mprF	bifunctional lysylphosphatidylglycerol flippase/synthetase MprF	0.635113
KQ76_RS06790		alanine racemase	0.628968
KQ76_RS07505		Hypothetical protein	0.621101
KQ76_RS06565	parC	DNA topoisomerase IV subunit A	0.586945
KQ76_RS09800		acyl-CoA thioesterase	0.542792
KQ76_RS04905		osmotic stress response protein	0.538974
KQ76_RS04170	dltD	D-alanyl-lipoteichoic acid biosynthesis protein DltD	0.537298
KQ76_RS03230		inorganic phosphate transporter	0.512248
KQ76_RS09455	yhaM	3'-5' exoribonuclease YhaM	0.508467
KQ76_RS13330	panC	pantoate--beta-alanine ligase	-0.50484
KQ76_RS11725		PH domain-containing protein	-0.53643
KQ76_RS02530		PIN/TRAM domain-containing protein	-0.54933
KQ76_RS02255	rsmA	16S rRNA (adenine(1518)-N(6)/adenine(1519)-N(6))-dimethyltransferase RsmA	-0.55135
KQ76_RS01225		TIGR01741 family protein	-0.61338
KQ76_RS00120		MBL fold metallo-hydrolase	-0.62953
KQ76_RS10825		aldehyde dehydrogenase family protein	-0.66492
KQ76_RS11955		galactose mutarotase	-0.69782
KQ76_RS12160		DUF2871 domain-containing protein	-0.71906
KQ76_RS01405		lipoate--protein ligase	-0.76489
KQ76_RS00850		Hypothetical protein	-0.78275
KQ76_RS04715		Hypothetical protein	-1.08626
KQ76_RS08305		SAS049 family protein	-1.17631
KQ76_RS11030		tRNA-Gln	-1.18244

Table S4. Unique DEGs identified in the planktonic vs nanospiked Ti comparison. GeneIDs are specific to *S. aureus* ATCC25923 reference genome, as listed on NCBI database. Gene symbols are provided where available and were acquired from the annotated reference genome. DEGs are sorted by log fold-change, where a positive value corresponds to an upregulation on HTE-Ti compared to planktonic.

GeneID	Symbol	Product Description	Log FC
KQ76_RS05980		Hypothetical protein	2.555589
KQ76_RS07475		DUF3113 family protein	2.449168
KQ76_RS07595		Hypothetical protein	2.218871
KQ76_RS00290	spa	staphylococcal protein A	2.167831
KQ76_RS09240		DUF1433 domain-containing protein	2.141849
KQ76_RS08560	rpmI	50S ribosomal protein L35	2.098789
KQ76_RS15110		Hypothetical protein	1.877204
KQ76_RS13860	cna	collagen adhesin Cna	1.854876
KQ76_RS04990	purF	amidophosphoribosyltransferase	1.558328
KQ76_RS04960	purE	5-(carboxyamino)imidazole ribonucleotide mutase	1.523435
KQ76_RS07480		DUF1064 domain-containing protein	1.495138
KQ76_RS08435		Hypothetical protein	1.40529
KQ76_RS07675		Hypothetical protein	1.398757
KQ76_RS02865		Rrf2 family transcriptional regulator	1.364921
KQ76_RS05160		spermidine/putrescine ABC transporter substrate-binding protein	1.24288
KQ76_RS07495		ATP-binding protein	1.096448
KQ76_RS11910	hutI	imidazolonepropionase	0.911249
KQ76_RS13120	pruA	L-glutamate gamma-semialdehyde dehydrogenase	0.851765
KQ76_RS07500		conserved phage C-terminal domain-containing protein	0.850492
KQ76_RS07575		transcriptional regulator	0.812446
KQ76_RS05410	sdhB	succinate dehydrogenase iron-sulfur subunit	0.804421
KQ76_RS07445		DUF1381 domain-containing protein	0.736383
KQ76_RS08220		acetyl-CoA carboxylase biotin carboxyl carrier protein subunit	0.68408
KQ76_RS01605	ssb	single-stranded DNA-binding protein	0.678081
KQ76_RS03630		UDP-N-acetylmuramate dehydrogenase	0.662163
KQ76_RS06900		GNAT family N-acetyltransferase	0.653498
KQ76_RS07555		Hypothetical protein	0.653268
KQ76_RS06950		thymidylate synthase	0.60972
KQ76_RS03320		TIGR00730 family Rossman fold protein	0.559462
KQ76_RS07245		ferredoxin	0.549694
KQ76_RS13075		hydroxymethylglutaryl-CoA synthase	0.519838
KQ76_RS07465		phi PVL orf 51-like protein	0.513307
KQ76_RS07345		Ig-like domain-containing protein	0.469806
KQ76_RS09720		glutamate-1-semialdehyde 2,1-aminomutase	0.462793
KQ76_RS12380		2,3-diphosphoglycerate-dependent phosphoglycerate mutase	-0.37241
KQ76_RS02350	hpt	hypoxanthine phosphoribosyltransferase	-0.3979
KQ76_RS05935	dprA	DNA-processing protein DprA	-0.42096
KQ76_RS08455		A24 family peptidase	-0.45714
KQ76_RS00205		TetR/AcrR family transcriptional regulator	-0.47698
KQ76_RS02935		DUF1934 domain-containing protein	-0.47713
KQ76_RS05535		TDT family transporter	-0.4862
KQ76_RS02880		DUF443 domain-containing protein	-0.49468
KQ76_RS13340		oxidoreductase	-0.51852
KQ76_RS11085	sepA	multidrug efflux transporter SepA	-0.51959

KQ76_RS02895		DUF443 family protein	-0.52915
KQ76_RS01725		Abi family protein	-0.55537
KQ76_RS13815		energy-coupling factor transporter transmembrane protein EcfT	-0.55653
KQ76_RS02280	spoVG	septation regulator SpoVG	-0.56215
KQ76_RS00150		Hypothetical protein	-0.56732
KQ76_RS11095		hemolysin III family protein	-0.57857
KQ76_RS12325		Txe/YoeB family addiction module toxin	-0.59744
KQ76_RS09215		DUF1433 domain-containing protein	-0.62965
KQ76_RS01220		Hypothetical protein	-0.64028
KQ76_RS12790		tandem-type lipoprotein	-0.67805
KQ76_RS15240		Hypothetical protein	-0.70879
KQ76_RS04390		Hypothetical protein	-0.73118
KQ76_RS14290		Hypothetical protein	-0.74717
KQ76_RS01615		type II toxin-antitoxin system PemK/MazF family toxin	-0.74989
KQ76_RS00490	capA	capsular polysaccharide type 5/8 biosynthesis protein CapA	-0.75664
KQ76_RS09325	sen	staphylococcal enterotoxin type N	-0.79941
KQ76_RS12260	narI	respiratory nitrate reductase subunit gamma	-0.8118
KQ76_RS00710		Hypothetical protein	-0.8359
KQ76_RS03945		Hypothetical protein	-0.85758
KQ76_RS01935		superantigen-like protein SSL11	-0.8598
KQ76_RS11605	mobB	molybdopterin-guanine dinucleotide biosynthesis protein B	-0.87355
KQ76_RS04385		L-threonylcarbamoyladenylate synthase	-0.89221
KQ76_RS02695		NAD(P)H-dependent oxidoreductase	-0.89359
KQ76_RS01520		DUF3169 family protein	-0.9132
KQ76_RS12890		LysE family transporter	-0.91346
KQ76_RS09205		DUF1433 domain-containing protein	-0.92525
KQ76_RS08885		Hypothetical protein	-0.96256
KQ76_RS15225		Hypothetical protein	-0.97658
KQ76_RS12420		QueT transporter family protein	-0.97958
KQ76_RS00170	mcrC	5-methylcytosine-specific restriction endonuclease system specificity protein McrC	-1.05957
KQ76_RS15065		Hypothetical protein	-1.15972
KQ76_RS10010		nitric oxide synthase oxygenase	-1.72181
KQ76_RS00920		L-lactate dehydrogenase	-1.80673
KQ76_RS13555	arcD	arginine-ornithine antiporter	-3.74501

Table S5 lists a summary of the spectral wavelength ranges of relevant chemical bond signatures associated with different biological structures. Lipids were identified by infrared signatures associated with C-H stretching of alkanes, proteins were identified by C=O stretching and N-H deformation in amides, and polysaccharides were identified by C-O stretching in 1° and 2° alcohols. LPG was identified using C-N stretching and N-H bending from its additional amine groups. D-alanylated teichoic acids were identified by the C-O-C vibration associated with esters.

Table S5. Summary of relevant *S. aureus* cell components and products, along with their chemical bond markers and associated spectral regions. Peaks identified in Fig. 4C are listed here as candidates that fit into the relevant spectral regions.

Cell component/product	Chemical bond indicator	Spectral region (wavenumber, cm^{-1})	Candidate peaks (wavenumber)
Lipids (general)	C-H stretching (alkane)	3000-2840 [14]	2963, 2923, 2855
Proteins (general)	C=O stretching (amide I)	1700-1600 [14]	1659, 1643, 1633,
	N-H deformation (amide II)	1600-1450 [14]	1550, 1543, 1513, 1451
Polysaccharides (general)	C-O stretching (1° and 2° alcohols)	1150-1000 [15]	1120, 1082
Lysyl-phosphatidylglycerol	C-N stretching (1° amine)	1250-1020 [16]	1167, 1120
	N-H bending (amines)	1650-1580 [16]	1643, 1633,
D-alanylated teichoic acid	C-O-C vibration (ester)	1210-1163 [16]	1167

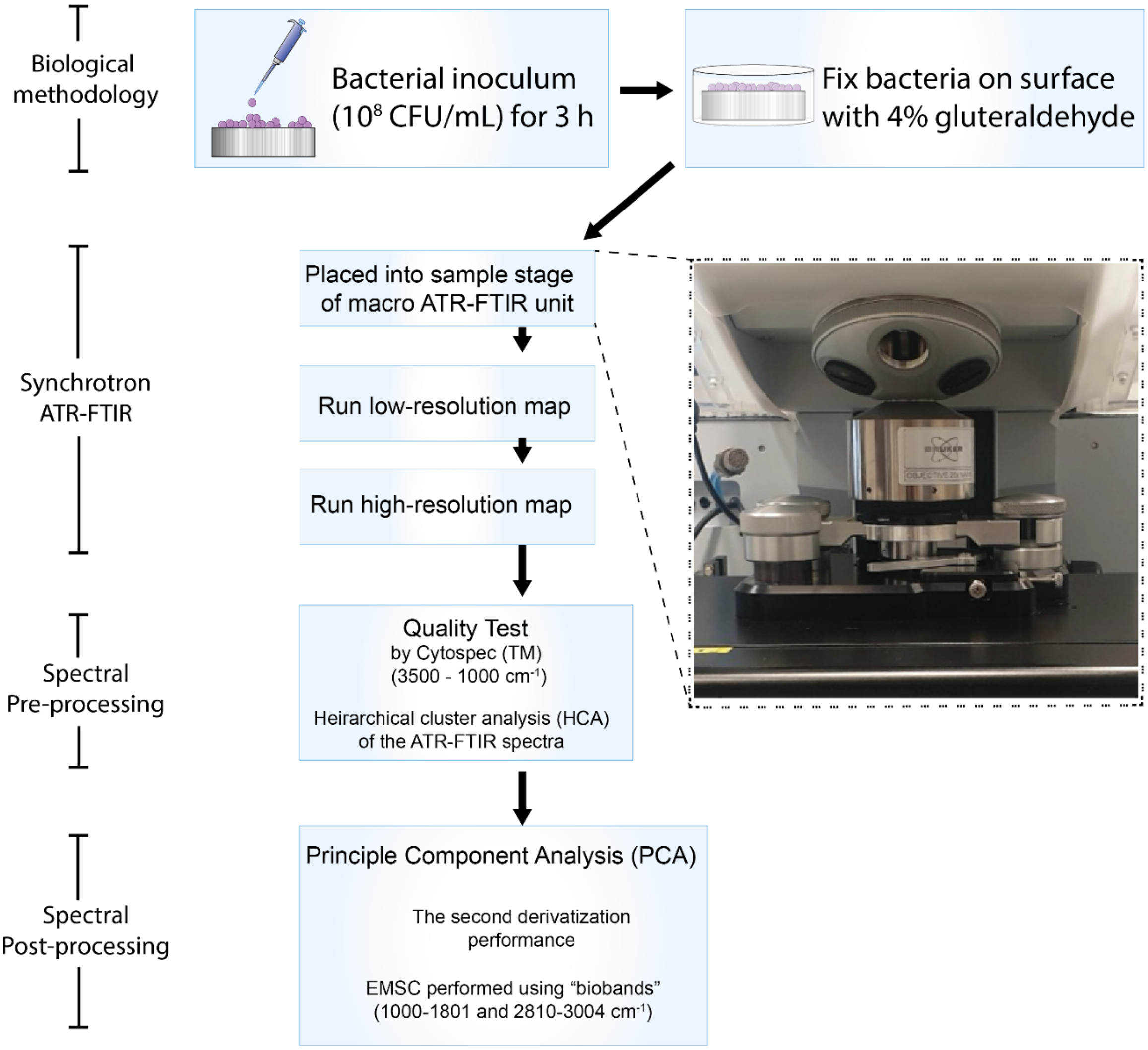

Fig. S4. The flow of analysis used to generate and process ATR-FTIR data

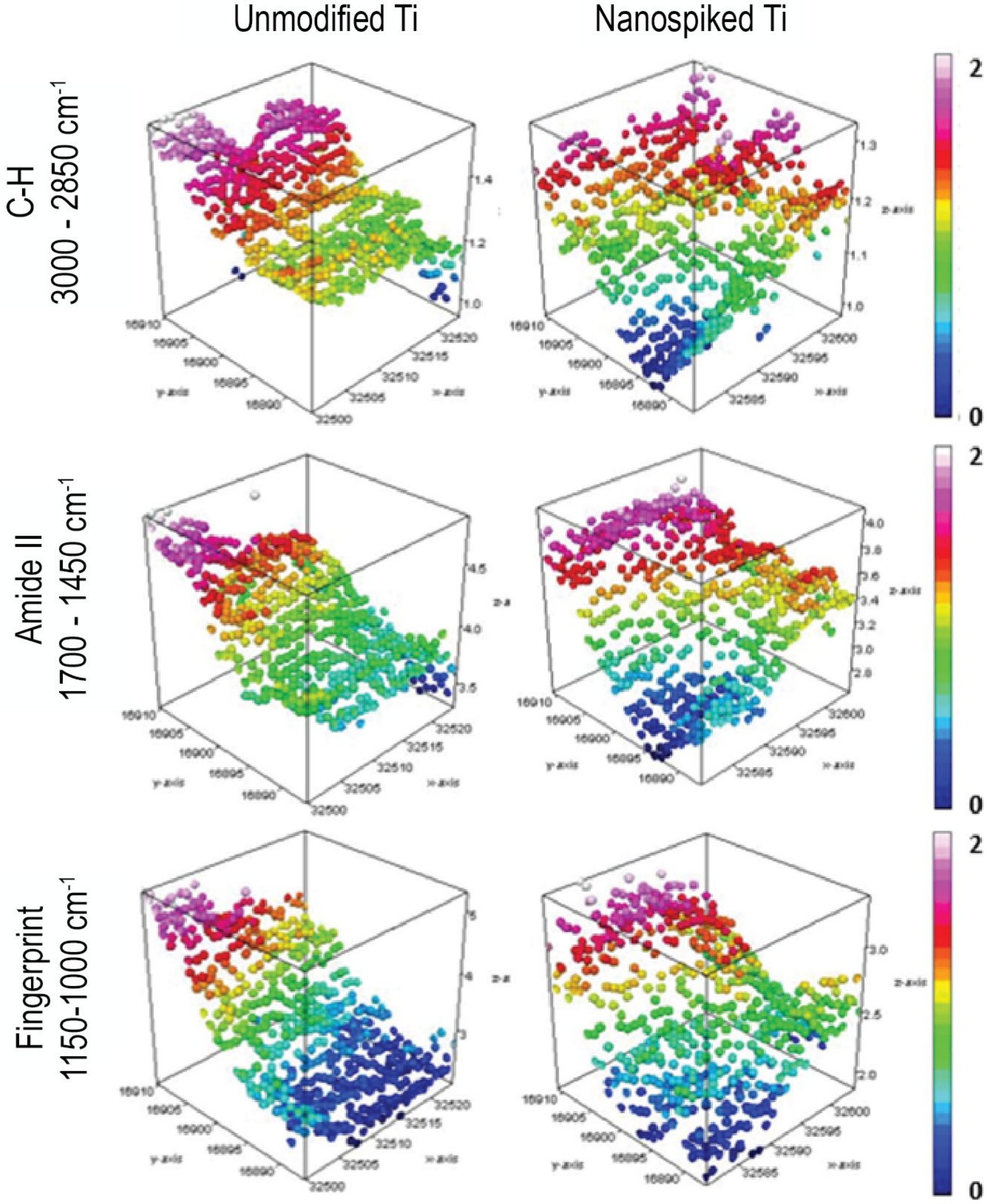

Fig. S5. 3D representations of the heat maps showing absorption intensity of the spectra associated with the 3 regions of biological interest.

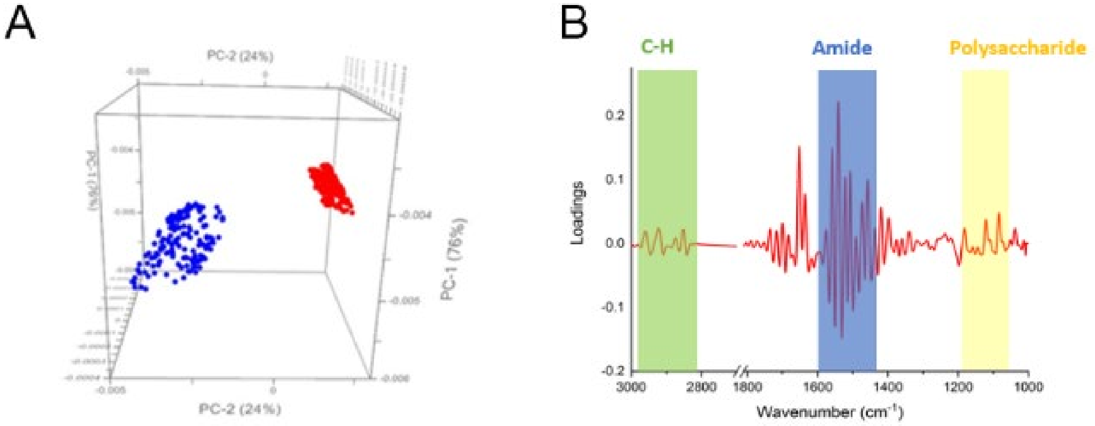

Fig. S6. Principal cluster analysis showing that PC-2 accounted for 24% of the biochemical differences between AR-Ti and HTE-Ti (A), and the associated loading spectra generated from the PC-2 analysis (B).

Minimum inhibitory concentration of vancomycin

We determined the minimum inhibitory concentration of vancomycin against planktonic cells, following the standards outlined by the Clinical and Laboratory Standards Institute.[5] Vancomycin had an MIC of 1 µg/mL against *S. aureus* ATCC 25923 (Fig. S6). This value is consistent with the commonly cited breakpoints for drug sensitivity.

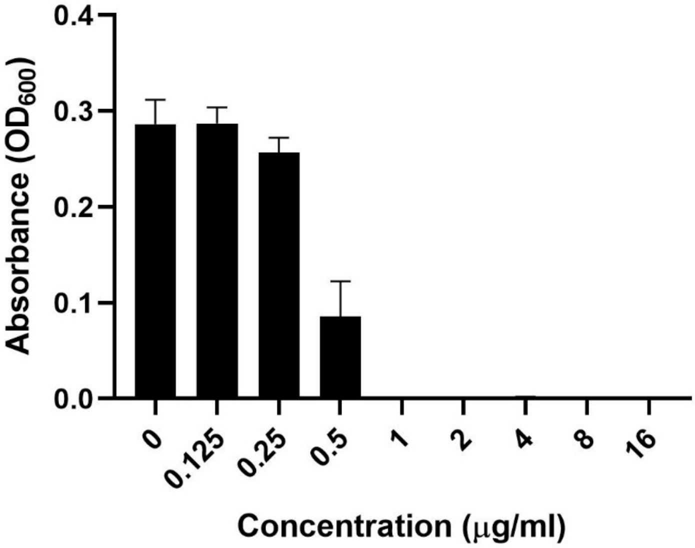

Fig. S7. Minimum inhibitory concentration of vancomycin against *S. aureus* ATCC25923

Methods

Fabrication of Nanospiked Ti surface

Ti6Al4V coupons of 10mm diameter and 3 mm height were obtained from Hamagawa Industrial SDN BHD (Kedah, Malaysia). The coupons were treated by alkaline hydrothermal processing using 1 M

KOH and heated at 150 °C for 5 h in a sealed steel vessel. Samples were then rinsed in ultrapure water and annealed for 5 h.

Material characterization of Nanospiked Ti surface

Topographical dimensions of titanium nanospikes were measured using high magnification SEM images obtained on a Zeiss Merlin FEG-SEM (Jena, Germany), with a 45° stage tilt. SEM micrographs were imported into ImageJ v1.53 (NIH, USA) for measurements. EDS spectra were obtained with an x-ray spectrometer (Aztec v3.1, Oxford Instruments, MA, USA) at 15 kV.

Wettability

Atomic Force Microscopy (AFM) of a 5 x 5 µm scan area was acquired in the air using a JPK NanoWizard III with instrument-specific software v5. An NT-MDT NSG03 silicon nitride cantilever with a conical tip rated by the manufacturer at a radius < 10 nm and a half side angle of 18° was used to perform AM tapping mode on an annealed Ti6Al4V polished control surface and a hydrothermally etched KOH nanostructure surface. Non-contact calibration of the cantilever derived a normal spring constant of 1.7 N/m. Scanning parameters were set to a scan rate of 0.7 Hz at a Set Point of 27.8 nm and a drive amplitude of 0.4 Volts. Roughness values were calculated through Gwyddion data analysis software v2.54. The Ti6Al4V control sample measured RMS at 15 nm and Ra at 12 nm. The TI6Al4V KOH nanostructure surface roughness measured RMS at 87.6 nm and Ra at 70.6 nm. Tip convolution resulting from the cantilever tip side angle and scan velocity reduces the measured surface roughness values, especially towards surface features with comparable magnitude to the tip radius.

Minimum inhibitory concentration of vancomycin

Minimum inhibitory concentration of vancomycin against *S. aureus* ATCC25923 was determined following the standards set by the Clinical and Laboratory Standards Institute (CLSI).[5] The protocol was adapted to use TSB in place of cation-adjusted Mueller-Hinton Broth. Briefly, *S. aureus* was incubated in TSB with a seeding density of $5x10^5$ cfu/mL and treated with two-fold serially diluted antibiotics between the concentrations of 0.125 and 16 µg/mL. The plates were then incubated at 37°C for 24 h, and the final cell density was measured by OD_{600} in a Synergy HTX Multi-Mode microplate reader (BioTek Instruments, Winooski, Vermont, USA).

References

1. Bright, R., A. Hayles, D. Fernandes, R.M. Visalakshan, N. Ninan, D. Palms, A. Burzava, D. Barker, T. Brown, and K. Vasilev, In Vitro Bactericidal Efficacy of Nanostructured Ti6Al4V Surfaces is Bacterial Load Dependent. *ACS Applied Materials & Interfaces*, 13(32): p. 38007-38017 (2021).

2. Marshall, C.G., G. Broadhead, B.K. Leskiw, and G.D. Wright, D-Ala-D-Ala ligases from glycopeptide antibiotic-producing organisms are highly homologous to the enterococcal vancomycin-resistance ligases VanA and VanB. *Proc Natl Acad Sci U S A*, 94(12): p. 6480-3 (1997).
3. Jia, Z., M.L. O'Mara, J. Zuegg, M.A. Cooper, and A.E. Mark, Vancomycin: ligand recognition, dimerization and super-complex formation. *The FEBS Journal*, 280(5): p. 1294-1307 (2013).
4. Po, H.N. and N.M. Senozan, The Henderson-Hasselbalch Equation: Its History and Limitations. *Journal of Chemical Education*, 78(11): p. 1499 (2001).
5. CLSI, *Performance Standards for Antimicrobial Susceptibility Testing. 30th ed*. 2020: Clinical and Laboratory Standards Institute.

CONCLUSIONS AND FUTURE WORK

Conclusions

Despite decades of improvements in surgical practices and biotechnologies, the ever-present threat of implant associated infection remains a considerable burden. The presence of a foreign material, such as a biomedical implant, will always be an enticing platform for microbial pathogens to attach and form a biofilm to evade the immune system and persist through antimicrobial drugs. This is further compounded by the rapidly emerging drug resistance in bacterial and fungal pathogens. As antimicrobial chemotherapies are steadily becoming less effective, the importance of prevention is becoming increasingly emphasized. Over the past decade, a significant amount of research has been focused on using surface modifications which mechanically disrupt and kill colonizing microbes. This strategy is enticing for multiple reasons. Firstly, a contact-dependent bactericidal mechanism is, in principle, a strong preventative force against microbial colonization. Secondly, microbes are much less likely to develop resistance mechanisms against mechano-bactericidal technologies, as this would require substantial structural and physiological changes to enable them to withstand the mechanical pressures involved. In the present thesis, we have produced a detailed characterization of the interactions between microbial pathogens (bacteria and fungi) and hydrothermally etched titanium (HTE-Ti, a promising mechano-bactericidal surface modification).

In the introduction of the present thesis, the context of the problem was introduced. The details of biofilm formation were briefly presented, and the medical implications of this were also discussed. The concept of mechano-bactericidal surfaces was then introduced, with reference to their origin in nature. This was then followed by a summary of the current methods of fabrication of synthetic analogues for mechano-bactericidal surfaces. Hydrothermal etching of titanium was then introduced as an attractive fabrication method, which is scalable, cheap, simple, and environmentally friendly. This was followed by a detailed analysis of how fabrication parameters can be optimized to enhance bactericidal efficacy, as well as a description of the mechanism of action. From the literature summarized in the introduction, gaps in the current knowledge were identified. This then served as a basis for the research questions subsequently investigated throughout this thesis.

Chapter 1 discusses the efficacy of HTE-Ti in combating the fungal pathogen *C. albicans*. This was an important research question because, as the name suggests, mechano-bactericidal surfaces have primarily been studied in the context of bacterial infections. In this study, it was determined that the interactions between HTE-Ti and *C. albicans* are markedly different to the interactions involving bacteria. This was somewhat expected, as *C. albicans* is a eukaryotic organism, and therefore its structural properties are distinct from those of bacteria. In this chapter, it was shown than HTE-Ti does not directly kill *C. albicans* cells, but instead it inhibits them from forming hyphae. This has implications for the pathogenesis of candidemia, a systemic fungal infection stemming from the invasion of *C. albicans* into the bloodstream. A differential gene expression analysis identified differences in key genes associated with hyphal formation. Overall, the net effect of HTE-Ti against *C. albicans* is a reduction in biofilm and an inhibited ability to form hyphae. Furthermore, these effects increased the efficacy of the antifungal drug amphotericin B, which was able to clear an established fungal biofilm only when incubated on the HTE-Ti surface.

In chapter 2, the research was focused on the efficacy of HTE-Ti against anaerobic pathogens commonly found in peri-implant disease. This was an important research question because evidence suggests that one of the key mechanisms responsible for the mechano-bactericidal effect is the intracellular generation of reactive oxygen species, and subsequently an oxidative stress response in the cell. Therefore, for HTE-Ti to be a suitable biomaterial for dental applications, the bactericidal effect must be active even in the absence of oxygen. To be closely relevant to peri-implantitis, the pathogens at the centre of this study were *S. mutans*, *F. nucleatum*, and *P. gingivalis*. Interestingly, it was shown that despite the lack of oxygen present in the anaerobic culture, the mechano-bactericidal effect still persisted, suggesting that the mechanical effect itself was sufficient to elicit bactericidal actions. The net effect of this was a reduction in biovolume of the 3 pathogens, and an increased susceptibility of *S. mutans* and *P. gingivalis* to the antibiotic azithromycin.

In chapter 3, the HTE-Ti surface was challenged with multiple bacterial species simultaneously. This study was important because, in the clinical setting, implant infections frequently involve more than a single species. Despite this, current literature has only focused on single species interactions. It is well established that bacteria not only interact within their own species, but also across species. Such cross-species interactions can lead to mutually beneficial outcomes such as enhanced biofilm formation and protection against the host immune system and antibiotics. Therefore, we investigated two dual-species interactions on HTE-Ti, either *E. coli* mixed with *S. aureus*, or *E. coli* mixed with *E. faecalis.* Overall, we found that the mechano-bactericidal effect was sufficient to reduced biofilm formation and viability of all species involved in these two mixed cultures. Furthermore, using fluorescence in situ hybridization, we observed a shift in species arrangements within the biofilms measured. When testing the *E. faecalis* and *E. coli* mixture, the HTE-Ti surface promoted a reduction in species diversity, favouring *E. faecalis* over *E. coli*. When polymicrobial infections are present, broad-spectrum antibiotics become necessary to provide inhibitory coverage to a range of involved species. This is actively detrimental because broad spectrum antibiotics strongly promote the emergence of drug resistance. Therefore, any means of reducing species diversity is a benefit.

In chapter 4, we address the prospective strategy of combining the bactericidal effects of prophylactic antibiotics and the mechano-bactericidal effect of HTE-Ti. This study was important because it addresses the situation that would occur during the surgical placement of an HTE-Ti implant. We tested this strategy with vancomycin, a cell-wall active antibiotic commonly used in surgical prophylaxis. We observed that when *S. aureus* was attached to HTE-Ti, it was still able to be completely eradicated using the antibiotic. This is an impressive result because when an unmodified surface is used, the antibiotic failed to clear the vast majority of cells. We further investigated the physiological difference between *S. aureus* cells on unmodified and HTE-Ti surfaces, and we identified differences in the expression of genes associated with modification of the charge of cell surface structures. Specifically, on the unmodified surface, *S. aureus* upregulated genes which reduce the net negative charge of teichoic acids and the phospholipid bilayer. This process did not occur on *S. aureus* cells incubated on the HTE-Ti surface. We further supported this observation using synchrotron ATR-FTIR, which revealed greater intensities in the spectral regions associated with the described structural modifications. Overall, these results suggests that implants with the HTE-Ti surface modification are able to support prophylactic antibiotic treatment, and therefore may reduce the incidence of surgical site infections from occurring.

Future Work

In the present thesis, a significant amount of work has been directed toward validating HTE-Ti as a suitable anti-infective surface modification that has the potential to minimize implant associated infection. The evidence presented here is promising, but still more data is needed before large scale commercialization can begin. The following is a series of points underscoring some of the future research that will be necessary in order to successfully translate this promising technology into a clinical reality.

1. *Enhancement of the mechano-bactericidal effect through altering the surface chemistry*

Although the bactericidal efficacy or HTE-Ti is evidently strong, particularly against Gram-negative bacteria, the nanoscale protrusions alone are unable to kill an entire Gram-positive population. As discussed in the introduction of this thesis, one of the factors influencing the bactericidal efficacy of HTE-Ti is the adhesive force between the bacterial cell and the nanoscale protrusions. A stronger adhesive force is likely to draw the adherent cell deeper into the nanostructured topography and improve the rates of bacterial cell death. One way of achieving this may be to add coatings to HTE-Ti to rationally manipulate the hydrophilicity and surface charge characteristics.

2. *The effects of long-term fouling on the bactericidal efficacy of HTE-Ti*

Throughout this thesis, the bactericidal performance of HTE-Ti was investigated over short periods of time, no longer than 10 days. However, it is conceivable that over longer periods of time, fouling of the surface may become an issue limiting its performance. This should be appropriately investigated using dynamic flow conditions to provide a consistent input of fresh culture media, in addition to a consistent output of exhausted media and cellular waste. Such a system can be operated for long periods of time, allowing for analysis of the surface fouling.

3. *In vivo models and clinical trials*

While all the data presented thus far has been promising, the most important aspect of a novel biomaterial is its safety and efficacy within its intended biological application. Throughout the research presented in this thesis, cytocompatibility measurements have been taken using a range of mammalian cell lines. In every case, the mammalian cells have been able to interact positively with the HTE-Ti surface, not losing any significant viability. However, these measurements alone do not provide sufficient biosafety information, and biocompatibility of the surface must be investigated in a mammalian host with all its complexities. Furthermore, it is still unclear how the bactericidal efficacy of the surface would be influenced following exposure to mammalian serum and synovial fluids. It is possible the protein adsorption to the HTE-Ti surface may enhance the bactericidal performance (by strengthening adhesion between bacteria and the nanoscale protrusions), or decrease its performance (by filling the interstitial spaces between protrusions and making them more blunt). Ultimately, these questions must first be answered in an appropriate animal model, before human clinical trials can take place.